Transport and real-time dynamics in one-dimensional quantum magnets and ultra-cold atomic gases

Stephan Markus Langer

München 2012

Transport and real-time dynamics in one-dimensional quantum magnets and ultra-cold atomic gases

Dissertation
an der Fakultät für Physik
der Ludwig-Maximilians-Universität
München

vorgelegt von
Stephan Markus Langer
aus Lüdenscheid

München, den 18. 6. 2012

Zusammenfassung

Ziel der hier vorliegenden Arbeit ist das Studium der Dynamik und der Transporteigenschaften von Quantenmagneten und ultrakalten Atomgasen in einer Raumdimension mithilfe numerischer Methoden. Der Schwerpunkt hierbei liegt auf der Frage nach diffusiver oder ballistischer Dynamik und einer genauen Analyse der in ballistischen Regimes auftretendend Geschwindigkeiten. Hierzu werden, unter anderem, zeitabhängige Dichteprofile im Nichtgleichgewicht mithilfe der adaptiven zeitabhängigen Dichtematrix-Renormierungsgruppe (DMRG) simuliert. Diese numerische Methode erlaubt die Simulation zeitabhängiger Wellenfunktionen in einer kontrollierten Art und Weise sowohl im als auch weit entfernt vom Gleichgewicht.

Motivation für das Studium ein-dimensionaler Quantenmagnete ist unter anderem die stark anisotrope und für Isolatoren überdurchschnittlich hohe Wärmeleitfähigkeit bestimmter Cuprate. Die Annahme einer linearen Antwort erlaubt das Studium von Transport bei beliebiger Temperatur, mithilfe der Kubo-Formel. Diese wird durch exakte Diagonalisierung kleiner Systeme und Berechnung der Strom-Strom Korrelationsfunktion ausgewertet und so auf drei unterschiedliche Fragestellungen angewendet. Zuerst diskutiere ich den Spintransport einer Spin$-1/2$ Heisenbergkette mit anisotroper Austauschwechselwirkung (XXZ-Kette) bei endlicher Temperatur.

Als zweite Anwendung exakter Diagonalisierung, hier in Verbindung mit zeitabängiger DMRG, werden die transversalen Komponenten der Strom-Strom Korrelationsfunktion diskutiert. Während für die Diskussion der Transporteigenschaften jediglich ein Zeeman-Feld in Betracht gezogen wird, untersuchen wir hier die Dynamik die durch ein zusätzliches transversales Feld induziert wird. Es stellt sich heraus, dass die transversale Komponente der Strom-Strom Korrelationsfunktion kohärente Oszillationen aufweist. Zuätzlich zur üblichen Larmor-Präzession tritt hierbei eine zweite, nicht-triviale Frequenz auf, deren Frequenz- und Feldabängigkeit studiert wird.

Anschliessend berechnen wir die frequenzabhängige Spin und Wärmeleitfähigkeit dimerisierter Spinketten im Magnetfeld. Motiviert durch die experimentelle Untersuchung des Phasendiagrams von $C_5H_{12}N_2CuBr_4$ wird die dimerisierte Spin$-1/2$ Kette als minimales Modell den experimentell gefundenen Phasen diskutiert und gezeigt das im Rahmen der Näherung einer linearen Antwort die Spin- und Wärmeleitfähigkeit in der feld-induzierten lückenlosen Phase deutlich ansteigen.

Die letzte Anwendung im Bereich der ein-dimensionalen Quantenmagnete ist die Simulation zeitabhängiger Energiedichten einer XXZ-Kette sowohl nah

6

am als auch fern vom Gleichgewicht, mithilfe der adaptiven zeitabhängigen Dichtematrix Renormierungsgruppe. Neben der Klassifizierung der Dynamik als diffusiv oder ballistisch war es möglich die im ballistischen Fall auftretenden Geschwindigkeiten zu verstehen.

Die Anwendungen auf ultrakalte Atomgase konzentrieren sich auf die abrupte Expansion eines Gases aus einer Falle heraus in ein leeres optisches Gitter. Diese wurde kürzlich von U. Schneider *et al.* im Fall des zweidimensionalen Fermi-Hubbard Modelles experimentelll durchgeführt und im Kontext des elektronischen Transports diskutiert. Zur Behandlung von drei verschiedenen Fragestellungen, simulieren wir hier zeitabhängige Dichte- und Impulsverteilungen.

Im Falle einer nicht-polarisierten Wolke aus Fermionen konnten wir das ballistische Regime identifizieren und so die mittlere Expansionsgeschwindigkeit definieren. Es stellt sich heraus, dass die Expansionsgeschwindigkeit in einem weiten Parameterbereich nur von einer kleinen Teilmenge der Anfangsbedingungen abhängt. Zum Beispiel, zeigt eine bekannte Phase des Fermi-Hubbard Modells, der Mottisolator, eine konstante Expansionsgeschwindigkeit unabhängig von der Stärke der Wechselwirkung.

Für die Expansion spinloser Bosonen verwenden wir Anfangszuständen mit fester Teilchenzahl pro Gitterplatz bei verschiedenen Fehlstellenkonzentrationen und ermitteln die Expansionsgeschwindigkeit als Funktion der Wechselwirkungsstärke. Desweiteren werden die zeitabängigen Impulsverteilungen auf Anzeichen eines sich dynamisch bildenden Quasikondensats untersucht.

Als letztes Beispiel simulieren wir die Expansion eines spin-polarisierten fermionischen Gases bei attraktiver Wechselwirkung. Hier steht der noch zu erbringende experimentelle Nachweis des Fulde-Ferrell-Larkin-Ovchinnikov-Zustands im Vordergrund. Unsere Analyse der Impulsverteilungen und der Paar-Wellenfunktion zeigen das einerseits die Charakteristika der FFLO-Phase schnell verschwinden, aber andererseits auch schnell eine stationäre Form der Impulsverteilungen erreicht wird. Diese wiederum kann auf den Anfangszustand zurück geführt werden, was eine indirekte Detektion ermöglichen könnte.

Abstract

The goal of this thesis is to study the transport properties and real-time dynamics of quantum magnets and ultra-cold atomic gases in one spatial dimension using numerical methods. The focus will be on the discussion of diffusive versus ballistic dynamics along with a detailed analysis of characteristic velocities in ballistic regimes. For the simulation of time-dependent density profiles we use the adaptive time-dependent density matrix renormalization group (DMRG). This numerical method allows for the simulation of time-dependent wave functions close to as well as far from equilibrium in a controlled manner.

The studies of one-dimensional quantum magnets are partially motivated by the experimental evidence for a highly anisotropic and for insulators comparably high thermal conductivity of certain cuprates. We use linear response theory to study transport coefficients at arbitrary temperatures by diagonalizing small systems exactly and then calculating the current-current correlation functions. As first application we discuss the spin transport in the spin-1/2 Heisenberg chain with anisotropic exchange interactions (XXZ-chain).

The second application of exact diagonalization, here in combination with time-dependent DMRG, is a discussion of the transverse components of the current-current correlation function. While usually only a Zeeman field is considered in the theory of transport coefficients, we here investigate the dynamic induced by an additional transverse magnetic field. We find that in this scenario the current-current correlation function exhibits coherent oscillations. In addition a second non-trivial frequency, different from the one expected from the usual Larmor precession, emerges and is studied varying temperature and field.

Finally we calculate the frequency-dependent spin and heat conductivity of dimerized spin chains in a magnetic field. Motivated by the recent experimental studies of the phase diagram of $C_5H_{12}N_2CuBr_4$ we take the dimerized chain as a minimal model that exhibits features of the low-temperature region of the observed phase diagram. As a main result, the spin and heat conductivity obtained from linear response theory are enhanced in the field-induced gapless phase.

The last application in the field of one-dimensional quantum magnets is the simulation of time-dependent energy-density wave-packets close to as well as far from equilibrium using the time-dependent density renormalization group. The main results are ballistic energy dynamics independently of how

far out-of-equilibrium the initial state is and a detailed understanding of the average expansion velocity.

The applications in the field of ultra-cold atomic gases focus on the sudden expansion of an initially trapped gas into an empty optical lattice. This setup was recently realized in an experiment performed by U. Schneider *et al.* and discussed in the context of electronic transport in the two-dimensional and the three-dimensional Fermi-Hubbard model. Here we investigate the sudden expansion of three different setups:

For the expansion of a spin-balanced cloud of fermions, we identify the ballistic regime, and therein investigate the average expansion velocity of the cloud. As a main result the expansion velocity is determined by a small subset of the initial condition over a wide range of parameters. For instance, the Mott-insulating phase of the Hubbard model is characterized by a constant expansion velocity independently of the strength of the interaction.

In the case of spinless bosons, we study the expansion from initial states that have a fixed particle number per lattice site and a certain concentration of defects. We study the expansion velocity as a function of interaction strength and investigate whether the time-dependent momentum distribution functions indicate a dynamical quasi-condensation.

The last example is the sudden expansion of a spin-polarized gas of fermions in the presence of attractive interactions. This study is motivated by current effort to experimentally detect the Fulde-Ferrell-Larkin-Ovchinnikov state. Our results for the time-dependent momentum distribution functions and the wave-function of the pair condensate suggest that the signatures of the FFLO state vanish quickly, yet a stationary form of the momentum distribution also emerges fast. The latter is shown to be determined by the initial conditions, which might eventually allow for an indirect detection of the FFLO phase.

List of publications

During the course of my work, the following articles have been published in peer-reviewed journals or made been available as preprints on www.arxiv.org. They also constitute the respective chapters of this thesis.

1. Long-time behavior of the momentum distribution during the sudden expansion of a spin-imbalanced Fermi gas in one dimension
   C.J. Bolech, F. Heidrich-Meisner, S. Langer, I.P. McCulloch, G. Orso, M. Rigol
   Preprint arxiv:1206.2019, submitted to Phys. Rev. Lett.

2. Ballistic dynamics during the sudden expansion of a two-component Fermi gas in a one-dimensional lattice
   S. Langer, M.J.A. Schuetz, I.P. McCulloch, U. Schollwöck, F. Heidrich-Meisner
   Phys. Rev. A 85, 043618 (2012)

3. Real-time energy dynamics in spin-1/2 Heisenberg chains
   S. Langer, M. Heyl, I. P. McCulloch, F. Heidrich-Meisner
   Phys. Rev. B 84, 205115 (2011)

4. Coherent spin-current oscillations in transverse magnetic fields
   R. Steinigeweg, S. Langer, F. Heidrich-Meisner, I. P. McCulloch, W. Brenig
   Phys. Rev. Lett. 106, 160602 (2011)

5. Field-dependent spin and heat conductivities of dimerized spin-1/2 chains
   S. Langer, R. Darradi, F. Heidrich-Meisner, W. Brenig
   Phys. Rev. B 82, 104424 (2010)

Contents

1   Introduction

The transport properties and dynamics of low-dimensional systems governed by the laws of quantum mechanics are a hot topic for experimental as well as theoretical physicists as it is being studied in many different fields such as quantum magnets [1, 2, 3], mesoscopic systems [4], nanoscience [5] and ultracold atomic gases [6, 7]. A great advantage for theorists is that essential physics of the systems, whose transport properties are measured in experiment, can be captured by model Hamiltonians that do not depend on the specifics of the sample such as its atomic structure. Among those model systems, one-dimensional quantum systems, such as a quantum wire or a spin chain, have the intriguing property that the role of interactions is of greater importance than in higher dimensions, only due to the dimensionality [8]. For instance, among interacting electrons in a one-dimensional wire, no electron can move without displacing its neighbors. Such strong correlation effects give rise to exotic phases such as the Tomonaga-Luttinger-Liquid [9, 10].

While historically one-dimensional systems were first seen as theoreticians' toy models, nowadays we have a steadily growing number of experimental systems available that realize such low-dimensional structures. A famous example are the experimental advances in the field of high-temperature superconductors, driving the pursuit to understand and predict novel phases of electrons confined to one or two spatial dimensions [11, 12]. The fact that fluctuations of magnetic origin are likely to play a role in this context [13, 14, 15] also renewed the interest in quantum magnetism [16]. Examples of bulk materials with strongly anisotropic magnetic interactions are the family of spin ladder materials $(\text{Sr,Ca,La})_{14}\text{Cu}_{24}\text{O}_{41}$ [17] or spin chains like Sr_2CuO_3 [18]. Many new applications for one-dimensional models can be found in experimental systems specifically engineered towards low-dimensionality, e.g. carbon nanotubes [19], quantum wires [20] or ultracold atomic gases in optical lattices [21].

As a famous example of one-dimensional model systems, the spin-1/2 Heisenberg chain is one of the fundamental models to describe magnetic properties of interacting electrons [22]. Yet, it is not only relevant to the physics of low-dimensional quantum magnets [23]. It has also been employed to describe ultra-cold atoms in optical lattices [24] and nanostructures [20, 25]. The other fundamental model of interest for this thesis is the one-dimensional Hubbard model [26], which describes fully interacting electrons and has been applied to a similarly broad range of problems as the Heisenberg model [27]. Although the Heisenberg and the Hubbard model are both exactly solv-

able in one spatial dimension by means of the Bethe ansatz [28] dynamical quantities, especially in real-time and out-of-equilibrium, are in general hard to access within this approach. To advance the theoretical understanding, many sophisticated approaches can be employed to obtain such quantities. Among them are powerful numerical methods such as quantum Monte-Carlo (QMC), exact diagonalization (ED) [see [29] for a recent review on both] and the density matrix renormalization group (DMRG) [30].

The goal of this thesis is to study the transport properties and real-time dynamics of quantum magnets and ultra-cold atomic gases in one spatial dimension using a combination of ED and DMRG methods. A recurrent theme will be the discussion of diffusive versus ballistic dynamics. When describing small perturbations, linear-response theory [31] is a powerful framework to analyze transport properties. Within linear response the question of ballistic and diffusive transport boils down to the analysis of the so called Drude weight [32], which is the prefactor of a delta-function at zero-frequency in the frequency-dependent transport coefficient. A finite Drude weight defines an ideal conductor in the sense that a finite part of a current driven through the system does not decay over time, which is one of the hallmarks of ballistic dynamics. In the case of a vanishing Drude weight the zero-frequency limit of the conductivity determines if the dynamics is diffusive for long times [33].

The common theme throughout this thesis is the connection between the transport properties and the real-time dynamics of density wave-packets and currents for a given model system. The main reason to establish such a connection is that, while linear response theory is a very useful approach for weakly perturbed states and will also be employed to obtain interesting results in the following, it is a priori not clear whether the results will have any relevance when the system is driven out-of-equilibrium. Using the adaptive time-dependent DMRG [34, 35] we are able to study the non-equilibrium dynamics in real-time by following the dynamics of initial states such as a highly perturbed spin chain, or a suddenly expanding gas released from a trap. Among the main results are the identification of ballistic regimes far from equilibrium and a detailed analysis of the relevant expansion velocities in these cases. In particular, we will show how the average expansion velocity can be used as a tool to probe the initial state of a trapped two component Fermi gas, for instance to study quantum phase transitions.

In the context of ballistic and diffusive dynamics, the spin-1/2 Heisenberg chain has remained a very interesting topic throughout the years [2]. Based on a strong connection between transport and conservation laws [36] this integrable model allows for rigorous conclusions. For instance, ballistic heat

transport in the linear response regime at arbitrary temperatures has been predicted [36] and been confirmed by numerical as well as analytical studies [37, 38, 39]. Yet, the spin transport properties are still subject of research [40, 41, 42, 43, 44, 45, 46]. Much less is known about out of equilibrium situations, such as real-time dynamics in out-of-equilibrium situations [47, 48, 49] or transport at large driving forces [50, 51, 52].

Besides the fundamental interest in understanding large-bias and out-of-equilibrium phenomena, research into transport properties of low-dimensional spin systems is strongly motivated by exciting experimental results on large thermal conductivities in spin ladder and chain materials. The family of spin ladder compounds $(Sr,Ca,La)_{14}Cu_{24}O_{41}$ and other materials, when subjected to transport measurements, exhibit anomalous anisotropic heat transport (see Refs. [3, 53] for reviews) which has been understood as magnetic contribution from the underlying one-dimensional quantum magnet. More recently, time resolved measurements of the spreading of heat on the surface of $Sr_9La_5Cu_{24}O_{41}$ after a short laser pulse [54, 55] have extended the experimental research to the non-equilibrium context. Modifying the geometry and strength of the interactions by growing new compounds is also actively pursued and yields interesting options for further experiments. For instance, organic superconductors have been shown to exhibit spin ladders which have exchange couplings two orders of magnitude lower than the copperoxide based compounds [56, 57]. As one of the interesting consequences, it was possible to experimentally access the magnetic phase diagram and study the field-induced gapless phase, which shows signatures of Luttinger liquid physics [56, 57].

Our results for quantum magnets can be summarized in three groups: First, we consider spin transport in the Heisenberg chain at finite temperatures in the linear response regime. Revisiting this still controversially discussed problem, we extract the spin Drude weight from ED data for the response functions and obtain reasonable agreement with recent DMRG data [58] and analytical results [59]. As ED is limited to small system sizes, we also address the choice of the thermodynamical ensemble in which we evaluate the response functions [60].

We then proceed to study a previously unexplored aspect of linear response theory, namely the transverse components of the current-current correlation functions, the basic building block of the linear response functions. Usually only a Zeeman field is considered in the theory. By adding a transverse component to the field we induce oscillations in the transverse current-current correlation function, which become coherent in the limit of low tem-

peratures. The frequency spectra of these oscillations exhibit a non-trivial frequency in addition to the expected Larmor precession. In the limit of high temperatures and Zeeman fields, we qualitatively explain this effect based on the two-magnon spectra. At intermediate temperatures we calculate the dependence of the frequency of the coherent oscillations on temperature and the Zeeman field using exact diagonalization. At zero temperature we use time-dependent DMRG to analyze the transverse component of the time-dependent spin current, finding the same frequency shift and also a quantitative agreement between the two methods regarding its field dependence.

Next we study the spin and heat conductivity of low-dimensional quantum magnets that exhibit a field-induced gapless phase. Motivated by the recent experimental observations of such phase transitions [56, 57], we study the dimerized spin-1/2 chain as a minimal model that exhibits the essential features of the phase diagram. Calculating the frequency-dependent transport coefficients with ED, we find both, spin and heat transport to be strongly enhanced throughout the field-induced gapless phase. This effect originates from clear signatures of the phase transition in the current-current correlation functions that should in principle be observable in transport measurements.

The final group of results on quantum magnets is obtained through studying the real-time dynamics of the energy density in a Heisenberg chain with anisotropic exchange interactions at zero temperature. We apply time-dependent DMRG to investigate the time-evolution of initial states which feature an inhomogeneous local energy density. As main result, we are able to show that the energy dynamics is ballistic independently the anisotropy and independently of how far we drive the system out of equilibrium. We compare our findings to those obtained within Luttinger liquid theory, which predicts ballistic spin and energy dynamics with a single fixed expansion velocity. Furthermore, we recover the expansion velocity of the Luttinger liquid from our numerical simulations in the limit of weak perturbations Finally, we are able to explain the average expansion velocity energy density far from equilibrium in terms of the difference between the momentum distribution of the initial state and the one of the groundstate.

Our motivation to study the non-equilibrium dynamics in the Hubbard model comes from the comparably young field of ultra-cold atomic gases, which has established a completely new playground for quantum physics [21]. By trapping and cooling bosonic atoms down to the nano Kelvin regime, experimentalists obtained access to the quantum degenerate regime, the first great achievement being the observation of Bose-Einstein condensation [61, 62, 63].

Engineering an optical lattice using counter-propagating laser beams, gives such systems the potential to realize the Hubbard model [64]. Using optical lattices also allows to choose the dimensionality of the system under investigation [65]. The last ingredient towards tunable realizations of strongly correlated quantum systems comes under the name of Feshbach resonance [21], a sign changing pole in the scattering length as a function of an external magnetic field allowing precise control of the interaction between the trapped atoms. While fermions are technically harder to cool to sufficiently low temperatures, several experiments have nevertheless achieved this feat [66, 67, 68]. To give an example for the investigation of a strongly correlated system, a three dimensional Mott insulator and other phases of the Hubbard model have been realized [69, 70] in experiments.

These techniques to experimentally study non-equilibrium dynamics within the Hubbard model have been applied successfully using both, fermionic [7, 71] and bosonic [72, 73] atoms. Many experiments studying the non-equilibrium dynamics of ultra-cold atomic gases, e.g. Refs [72, 73], investigated dynamics induced by globally quenching a model parameter. With the focus being on topics like relaxation and thermalization (see [6] for a recent review) a finite net current is usually not desired and hence sought to suppress. Yet, several recent experiments were deliberately performed in the presence of finite spin or particle currents [7, 71, 74, 75, 76, 77]. These experiments provide a complementary point of view on the dynamical properties of the underlying lattice model as the initial states engineered are often not typical for bulk systems [74]. An important aspect of this thesis is motivated by sudden expansion experiments such as the one performed in Ref. [7]. The idea is to have an initially trapped cloud of bosonic or fermionic atoms, in a confining potential. At time $t = 0$ the confinement is removed and the gas expands freely under the action of the respective lattice Hamiltonian. In particular, Ref. [7] studies the expansion starting from a fermionic band insulator (exactly two particles per site) into a homogeneous empty optical lattice in two and three spatial dimensions. While transport in bulk systems is usually considered in the presence of a finite background density of spins or electrons, here all particles participate in the expansion and hence the background density is time-dependent. To illustrate this idea Fig. 1 sketches the two different types of real time dynamics studied in this thesis. The left panel shows the expansion of a idealized gaussian density wave-packet on top a homogeneous background density. The right panel illustrates the sudden expansion of an initially trapped cloud of atoms induced by the removal of the harmonic confining potential. The cloud then expands freely into the
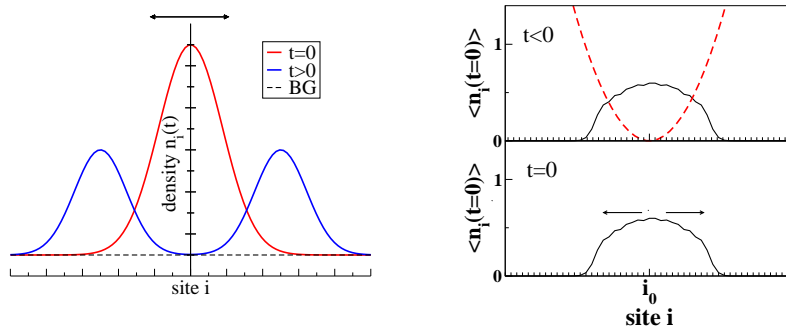
Figure 1: A sketch of a the two different scenarios, for which, the real-time dynamics of a density $n_i(t)$ on a lattice model will be investigated in this thesis. Left: Expansion of a density wave-packet on top of a finite background density (BG). Right: Sudden expansion of a initially trapped density cloud into an empty (optical) lattice, after the removal of the confining potential.

empty lattice.

We consider the sudden expansion of an initially trapped cloud of atoms described either by the Bose-Hubbard or the Fermi-Hubbard model in one spatial dimension under three different aspects. First, we study the expansion of a repulsive spin-balanced Fermi gas and analyze the nature of the dynamics. As a main result we find that the dynamics is ballistic whenever the initial density inside the trap is smaller or equal to one. As a necessary consequence of the ballistic dynamics, the cloud radius $R(t)$ increases linearly in time, which allows us to define the average expansion velocity as the slope of $R(t)$. We then analyze the expansion velocity as a function of interaction and density, finding that the main effect of repulsive interactions is to change the energy of the initial state in the trap and through that, to also change the expansion velocity. Furthermore, we argue that probing the average expansion velocity indirectly probes the momentum distribution of the initial state. Therefore, sudden expansion experiments or simulations can be used to probe quantum phase transitions in the initial state if the respective transitions changes the momentum distribution function drastically. To give an example, we show that the expansion velocity for the expansion from an initial state in the Mott-insulating phase is completely determined by symmetry and independent of the strength of the interaction. We finally show that our qualitative findings are robust against the presence of a harmonic trap where the density in the initial state is inhomogeneous. Thus we make

exact predictions for experiments which would realize the setup of Ref. [7] in one spatial dimension, yet with different initial states.

Second, we consider the sudden expansion of bosons, but instead of starting from the ground state of the trap, we prepare the system in a pure Fock state, where each particle sits on a given lattice site. The reason is twofold: On the one hand, such an initial state can be experimentally prepared by ramping up the lattice before the sudden expansion. One the other hand, pure Fock states have been shown to exhibit the most pronounced dynamical quasi-condensation at finite momenta upon expanding [78, 79, 80]. Dynamical quasi-condensation in this context means the dynamical emergence of coherence during the sudden expansion. Furthermore non-zero momenta $\pm k$ become macroscopically occupied during the expansion, even though the initial momentum distribution is flat. While an initial Fock state is completely uncorrelated and a bosonic Mott insulator has exponentially decaying correlations the expanding gas shows a power-law decay of correlations [78, 79, 80]. Here we investigate the expansion velocity for the sudden expansion from pure Fock states and the dynamical quasi-condensation at intermediate interaction strength. Then we introduce a finite defect density, namely holes in the Fock state and doubly occupied sites, which are both likely to be present in a typical experiment. We find the phenomenon of dynamical quasi-condensation at finite momenta to be remarkably stable against the presence of holes in the initial Fock state for large interactions and small systems. Furthermore we analyze the expansion velocity's dependence on interaction strength and defect concentration.

Third, we revisit the Fermi-Hubbard model but study attractive interactions and initial states with a finite spin polarization. In one spatial dimension, the partially polarized phase was found to be the analogue of the Fulde-Ferrell-Larkin-Ovchinnikov (FFLO) phase [81, 82, 83, 84, 85, 86, 87]. The FFLO state (see Ref. [88] for a review) was originally proposed to allow pair condensation at finite polarizations, despite to the mismatch of the two Fermi surfaces [89, 90]. The mechanism proposed to this end is the formation of pairs with a finite center-of-mass momentum. The motivation to study a sudden expansion of a trapped spin imbalance Fermi gas is twofold: First the spatial structure of it was investigated theoretically [87, 91, 92, 93] with the result that a partially polarized phase of FFLO-type occupies the center of the trap over a sufficiently large and stable region of the phase diagram (see Ref. [94] for a recent review). Second, the theoretically proposed spatial structure inside the trap was experimentally observed by Liao *et al.* in Ref. [95]. Yet, up to now, experimentalists have not found clear signature of

the FFLO-state in one-dimensional Fermi gases. Here we show that, during the sudden expansion from the FFLO state, the momentum distributions of the pairs, and both spin species, rapidly converge to a time-independent distribution. We find that the signatures of the FFLO state such as peaks in the momentum distribution of the pairs and the nodal structure of the quasi-condensate are quickly lost in the process. Yet, the quickly emerging stationary form can be related to the initial state and the integrals of motion in terms of the corresponding Bethe ansatz solution [27]. The stationary form of the momentum distributions should in principle be observable in an experiment that combines the techniques of [7, 74, 95], eventually allowing for an indirect detection of the FFLO state.

This thesis is organized in three parts: The first part introduces the adaptive time-dependent density matrix renormalization group whose application to transport problems and non-equilibrium dynamics is the main tool used in this thesis. Chapter 2.1 reviews the historical formulation of groundstate DMRG [30] and illustrates why it works especially well for one dimensional lattice systems. Chapter 2.2 introduces matrix product states (MPS) [96], which after realizing the common structures became a useful tool to formulate and extend DMRG algorithms. Among those are the time evolution methods presented in Chap. 2.3, where we discuss different variants to effectively approximate the time evolution operator, and the truncation scheme that is at the heart of adaptive time-dependent DMRG [34, 35]. Finally, Chap. 2.4 reviews the implementation of symmetries in MPS-based methods, especially non-abelian ones [97].

The second part focusses on transport in low-dimensional quantum magnets. We first review the framework of linear response theory necessary to calculate the spin conductivity of the Heisenberg chain in Chap. 3.1. Chapter 3.2 then revisits the evaluation of the spin Drude weight using ED and compares different finite-size extrapolations with some recent theoretical results. Chapter 3.3 presents the result of a combined effort comparing time-dependent current densities at zero temperature to current-current correlation functions at finite temperature to study a previously overlooked aspect of linear response theory, namely the dynamics of the transverse components of the current current correlation functions. In addition to the usual Larmor precession, we are able to identify a second non-trivial frequency in the coherent current oscillations driven by a transverse magnetic field. This effect is analyzed as a function of temperature and Zeeman field. Chapter 3.4 then briefly discusses recent experimental studies of the field-induced gapless phase of the organic superconductor $C_5H_{12}N_2CuBr_4$. We then proceed with

a detailed study of the frequency-dependent spin and heat conductivities of a dimerized spin$-1/2$ chain which is a minimal model that exhibits such a field-induced gapless phase [98, 99]. In Chap. 3.5 we discuss a few of the relevant materials and experiments that feature the unusual heat transport in low-dimensional quantum magnets, comparing state of the art steady-state transport measurements [3] to more recent time-dependent setups [54, 55]. The time-dependent setups discussed give access to the time-resolved temperature distribution on the surface of a bulk sample which serves as a motivation for Chap. 3.6 where we discuss an alternative to linear response theory, namely an investigation of the dynamics of the system based on the real-time dynamics of density wave-packets. Finally, Chap 3.7 follows this approach and presents the results for the study of the time-dependent energy density of an anisotropic Heisenberg chain starting from initial states far from equilibrium.

The third part transitions from traditional condensed matter systems to ultra-cold atomic gases in an optical lattice. Chapter 4.1 gives a brief introduction to the concepts and experimental techniques in this field, as far as they are relevant for the following discussion. Chapter 4.2 then discusses a recent example of an experiment on ultra-cold fermions that is related to transport in condensed matter systems. Chapter 4.3 presents our results for the sudden expansion of a spin-balanced two-component Fermi gas from a trap into an empty optical lattice in the presence of repulsive interactions. We identify the ballistic regime and analyze the average expansion velocity as a function of the initial conditions in the trap, making predictions relevant for future experiments. Chapter 4.4 presents the results for the expansion of spinless bosons starting from Fock state. In this case we analyze the dependence of the expansion velocity on experimentally relevant defect constellations in the initial state. We furthermore discuss how robust the dynamical quasi-condensation at finite momenta is against the presence of defects. Chapter 4.5 presents the results for the expansion of a spin-imbalanced mixture. Here we find a fast convergence with respect to time of all three relevant momentum distribution functions (up-spins, down-spins, pairs) which is then discussed in the context of the corresponding Bethe ansatz solution and the possibility of an indirect experimental detection of FFLO-correlations in the initial state. We conclude with a summary and an outlook on the real-time dynamics at finite temperatures in Chap. 5

2 The adaptive time-dependent density matrix renormalization group

For the following discussion of the transport properties and real-time dynamics of strongly correlated systems, we resort to numerically exact methods to solve the fully interacting many-body problem. A seemingly simple solution would be to treat a matrix representation of the Hamiltonian on a finite lattice system in an exact manner. Yet, since the dimension of a lattice Hamiltonian scales exponentially with the system size, exact diagonalization (ED) studies are restricted to rather small system sizes, e.g., the treatment of 42 spin-1/2 sites on the star lattice [100] being among the largest. Still, exact information obtained from small systems can be very valuable, see, e.g., Chap. 3.2 and 3.4. Quantum Monte Carlo simulations (see e.g., Ref. [29] and references therein) can very successfully simulate large spin systems, via stochastic sampling in a classical state space, but some fermionic systems and frustrated magnets are plagued by the famous sign problem [101].

Over the last twenty years the density matrix renormalization group (DMRG) [30] has emerged as a powerful method for local Hamiltonians on one-dimensional lattices (see [96, 102, 103] for excellent reviews). The method works best for mildly entangled states, which is usually the case for short-ranged interactions, and in some cases up to the order of a thousand lattice sites.

In its adaptive time-dependent formulation [34, 35, 104] this method has given rise to many important results on the dynamical properties of one-dimensional model systems. Examples are the time-dependent spin current for an initial state far from equilibrium [47], real-time simulation of spin-charge separation in the one-dimensional Hubbard model [105, 106, 107], local relaxation dynamics of a one-dimensional bose gas [73, 108, 109] and charge transport in nano-structures at large driving forces [110, 111] to list only a few. It will also be the main workhorse for important results of this thesis. This chapter gives a brief overview of DMRG evolved from the proposal by White in 1992 [30] into the "Age of matrix product states" [96].

2.1 A brief summary of groundstate DMRG

In order to treat systems of a finite-size numerically, an efficient implementation and reasonable, well controlled approximations are needed. We are interested in model Hamiltonians describing the physics on a one dimensional lattice where a local number of degrees of freedom, or local physical

dimension d can be attributed to each lattice site. One example is a single spin-1/2, which can point either up or down, thus $d = 2$. A single electron site can already contain zero to two electrons. Since two electrons with equal spin on the same site are excluded by the Pauli principle, $d = 4$ in that case. The full Hilbert space of a finite chain of length L has to be constructed as a tensor product of the local state spaces $\{|\sigma_i\rangle\}$, which results in a dimension $dim(\mathcal{H}) = d^L$. Thus, on a given lattice, the most general quantum state is parametrized by d^L complex coefficients:

$$|\psi\rangle = \sum_{\sigma_1,\ldots,\sigma_L} c_{\sigma_1\ldots\sigma_L} \bigotimes_{i=1,\ldots,L} |\sigma_i\rangle . \tag{1}$$

The paradigm of DMRG based methods is to take into account only a small subset of the full Hilbert space which contains the most relevant information about $|\psi\rangle$. For this purpose, we introduce a bipartition of the lattice into two parts A and B, rewriting Eq.(1) accordingly:

$$|\psi\rangle = \sum_{i,j} c_{i,j} |i_A\rangle \otimes |j_B\rangle , \tag{2}$$

and we define the reduced density matrix of subsystem A as partial trace over B:

$$\rho_A := \text{Tr}_B \rho = \sum_{\{i_B\}} \langle i_B|\psi\rangle\langle\psi|i_B\rangle . \tag{3}$$

The crucial steps in White's original prescription [30] are to obtain and diagonalize ρ_A for the exact groundstate of a small system, to order the eigenvalues of ρ_A by size and the truncation of the Hilbert space retaining only the m eigenvectors which correspond to the largest eigenvalues. The same can be achieved by calculating the singular value decomposition (SVD) of the matrix $c_{i,j}$ in Eq. (2) and projecting onto the basis corresponding to the m largest singular values. The SVD of $c_{i,j}$ is given by:

$$c_{i,j} = \sum_k U_{i,k} D_{k,k} V_{k,j}^\dagger , \tag{4}$$

where U and V are rectangular matrices, and D is a diagonal matrix containing the so called singular values. Using a SVD to rewrite the state $|\psi\rangle$ [Eq.(1)], we obtain the so-called Schmidt decomposition:

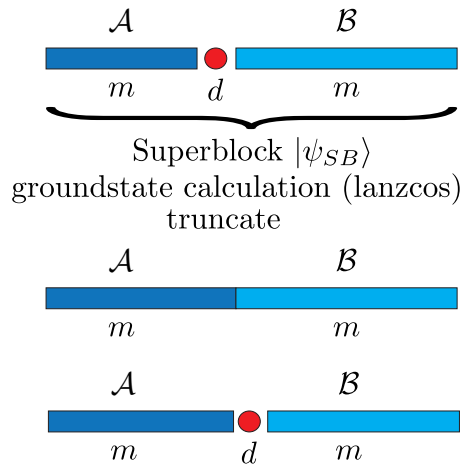$$|\psi\rangle = \sum_k \lambda_k |\lambda_{k,A}\rangle |\lambda_{k,B}\rangle , \tag{5}$$

Figure 2: A sketch of a single step of the DMRG algorithm and the superblock concept: We have, from a previous step, A and B represented by m states and in between one or two exactly represented sites (•). The product $A \bullet B$ defines the superblock, on which we target the groundstate, e.g., using the Lanczos method. Performing an SVD of the groundstate of the superblock and truncating to m states, we arrive at a new basis for A and B which then serves as input for the next step.

where $|\lambda_{k,A}\rangle$ is a basis of A and $|\lambda_{k,B}\rangle$ is a basis of B, respectively, transformed via U and V and the λ_k are the singular values. Calculating the reduced density matrix ρ_A from Eq. (5), reveals that it is diagonal in the basis $\{|\lambda_{k,A}\rangle\}$ with eigenvalues λ_k^2.

To obtain the groundstate, DMRG uses the following scheme: Assume that we know the groundstate from the previous step and that it consists of a system Block A and an environment block B. After truncating the groundstate to an effective basis of size m for each block, for instance, via an SVD as stated above, we shift the blocks by moving one or by two sites [1] from the environment to the system, i.e., $AB \to A \bullet B'$. The • stands for one or two exactly represented lattice site. At this point A and B are both represented in a reduced basis. The reduced basis for B' is in general known from a previous step of the algorithm. The object $A \bullet B'$ is called superblock

---

[1]Moving two sites is used in the original formulation and favorable in many cases[112], while the single site variant is directly equivalent to the MPS approach outlined in Chap. 2.2. For a detailed comparison and a MPS version of the two site variant see [96].

in the literature and the procedure is illustrated in Fig. 2. For this superblock, which has dimension m^2d, we calculate the groundstate of the Hamiltonian, e.g., by Lanczos iteration. Afterwards the two blocks $A\bullet$ and B' are relabeled as A and B and truncated back to m states, via SVD or diagonalization of ρ_A. The procedure can be repeated until the environment consists of only the minimal number of lattice sites chosen to be represented exactly in each step. Then the role of system and environment is exchanged. Going one time from minimal system size to a minimal environment size and back is called a sweep. Before starting the algorithm, an initial guess for each basis of A and B that appears in the process is needed, which can either be random or a physically motivated guess. The algorithm outlined above can be run until convergence, increasing the number of states m ideally after convergence with respect to the number of sweeps has been achieved. One of the main features of the method is the precise control of the error. On the one hand, the method is exact for $m = dim(\mathcal{H})$. On the other hand the maximal m can always be improved by increasing the computational resources. The measure that is usually studied to quantify the error in a given DMRG calculation is the discarded weight in the reduced density matrix:

$$|\psi\rangle = \sum_{k=1}^{m} \lambda_k |\lambda_{k,A}\rangle |\lambda_{k,B}\rangle \;\; \Rightarrow \delta\rho = \sum_{k>m} \lambda_k^2, . \tag{6}$$

In many cases, the assumption that expectation values of physical operators will have an absolute error of magnitude $\delta\rho$ holds. This can be seen by calculating the expectation value for any local, bounded operator O_A defined on A. Let O_A be an operator for which

$$\max_{|\phi\rangle \in A} \frac{\langle\phi|O_A|\phi\rangle}{\langle\phi|\phi\rangle} \leq c \tag{7}$$

holds. Then [102, 113]:

$$\langle O_A\rangle = Tr_A\rho_A O_A; \;\; \langle O_A\rangle_{\text{DMRG}} = \sum_{k=1}^{m} \lambda_k^2 \langle\lambda_{k,A}|O_A|\lambda_{k,A}\rangle \tag{8}$$

$$|\langle O_A\rangle_{\text{DMRG}} - \langle O_A\rangle| \leq c \sum_{k>m} \lambda_k^2 = c \cdot \delta\rho \tag{9}$$

This upper bound to the error in an observable is also the main reason why DMRG is regarded as a "numerically exact" method in the literature as errors vanish as m approaches the true dimension of the Hilbert space.

One drawback is of course that the statements above depend heavily on the nature of the spectrum of the reduced density matrix, i.e., the distribution of weights λ_k^2 in Eq. (5). Very fast convergence with minimum resources can be obtained if the λ_k^2 decay exponentially. If all of them are equal, the approximation Eq. (6) is no longer beneficial and achieving convergence with respect to m will be obviously hard. The ability to approximate a given state by a finite number of states within a DMRG scheme can be quantified utilizing concepts from quantum information theory, the simplest being the von-Neumann entropy:

$$S_{vN} = -Tr\rho_A log_2(\rho_A).$$ (10)

As the maximal entanglement between two m-dimensional state spaces can be $log_2 m$ [96] the number of states needed to describe a bipartite wave function with entanglement entropy S within a given error bound $\delta\rho$ scales as $m \sim 2^S$. In general, we know only the truncated state spaces from the DMRG side, but general laws for S are available under the name of area laws [114, 115, 116, 117]: Considering a short-ranged Hamiltonian with a gapped spectrum in $\mathcal{D}$ spatial dimensions and a bipartition where A is of size $L^{\mathcal{D}}$ and B is in the thermodynamic limit, the entanglement entropy is proportional to the surface of the cut, that is $S \sim L^{\mathcal{D}-1}$. Hence $S(L)$ saturates for one-dimensional systems once L exceeds the correlation length, which is favorable for DMRG based methods. For critical systems with open boundary conditions in one dimension, the entanglement entropy of a block of length l can be obtained from conformal field theory and scales as [118]

$$S = \frac{c}{6} log_2 \left[\frac{L}{\pi} \sin\left(\frac{\pi}{L}l\right) \right] + \text{const}$$ (11)

where c is the central charge of the conformal field theory (see [119] for a recent review). Two technical remarks are in order: First, the statements on entanglement scaling above apply to groundstate calculations, the time dependence of S is discussed in Chap. 2.3. Second, while the von-Neumann entropy does allow for the estimation of resources on a qualitative level in most cases, the explicit construction of states where such estimates are wrong is possible [120]. A generalized version, the so called Reny-entropies, allow for a mathematical rigorous treatment of simulability [120, 121].

2.2 Matrix product states

While the original DMRG algorithm has been very successful, many of the concepts can be phrased more elegantly in the language of matrix product

states (MPS). Other applications of MPS in the context of strongly correlated systems include, e.g., the construction of an exact groundstate as an MPS for the AKLT Hamiltonian [122], or the studies of translationally invariant, finitely correlated states in the context of quantum spin chains [123].

A general matrix product state on a one-dimensional chain of length L is given by :

$$|\psi\rangle = \sum_{\{\sigma_i\}} A^{\sigma_1} A^{\sigma_2} \; ... \; A^{\sigma_{L-1}} A^{\sigma_L} \bigotimes_{i=1..L} |\sigma_i\rangle \,, \qquad (12)$$

where every A^{σ_i} is a matrix of dimension m_i and the states $|\sigma_i\rangle$ encode the local physical degrees of freedom. Eq. (12) has a structure very similar to the one of Eq. (1). It replaces each of the complex coefficients of a general quantum state by a product of $d \cdot L$ complex matrices where d is the number of local degrees of freedom. In the following, a brief introduction is given and the minimal formalism required for the subsequent time evolution methods is established. For a complete review of state-of-the-art MPS manipulation, see [96].

First, we show that, using the Schmidt decomposition, every general quantum state can be approximated by an MPS of dimension m. Following [96], let us consider a matrix Ψ of dimension $d \times d^{L-1}$ that encodes the d^L coefficients and subject it to an SVD:

$$c_{\sigma_1 \; ... \; \sigma_L} = \Psi_{\sigma_1,(\sigma_2, \; ... \; \sigma_L)} = \sum_{a_1}^{r_1} U_{\sigma_1,a_1} D_{a_1,a_1} V^{\dagger}_{a1,(\sigma_2, \; ... \; \sigma_L)} \,, \qquad (13)$$

where $r_1 \leq d$ is now the full rank of the SVD. Since U has dimension $d \times r_1$ we can decompose it as d row vectors A^{σ_1} with entries $A^{\sigma_1}_{a_1} = U_{\sigma_1,a_1}$. The remaining product between S and $V^{\dagger}$ is a matrix $\Psi_{(a_1\sigma_2),(\sigma_3,...\sigma_L)}$ of dimension $r_1 d \times d^{L-2}$. An SVD of $\Psi_{(a_1\sigma_2),(\sigma_3,...\sigma_L)}$ yields:

$$\sum_{a_1} \sum_{a_2} A^{\sigma_1}_{a_1} U_{(a_1\sigma_2),a_2} S_{a_2,a_2} V^{\dagger}_{a_2,(\sigma_3,...,\sigma_L)} = \sum_{a_1} \sum_{a_1} A_{a_1} A_{a_1,a_2} \Psi_{(a_2,\sigma_3),(\sigma_4,...,\sigma_L)}$$

$$(14)$$

where $A^{\sigma_2}_{a_1,a_2}$ is now a set of d matrices of dimension $r_1 \times r_2$. Repeating this procedure L times we can indeed construct an exact MPS representation of an arbitrary quantum state with:

$$c_{\sigma_1 \; ... \; \sigma_L} = \sum_{a_1,...,a_L} A^{\sigma_1}_{a_1}...A^{\sigma_L}_{a_L} \,. \qquad (15)$$

Up to this point this is an exact rewriting of the coefficients and for a general quantum state the ranks of the SVDs involved can exhaust the full Hilbert

space dimension. However, one could also truncate to a maximum number of states retained for every matrix. As outlined in the previous section for the DMRG algorithm, the feasibility of expressing a given quantum state as MPS with $m < dim(\mathcal{H})$ is strongly tied to the scaling properties of the entanglement entropy. An important consequence of the natural notion of truncation in the MPS framework is possibility to reformulate the original DMRG algorithm as a variational method in the space of matrix product states [124, 125]. To this end, one realizes that one sweep in the DMRG algorithm corresponds to minimizing the energy expectation value with respect to all consecutively addressed A-matrices.

As the next step, in a similar fashion as in Eq. (13), one can reorganize the matrix elements of a given operator as a matrix product operator (MPO)

$$O = \sum_{\sigma} \sum_{\sigma'} M^{\sigma_1,\sigma'_1}...M^{\sigma_L,\sigma'_L} |\sigma_1\rangle\langle\sigma'_1| \otimes ... \otimes |\sigma_L\rangle\langle\sigma'_L| \,. \qquad (16)$$

The main difference is that each tensor has two physical indices to account for in and outgoing states. Several advantages of the formalism unveil themselves upon applying an MPO to an MPS [96]: First, the structure of the MPS remains invariant, second, the local dimension m grows in a controlled way, and third, the resulting MPS can be compressed afterwards to the original m with the error bounds established beforehand.

In the presented framework, it is now very feasible to formulate algorithms for the time evolution of a wave function based on the application of MPOs to MPS while maintaining control of the error involved in the necessary approximation.

2.3 Time evolution with MPS

In order to formulate an efficient algorithm to calculate the time evolution of a wave function two ingredients are crucial. First, one needs a faithful representation of the time evolution operator, namely the matrix exponential e^{-iHt}. One route to achieve this goal is to utilize the structure of the Hamiltonian. Short-ranged lattice Hamiltonians can all be written as a sum over operators, acting only on a few, ideally neighboring, bonds:

$$H = \sum_{i=1}^{L-1} h_i \,. \qquad (17)$$

An important fact to realize about Eq. (17) is that the h_i on the even and the h_i on the odd bonds commute. In addition, the time evolution of a single

bond can be done exactly as the matrix dimensions are sufficiently small. These ideas are exploited by the Suzuki-Trotter approximation. Discretizing time such that

$$e^{iHt} = \left(e^{iH\delta t}\right)^M \tag{18}$$

we can approximate the time evolution operator for each time step by [126] by:

$$e^{-iH\delta t} = e^{-iH_{\text{even}}\delta t} e^{-iH_{\text{odd}}\delta t} + O(\delta t^2), \tag{19}$$

where $e^{-iH_{\text{odd}}t}$ is the sum of all h_i with odd indices and $e^{-iH_{\text{even}}t}$ is the sum of all h_i with even indices. The error $\sim \delta t^2$ originates from the non-vanishing commutator $[h_i, h_{i+1}]$ in Eq. (19) and is called Trotter error in the literature. It can be reduced by choosing either smaller time steps δt, higher orders of the decomposition [126, 127] or both. An important fact to realize about Eq. (19) is that the time evolution can be formulated in terms of only two MPOs, namely $e^{-iH_{\text{odd}}t}$ and $e^{-iH_{\text{even}}t}$, each having a bond dimension of d^2 among themselves. The resulting wave function after each time step thus will have a dimension of $d^2 m$ if it was originally m.

Besides being very successful and easy to implement, this approximation has two major drawbacks: The first one is the interplay between the Trotter error and the bond dimension. Whenever we decrease the time step δt to minimize the Trotter error, the additional time steps increase the bond dimension before truncation substantially. Hence we need to keep a larger number of states to maintain a constant $\delta\rho$ as the truncation error accumulates faster. Second, the approach is not ideal for long range interactions as the identification of mutually commuting terms among the h_i depends on the details of the model.

An alternative route pursued throughout the following applications is the time evolution via a Krylov subspace method. Instead of calculating the time evolution of each bond, this approach consists of searching for $|\psi(t+\delta t))\rangle$ in the Krylov subspace, which is spanned by the vectors.

$$|K_0\rangle = |\psi(t)\rangle, \ |K_1\rangle = H|\psi(t)\rangle, \ |K_2\rangle = H^2|\psi(t)|\rangle, \dots . \tag{20}$$

This idea originates from the theory of large linear systems (see [128] and references therein) and has been first formulated for unitary time evolution by Park and Light [129]. Given a large complex square matrix H, power methods such as the Lanzcos or Arnoldi process (see, e.g., [130]) can be used to generate an orthonormal basis V_r of the r-dimensional Krylov subspace such that an analytic function f of H, for instance the matrix exponential,

can be approximated by

$$f(H)|\psi\rangle \approx V_r f(H_r)\,. \tag{21}$$

Krylov subspace approaches are known to converge rapidly with respect to r and error bounds have been studied extensively [128]. The beauty of this approach, in an MPS context, lies in the fact that each of the Krylov vectors can be setup as a separate MPS $|K_r\rangle$ with individual bond dimension m_r. On top of that, the error bounds from the mathematical literature allow for a combined error bound per time step. As applying powers of the full Hamiltonian leads to rapidly increasing bond dimensions, each Krylov vector can only be obtained to a finite accuracy, which decreases as r increases. At the same time the coefficients c_r in the expansion

$$|\psi(t+\delta t)\rangle = \sum_{r=0}^{r_{\max}} c_r H^r |\psi(t)\rangle \tag{22}$$

decay exponentially [128]. On a quantitative level, the error in the evolved wave function can be estimated by the last coefficient $c_{r_{\max}}$ in Eq. (22). Yet one has to take into account that the m_r can be very large such that the sum in Eq. (22) cannot be taken efficiently without truncation. The implementation used in Chaps. 3 and 4 is part of I.P. McCulloch's Matrix Product Toolkit [131].

The second ingredient to an efficient time evolution is a philosophy how to keep the numerical cost under control. Both, the Suzuki-Trotter approach and the Krylov subspace approach, rely on the application of MPOs and thus feature a rapid growth of the bond dimension after each time step. Hence the task is to find a prescription of how to choose a truncated basis that faithfully describes $|\psi(t)\rangle$. The increase of bond dimension due to the entanglement growth during the time evolution is independent of the method and discussed at the end of this section.

The breakthrough came with the reformulation of the time evolving block decimation (TEBD) algorithm [104, 132], in the DMRG language [34, 35]. The paradigm of this method, which became known as adaptive time-dependent DMRG, is to choose a new optimal basis after every time step. First one approximates the initial state by an MPS of dimension m_0. Then the time evolution operator is applied several times with timesteps δt to achieve the desired final time. After each and every time step, a truncation step is included. In principle, two ways of truncating are viable: First, one could limit the maximum number of states in each truncation step, monitoring the
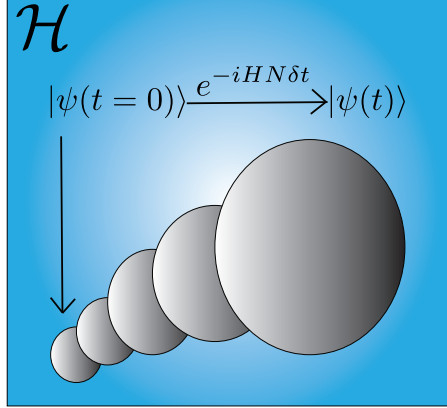
Figure 3: Sketch illustrating the basic idea of adaptive time-dependent DMRG. The circles represent the size of the basis optimal with respect to the desired error bound. The initial state $|\psi(t = 0)\rangle$ is compressed with a small number of states retained compared to the full Hilbert space $\mathcal{H}$. After each time step, a different basis is chosen, increasing the number of states to maintain a constant truncation error per time step. While the maximal time is ultimately limited by the entanglement growth, a single subspace to describe the wave function at all times of interest with equal accuracy would be way more costly.

truncation error as a function of time. This leads to the so called run-away error [47], as the fixed number of states is prone to becoming less and less optimal. Therefore, convergence of the wave function with respect to the control parameter m has to be monitored carefully. The second option is to increase the number of states kept after every time step to maintain a fixed error per time step. In that case the error increases at most linearly in time but the computational resources available might be exceeded at some point. The latter approach was used throughout this thesis and is sketched in Fig. 3. Note that, for all observables calculated from the wave function the error bound given by Eq. (9) still holds.

Recently proposed alternatives how to tackle the problem of time evolution, such as the transverse folding algorithm proposed in [133] or working directly in the Heisenberg picture [134] have yet to prove their superiority, be it only for a certain class of problems. Given comparably efficient implementations of the two methods presented in this chapter, it is merely a matter of taste and range of interactions which one to use.

As discussed in Chap. 2.1, the physical limitation of any DMRG or MPS based approach is the entanglement present in the state of interest. As opposed to the picture for groundstates, which favors a MPS representation in one spatial dimension due to the existence of area laws, for a general non-equilibrium state, the entanglement entropy is only bounded by the maximal speed at which information can propagate [135, 136], thus $S_{vN} \sim t$, in the worst case. Yet the argumentation from 2.1 still applies, namely that matrix dimensions for a fixed $\delta\rho$ per time step will have to grow exponentially if the bound on $S(t)$ is exhausted. For a certain specific setup, such statements can be checked by computing the time-dependence of the entanglement entropy [137, 138]. As an example, we find a mild logarithmic increase for the setup discussed in Chap. 3.7 which is common for so called local quenches [139]. In such cases, the matrix dimensions grow only linear in time. The increase of computational resources needed due to such growing matrix dimensions can be slowed to a certain degree by the inclusion of symmetries, especially non-abelian ones [97].

2.4   Symmetries

While everything discussed in this chapter up to now, can be done with moderate computational resources compared to an exact treatment of the full Hilbert space, we have also seen the limitations. In general the time evolution of a strongly correlated system out of equilibrium is very well limited by the current technologies as the number of states needed to maintain a constant error scales exponentially with the entanglement entropy. Even though the worst case of an exponential growth of resources needed cannot be compensated this way, the implementation of symmetries can extend the accessible time scales substantially.

The simplest case would be a single abelian symmetry group, corresponding to a single scalar quantum number, which already gives a considerable speedup [102]. Common examples would be the total particle number or the global magnetization, but any operator that commutes with H generates a symmetry group (not necessarily abelian though). The implementation of such a scalar quantum number requires rigorous bookkeeping. By taking the original basis in Eq .(1) to be eigenstates of the conserved quantity, the A-matrix on each site can be written in block diagonal form. To illustrate this, we consider a system in a state with global quantum number Q, a separate quantum number Q_i can be attributed to each subsystem. Now consider an MPS which is split into three parts, as in a single step of a sweep in the

DMRG algorithm, which addresses the matrix A^{σ_r}. Labeling the quantum number of the block encoded in the matrices A^{σ_i} where $i < r$ with Q_1, the quantum number of the block encoded in the matrices A^{σ_i} where $i > r$ with Q_3 and the contribution of A^{σ_r} itself with Q_2, $Q_1 + Q_2 + Q_3 = Q$ must hold for each non-zero matrix element of A^{σ_i}. In practice, the number of matrix elements needed to be stored to represent a given wavefunction faithfully is reduced by an order of magnitude for every scalar quantum number [102].

Even more powerful, although harder to implement, are non-abelian symmetries such as the conservation of total spin $\vec{S}$ in the Heisenberg chain [97] In the following, we restrict the discussion to the case of a single $SU(2)$ symmetry to minimize the notational overhead but the arguments generalize naturally to larger symmetry groups [140]. Applying the reasoning for the scalar quantum numbers above does not lead to a block-diagonal structure [141, 142]. Resolving this issue requires a deeper mathematical understanding of the structure of the involved symmetry groups: Instead of working with the eigenstates of the vector operator $\vec{S}$, the DMRG algorithm itself has to be formulated in a reduced basis, corresponding to the irreducible representation of $\vec{S}$. The key to find an irreducible representation of the corresponding $SU(2)$ symmetry group is the Wigner-Eckart theorem, which is a relation between an irreducible representation and the reduced matrix elements [143]. Given a general irreducible tensor operator $T_q^{(k)}$ of rank k it states that the matrix elements are given by:

$$\langle j', m'|T_q^{(k)}|j, m\rangle = (j, k, m, q|j', m')\langle j'\|T^{(k)}\|j\rangle \tag{23}$$

where the $(j, k, m, q|j'm')$ are the Clebsch-Gordon coefficients and $\langle j'\|T^{(k)}\|j\rangle$ are the so-called irreducible matrix elements [144] which are independent of m, m' and q. In the case of the spin $SU(2)$, $k = 1$, and q labels the components, usually $q = x, y, z$. The simplest case, the coupling two of spin-1/2 sites is a standard textbook application for the addition of angular momenta. For an arbitrary $SU(2)$ symmetric problem, the Clebsch-Gordon coefficients can be obtained, e.g., via a recursion analogous to the case of two spins [145] or via a closed formula [144]. The basis of the irreducible matrix elements can again be used to obtain a block structure in the A-matrices where non-zero matrix elements now represent a multiplet of states at once. The first and still one of the most efficient implementations was accomplished by McCulloch [97] and is part of his Matrix Product Toolkit [131] which is used for the $SU(2)$ symmetric calculations in Chapter 3 and 4. For a recent review in a matrix product context see [146]. To illustrate the practical use of non-abelian symmetries we discuss an example out of Chap. 3.7, where we
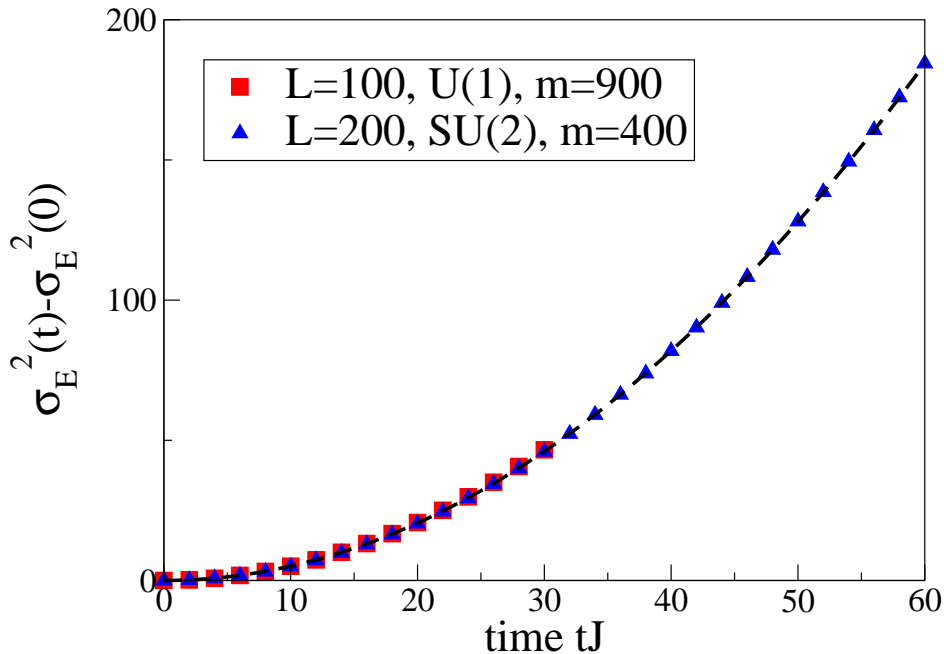
Figure 4: Time evolution of the spatial variance of an inhomogeneous energy density, comparing SU(2) and U(1) symmetric simulations using roughly comparable computational resources.

calculate the real-time dynamics of energy density wave-packets. Figure 4 shows the time-dependent spatial variance of such a energy density wave-packet for the Heisenberg chain:

$$H = \sum_{i=1}^{L-1} \vec{S}_i \cdot \vec{S}_{i+1} \,. \tag{24}$$

Using only the $U(1)$ symmetry, namely the conservation of magnetization we restricted the dynamics to chains of $L = 100$ spins and can simulate times of $30/J$ using at most $m = 900$ states with an error bound of $\delta\rho = 10^{-4}$. Performing the time-evolution in the $SU(2)$ invariant basis, we are able to calculate the time evolution of a chain of $L = 200$ spins up to $60/J$ within the same error bound using at most $m = 400$ states. Both curves were produced

using the Krylov subspace approach from Chap. 2.3 with a timestep of $J/4$. This shows how a single non-abelian symmetry can be utilized to increase maximal simulation times or the accuracy up to an order of magnitude.

3 Spin and heat dynamics in low-dimensional quantum magnets

Low-dimensional quantum magnets continue to be an interesting field of research as they exhibit a wealth of phases of condensed matter such as Tomonaga-Luttinger liquids [8], quantum dimer chains or valence bond solids (see [23] for a review). On the one hand, there is a growing variety of bulk crystals and organic materials that realize one-dimensional magnetic structures. These are referred to as spin-chain or spin-ladder materials depending on the respective geometry realized [11]. On the other hand, we have model systems which allow for an variety of powerful theoretical methods to be applied [16]. This situation gives rise to many fruitful interactions between theory and experiment, for instance, the investigation of the spectrum of magnetic excitations, see e.g., Refs. [147, 148, 149, 150, 151, 152].

In this chapter, the model system we discuss predominately is the anisotropic spin$-1/2$ Heisenberg chain:

$$H = J \sum_i [\frac{1}{2}(S_i^+ S_{i+1}^- + H.c.) + \Delta S_i^z S_{i+1}^z] . \tag{25}$$

Here S_i^x, S_i^y and S_i^z are the components of a spin-1/2 operators acting on site i, $S_i^\pm = \frac{1}{2}(S_i^x \pm S_i^y)$ are the corresponding raising and lowering operators, the exchange coupling J sets the global energy scale and Δ parametrizes the exchange anisotropy. The groundstate properties and thermodynamics in equilibrium of the model defined by Eq. (25) have been studied extensively on the theoretical side [153], yet the transport properties [1, 2], especially far from equilibrium [47, 48, 49, 50, 51, 52], are not fully understood.

On the experimental side, the model can be used to explain the physics of spin chain materials such as $SrCuO_2$ [154] and Sr_2CuO_3 [155, 156] (see Chap. 3.5), or many other materials (see Refs. [23, 157, 158] for reviews). The Heisenberg model [Eq. (25)] has yet to be realized in ultra-cold atomic gases, but important steps have already been taken [24, 159, 160, 161].

This chapter discusses our results on the spin and heat transport as well as the real-time dynamics of low-dimensional quantum magnets, which are organized in three groups. Chapter 3.1-3.3 focus on the spin transport in the anisotropic Heisenberg chain [Eq. (25)]. Chapter. 3.1 introduces the basic framework of linear response theory necessary to calculate the spin conductivity of the Heisenberg chain at finite temperature. Within this framework the real parts of the frequency-dependent conductivities $\sigma(\omega)$ of this model

can be written as

$$\mathrm{Re}\,\sigma(\omega) = D_s \delta(\omega) + \sigma_{\mathrm{reg}}(\omega)\,, \tag{26}$$

where D_s is the so called spin Drude weight. For finite temperatures, ballistic transport in the linear response regime is defined by a non-zero Drude weight while $D_s = 0$ is necessary for diffusive transport. Furthermore, the formalism exhibits a strong connection between transport and conservation laws, which, e.g., renders the energy transport in the Heisenberg chain ballistic [36]. While the ballistic energy transport in the linear response picture for Eq. (25) at arbitrary temperatures has been confirmed by a variety of theoretical approaches [36, 38, 37], finite temperature spin transport in the isotropic Heisenberg chain at zero magnetization is still under scrutiny [40, 41, 42, 43, 44, 45, 46]. Exact diagonalization [43, 162] studies suggest a finite spin Drude weight for $|\Delta| < 1$ while agreement for $\Delta = 1$ as well as agreement on the qualitative temperature dependence is lacking. There is also large interest in the regular part of the spin conductivity. For instance, Ref. [163] adressed the problem of spin transport at low but finite temperatures within field theory and finds a large diffusive contribution. These findings were also corroborated by QMC data in Ref. [164] .

In Chap. 3.2 we compare recent theoretical results regarding the Drude weight of an anisotropic Heisenberg chain at intermediate $(T \sim J)$ and high temperatures $(T \to \infty)$. First, Prosen [59] found a non-local conserved quantity, that has a finite overlap with the spin current for $0 \le \Delta < 1$ at high temperatures which is used to derive a lower bound for the spin Drude weight. Second Karrasch *et al.* improved time-dependent DMRG at finite temperatures [165], which allowed the calculation of the current-current correlation function at finite temperature up to so far unprecedented time scales [58]. If the current-current correlation function decays to a non-zero time independent value as time approaches infinity, then this value is directly proportional to the Drude weight [58]. In addition, Herbrych *et al.* presented a another analysis of exact diagonalization data [60], evaluated in the canonical ensemble,*i.e.*, at fixed magnetization. We compare these recent findings with our reevaluation of the spin Drude weight obtained via ED using the grand-canonical ensemble [43], extrapolating data for odd system sizes L in polynomials of $1/L$. We find reasonable agreement between the finite temperature DMRG data and our ED data. Furthermore, the analytical bound from Ref. [59] is exhausted for special values of the anisotropy, given by $\Delta = \cos(\pi/m)$ by both methods. By switching to a canonical ensemble we illustrate that at the isotropic point $(\Delta = 1)$ any extrapolation in powers of $1/L$ is inconclusive for the accessible system sizes as we are lacking a theory

(a) Field configuration: Static Bias and perturbation
(b) Spin precession in the chain
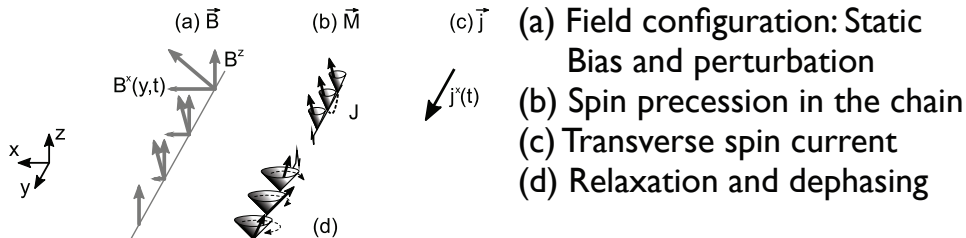(c) Transverse spin current
(d) Relaxation and dephasing

Figure 5: Sketch illustrating the model and setup used to study of the transverse component of the spin current correlation functions. Adapted from Ref. [166], see Chap. 3.3

for $D_s = D_s(1/L)$. Yet, the extrapolation of grand canonical data suggests a finite spin Drude weight at $\Delta = 1$, in agreement with Ref. [58].

We conclude our investigations of the spin transport in the XXZ-chain by a study of the transverse components of the current-current correlation function in Chap. 3.3. The magnetic field gradient ∇B that serves as the perturbation in the linear response ansatz presented in Chap. 3.1 is usually chosen parallel to the quantization axis of the magnetization. Hence, only the longitudinal component of the spin current appears in current-current correlation function which are used to calculate the conductivity. Here, we consider spin-chains, where the chains are oriented along the y-direction, their magnetization points in the z-direction, and the magnetic field is applied in the x-direction. Now we consider an additional homogeneous Zeeman field $B = (0, 0, B^z)$, $B^z \neq 0$, which induces a spin precession and gives rise to oscillations in the x-component of the spin-current autocorrelation function. In such a setup (see Fig. 5 for a sketch) all components of the spin current $\vec{j}_s = (j_x, j_y, j_z)$ are non-zero. We study the temperature and field-dependence of the x-component of the frequency-dependent current-current correlation function, finding coherent current oscillations at the Larmor frequency. At finite temperature a second frequency emerges and we find that the corresponding oscillation becomes coherent in the limit of zero temperature and large B^z. We show that this frequency shift in the spectrum cannot be explained by single magnetic excitations and hence is a unique many-body effect. We then complement these findings by calculating the real-time dynamics of the spin current at zero temperature using tDMRG, in the presence of a transverse magnetic. Within the DMRG based approach we study the j_x itself at zero temperature, instead of its correlation functions

at finite temperature. The main result, a frequency shift in the current's oscillations remains and even a quantitative agreement on the magnitude of the frequency shift and it's dependence on B^z is obtained between ED and DMRG.

The second block consists of Chap 3.4 and discusses the spin and heat transport in field-induced gapless phases. We first discuss recent experiments on the organic superconductor $C_5H_{12}N_2CuBr_4$ [56, 57], which made it possible to study magnetic phase diagram due to a comparably small exchange coupling. Motivated by these results, Chap. 3.4 focusses on the frequency-dependent conductivities of a dimerized spin-1/2 chain. This model is one of the minimal models to exhibit a field-induced gapless phase [98, 99]. We investigate the spin conductivity and the thermal conductivity as a function of temperature and in a homogeneous magnetic field. As a main result, we find enhanced spin and heat transport in the field-induced gapless phase, which manifests itself as an increased weight in the low-frequency regime of both spin and heat conductivity. The increased weight originates from a clear signature of the phase transition in the current-current correlation functions. We also investigate the dependence on the dimerization, and include magnetothermal corrections, which then lead to a decrease of the conductivities, as was known for the Heisenberg chain [167].

For the last part of this chapter we go beyond the linear response regime to study the spin and energy dynamics of the Heisenberg chain out-of-equilibrium. These studies are highly motivated by the recent progress in heat transport experiments on $Sr_9La_5Cu_{24}O_{41}$ [54, 55]. Chapter 3.5 introduces examples of different experimental techniques and materials to study heat transport in low-dimensional quantum magnets. The family of materials $(Sr,La,Ca)_{14}Cu_{24}O_{41}$ played an important role in the discovery of magnetic heat transport [155, 168]. The compound $Sr_9La_5Cu_{24}O_{41}$ exhibits the most pronounced effect [168], and was later also investigated by optical means in a pump-probe like setup which made it possible to follow the anisotropic heat dynamics in real-time [54, 55]. As an example for experiments on spin chains, we discuss the double chain compound $SrCuO_2$, which has recently, in a study of samples of previously unachieved purity, exhibited the highest κ_{mag} to date and a macroscopic mean free path for the magnons of the order of $1\mu m$ [154]. In Chap. 3.6 we establish an alternative perspective to the linear response approach, namely the study of transport properties based solely on the real-time evolution of density profiles. This approach is based on analyzing the spatial variance of a time-dependent density profile and is suitable to study the dynamics of initial states both far and close to equilib-

rium. Instead of working in the (Δ, T) plane, the distance in energy between the initial state and the groundstate is tuned at zero temperature, e.g., by a magnetic field. Since the approach outlined here is suitable to treat large energy differences, we are able to contribute results far from equilibrium to the discussion of spin and heat dynamics. The approach has also already been applied to the magnetization dynamics in the XXZ-chain [48], with the result that the spin dynamics far from equilibrium are ballistic in the gapless phase $(0 \leq \Delta \leq 1)$, while the numerical results for the gapped phase $(\Delta > 1)$ show a hint at diffusive dynamics. In Chap. 3.7 we apply the approach outlined in Chap 3.6 to investigate the energy dynamics in the XXZ-chain in the absence of spin currents. We find ballistic energy dynamics independently of Δ and of the distance between the initial state and the groundstate. Our findings thus extend the established linear response results to scenarios far from equilibrium. The problem is also investigated using Luttinger liquid theory, with the result that both, energy and magnetization wave-packets expand ballistically with the characteristic sound velocity within this approach. For the non-equilibrium case the average expansion velocities are analyzed in detail and understood in terms of the change in the momentum distributions of the perturbed initial states compared to the groundstate. Furthermore we study the time-dependent energy currents in the system, further corroborating the ballistic dynamics by showing that a finite time-independent energy current emerges after short transient dynamics. We also derive a relation between the spatial variance and the current operator which provides an alternative way to determine the average expansion velocity. Finally, the dynamics induced by a gaussian magnetic field [48] are revisited to obtain agreement between the numerical calculations and Luttinger liquid theory for the expansion velocity in the limit of weakly perturbed initial states.

3.1 Linear response theory

Linear response theory [31, 169] expresses the response of the system to a weak external perturbation via correlation functions of the system in equilibrium. While the approach can be formulated for arbitrary model systems, the required correlation functions can in general not be calculated easily, leaving interesting open questions for many models. For instance, in Chap. 3.2 we devote special interest to the case of a single one-dimensional Heisenberg chain, where up to now, the spin transport of an isotropic antiferromagnetic chain is still under scrutiny [40, 41, 42, 43, 44, 45, 46]. Yet, before discussing this particular problem in more detail, the general framework is established

[31, 169], with the application of spin transport in the Heisenberg chain in mind. Consider a system in equilibrium described by H_0, subjected to a small perturbation H_t at a fixed time t_0. For the time independent system expectation values of an arbitrary operator A are given by:

$$\langle A \rangle_0 = \mathrm{Tr}\rho A = \frac{1}{Z}\sum_n e^{-\beta E_n}\langle n|A|n\rangle \,, \tag{27}$$

where $E_n, |n\rangle$ are eigenenergies and eigenstates of H_0 respectively and $Z = \mathrm{Tr}\rho$ is the partition function. Including the perturbation, the time evolution is described by a time-dependent Hamiltonian given by:

$$H(t) = H_0 + \theta(t - t_0)H_t \,. \tag{28}$$

Treating the time-dependent expectation value in the interaction picture up to first order in the time-dependent perturbation, $\langle A(t)\rangle$ can be calculated as [169]:

$$\langle A(t)\rangle = \langle A\rangle_0 - i\int_{t_0}^t dt' \frac{1}{Z}\sum_n e^{-\beta E_n}\langle n|[A(t), H_t(t')]|n\rangle \,. \tag{29}$$

This is the most general form of the Kubo formula, which relates the response to an external perturbation to a time-dependent correlation function of the system in equilibrium. It is usually convenient to work with the Fourier components of the perturbation:

$$H_t = \int \frac{d\omega}{2\pi}e^{-i\omega t}H_\omega \,. \tag{30}$$

As an example, we discuss the spin transport in a Heisenberg chain of length L [Eq. (25)]. The spin current follows from the equation of continuity for the conserved total magnetization $S^z = \sum_{l=1}^L \langle S_i^z\rangle$:

$$j_{\mathrm{s}} = i\sum_l [h_{l-1}, S_l^z] \,, \tag{31}$$

where the h_l denote the local terms of the lattice Hamiltonian such that $H = \sum_{l=1}^{L-1} h_l$. The linear response equation for this case reads [170]:

$$j_s(\omega) = -\sigma(\omega)\nabla B(\omega) \tag{32}$$

where ∇B is the gradient of the magnetic field driving the spin current. In general, the temperature gradient also couples to the spin current, leading

to the 2×2 system of conductivities discussed in detail in Chap. 3.4. Using the Kubo formula [Eq.(29)] and Eq. (31) the frequency-dependent conductivity $\sigma(\omega)$ is expressed as a function of the time-dependent current-current correlation function [31]:

$$\sigma(\omega) = \frac{1}{L} \int_0^\infty dt e^{-i(\omega - i0^+)t} \int_0^\beta d\tau \langle j_s(0) j_s(t + i\tau) \rangle \,, \qquad (33)$$

In the following we want to discuss the real part of $\sigma(\omega)$ for a finite lattice system. Inserting a spectral representation $\mathbb{1} = \sum_o |o\rangle\langle o|$ of the lattice Hamiltonian leads to

$$\operatorname{Re} \sigma(\omega) = D_s \delta(\omega) + \sigma_{\text{reg}}(\omega) \,, \qquad (34)$$

where

$$D_s = \frac{\pi\beta}{ZL} \sum_{\substack{n,o \\ E_n = E_o}} e^{-\beta E_n} \langle n|j_s|o\rangle\langle o|j_s|n\rangle \,, \qquad (35)$$

and

$$\sigma_{\text{reg}} = \frac{\pi}{ZL} \frac{1 - e^{-\beta\omega}}{\omega} \sum_{\substack{n,o \\ E_n \neq E_o}} e^{-\beta E_n} \langle n|j_{\text{s}}|o\rangle\langle o|j_{\text{s}}|n\rangle \delta(\omega - \Delta E) \,. \qquad (36)$$

D_s is called spin Drude weight in the literature and plays an important role in transport theory. In real-time, the current-current correlation function reads:

$$C(t, \beta) := \langle j_s(t) j(0) \rangle = \frac{1}{ZL} \sum_{n,o} e^{-\beta E_n} e^{-it(E_n - E_o)} |\langle n|j_s|o\rangle|^2 \,, \qquad (37)$$

where the time-independent contributions are proportional to Eq. (35). Hence, a finite Drude weight in Eq. (34) indicates that the current-current correlation function of the system will not decay to zero, but to a finite time-independent value at infinite times. In contrast, for a diffusive model in one spatial dimension, the current-current correlation function $C(t, \beta)$ must decay as $1/\sqrt{t}$ [1, 33]. The anomalous behavior indicated by a finite Drude weight is usually called ballistic transport. It is a fundamental theoretical question which models, exhibit such diverging transport coefficients and under which circumstances. Besides directly calculating the correlation functions, important insights can be gained using Mazur's inequality [36, 171, 172]:

$$D_s \geq \frac{\pi\beta}{L} \sum_m \frac{\langle j_s Q_m \rangle^2}{\langle Q_m^2 \rangle} \,, \qquad (38)$$

where we sum over a subset $\{Q_m\}$ of the orthogonal conserved quantities Q ($\langle Q_m Q_{m'} \rangle) = \delta_{m,m'}$ [36] of the model of interest. Eq. (38) becomes an equality when either the full set is known [171, 173], which is difficult in general, or if the bound is exhausted by a few Q_m. Formulated for the thermal Drude weight, the Mazur inequality [Eq. (38)] has important implications for the Heisenberg chain. First, the energy current j_E itself is one of the Q_m, namely Q_3 [36]. In that case Eq. (29) already implies a finite thermal Drude weight since the commutator $[j_{\text{th}}, H]$ vanishes, as well as that Eq. (38) is exhausted due to the orthogonality $\langle Q_i Q_j \rangle = \delta_{i,j}$. Second, the energy current and the spin current have a finite overlap $\langle j_s j_E \rangle$ at finite magnetization, leading to a non-zero Drude weight at non-zero magnetization [36]. Even including all conserved quantities, which can be constructed due to the integrability [174] of the Heisenberg chain, in the analysis of Eq. (38) does not allow for conclusions at zero magnetization [36] since there all $\langle j_s Q_m \rangle$ vanish. The following chapter presents a survey of the theoretical results on this issue and the most recent attempts to resolve it.

3.2   Comparison of recent results for the spin Drude weight

One of the intriguing open questions in linear response theory applied to one-dimensional quantum magnets is the spin Drude weight of the isotropic Heisenberg chain [Eq. (25) at $\Delta = 1$] at zero magnetization and finite temperature [40, 41, 42, 43, 44, 45, 46]. As outlined in Chap. 3.1, in the case of spin transport at zero magnetization, the bound provided by Eq. (38) vanishes for all local conserved quantities [36] except for $\Delta = 0$ where the spin current itself is conserved. At zero temperature the spin Drude weight can be calculated exactly, and is given by [175]:

$$D_s = \frac{\pi}{4} \frac{\sin \nu}{\nu(\pi - \nu)} \, , \qquad (39)$$

where $\Delta = \cos(\nu)$. Therefore, we have a finite Drude weight indicating a conducting state for $-1 \leq \Delta \leq 1$ and a sharp transition to an insulating behavior as the Drude weight discontinuously drops to zero for $\Delta = 1$ at T=0 [32, 176].

One approach to study spin transport at finite temperatures pursued in the literature is to evaluate Eq. (35) and (36) using exact diagonalization of small systems (see [2] for a review). As shown in Refs. [43, 162] such numerical studies are consistent with $D_s(T) > 0$ for $0 \leq \Delta \leq 1$. Since the

full spectrum is needed, system sizes are usually not larger than $L = 21$ spins and the data is extrapolated in $1/L$. $D_s(T) > 0$ for $0 \leq \Delta \leq 1$ has also been suggested by QMC data, e.g., in Ref. [42]. Another approach is the exact calculation of D_s within an extension of the thermodynamic Bethe ansatz [177]. For instance, Ref. [41] finds the Drude weight to be a monotonically decreasing function of temperature for $0 \leq \Delta \leq 1$ which vanishes for all temperatures at the isotropic point $\Delta = 1$. Yet, the results obtained for the temperature dependence and the value at the isotropic point ($\Delta = 1$) deviate depending on details of the approach [45]. Ref. [45] argues that it can also be used to show that the results for $D_s(T)$ are finite for T=0, as well as for $T > 0$ at $\Delta = 1$. Recently the question of diffusive versus ballistic spin transport was also addressed within low-energy field theory, with the result that a dominant diffusive channel exists at finite but low temperature, although a ballistic contribution cannot be excluded [163]. These findings have also been corrobarated by QMC data in Ref. [164].

Here we compare some very recent results that have provided new directions for this interesting question. First, Prosen found a quasi-non-local conserved quantity that has a finite overlap with the spin current for $0 \leq \Delta < 1$ [59]. Ref [59] focusses on the high temperature limit, in which the leading order in the high temperature expansion of D_s is studied instead of the Drude weight, namely:

$$C_s = \lim_{\beta \to 0} \frac{1}{\beta} D_s = \frac{\pi}{ZL} \sum_{\substack{m,n \\ E_n = E_m}} |\langle m|j_s|n\rangle|^2 \tag{40}$$

The main result of Ref. [59] is a lower bound to C_S via Eq. (38). The second example is the numerical calculation of the current-current correlation function at finite temperatures by Karrasch *et al.*, using time-dependent DMRG [58]. They evaluate the current-current correlation function in real-time which decays on the accessible time-scales to a non-zero time independent value for $0 \leq \Delta \leq 1$. The stationary value then is directly proportional to the Drude weight. They suggest a finite spin Drude weight at $\Delta = 1$ in their analysis which involves simulation times ranging from $10/J$ to $30/J$. The third example is the recent work by Herbrych *et al.* [60], in which a evaluation of ED data using the canonical ensemble and odd system sizes was done. Their reason for this approach is acclaimed faster convergence with respect to the system size. Odd system sizes have also been reported to have a more favorable finite size scaling using the grand canonical ensemble [43]. The results of Ref. [60] for the spin Drude weight is consistent with [41], in particular they conclude $D_s = 0$ at $\Delta = 1$ within their approach.
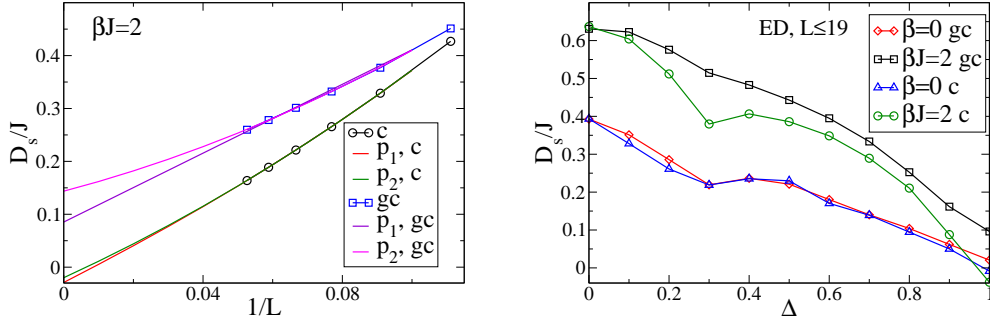
Figure 6: Exact diagonalization data for the spin Drude weight comparing the grand canonical (gc) and the canonical ensemble (c). Left: Fitting p_1 and p_2 to the data for D_s at $\Delta = 1$ for $\beta J = 2$. Right: $C_s(\Delta)$ at $\beta = 0$ and $D_s(\Delta)$ at $\beta J = 2$.

For a comparison with the findings of Refs. [58],[59] and [60] we revisit the evaluation of the spin Drude weight D_s using exact diagonalization and Eq. (35). A priori, Eq. (35) does not state which thermodynamical ensemble is used to evaluate the expectation values. Since we are interested in the behavior at zero magnetization and restricted to finite systems, one has to consider the following if using a canonical ensemble: For an even number of spins it is straight forward to see that restricting the sum in Eq. (35) to states with zero magnetization leads to a vanishing spin Drude weight due to particle-hole symmetry. The Hilbert space of a system of odd length though only has a subspace with zero magnetization in the thermodynamic limit. Ref. [60] calculates the spin Drude weight of anisotropic Heisenberg chains using a canonical evaluation of Eq. (35), specifically restricting Eq. (35) to the sector with the lowest possible magnetization, $M = \sum_r \langle S_r^z \rangle = 1/L$. The data is then extrapolated to second order in $1/L$. In Fig. 3.2 we reproduce their results in the high temperature limit $\beta = 0$ and for intermediate temperatures $\beta J = 2$. We extrapolate the data in polynomials of $1/L$:

$$D_s \approx p_i := \sum_{r=0}^{i} c_r \frac{1}{L^r} \, , \qquad (41)$$

using both, the canonical and the grandcanonical ensemble. For the canonical ensemble at $\beta J = 2$ we find that up to fourth order $D_s(L \to \infty) < 0$ at
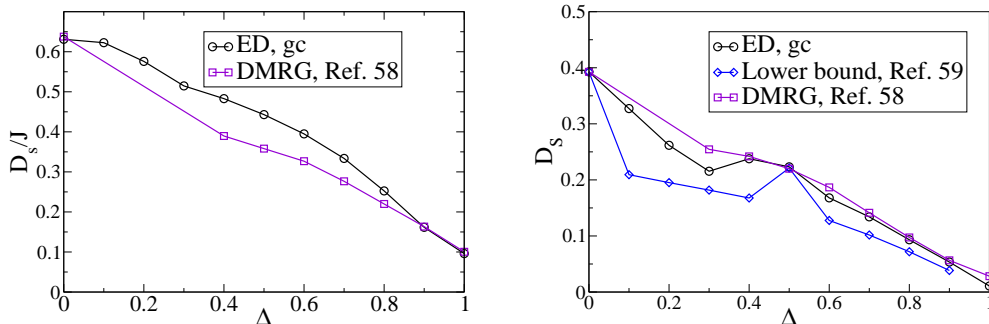
Figure 7: Left: ED data for the spin Drude weight D_s obtained from a grand-canonical (gc) evaluation of Eq. (35) at $\beta J = 2$ compared to the DMRG data of Ref. [58]. Right: Comparison of ED data for the high temperature limit of the spin Drude weight C_s obtained from a grandcanonical (gc) evaluation of Eq. (40) at $\beta J = 0$ to the infinite temperature results of Refs. [58] and [59].

$\Delta = 1$. The data for both ensembles and the fits to p_1 and p_2 are shown in the left panel of Fig. 3.2. From this unphysical behavior we conclude that, at $\Delta = 1$ a finite-size extrapolation of the canonical spin Drude weight from odd systems sizes at finite temperature is rather involved as the full $D_s(1/L)$ is likely to have a very small slope, since $D_s \geq 0$ must hold for all system sizes. The right panel of Fig. 3.2 shows a comparison of the extrapolated data for both ensembles at $T = \infty$ and $T = 1/2J$ where we averaged over the results obtained from p_1, p_2, p_3 and p_4. For $\beta = 0$ we find a reasonable agreement between the two approaches while for $\beta J = 2$ the canonical D_s deviates stronger from the grandcanonical D_s the closer we get to $\Delta = 1$.

Next we compare our results for the spin Drude weight in the grand canonical ensemble for both infinite and intermediate temperature to the findings of Refs. [58] and [59]. The left panel of Fig. 3.3 shows our results at $T = J$ compared to the DMRG data from Ref. [58]. In addition to the reasonable agreement obtained, both results are in favor of a finite spin Drude weight at intermediate temperatures for $0 \leq \Delta \leq 1$. Figure 3.3 compares ED data, DMRG data and the rigorous lower bound for $D_s(\Delta)$ from Ref. [59] in the high temperature limit. First, both numerical results indicate a finite Drude weight for $0 \leq \Delta \leq 1$ and show remarkable agreement. Second the

rigorous lower bound by Prosen is exhausted at certain commensurate points $\Delta = \cos(\pi/m)$ the first one being $\Delta = 0.5$. For all other $\Delta \geq 0$ the lower bound is smaller than the numerical results, but the deviations at those incommensurate points become smaller as Δ increases.

   To summarize this chapter we have briefly reviewed the current state of discussion regarding the spin Drude weight of the one dimensional Heisenberg chain. We find that time-dependent DMRG and exact diagonalization in the grand canonical ensemble are in favor of a finite spin Drude weight at the isotropic point. The lower bound based on Eq. (38) also agrees reasonable well with the numerical data and is exhausted at the commensurable points $\Delta = cos(\pi/m)$. Switching to a canonical ensemble within the ED approach unveils that the finite-size extrapolation in that case is highly non-trivial and leaves questions open to be addressed in the future. A theory for $D_s = D_s(1/L)$ would be highly desirable. Furthermore, a quantitative study of the full temperature dependence certainly is another interesting direction for further research.

3.3   Coherent spin-current oscillations in transverse magnetic fiels

In the previous chapter and common in the literature, the analysis of linear response functions was restricted to only the longitudinal component of the current. Yet, each spin on the chain, as well as the spin current, have three components that can be excited separately by an appropriate magnetic field. This chapter presents a study of the oscillations in the transverse components of the current-current correlation function. They are induced by a magnetic field $B = (B^x, 0, B^z)$ where B^x is the driving force in the linear response equations and B^z is a homogenous field in which the spins precess. In addition to the expected Larmor precession, we were able to identify a second frequency in the transverse current-current correlation function's oscillations, which becomes coherent for low temperatures and large B^z. We find that this additional frequency is a many-body effect as it cannot be described by single magnetic excitations. The problem is studied using an analytical approximation for high temperatures, exact diagonalization for intermediate temperatures and time-dependent DMRG at zero temperature, mapping out the frequency shift as a function of the homogenous field B^z and temperature. We find remarkable agreement between the DMRG and the ED data regarding the frequency shifts dependence on B^z.

Coherent Spin-Current Oscillations in Transverse Magnetic Fields

Robin Steinigeweg,[1,*] Stephan Langer,[2] Fabian Heidrich-Meisner,[2] Ian P. McCulloch,[3] and Wolfram Brenig[1]

[1]*Institute for Theoretical Physics, Technical University Braunschweig, D-38106 Braunschweig, Germany*
[2]*Department of Physics and Arnold Sommerfeld Center for Theoretical Physics, Ludwig-Maximilians-Universität München,
D-80333 München, Germany*
[3]*School of Physical Sciences, The University of Queensland, Brisbane, QLD 4072, Australia*
(Received 12 October 2010; revised manuscript received 25 March 2011; published 20 April 2011)

We address the coherence of the dynamics of spin-currents with components transverse to an external magnetic field for the spin-1/2 Heisenberg chain. We study current autocorrelations at finite temperatures and the real-time dynamics of currents at zero temperature. Besides a coherent Larmor oscillation, we find an additional collective oscillation at higher frequencies, emerging as a coherent many-magnon effect at low temperatures. Using numerical and analytical methods, we analyze the oscillation frequency and decay time of this coherent current-mode versus temperature and magnetic field.

Controlling quantum coherence is paramount for future information processing [1]. The coherence of localized quantum spin degrees of freedom has been studied in a wide variety of systems, including semiconductor quantum dots [2,3], molecular magnets [4], nitrogen vacancies in diamond [5], carbon nanotubes [6], and ultracold atoms [7]. Coherence in spin transport has been addressed primarily in semiconductors [8]. A new route into coherent spin transport may arise from quantum magnets. Here, magnetization is transported solely by virtue of exchange interactions and (de)coherence of spins will emerge as a purely intrinsic many-body phenomenon. In one-dimensional (1D) spin systems, magnetic transport has experienced an upsurge of interest in the last decade due to the discovery of very large magnetic *heat* conduction [9] and long nuclear magnetic relaxation times [10]. Genuine *spin* transport in such materials remains yet to be observed experimentally and if combined with materials with small exchange couplings [11,12], the coherent manipulation of spin transport using laboratory magnetic fields may become feasible. Theoretically, spin transport has already been given significant attention (see Refs. [13,14] for a review); previous studies, however, have focused on the longitudinal spin conductivities only, excluding the physics of coherence. Therefore, in this Letter we investigate the dynamics of spin-currents with components transverse to an externally applied magnetic field, as sketched in Fig. 1. This setup allows us to study the collective precession frequency of the transverse spin-current and its decay time, which will be at the prime focus of this Letter. We will show that, besides a coherent oscillation at the Larmor frequency, a second nontrivial collective oscillation at higher frequencies emerges at low temperatures. This oscillation is identified as a pure many-magnon effect and also becomes coherent in the low-temperature limit.

In this Letter, we study the antiferromagnetic Heisenberg spin chain, one of the fundamental models to describe magnetic properties of interacting electrons. It is relevant to the physics of low-dimensional quantum magnets [15], ultracold atoms [16], nanostructures [17], and—seemingly unrelated—fields such as string theory [18] and quantum Hall systems [19]. The Hamiltonian reads

$$H = J \sum_{r,\alpha}^{N} S_r^\alpha S_{r+1}^\alpha - B^z \sum_r^N S_r^z. \tag{1}$$

S_r^α ($\alpha = x, y, z$) are the components of spin-1/2 operators at site r, N is the number of sites, $J > 0$ is the exchange coupling constant, B^z is a longitudinal magnetic field, and $\hbar \equiv 1$ [20]. For $B^z < B_c^z = 2J$, Eq. (1) implies a gapless Luttinger liquid [21,22] and, for $B^z > B_c^z$, a gapped ferromagnetic ground state.

We investigate the transverse spin-current dynamics for two complementary scenarios and use methods appropriate for each situation. First, we study current autocorrelations
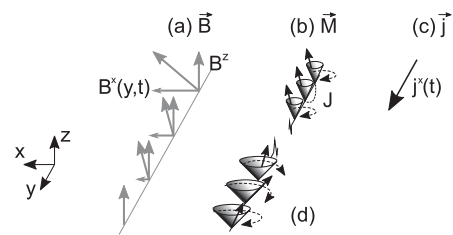

FIG. 1. Quasiclassical sketch of transverse spin transport in a spin chain directed along the *y*-direction: (a) External magnetic field with a static "bias" component B^z and a perturbing, space- and time-dependent component $B^x(y, t)$; (b) B^z produces a magnetization $\vec{M}$ with a *homogeneous* transverse component and a Larmor precession, $B^x(y, t)$ produces an *inhomogeneous* transverse component driving (c) a transverse spin-current $j^x(y, t)$ in y direction. The dynamics of $j^x(y, t)$ is controlled by the intrinsic exchange coupling J. (d) As a function of time, the magnetization relaxes and the transverse component dephases.

at finite temperature, using numerically exact diagonalization (ED) and an asymptotic analytic analysis (AAA). Second, applying the adaptive time-dependent density matrix renormalization group (tDMRG) [23], we analyze the real-time dynamics of currents at zero temperature during the evolution from initial states with an inhomogeneous magnetization. Qualitatively, the same physics explains our observations in both scenarios, and even a quantitative agreement can be obtained.

We begin by discussing the current autocorrelations $\tilde{C}^{\mu\nu}(\omega) = \sum_{lm} e^{-\beta E_m} \langle l|j^\mu|m\rangle \langle m|j^\nu|l\rangle \delta(\omega - E_m + E_l)/ZN$ [24], where $|l\rangle$, $|m\rangle$ and $E_{l,m}$ are eigenstates and -energies of Eq. (1), $\beta = 1/T$ is the inverse temperature, j^μ is the zero-momentum spin-current, μ, $\nu = x$, y, z, Z is the partition function, and ω is the frequency. More precisely, we consider a symmetrized version $C^{\mu\nu}(\omega) = [\tilde{C}^{\mu\nu}(\omega) + \tilde{C}^{\mu\nu}(-\omega)]/2$; i.e., in the time domain, we focus on the real part $C^{\mu\nu}(t) = \text{Re}[\tilde{C}^{\mu\nu}(t)]$. While B^z breaks total spin conservation, a spin-current can still be defined by decomposing the time derivative of the spin-density at momentum q as $\partial_t S_q^\mu = \partial_t S_q^\mu|_{J=0} - \iota q j_q^\mu$ into a local source (sink) term due to B^z (present without any exchange interactions) and the actual exchange mediated spin-current j_q^μ. The latter then derives from the continuity equation for S_q^μ at $B^z = 0$. In turn $\vec{j} = \iota \sum_r \vec{S}_r \times \vec{S}_{r+1}$, where $\vec{j} = \vec{j}_{q=0}$. The eigenstates (energies) are classified according to the total spin z component $\sum_r S_r^z|l\rangle = M|l\rangle$. Since $|l\rangle$ is *independent* of B^z and $C^{\mu\nu}$ is diagonal at $B^z = 0$, it will remain diagonal at any B^z. Moreover, by symmetry $C^{xx} = C^{yy}$. However, since j^x mediates transitions between sectors with $\Delta M = \pm 1$ while j^z conserves M, the autocorrelations C^{xx} (transverse) and C^{zz} (longitudinal) *differ* at $B^z \neq 0$. This difference is solely due to the field dependence of the eigenenergies. Formally speaking, this aspect is at the center of this Letter. For the remainder we abbreviate $C^{xx(zz)}$ by $C^{x(z)}$. Note that by the continuity equation the current autocorrelations at small q are related to the dynamic spin structure factor $S^{\mu\nu}(q, \omega)$, exhibiting a matrix symmetry identical to $C^{\mu\nu}(\omega)$ at $B^z \neq 0$ [25].

Generically, the longitudinal autocorrelation decomposes into a Drude weight D^z and a regular part, i.e., $C^z(\omega) = D^z\delta(\omega) + C^z_{\text{reg}}(\omega)$. A significant body of evidence in favor of $D^z(T \geq 0) \neq 0$ for $B^z < B^z_c$ has been gathered [13,14,26], with thermally activated behavior of $D^z(T)$ for $B^z > B^z_c$ [14]. Less is known on the specific shape of the regular part [26]. The previous discussion of symmetries of $C^{\mu\nu}$ implies that $C^x(\omega) = \sum_\pm [D^x\delta(\omega \pm B^z) + C^x_{\text{reg}}(\omega \pm B^z)]$. In general, D^x and C^x_{reg} will *not* be identical to $D^z/2$ and $C^z_{\text{reg}}/2$, respectively, due to the different B^z-dependence of Boltzmann weights in C^z and C^x. In the time domain, D^x implies a coherent, nondecaying oscillation of the transverse current at the Larmor frequency $\omega_L = B^z$, permitted by the integrability of Eq. (1) [13]. On the other hand, C^x_{reg} *a priori* implies

only decoherence and damping. In the following, however, we demonstrate that at sufficiently low T and finite B^z, out of C^x, a new collective quasicoherent oscillation of the current emerges. The oscillation frequency differs from the "simple" Larmor frequency and cannot be understood within a one-magnon picture.

First, we discuss high temperatures, i.e., $\beta = 0$. A straightforward analysis yields

$$C^x(\omega) = [C^z(\omega - B^z) + C^z(\omega + B^z)]/2. \quad (2)$$

Figure 2(a) displays $C^x(\omega)$ for $B^z/J = 2$. As can be seen from Fig. 2(b), this approximately transforms into $C^x(t) \approx [R(t) + D^x]\cos(\omega_L t)$ in the time domain, with $R(t)$ *rapidly* decaying within $\sim 1/\omega_L$ and a "trivial" coherent oscillation due to the Drude weight.

Next we reduce the temperature to $\beta J = 2$ at $B^z/J = 2$. Figure 2(c) clearly shows two effects. First, the Drude weight D^x is strongly reduced. This reduction continues monotonically with increasing B^z (as discussed within the AAA below). Second, the regular part C^x_{reg} is strongly enhanced and undergoes an asymmetric weight redistribution with a major peak developing at a frequency ω *larger* than ω_L (and a minor peak at $\omega < \omega_L$). This is consistent with B^z breaking particle-hole symmetry. In the time domain, see Fig. 2(d), we find that

$$C^x(t) \approx R(t)\cos[(\omega_L + \delta\omega)t] + D^x\cos(\omega_L t) \quad (3)$$

allows for a reasonable leading-order fit of $C^x(t)$ over several oscillation periods by assuming an exponential behavior $R(t) = R_0\exp(-t/\tau)$, i.e., a single decay time τ. In fact, $C^x(\omega)$ is rather close to a Lorentzian in Fig. 2(c). We find this approach to apply at least to $B^z/J \leq 3$ and $\beta J \leq 3$ and to have very little finite-size effects for the system sizes ($N = 10, \ldots, 18$) and time scales ($tJ \leq 20$) studied [20]. Figure 2(c) is a central result of this Letter. It unveils the emergence of a new collective
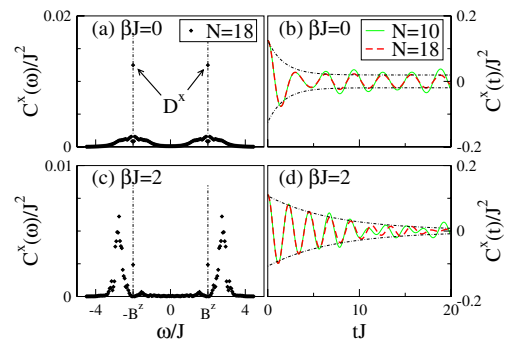

FIG. 2 (color online). Frequency and time dependence of the autocorrelation C^x for $B^z/J = 2$ and (a), (b) $\beta = 0$, (c), (d) $\beta J = 2$ (ED). The Drude weight in (a), (c) is visible exactly at the Larmor frequency $\omega_L = B^z$ (vertical dashed-dotted lines). In (b),(d) the envelopes of fits [as defined in Eq. (3)] to data for $N = 18$ are shown (dashed-dotted curves).

frequency scale, namely, at $\omega_L + \delta\omega$, in the transverse transport process besides the Larmor frequency. Moreover, for $\tau \to \infty$ this process would be coherent.

In Fig. 3 we summarize our findings for τ and $\delta\omega$ over a range of temperatures and fields of $0 \leq \beta J \leq 3$ and $1 \leq B^z/J \leq 3$. Figure 3(a) shows that τ increases roughly linearly with β, with an increasing slope as B^z increases. While finite system studies will not clarify if this result implies true coherence for a particular range of B^z as $T \to 0$, Fig. 3(a) is at least strongly indicative of a large τ in that limit. Regarding $\delta\omega$, Fig. 3(b) clearly signals a saturation roughly at $\beta J \sim B^z/J$ with the value at saturation increasing with B^z. We emphasize that $\delta\omega \neq 0$ directly implies that the transverse current *cannot* be described in terms of transitions between the zero- and one-magnon sector. The dominant spectral weight of such one-magnon excitations at $q = 0$ is exactly at ω_L [25], leading to $\delta\omega = 0$.

To gain insight into the origin of $\delta\omega \neq 0$ we present an AAA for $B^z > B_c^z$ and low T. Here, the contribution of different M sectors to C^x can be dissected asymptotically and, after an extensive analysis [20], we arrive at a simple picture: the transverse current is carried dominantly by transitions from the one-magnon sector around $q \sim \pi$ into antibound states of the *two-magnon* continuum at the same q. The related frequencies $\sim \omega_L + J$ and also the asymptotic form of $C^x(t)$ can be obtained analytically:

$$C_{\text{AAA}}^x(t) \approx \sqrt{\frac{J^3}{\pi}} e^{-\beta(B^z - 2J)} \text{Re}\left(\frac{e^{i(\omega_L + J)t}}{\sqrt{2\beta + it}}\right). \qquad (4)$$

This is consistent with Fig. 3(b), which also suggests that $\delta\omega \to J$ as B^z increases and $\beta \to \infty$. The thermal activation in Eq. (4) stems from the one-magnon energy at $q = \pi$. The damping results from summing over all transitions in the vicinity of $q = \pi$ and its power-law behavior, i.e. $\sim t^{-1/2}$, for $t \to \infty$ clearly shows that the single-scale exponential used for $R(t)$ in Eq. (3) is an approximation for not too low temperatures T only. Nevertheless, for a comparison with Fig. 3(a), we extract a "decay time" from the

envelope of Eq. (4), i.e. $|C_{\text{asy}}^x(t)/C_{\text{asy}}^x(0)| \leq 1/e$ for $t \geq \tau$, leading to $\tau = 2\beta\sqrt{e^4 - 1} \approx 15\beta$. As shown in Fig. 3(a) (straight line), our ED data for $B^z/J = 3$ are consistent with the asymptotic line; e.g., the slope $d\tau/d\beta$ is already close to 15β at $\beta J \sim 2$.

Now we turn to the real-time evolution of the spin-current derived from a Krylov-space based tDMRG approach [23]. This allows us to study larger systems than with ED, however, at zero temperature and only below the saturation field. The latter follows since there are no current-carrying states for $B^z > B_c^z$ at $T = 0$. Moreover, since ED and AAA already suggest that $\tau \to \infty$ as $T \to 0$, limitations in the accessible simulation times confine the tDMRG to an analysis of $\delta\omega$. To induce a current we add a perturbation $H_1 = \sum_r B_r^x S_r^x$ to Eq. (1) with $B_r^x = B^x \cos(2\pi k r/N)$. First, the ground state of $H + H_1$ is evaluated using DMRG, then the system is left to evolve under H alone.

Typical transverse magnetization profiles $\langle S_r^x \rangle$ at $t = 0$ are shown in Fig. 4(a) for $(B^z, B^x)/J = (1.5, 1)$ and for small values of k. $\langle S_r^x \rangle$ follows B_r^x qualitatively, with additional $2k_F$-oscillations from the underlying Luttinger liquid. We perform the time evolution using $m = 200$ states for the ground-state calculation, a time step of $\delta t J = 0.25$, and a fixed discarded weight [20,23]. Although H_1 breaks $U(1)$ symmetry, we can still obtain reliable results for $L \leq 64$ lattice sites. To analyze currents free of spatial oscillations we coarse-grain the data by averaging over suitable parts of the chain. Figure 4(b) shows an example of the time evolution of the current $\langle j_{N/2}^x(t) \rangle$, averaged over the left half of the chain, at $(B^z, B^x)/J = (1.5, 1)$ for $k = 0.5$. For the times reached in the simulation ($tJ \approx 80$), no relaxation can be observed. This is consistent
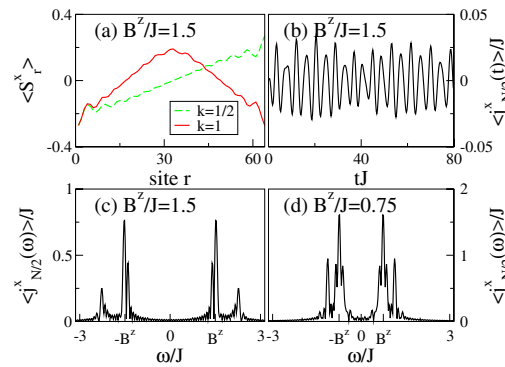

FIG. 4 (color online). Simulation of the transverse spin-current dynamics using tDMRG: (a) Initial magnetization profiles $\langle S_r^x \rangle$ at $t = 0$ for different k; (b) Coherent oscillation of the spatially averaged current $\langle j_{N/2}^x(t) \rangle$ for $k = 0.5$ and $B^z/J = 1.5$; (c), (d) Discrete Fourier transform for (b) and for $B^z/J = 0.75$. Besides the dominant peak at the Larmor frequency $\omega_L = B^z$, there is another significant peak at a higher frequency $\omega_L + \delta\omega$. For more details, see Ref. [20].
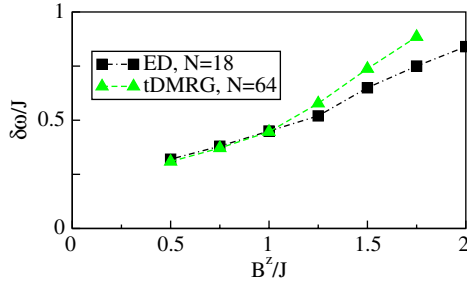

FIG. 3 (color online). (a) Decay time τ and (b) frequency shift $\delta\omega$ w.r.t. β for different B^z. Data are extracted from the autocorrelation $C^x(t)$, using ED for $N = 18$ (symbols). Solid lines represent the low-temperature asymptote above the critical field, dashed curves are guides to the eye.

FIG. 5 (color online). Frequency shift $\delta\omega$ with respect to the magnetic field B^z, as obtained from ED ($\beta J = 3$) and tDMRG.

with the expectation for $T = 0$ drawn from ED and AAA. In view of the substantial number of periods covered in Fig. 4(b) we have chosen to directly study the discrete Fourier transform of the real-time data in order to obtain the *dominant* frequencies. This is shown in Figs. 4(c) and 4(d) for $\langle j_{N/2}^x(t)\rangle$ at $(B^z, B^x)/J = (1.5, 1)$ and $(B^z, B^x)/J = (0.75, 1)$ at $k = 0.5$. These two figures clearly evidence the main result from tDMRG, namely, that, fully consistent with the findings from ED and AAA, there are two characteristic frequencies in the current dynamics, namely ω_L and $\omega_L + \delta\omega$. In contrast to the linear-response regime, the analysis of the relaxation scenario finds the contribution at ω_L to be the larger one. This is not surprising since two different scenarios are compared, characterized by similar yet different correlation functions. We have checked that the results of Figs. 4(b)–4(d) are insensitive (i) to the details of the coarse-graining, (ii) to varying k within the small k regime, and (iii) to the strength of B^x, at least up to $B^x/J = 1$, as used here [20]. The latter implies a minor role of nonlinearity (nonequilibrium).

Finally, in Fig. 5 we compare $\delta\omega$ from ED with tDMRG for $0.5 \le B^z/J \le 2$. The agreement is remarkably good, not only in view of the different scenarios. For intermediate fields ($B^z/J = 0.5$, 0.75, 1) the frequency shifts match each other almost exactly, while we attribute the slight deviation of ED from tDMRG at larger fields to finite temperature effects, where convergence to the $T = 0$ values has not been reached yet [see $B^z/J = 3$ in Fig. 3(b)]. For $B^z/J < 0.5$, the accessible time scales prevent a reliable determination of $\delta\omega$ in our approaches.

In summary, we studied the transverse spin-current dynamics in the spin-$1/2$ Heisenberg chain. As a main result, besides a coherent oscillation at the Larmor frequency, we provided evidence for a second nontrivial collective oscillation at higher frequencies, emerging at low temperatures

as a genuine many-magnon effect and turning coherent as the temperature is lowered.

———————————

*r.steinigeweg@tu-bs.de
[1] J. Fischer and D. Loss, Science **324**, 1277 (2009).
[2] D. J. Reilly *et al.*, Science **321**, 817 (2008).
[3] S. Foletti *et al.*, Nature Phys. **5**, 903 (2009).
[4] A. Ardavan *et al.*, Phys. Rev. Lett. **98**, 057201 (2007).
[5] G. Balasubramanian *et al.*, Nature Mater. **8**, 383 (2009).
[6] H. O. H. Churchill *et al.*, Phys. Rev. Lett. **102**, 16682 (2009).
[7] J. Beugnon *et al.*, Nature Phys. **3**, 696 (2007).
[8] Y. Kato *et al.*, Nature (London) **427**, 50 (2004); B. Huang, D. J. Monsma, and I. Appelbaum, Phys. Rev. Lett. **99**, 177209 (2007); N. P. Stern *et al.*, Nature Phys. **4**, 843 (2008).
[9] A. V. Sologubenko *et al.*, Phys. Rev. Lett. **84**, 2714 (2000); C. Hess *et al.*, Phys. Rev. B **64**, 184305 (2001); N. Hlubek *et al.*, Phys. Rev. B **81**, 020405 (2010).
[10] K. R. Thurber *et al.*, Phys. Rev. Lett. **87**, 247202 (2001).
[11] M. Klanjšek *et al.*, Phys. Rev. Lett. **101**, 137207 (2008).
[12] H. Kühne *et al.*, Phys. Rev. B **80**, 045110 (2009).
[13] X. Zotos and P. Prelovšek, in: *Transport in One Dimensional Quantum Systems* (Kluwer Academic Publishers, Dordrecht, 2004).
[14] F. Heidrich-Meisner, A. Honecker, and W. Brenig, Eur. Phys. J. Special Topics **151**, 135 (2007).
[15] D. C. Johnston *et al.*, Phys. Rev. B **61**, 9558 (2000).
[16] S. Trotzky *et al.*, Science **319**, 295 (2008).
[17] P. Gambardella, Nature Mater. **5**, 431 (2006).
[18] M. Kruczenski, Phys. Rev. Lett. **93**, 161602 (2004).
[19] Y. B. Kim, Phys. Rev. B **53**, 16420 (1996).
[20] See supplemental material at http://link.aps.org/supplemental/10.1103/PhysRevLett.106.160602 for more details.
[21] R. B. Griffiths, Phys. Rev. **133**, A768 (1964).
[22] F. D. M. Haldane, Phys. Rev. Lett. **45**, 1358 (1980).
[23] A. J. Daley *et al.*, J. Stat. Mech. P04005 (2004); S. R. White and A. E. Feiguin, Phys. Rev. Lett. **93**, 076401 (2004); G. Vidal, Phys. Rev. Lett. **93**, 040502 (2004).
[24] G. D. Mahan, *Many Particle Physics* (Plenum Press, New York, London, 1980).
[25] S. Grossjohann and W. Brenig, Phys. Rev. B **79**, 094409 (2009).
[26] For $M > 0$, $D^z(T > 0) > 0$ [13]. The $M = 0$ case is still under scrutiny: see J. Sirker, R. G. Pereira, and I. Affleck, Phys. Rev. Lett. **103**, 216602 (2009); S. Grossjohann and W. Brenig, Phys. Rev. B **81**, 012404 (2010); Refs. [13,14], and references therein.

Supplementary Material for: Coherent Spin-Current Oscillations in Transverse Magnetic Fields

Robin Steinigeweg,[1, *] Stephan Langer,[2] Fabian Heidrich-Meisner,[2] Ian P. McCulloch,[3] and Wolfram Brenig[1]

[1]*Institute for Theoretical Physics, Technical University Braunschweig, D-38106 Braunschweig, Germany*
[2]*Department of Physics and Arnold Sommerfeld Center for Theoretical Physics,*
Ludwig-Maximilians-Universität München, D-80333 München, Germany
[3]*School of Physical Sciences, The University of Queensland, Brisbane, QLD 4072, Australia*
(Dated: March 24, 2011)

I. DERIVATION OF THE ASYMPTOTIC APPROXIMATION

In this section we give a detailed derivation of the asymptotic approximation in Eq. (4) of the Letter. For convenience, we shift the zero point of the energy E to $N(J/4 - B^z/2)$ and of the quantum number M to $N/2$. The shifted quantities will be denoted by $\mathcal{E}$ and $\mathcal{M}$ in the following,

$$\mathcal{E} = E - N(\frac{J}{4} - \frac{B^z}{2}), \quad \mathcal{M} = -(M - \frac{N}{2}). \quad (1)$$

Above the critical field the ground state is fully polarized

$$\psi_{(\mathcal{M}=0, q=0)} = |\uparrow\uparrow \dots \uparrow\uparrow\rangle \quad (2)$$

with momentum $q = 0$ and energy $\mathcal{E}_{(0,0)} = 0$, see Fig. 1 (triangle). Periodic boundary conditions are assumed in this section. This state is an eigenstate of the current operator with the eigenvalue zero

$$j^x \psi_{(0,0)} = 0. \quad (3)$$

In the limit of $T = 0$ only matrix elements from this initial state contribute to the current autocorrelation function $C^x(\omega)$. Therefore $\lim_{T \to 0} C^x(\omega) = 0$. At any finite temperature, $\beta J \gg 1$, initial states from the subspace with $\mathcal{M} = 1$, i.e. one-magnon states, start to contribute to the current autocorrelation function. Using the operator T^μ, which translates a state by μ sites, the eigenstates of the Hamiltonian H in Eq. (1) of the Letter read in this subspace

$$\psi_{(1,q)} = \frac{1}{\sqrt{N}} \sum_{\mu=0}^{N-1} e^{\imath q \mu} T^\mu |\downarrow\uparrow\uparrow \dots \uparrow\uparrow\rangle, \quad (4)$$

$q = 2\pi k/N$, $k = 0, 1, \dots, N-1$. Their energies are

$$\mathcal{E}_{(1,q)} = J(\cos q - 1) + B^z, \quad (5)$$

see Fig. 1 (crosses). At non-zero momentum these one-magnon states obviously carry a net-current, however, they are not eigenstates of the current operator. In fact one readily obtains
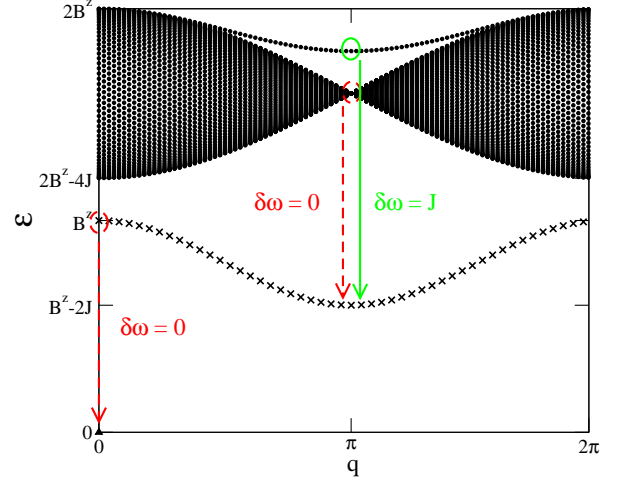

FIG. 1: The spectrum of the Hamiltonian in the $\mathcal{M} = 0$-, 1-, and 2-magnon subspaces (symbols). Additionally, those transitions of the transverse current are indicated that are relevant for the asymptotic approximation at low temperatures above the critical magnetic field: 'Forbidden' transitions (red, dashed lines) yielding no contribution as well as 'allowed' transitions (green, solid lines) leading to the dominant contribution. The latter transitions involve a two-magnon band at the edge of the Brillouin zone, i.e., $q = \pi$. The associated frequencies are larger than the Larmor frequency $\omega_L = B^z$, namely, these frequencies are shifted by $\delta\omega = J$.

$$j^x \psi_{(1,q)} = \imath \frac{J}{2} (1 - e^{\imath q}) \varphi_{(2,q)}, \quad (6)$$

where $\varphi_{(2,q)}$ are states from the subspace with $\mathcal{M} = 2$, i.e. the two-magnon subspace. They read

$$\varphi_{(2,q)} = \frac{1}{\sqrt{N}} \sum_{\mu=0}^{N-1} e^{\imath q \mu} T^\mu |\downarrow\downarrow\uparrow\uparrow \dots \uparrow\uparrow\rangle. \quad (7)$$

In general, and in contrast to Eqs. (4), (5), these states are *no* eigenstates of the Hamiltonian H in Eq. (1) of the Letter, but

$$H \varphi_{(2,q)} = (2B^z - J) \varphi_{(q,2)} + \frac{J}{2}(1 + e^{\imath q}) \tilde{\varphi}_{(2,q)}, \quad (8)$$

where $\tilde{\varphi}_{(2,q)}$ refers to states generated by the transverse fluctuations of H, which separate the two adjacent

flipped spins by one site. However, in the vicinity of $q = \pi$, the prefactor $(1 + e^{\imath q})$ suppresses these contributions rendering $\varphi_{(2,\pi)}$ an exact eigenstate of H. From its eigenenergy $(2B^z - J)$ and Fig. 1 (green circle), it is obvious that this state is the (anti)bound two-magnon state $\psi^r_{(2,q)}$ at $q = \pi$, well known from Bethe-Ansatz. Its dispersion over the complete Brillouin zone is [1]

$$\mathcal{E}^r_{(2,q)} = \frac{J}{2}\left(\cos q - 1\right) + 2B^z \qquad (9)$$

and is situated above the two-magnon continuum.

Due to their Boltzmann weight the transitions from $\psi_{(1,q)}$ into $\varphi_{(2,\pi)}$ at $q \approx \pi$ dominate the current autocorrelation function asymptotically for $\beta J \gg 1$. Therefore, the leading contribution to C^x results from projecting all intermediate states *solely* onto $\psi^r_{(2,q)}$. Since the antibound state is separated by a gap of $\mathcal{O}(J)$ from the two-magnon continuum at $q \approx \pi$, we may use $\langle \varphi_{(2,q)} | \psi^r_{(2,q)} \rangle \approx 1$ in that region, leading to

$$\tilde{C}^x_{\text{AAA}}(\omega) \approx \frac{1}{N}\sum_q e^{-\beta\mathcal{E}_{(1,q)}} |\langle \psi_{(1,q)}|j^x \psi^r_{(2,q)}\rangle|^2$$
$$\times \, \delta(\omega - [\mathcal{E}^r_{(2,q)} - \mathcal{E}_{(1,q)}]). \qquad (10)$$

Using Eq. (6) and introducing the frequency $\omega_q = J/2\,(1 - \cos q)$ this can be rewritten as

$$\tilde{C}^x_{\text{AAA}}(\omega) \approx \frac{J}{N} e^{-\beta B^z} \sum_q \omega_q\, e^{2\beta\omega_q}\, \delta(\omega - [B^z + \omega_q]). \quad (11)$$

Since momentum enters only through ω_q, we may introduce the corresponding density of states and replace the sum by an integral with respect to ω_q. This results in

$$\tilde{C}^x_{\text{AAA}}(\omega + B^z) \approx \frac{J}{2\pi}\, \frac{e^{\beta(2\omega - B^z)}}{\sqrt{J/\omega - 1}}\, \Theta(\omega)\,\Theta(J - \omega), \quad (12)$$

where $\Theta(\omega)$ is the Heaviside function. Fourier transforming this to the time domain we get

$$\tilde{C}^x_{\text{AAA}}(t) \approx \frac{J^2}{2} e^{-\beta(B^z - J)}\, e^{\imath(B^z + J/2)t}$$
$$\times \left[\mathcal{I}_0(J\,[\beta + \tfrac{\imath t}{2}]) + \mathcal{I}_1(J\,[\beta + \tfrac{\imath t}{2}])\right], (13)$$

where $\mathcal{I}_{0,1}(z)$ are modified Bessel functions of the first kind. At low temperatures, i.e. for $\beta J \gg 1$, we may insert their asymptotic forms for $|z| \gg 1$, which are $\mathcal{I}_{0,1}(z) \approx e^z/\sqrt{2\pi\,z}$. Therefore

$$\tilde{C}^x_{\text{AAA}}(t) \approx \sqrt{\frac{J^3}{\pi}}\, e^{-\beta(B^z - 2J)}\, \frac{e^{\imath(B^z + J)t}}{\sqrt{2\beta + \imath t}}. \qquad (14)$$

The real part of this, i.e. $C^x_{\text{AAA}}(t) = \text{Re}\,\tilde{C}^x_{\text{AAA}}(t)$, is Eq. (4) of our Letter, with $\omega_L = B^z$.
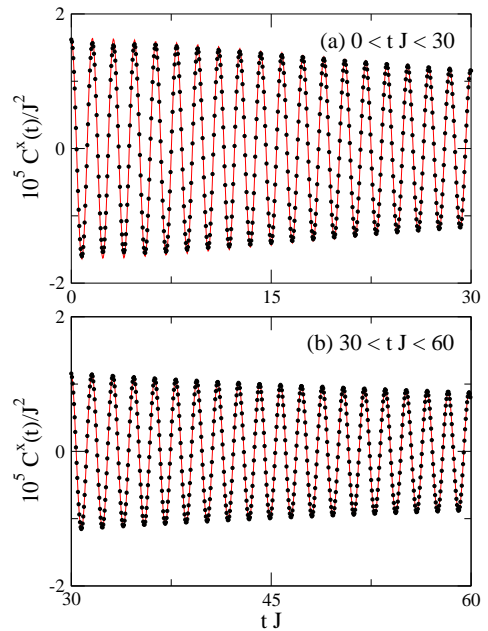

FIG. 2: The current autocorrelation function $C^x(t)$ for (a) $0 \leq tJ \leq 30$ and (b) $30 \leq tJ \leq 60$, restricted to the transitions into the subspaces $\mathcal{M} \leq 1$ (one-magnon subspace). Data are evaluated numerically by the use of ED (circles) and are shown for the parameters $\beta J = 9$, $B^z/J = 3$, and $N = 200$. For comparison, the asymptotic approximation according to Eq. (4) of the Letter is included (curves).

To assess the quality of the asymptotic approximation, we compare this result with ED for the current autocorrelation function above the saturation field, restricting the intermediate-state Hilbert space to two-particle states. This corresponds to taking the limit $\beta J \gg 1$. Due to this restriction ED is possible for rather large systems sizes N. We choose $N = 200$. As shown in Fig. 2, the agreement is excellent. This validates the approximations involved in going from Eq. (6) to (14).

II. ED CALCULATIONS

In this section we provide supplementary material on our ED calculations concerning a potential impact of the finite system size. Specifically, we demonstrate that for the systems of size $N = 18$ and time scales $tJ \lesssim 20$, as used in the Letter, finite-size effects in the frequency shift $\delta\omega$ and the relaxation time τ can be neglected. *Both* of these quantities are determined by assuming a single exponential $R(t) = \exp(-t/\tau)$ to model the envelope of the decay of the coherent oscillation as in Eq. (3) of the Letter. This procedure leads to satisfactory fits to the ED results for not too low temperatures, $\beta J \lesssim 3$. Examples of this are shown in Fig. 2 of the Letter.
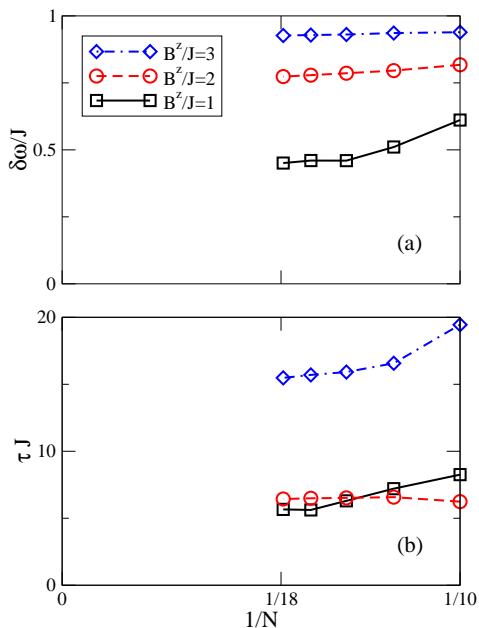
FIG. 3: The extracted (a) frequency shift $\delta\omega$ and (b) decay time τ as a function of the inverse size $1/N$ for the parameters $\beta J = 2$ and $B^z/J = 1$, 2, and 3 (symbols). Lines are guides to the eyes.

Figure 3 summarizes our results for $\delta\omega$ and τ as obtained from $N = 10$, 12, 14, 16, and 18 for various magnetic fields at $\beta J = 2$. This figure clearly demonstrates that both, $\delta\omega$ and τ either display almost no finite size dependence or a clear tendency towards saturation as a function of $1/N$. In all cases shown, the absolute changes in going from $N = 16$ to 18 are negligible. Significant finite size effects can only be seen at systems sizes $N \leq 14$. Therefore, for the temperatures and fields considered in the Letter, it is justified to use $N = 18$ data to obtain $\delta\omega$ and τ (see Fig. 3 of the Letter).

III. DMRG CALCULATIONS

In this section we provide details of our DMRG simulations of the real-time evolution of the transverse current. We will focus on three aspects: (i) the coarse graining of the current, (ii) the dependence on the initial state and its characteristic wave length k, and (iii) the numerical determination of the frequency shift $\delta\omega$, depending on the maximum simulation time and system size. The simulations were carried out with a fixed discarded weight, which we have varied from 10^{-4} to 10^{-6} in order to check convergence of our results.

Figure 4 shows the Fourier spectrum of the transverse current for two different coarse graining schemes. The solid, black line is taken from Fig. 4(c) of the Letter where
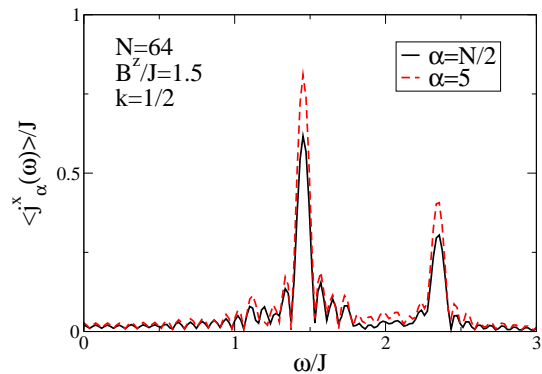
FIG. 4: Coarse graining: The solid, black line is the frequency-dependent current averaged over the left half of the system while the dashed, red line is averaged over five sites, counting away form the center of the system with $N = 64$ (to be precise, these are sites $r = 30$, 31, 32, 33, 34). The main features, i.e., the dominant frequencies do not depend on the coarse graining.

we average the current over the left half of the chain (labeled by $\alpha = N/2$ in Fig. 4). The dashed, red line is the result from averaging the current over five sites in the middle of the chain (denoted by $\alpha = 5$); in this example, the coarse graining is taken over sites $r = 30$, 31, 32, 33, 34 in a system with $N = 64$. As the figure clearly shows, the position of the two maxima, i.e., the one at the Larmor frequency ω_L and the one at $\omega_L + \delta\omega$, as well as their (relative) weights are insensitive to the coarse graining.

Turning to the initial states of the real-time evolution, they are constructed by adding a site-dependent transverse field via a term $\sum_r B_r^x S_r^x$ to the Hamiltonian with
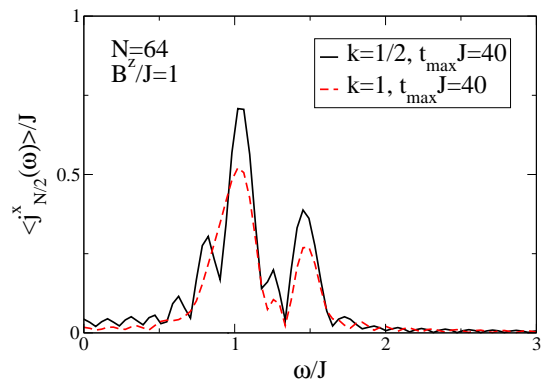

FIG. 5: Dependence on the initial state: Spectrum of the transverse current for two different values of k: $k = 1/2$ (solid, black line) and $k = 1$ (dashed, red line). In both cases, $B^x/J = 1$, $B^z/J = 1$ and $N = 64$. The Fourier transform is taken with $t_{\max} J = 40$ due to the higher numerical costs at larger k.
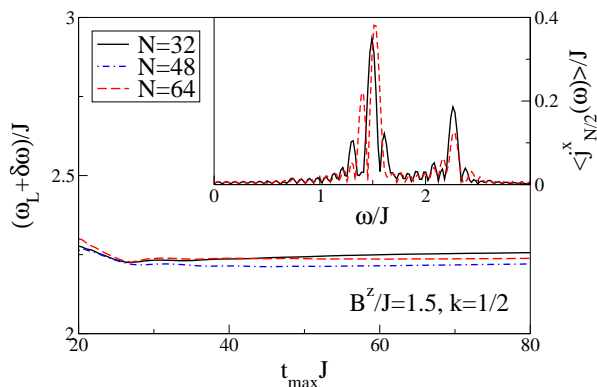
FIG. 6: Numerical determination of $\omega_L + \delta\omega$ in dependence of the simulation time, for three different system sizes: $N = 32$ (solid, black line), $N = 48$ (dash-dotted, blue line) and $N = 64$ (dash-dotted, red line). The final values are all within the overall numerical accuracy and no systematic finite size effects are visible. The inset shows the spectra at $t_{\max}J = 80$ for $N = 32$ (solid, black line) and $N = 64$ (dashed, red line).

$B_r^x = B^x \cos(2\pi k r/N)$. Figure 5 illustrates that a central result of our Letter, namely the positions of the maxima in the current's Fourier spectrum, does not depend on the wave vector k of the perturbing field B_r^x in the long wave-length limit. Computational constraints lead to a decrease of the maximum simulation times accessible as k is increased. For a comparison of $k = 1/2$ and 1 this implies that we have to confine ourselves to $tJ \lesssim 40$. Therefore, the features in Fig. 5 are broader than in Fig. 4 (c) of our Letter.

In Fig. 6, we address the convergence of the position of the second maximum in $j_{N/2}^x(\omega)$ at $\omega_L + \delta\omega$ as a function of the simulation time and the system size. Since we perform a discrete Fourier transform on a finite time window to obtain $j_{N/2}^x(\omega)$ from the real-time data $j_{N/2}^x(t)$, the resulting spectrum depends on the maximum simulation time. After a minimum time needed to resolve the two frequencies has been reached we compute the spectrum after each time step and extract both frequencies. The quantity displayed in the figure is $\omega_L + \delta\omega$ averaged over these spectra obtained from $t_{\max}J = 20$ up to the maximum simulation time $t_{\max}$. For $N = 32$ and 48 (solid, black and dash-dotted, blue line, respectively), $\omega_L + \delta\omega$ weakly increases with $t_{\max}$, while for $N = 64$ (dashed red line), the convergence is much faster. The finite-size effects in $\omega_L + \delta\omega$ are non-monotonous and result in a small uncertainty of about 2-3%, well within the overall numerical accuracy of the simulations. The inset shows the spectrum of the current as a function of frequency at $t_{\max}J = 80$ for $N = 32$ and $N = 64$. While the dominant frequencies are only slightly affected by finite-size effects, spurious additional peaks appear on the smaller system that are irrelevant for the results and discussion presented in the Letter.

IV. COMMENT ON UNITS

In the Letter all quantities are expressed in units of the exchange coupling constant J. Moreover, and to abbreviate the theoretical analysis, Planck's constant $\hbar$ has been set to unity as usual. Similarly, the Bohr magneton μ_B and the spin Landé factor g_S have been absorbed into the definition of the magnetic field. The correspondence between these units and SI-units is summarized in Tab. I. Therein, J is expressed in units of temperature, i.e., divided by the Boltzmann constant k_B.

quantity	unit	
	Letter	**SI**
magnetic field	J	$k_B/(\mu_B\, g_S)$ (J/k_B) $\approx 0.744\,\text{T/K}$ (J/k_B)
frequency	J	$k_B/\hbar$ (J/k_B) $\approx 1.309 \cdot 10^{11}\,\text{Hz/K}$ (J/k_B)
time	$1/J$	$\hbar/k_B$ (k_B/J) $\approx 7.638 \cdot 10^{-12}\,\text{sK}$ (k_B/J)

TABLE I: Correspondence between the units in the Letter and SI-units.

---

* Electronic address: r.steinigeweg@tu-bs.de
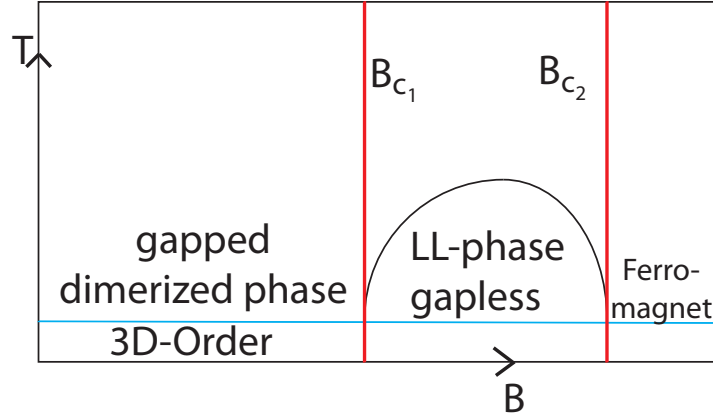[1] H. Bethe, Z. Phys. A **71**, 205 (1931).

Figure 8: Sketch of the phase diagram of a bulk material exhibiting a field-induced Luttinger Liquid phase at low temperatures

3.4 Field-dependent spin and heat conductivities of dimerized spin-$\frac{1}{2}$ chains

We now leave the Heisenberg chain and employ linear response theory to study the transport properties of gapped quantum magnets in a homogeneous magnetic field. While the physics of a spin Luttinger liquid, which is a critical phase with algebraic decaying spin-spin correlations, can very well be studied theoretically using the Heisenberg chain [8], experimental access to the Luttinger liquid physics in low dimensional quantum magnets is rare [56, 57]. For quantum magnets which have a spin gap in the groundstate such as spin ladders or dimerized chains, the Luttinger liquid phase can be induced by a magnetic field. As a experimental motivations, we introduce the organic spin ladder compound $C_5H_{12}N_2CuBr_4$ (Refs. [56] and [57]). This material has recently gained attention as it allows for the experimental access to field-driven quantum phase transitions at low temperatures up to the saturation field. While the exchange couplings of the majority of copper based spin ladder materials (see [11] and Chap. 3.5) exceed the magnetic fields available in the laboratory, for this material, the phase diagram with respect to temperature and magnetic field has been explored by a large variety of experimental probes [56, 57, 178, 179, 180]. A sketch of the relevant features of phase diagram found in these experiments [57] is shown in Fig. 8.

For very low temperatures real low-dimensional quantum magnets exhibit a ordered phase in which the anisotropic exchange interaction in the planes is no longer dominant. At higher, yet sufficiently low temperatures and zero magnetic field the phase is gapped and dimerized, which was also reported for $C_5H_{12}N_2CuBr_4$. Once the magnetic field exceeds B_{c_1} the gap closes and the material exhibits a spin liquid phase with algebraic decaying spin-spin correlations. Further increasing the magnetic field amplitude beyond B_{c_2} induces a second phase transition to a ferromagnetic phase.

In the following we take a dimerized spin chain as minimal model of a quantum magnet that exhibits such a field-induced gapless phase [98, 99]. The spin gap as a function of dimerization can be tuned to the value found experimentally for $C_5H_{12}N_2CuBr_4$ [56, 57, 178]. We do expect to observe qualitatively similar magnetothermal transport properties. We apply the linear response formalism established in Chap. 3.1 to calculate the frequency-dependent spin and heat conductivities of dimerized spin chains as a function of temperature and magnetic field. As a main result, we find enhanced spin and heat transport in the field-induced gapless phase, which manifests itself as an increased weight in the low-frequency regime of both spin and heat conductivity for all values of dimerization. While we focus on the experimentally relevant value, it is important to note though that recent experiments have not found distinct features in the thermal conductivity of $C_5H_{12}N_2CuBr_4$ [181]. Furthermore, we include magnetothermal corrections, which then lead to an decrease of the conductivities, as was known for the Heisenberg chain [167].

Field-dependent spin and heat conductivities of dimerized spin-$\frac{1}{2}$ chains

S. Langer,[1] R. Darradi,[2] F. Heidrich-Meisner,[1] and W. Brenig[2]

[1]*Department of Physics and Arnold Sommerfeld Center for Theoretical Physics, Ludwig-Maximilians-Universität München, D-80333 München, Germany*

[2]*Institut für Theoretische Physik, Technische Universität Braunschweig, D-38106 Braunschweig, Germany*

We study the spin and heat conductivity of dimerized spin-$\frac{1}{2}$ chains in homogeneous magnetic fields at finite temperatures. At zero temperature, the model undergoes two field-induced quantum phase transitions from a dimerized, into a Luttinger, and finally into a fully polarized phase. We search for signatures of these transitions in the spin and heat conductivities. Using exact diagonalization, we calculate the Drude weights, the frequency dependence of the conductivities, and the corresponding integrated spectral weights. As a main result, we demonstrate that both the spin and heat conductivity are enhanced in the gapless phase and most notably at low frequencies. In the case of the thermal conductivity, however, the field-induced increase seen in the bare transport coefficients is suppressed by magnetothermal effects, caused by the coupling of the heat and spin current in finite magnetic fields. Our results complement recent magnetic transport experiments on spin-ladder materials with sufficiently small exchange couplings allowing access to the field-induced transitions.

PACS number(s): 75.10.Jm, 72.10.−d, 05.60.Gg, 75.40.Gb

I. INTRODUCTION

While low-dimensional quantum magnets have been intensely studied for the past decade, the transport properties still pose viable challenges for experimental and theoretical physicists.[1–4] On the theoretical side, the ground-state properties of low-dimensional spin systems are very well studied by means of powerful techniques such as the Bethe ansatz, bosonization, the density matrix renormalization group (DMRG) method, quantum Monte Carlo, and exact diagonalization (see Refs. 5–7 for reviews). Finite-temperature transport properties, though, remain an exciting and active field of research. One of the best established results is the ballistic thermal transport in the integrable *XXZ* spin-$\frac{1}{2}$ chain.[8–11] In general, however, transport properties are not that easily obtained, especially far from equilibrium or in nonintegrable models but even spin transport in exactly solvable models is still an active field of research with open pending questions.[11–18] In the nonequilibrium case, one has to resort to numerical simulations of either systems coupled to external baths[19–21] or closed systems prepared in a state out of equilibrium.[22,23]

For nonintegrable systems, finite-temperature transport is expected to be diffusive,[24,25] which is consistent with the numerical observation of a vanishing Drude weight for both heat and spin transport.[11,26–29] While this result has been accepted for massive phases in the high-temperature regime, the situation for massless phases of nonintegrable systems at low temperatures and in the vicinity of integrable models[11,30–32] is less clear, in the sense that numerical studies yield large ballistic contributions to transport coefficients in massless phases and on finite systems.[2,30,33]

Theoretical research into the transport properties of low-dimensional magnets[1,2] has been strongly motivated by exciting experimental results on materials with low-dimensional electronic structures.[3,4] The large thermal conductivities found in the spin-ladder materials $(\mathrm{Sr,Ca,La})_{14}\mathrm{Cu}_{24}\mathrm{O}_{41}$ establish a link between the thermal

conductivity and magnetic excitations.[34–37] There is also a variety of spin-chain materials with magnetic contributions to the heat conductivity, most notably $\mathrm{Sr}_2\mathrm{CuO}_3$, SrCuO_2 (Refs. 38–40), and $\mathrm{CaCu}_2\mathrm{O}_3$ (Ref. 41). Recent successes in sample preparation have resulted in very clean samples of SrCuO_2, exhibiting the largest thermal conductivity so far observed in low-dimensional quantum magnets.[40] This has been interpreted as experimental evidence for ballistic heat transport in clean Heisenberg chains, where phonons are the main source of external scattering.[40]

The magnetic field dependence of the thermal conductivity has been the case of interest in several experimental studies,[34,42,43] yet in most of the known materials, exchange couplings are orders of magnitude larger than the magnetic fields available in a laboratory. Only recently, the quasi-one-dimensional organic compound $(\mathrm{C}_5\mathrm{H}_{12}\mathrm{N})_2\mathrm{CuBr}_4$ (Refs. 44 and 45) has gained attention in this context. It has exchange couplings small enough to allow experimental access to field-driven quantum phase transitions at low temperatures up to the saturation field. In these experiments, the phase diagram with respect to temperature and magnetic field has been explored by a large variety of experimental probes, establishing the presence of a field-induced gapless phase at low temperatures.[46–50] Recent measurements of the thermal conductivity of these compounds in external magnetic fields have been interpreted in terms of the absence of spin-mediated heat transport.[51]

The field-dependent thermal transport in the *XXZ* chain has previously been addressed with several theoretical approaches,[52–54] emphasizing the role of magnetothermal corrections to the thermal conductivity due to the coupling of the spin and the heat current, similar to the Seebeck effect.[55] The possibility of controlling the heat transport in spin chains by varying a magnetic field has been addressed in Ref. 56. The zero-field transport properties of the dimerized chain have been studied in Refs. 2 and 11 while the field dependence of the thermal Drude weight of noninteracting, dimerized *XX* chains has been discussed in Ref. 57.

Our present goal is to understand the dependence of the spin and heat conductivities of dimerized spin chains on external magnetic fields. Within linear-response theory, the frequency-dependent conductivity has two contributions, a delta peak at zero frequency whose weight is the Drude weight and a regular part,

$$\sigma[\kappa](\omega) = D_{s[th]}\delta(\omega) + \sigma[\kappa]_{\text{reg}}(\omega). \qquad (1)$$

Using exact diagonalization to evaluate Kubo formulas,[55,58] we compute these quantities for a value of the spin gap that is comparable to the one found in $(C_5H_{12}N)_2CuBr_4$ (Refs. [46] and [47]).

As a main result, we find an increased weight in the low-frequency regime of both $\sigma(\omega)$ and $\kappa(\omega)$ in the field-induced phase. This allows for a direct interpretation in terms of transport channels opened in the vicinity of the Fermi points of the corresponding Luttinger liquid. These channels lead to a strong enhancement of the transport coefficients for spin and heat conduction. On the finite systems that we have access to with exact diagonalization, the main contribution to the increase in the conductivities at low frequencies and low but finite-temperature stems from the Drude weight. In the case of the spin conductivity this increase is roughly an order of magnitude larger than the one observed in the regular part whereas for the thermal conductivity, the picture is more involved. At zero magnetic field and low temperatures, the bare thermal Drude weight (without any magnetothermal corrections) dominates the regular part, yet when increasing the field, the regular part increases more strongly than the thermal Drude weight. Finally, taking into account the magnetothermal corrections, the increase in the thermal weight with increasing field becomes a *decrease*, as expected from the results for the *XXZ* chain.[54]

We further study the dependence of the transport coefficients on the strength of the dimerization, varying it between the limits of uncoupled dimers and the Heisenberg chain. We expect that our results are generic for dimerized quasi-one-dimensional systems, while the obvious advantage of working with the dimerized chain is that with exact diagonalization, we can reach longer chains than in the case of a ladder. We shall stress that our work is concerned with the intrinsic transport properties of dimerized systems whereas for a complete description of the experimental results, phonons may play an important role, as has been emphasized in Refs. [59–61].

The paper is organized as follows: first, we introduce the model and briefly review the ground-state properties. Second, we proceed by summarizing the necessary framework to compute transport coefficients and conductivities within linear-response theory. Section IV presents the results. We study the Drude weights in Sec. IV A, the frequency-dependent conductivities in Sec. IV B and the spectral weights in Sec. IV C, all as a function of the magnetic field and temperature. The influence of the strength of the dimerization is discussed in Secs. IV D and IV E covers magnetothermal effects. Finally, we summarize our findings in Sec. V. The dependence of the Drude weights at finite fields on the system size is presented in the Appendix.
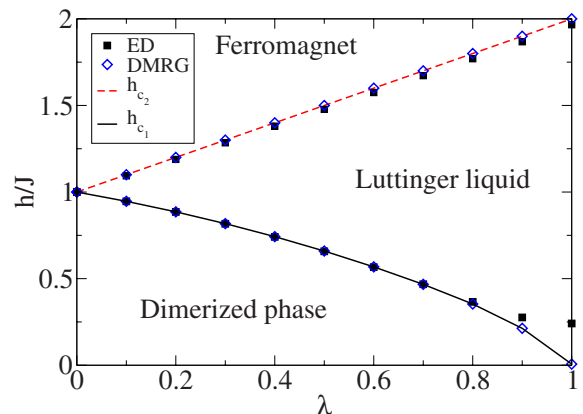

FIG. 1. (Color online) (h,λ) plane of the phase diagram of the dimerized spin chain at temperature $T=0$ (see Refs. [62] and [63]). The upper (red dashed) line is the saturation field. The lower (solid black) line corresponds to the spin gap (Refs. [64–67]). The critical fields h_{c_1} and h_{c_2} are obtained from exact diagonalization of chains of length $L=18$ (squares). The blue diamonds are DMRG data, extrapolated in the inverse system size.

II. MODEL

We study the spin and thermal conductivity of dimerized spin chains in a homogeneous magnetic field. The model Hamiltonian for a chain of length L is given by

$$H = \sum_{i=1}^{L} h_i = J \sum_{i=1}^{L} [\lambda_i \vec{S}_i \cdot \vec{S}_{i+1} - h S_i^z], \qquad (2)$$

where the dimerization is introduced via $\lambda_i = \lambda$ for i even and $\lambda_i = 1$ for i odd, $\vec{S} = (S^x, S^y, S^z)$, S_i^μ and $\mu = x, y, z$ are the components of a spin-$\frac{1}{2}$ operator acting on site i and h denotes the magnetic field. We use periodic boundary conditions. The exchange coupling J sets the global energy scale and the model includes the Heisenberg spin chain ($\lambda = 1$) and uncoupled dimers ($\lambda = 0$) as limiting cases.

The magnetic phase diagram,[62,63] shown in Fig. 1, is very similar to the one of the two-leg ladder system.[68] The upper (red dashed) line is the saturation field. The lower (solid black) line corresponds to the spin gap which has been intensely studied by analytical and numerical means.[64–67] Since the Heisenberg chain is gapless a careful finite-size scaling for the lower critical field is necessary. The blue diamonds are DMRG data for open boundary conditions, extrapolated in inverse system size, which we compare to exact diagonalization results obtained with $L=18$ sites and periodic boundary conditions (squares). This illustrates that for $\lambda \lesssim 0.8$, the phase boundaries exhibit very small finite-size effects; thus, for the system sizes that we shall use in our exact diagonalization analysis, we are already very close to the bulk value for the gap. The Luttinger liquid phase here is similar to the Luttinger-liquid phase in the *XXZ* model where the transition from the gapped to the gapless phase is of the commensurate-incommensurate type (see, e.g., Refs. [69] and [70]).

III. TRANSPORT COEFFICIENTS AND CONDUCTIVITIES

Here we summarize the central equations for magnetic transport in the linear-response regime. The expectation values of the spin and thermal currents, j_1 and j_2, are given by[55]

$$\langle j_l \rangle = \sum_m L_{lm} f_m, \qquad (3)$$

where $f_1 = \nabla h$ and $f_2 = -\nabla T$ refer to the magnetic field and temperature gradients. L_{lm} is the conductivity matrix. j_1 and j_2 can be expressed via the spin and energy currents j_s and j_{th} by

$$j_1 = j_s, \quad j_2 = j_{th} - h j_s, \qquad (4)$$

where

$$j_{s[th]} = i \sum_{l=1}^{L-1} [h_{l-1}, d_l]. \qquad (5)$$

h_l denotes the local energy densities defined by Eq. (2) at zero magnetic field, i.e., $d_l = h_l = \lambda_i S_i^\mu S_{i+1}^\mu$ for heat transport, while $d_l = S_l^z$ for spin transport. The conductivities satisfy

$$\sigma_{lm}(\omega) \equiv \text{Re } L_{lm}(\omega) = D_{lm} \delta(\omega) + \sigma_{reg,lm}(\omega) \qquad (6)$$

with

$$D_{lm} = \frac{\pi \beta^{r+1}}{ZL} \sum_{\substack{n,o \\ E_n = E_o}} e^{-\beta E_n} \langle n|j_l|o \rangle \langle o|j_m|n \rangle, \qquad (7)$$

where $r = 0(1)$ for $m = 1(2)$ and

$$\sigma_{reg,lm} = \frac{\pi \beta^r}{ZL} \frac{1 - e^{-\beta\omega}}{\omega} \sum_{\substack{n,o \\ E_n \neq E_o}} e^{-\beta E_n}$$
$$\times \langle n|j_l|o \rangle \langle o|j_m|n \rangle \delta(\omega - \Delta E). \qquad (8)$$

$\beta = 1/T$ is the inverse temperature, $|n\rangle$ and E_n are the eigenstates and energies of H, $Z = \sum_n e^{-\beta E_n}$ denotes the partition function, and $\Delta E = E_o - E_n$. Next we define

$$\left.\begin{array}{c} \sigma(\omega) \\ \kappa(\omega) \\ \sigma_{th,s}(\omega) \end{array}\right\} \equiv \left\{\begin{array}{l} \sigma_{11}(\omega) \\ \sigma_{22}(\omega)|_{j_2 \to j_{th}} \\ \sigma_{21}(\omega)|_{j_2 \to j_{th}}, \end{array}\right. \qquad (9)$$

and the Drude weights D_s, D_{th}, and $D_{th,s}$ of $\sigma(\omega)$, $\kappa(\omega)$, and $\sigma_{th,s}(\omega)$, respectively. The latter set of quantities corresponds to a choice for the currents alternative to Eq. (4), namely, $j_1 = j_s$ and $j_2 = j_{th}$. Note that $TD_{12(s,th)} = D_{21(th,s)}$. As in Refs. 2, 11, 26, and 54 we will evaluate $\sigma(\omega)$, $\kappa(\omega)$, and $\sigma_{th,s}(\omega)$ using exact diagonalization. From these quantities all transport coefficients $\sigma_{lm}(\omega)$ at finite fields can be obtained using Eqs. (4), (7), and (8). The Drude weight K_{th} for *purely* thermal transport accounts for the situation of *no* spin current, i.e., at $\langle j_s \rangle = 0$. It is obtained analogously to the Seebeck effect as

$$K_{th} = D_{th} - \frac{D_{th,s}^2}{TD_s}, \qquad (10)$$

or equivalently, using Eqs. (4) and (7): $K_{th} = D_{22} - D_{21}^2/(TD_{11})$. We will study the field dependence of the magnetothermal coupling in Sec. IV E.

For the spin Drude weight, an alternative expression fully equivalent to Eq. (7) exists[71]

$$D_s = \frac{\pi}{ZL} \left[\langle -\hat{T} \rangle - 2 \sum_{\substack{n,o \\ E_n \neq E_o}} e^{-\beta E_n} \frac{|\langle o|j_s|n \rangle|^2}{\Delta E} \right], \qquad (11)$$

where $\langle \hat{T} \rangle$ denotes the kinetic energy. This expression will be used to evaluate D_s in this paper since it gives the correct contribution to the optical sum rule Eq. (13) on finite systems at low temperatures (see the discussion below).[54]

Finally, we define the integrated spectral weights

$$I_{s[th]}(\omega) := \int_{-\omega}^{\omega} \sigma[\kappa](\omega) d\omega = D_{s[th]} + 2 \int_{0^+}^{\omega} \sigma[\kappa]_{reg}(\omega), \qquad (12)$$

and $I_{s[th]}^0 \equiv I_{s[th]}(\infty)$. For the spin conductivity, one obtains the optical sum rule,[72]

$$I_s^0 := \int_{-\infty}^{\infty} \sigma(\omega) d\omega = \frac{\pi}{L} \langle -\hat{T} \rangle. \qquad (13)$$

The right-hand side of the corresponding sum rule for thermal transport[73] at finite temperatures depends on the model and the choice for the local energy density.

IV. RESULTS

We present our results for the transport coefficients of dimerized spin chains, starting with the dimerization strength $\lambda = 0.5$, yielding a gap close to the one of the experimental system. We separately analyze the Drude weights (Sec. IV A) and the conductivities (Sec. IV B) and then combine them to get the spectral weight (Sec. IV C), all as a function of temperature and magnetic field. As a result, we find that the dominant effect of applying a magnetic field for this fixed value of λ is an enhancement of the low-frequency spin as well as heat conductivity. In Sec. IV D, we analyze this enhancement at different strengths of the dimerization. Section IV E discusses the magnetothermal coupling.

A. Drude weights as a function of *T* and *h*

We start focusing on $\lambda = 0.5$, resulting in a value of the spin gap $\Delta = 0.66$ in units of J. One of the two contributions to the integrated spectral weights is the Drude weight in Eq. (1). Figure 2 shows the spin Drude weight D_s and the thermal Drude weight D_{th} as a function of the magnetic field for $T/J = 0.25, 0.5, 1$ and chains consisting of $L = 18$ spins. At low temperatures ($T = 0.25J$, solid black lines), we find a strong enhancement of both quantities between the critical fields $h_{c_1} = 0.66J$ and $h_{c_2} = 1.48J$. Increasing the temperature weakens this feature significantly, especially for thermal
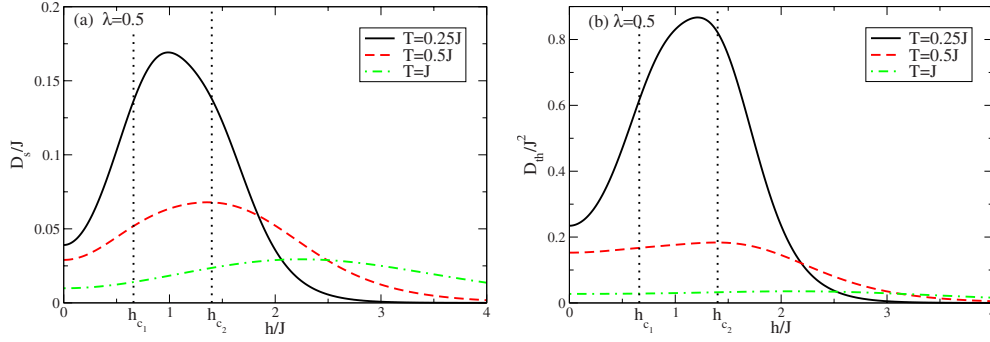
FIG. 2. (Color online) Drude weight for spin (a) and thermal (b) transport at $\lambda=0.5$ and different temperatures for chains of length $L=18$. At low temperatures ($T=0.25J$, solid black lines) we find a significant increase in both quantities in the field-induced phase. At larger temperatures, the peak becomes less pronounced and is located at higher magnetic fields. The black dotted vertical lines are guides to the eyes which mark the critical fields $h_{c_1}=0.66J$ and $h_{c_2}=1.4J$.

transport. This feature is addressed quantitatively in the discussion of the spectral weights (Sec. IV C). It is also worth noting that the maximum in the Drude weights $D_{s[th]}=D_{s[th]}(h)$ moves to higher fields as the temperature increases. At low temperatures, the question arises whether there are any features in $D_s=D_s(h)$ at the critical field, i.e., whether the finite systems we investigate exhibit remnants of the quantum critical behavior to be expected at h_{c_1}. We shall comment on this point in Sec. IV D, where we will discuss the λ dependence of the Drude weights.

B. Dynamical conductivities

The second contribution to the spectral weight is the regular part [Eq. (8)] of the dynamical conductivity. By inspecting the spectral representations, one realizes that the field can only enter via the Boltzmann factors, thus a magnetic field can only enhance or reduce existing weight but does not change the position of the poles $\omega=\Delta E$. Note that at zero

magnetic field, the weight in the gap is suppressed at low temperatures as the system approaches its dimerized ground state and can be tuned to finite values by increasing either the magnetic field or temperature.[2]

Our numerical results are depicted in Fig. 3. At zero magnetic field and low temperatures, there is almost no weight in the regular part of $\sigma(\omega)$ [dashed line in Fig. 3(a)] below a value of ω approximately corresponding to h_{c_1} (compare Ref. 2 for the case of $\lambda=0.1$ and $h=0$) beyond which the dominant peak is located. Turning on a magnetic field larger than h_{c_1} influences the curve drastically. The major portion of the weight still lies above the gap but is much smaller and without significant peaks [solid line in Fig. 3(a)]. In addition to the overall reduction we find spectral weight at very small frequencies which is not the case at zero field. Going to higher temperatures [Fig. 3(b)] results in a smooth curve due to thermal excitations while the influence of the magnetic field is much weaker and does only change the numerical values without modifying the structure.
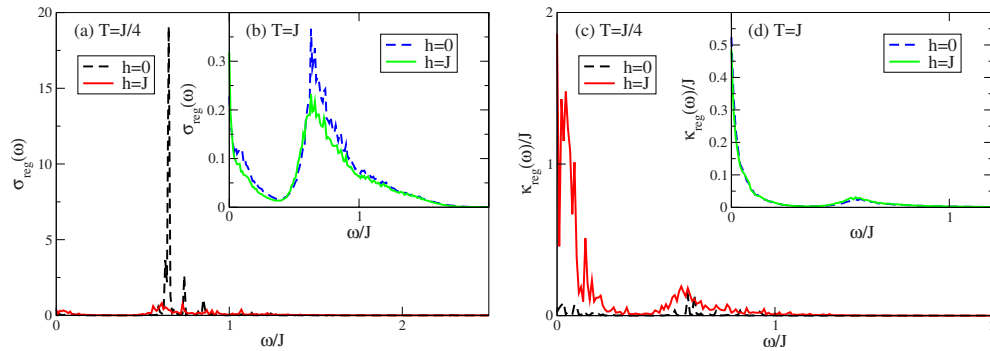

FIG. 3. (Color online) Regular part of the dynamical conductivities $\sigma(\omega)$, $\kappa(\omega)$ as a function of frequency for different magnetic fields and temperatures. (a) shows the spin conductivity at low temperatures ($T=0.25J$) and zero magnetic field (dashed black line) as well as $h=J$ (solid red line) for a chain with $L=18$ spins and a dimerization of $\lambda=0.5$. In the presence of a field $h=J$, $\sigma_{\text{reg}}(\omega)$ increases in the gap but strongly decreases at higher frequencies. The inset (b) shows the same at a higher temperature ($T=J$) where the effect of h is less strong. (c) and (d) show $\kappa_{\text{reg}}(\omega)$ of the same system. (c) For low temperatures, the magnetic field gives rise to an increase in $\kappa_{\text{reg}}(\omega)$ over the whole spectrum (solid red line). The inset (d) shows $\kappa_{\text{reg}}(\omega)$ at higher temperatures ($T=J$), where $\kappa_{\text{reg}}(\omega)$ is a smooth curve and barely influenced by the field.
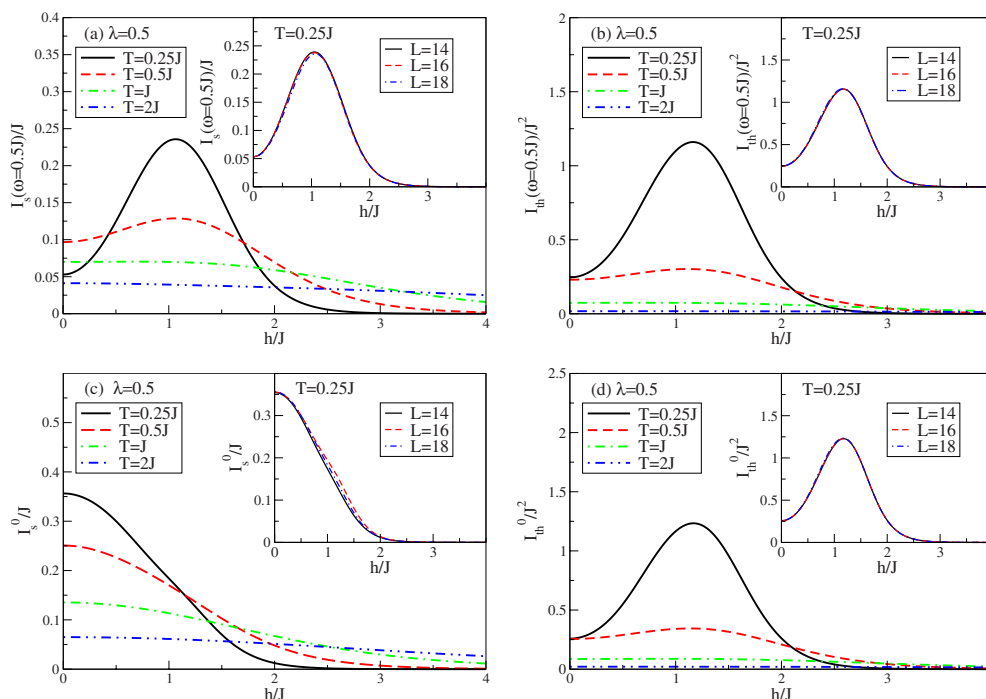
FIG. 4. (Color online) (a) Spectral weight $I_s(\omega)$ for spin transport integrated up to $\omega=0.5J$ as a function of magnetic field h for $L=18$ spins and at different temperatures. (b) Spectral weight $I_{th}(\omega)$ for heat transport integrated up to $\omega=0.5J$. At low temperatures, there is a large peak in both quantities indicating the enhancement of transport in the field-induced gapless phase. As temperature increases, this effect vanishes up to the point where the magnetic field causes the decrease in spectral weight in the gap. For heat transport, the magnetic field has almost no effect at large temperatures ($T=J,2J$). (c) and (d) When extending the upper bound on the frequency ω to infinity, the effect of the magnetic field on spin transport is hidden under the large contributions of the regular part above the gap (c) while I_{th}^0 behaves similar to $I_{th}(\omega=J/2)$ (d). The inset in each panel illustrates the small dependence on the system size at low temperatures.

In the case of thermal transport [Fig. 3(c)], the basic structure is different and the role of the magnetic field at low temperatures is even more important. Without a field (dashed line) a significant amount of spectral weight is found around $\omega=0$ while another important contribution is at the lower edge of the one-triplet band, similar to the spin conductivity. Switching on a magnetic field larger than h_{c_1} (solid line) enhances the heat conductivity strongly, especially at low frequencies. Increasing the temperature up to $T=J$ smoothens the curve while completely suppressing the influence of the magnetic field.

Concentrating on the regular parts alone, one would conclude that both spin and heat transport are not influenced by the magnetic field at high temperatures. At low temperatures, the weight in $\sigma_{reg}(\omega)$ is strongly reduced by the magnetic field yet comes along with an increase in the weight at low frequencies, which is the effect we are interested in. By contrast, $\kappa_{reg}(\omega)$ is enhanced by the field at low temperatures at all frequencies, with most of this increase originating from the low-frequency range $\omega<h_{c_1}$. At higher temperatures, both effects are suppressed. To understand the interplay of the Drude weights and the regular parts, one has to study the spectral weight.

C. Field dependence of the spectral weight

Now that we have shown how the transport enhancement takes place via increasing weight at low frequencies we study the integrated spectral weight $I_{s[th]}(\omega)$. Figure 4 shows our results for $I_s(\omega=0.5J)$ and $I_{th}(\omega=0.5J)$ as well as the total spectral weights $I_{s[th]}^0$. We have chosen the upper bound of integration to be $\omega=0.5J$ to measure how the weight in the gap of the system behaves as a function of temperature and field. Our findings in the case of low temperature and $\lambda=0.5$ are the following: for both spin and heat transport, we find a strong enhancement of transport in the field-induced gapless phase at low temperatures $T<h_{c_1}$. As temperature increases, the field dependence becomes less pronounced. From Fig. 4, it is obvious that the total weight in the spin conductivity, i.e., $I_s^0 \propto \langle -\hat{T} \rangle$ typically decreases as a function of increasing field, due to the increasing weight of strongly polarized states. Therefore, the enhanced low-frequency weight seen in both the Drude weight and the regular part has to be accompanied by a decrease in spectral weight at higher frequencies in order to satisfy the optical sum rule Eq. (13), consistent with our discussion of Fig. 3(a).

In the case of thermal transport, the influence of temperature on I_{th}^0 is much more drastic: the maximum in I_{th}^0 seen at
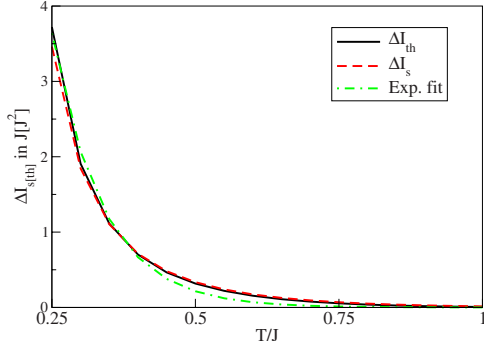
FIG. 5. (Color online) Relative enhancement $\Delta I_{s[th]}$ of the spectral weights as a function of temperature ($L=14$). The curves for thermal transport (solid black line) and spin transport (dashed red line) almost coincide and decay slightly slower than exponentially [$\Delta I_{s[th]} \sim \exp(-cT)$, green dashed-dotted line] as the temperature increases.

$T=0.25J$ is quickly washed out at temperatures $T > h_{c_1}$. By contrast, for spin transport and in I_s^0, the interesting features are hidden at all temperatures under the large field-induced decrease in the regular part as ω approaches the gap [Fig. 4(c)] whereas in the case of thermal transport, the low-frequency behavior dominates the field dependence of I_{th}^0 at $T < h_{c_1}$ [Fig. 4(d)]. For $T > 0.25J$, the finite-size effects of the integrated weights become very small, which is shown in the insets of Fig. 4, illustrating that this quantity is very robust. In other words, the maximum of $I_{s[th]}(\omega=0.5J)$ in the window $h_{c_1} < h < h_{c_2}$ is stable against a variation in L.

The field-dependent enhancement of $I_{s[th]}(\omega=0.5J)$ in Figs. 4(a) and 4(b) ($T=0.25J$) is well described by $I_{s[th]} \sim h^2$ for $h \le h_{c_1}$. Furthermore, we present

$$\Delta I_{s[th]} = \frac{\max_h[I_{s[th]}(\omega=0.5J, h)] - I_{s[th]}(\omega=0.5J, \; h=0)}{I_{s[th]}(\omega=0.5J, \; h=0)}$$

in Fig. 5 as a function of temperature for $L=14$ spins. The

data are already converged with respect to the system size for the temperatures shown. While the field dependence of $I_{th}(\omega=0.5J)$ and $I_s(\omega=0.5J)$ is only qualitatively similar, ΔI_{th} (black solid line) and ΔI_s (red dashed line) almost coincide. The green dashed-dotted line is an exponential decay fitted to ΔI_{th} to illustrate that the decay is slightly slower than exponential for spin as well as for heat transport.

Regarding the temperature dependence of the thermal spectral weight at lower temperatures ($T < 0.25J$) we expect an exponential suppression at low temperatures in gapped phases[11,57,74] ($h < h_{c_1}$ or $h > h_{c_2}$). For the Luttinger-Liquid phase ($h_{c_1} < h < h_{c_2}$), we expect $I_{s[th]}=I_{s[th]}(T) \sim T$ based on previous work on the temperature dependence of the thermal drude weights of the *XXZ* spin-$\frac{1}{2}$ chain in a magnetic field.[54] At zero magnetic field we indeed find an exponentially suppressed weight converged with respect to the systems size for $T < 0.25J$ but in the gapless phase ($h=J$), the finite-size effects do not allow for a definite conclusion on the temperature dependence.

To clarify the role of the Drude weight on finite systems in this context, it is plotted in Fig. 6 as a fraction of the corresponding total spectral weight. In the case of spin transport [Fig. 6(a)], the Drude weight contributes very little to the total weight but its significance increases monotonously with the field. D_s/I_s^0 saturates at a finite value above the saturation field. These observations hold for all temperatures studied ($T/J=0.25, 0.5, 1$), only the value at saturation and the field necessary for reaching it depends on temperature. For instance, at $T=0.25J$ (solid black line) the Drude weight accounts for 60% of the total weight above $h=2J$. At $T=0.5J$ (dashed red line), D_s/I_s^0 saturates at $h=3.5J$ at a value of 48%. However, Fig. 6 should not be interpreted in terms of a large absolute value of the Drude weight above saturation in the thermodynamic limit, neither at zero or finite temperatures. At zero temperature, for $N \to \infty$ and in the two gapped phases $h < h_{c_1}$ and $h > h_{c_2}$, we expect the spin Drude weight to vanish, according to Kohn's reasoning.[71] As far as the gapless phase is concerned, the zero-temperature Drude weight should consequently be finite in the thermodynamic limit, yet the contribution of the Drude weight relative to the
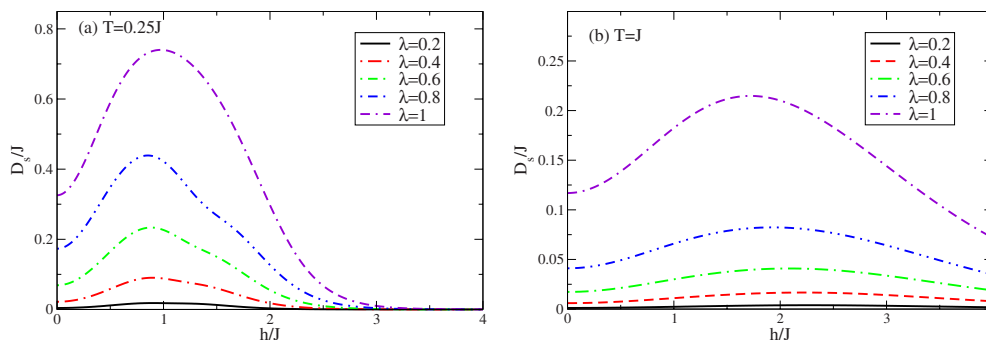

FIG. 6. (Color online) Drude weights normalized by the total spectral weight $I_{s[th]}^0$ as a function of magnetic field. (a) In the case of spin transport, the Drude weight is a small contribution at zero field but increases with the magnetic field up to a saturation value that strongly depends on temperature. (b) For heat transport, the Drude weight is the dominant contribution even at zero field and low temperatures. At low temperatures, the normalized Drude weight has a minimum as the field increases. At $h \approx 2J$, it reaches its final value. Such a minimum is not visible at $T=J$. The black dotted vertical lines are guides to the eyes which mark the critical fields $h_{c_1}=0.66J$ and $h_{c_2}=1.4J$.

FIG. 7. (Color online) Spin Drude weight as a function of magnetic field h for a system of length $L=16$ and different values of λ. (a) At low temperatures ($T=0.25J$), the spin Drude weights show a significant peak between the critical fields (compare Fig. 1 at $T=0$). (b) For larger temperatures ($T=J$) the peak is less pronounced and moves to larger fields. In both cases increasing λ gives rise to a strong increase in the numerical values but the position of the peak moves only slightly toward smaller fields. The qualitative field dependence is almost independent of λ. For all values of λ, the peak is located at marginally smaller fields than for the Heisenberg chain [long dashed lines in (a)].

regular conductivities remains an open issue for low temperatures.

In the case of heat transport [Fig. 6(b)], the picture has more facets. For low temperatures ($T=0.25J$, solid black line), D_{th}/I_{th}^0 decreases in the field-induced phase as there is a huge increase in the regular part of the conductivity [compare Fig. 3(c)]. This results in a minimum in D_{th}/I_{th}^0 at $h \approx J$, roughly where the field-dependent thermal Drude weight has its maximum. At $h \approx 2J$, the Drude weight is restored as the dominant contribution at $D_{th}/I_{th}^0 \approx 0.9$ at low T. This effect is weakened by temperature [compare Fig. 3(d)], eventually resulting in a monotonous increase in D_{th}/I_{th}^0 with h at $T=J$. Our results clearly suggest that the Drude weight is a significant contribution in the field-induced gapless phase on *finite* systems. Several comments are in order. First, a finite Drude weight at $T>0$ in a nonintegrable system would be surprising while on the other hand, this observation is consistent with the fact that thermodynamic properties in the phase are well described by an effective *XXZ* model,[48,75] which is believed to have ballistic transport properties in its gapless zero-field phase.[2,12] Moreover, in the ferromagnetic phase $h > h_{c_2}$, the physics is expected to be well approximated by a weakly interacting gas of magnons which in turn renders the Drude weight large in relation to the total weight. We stress that similar to D_s, this is a statement about finite systems and temperatures, and much larger system sizes (see the Appendix) would be required to extrapolate the ratio D_{th}/I_{th}^0 to the thermodynamic limit. We can therefore not pursue this question here. Note though, that in the high-temperature limit ($\beta=0$) the magnetic field dependence drops out. In this limit, exact diagonalization yields a systematic decrease in the Drude weight with the system size.[11]

To summarize the discussion of the behavior at $\lambda=0.5$, in the low-temperature regime, which is our main case of interest, the field-driven enhancement is visible in the conductivities as well as in the Drude weights and therefore also in the spectral weight but the Drude weights contribute the most. Further, we can distinguish a field- and a temperature-dominated regime: qualitatively, at $T < h_{c_1}$, a variation in the

magnetic field influences the conductivities whereas for $T > h_{c_1}$, the magnetic field has little effect on both the structure and the weight in the conductivities. Figure 4 contains the main result of our work: a field-induced increase in both transport coefficients at low frequencies $\omega < h_{c_1}$.

D. Dependence on λ

Next we turn to the discussion of the influence of the strength of dimerization λ. Since we have presented evidence that the Drude weights are the dominant contribution in the field-induced phase, we concentrate on these quantities, expecting them to reflect the main qualitative behavior. Figure 7 shows the spin Drude weight as a function of the external magnetic field at different temperatures and strengths of dimerization. In all cases, the Drude weight for spin transport exhibits a maximum at intermediate fields. We expect that in the thermodynamic limit and at sufficiently low temperatures, the transition into the field-induced Luttinger phase should lead to signatures in the Drude weights at h_{c_1} and h_{c_2}. Yet, for the system sizes we can study, and thus the accessible T, the location of the inflection points of D_s do not exhibit a clear correlation with critical fields h_{c_1} and h_{c_2} of Fig. 1. This remains to be analyzed in the future.

As temperature increases [compare Figs. 7(a) and 7(b)], the maximum in the Drude weights moves from between the critical fields to higher values of h while the absolute value of D_s decreases. Sending $\lambda \to 0$ decreases the values of D_s for all fields while the field-driven increase is not affected qualitatively. This is true for small as well as high temperatures. Note that increasing the temperature suppresses the spin Drude weight much more severely than altering λ. In the case of thermal transport [Fig. 8(a)] we find a stronger quantitative dependence on λ while the fact that altering λ does not change the field dependence remains qualitatively correct. The former is not surprising since uncoupled dimers cannot carry any heat current while the Heisenberg chain is known for its ballistic heat transport.[8–11]

E. Magnetothermal couplings

The last effect to investigate is the influence of the magnetothermal coupling Eq. (10). In the case of the *XXZ* chain,
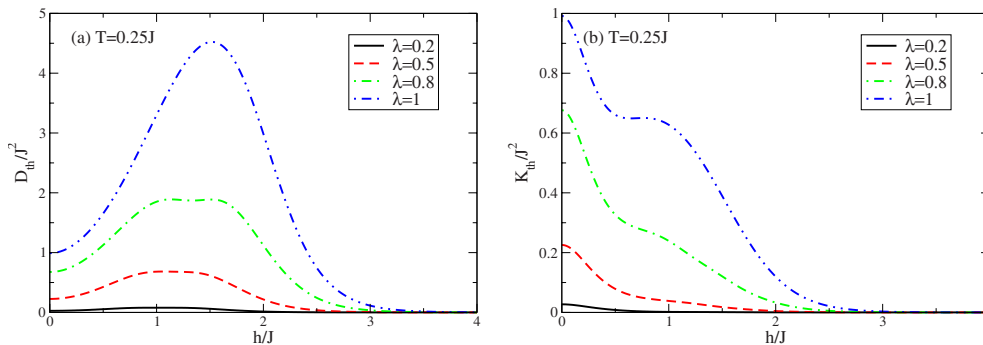
FIG. 8. (Color online) (a) Thermal Drude weight D_{th} as a function of magnetic field h for a system of length $L=16$ and different values of λ at low temperatures ($T=0.25J$). While the thermal Drude weight decreases fast as λ decreases, the field dependence is not affected. (b) Corrected thermal Drude weight K_{th}. We find that the magnetothermal coupling prohibits the strong increase in the thermal Drude weight in the field-induced phase.

it has been shown that this correction suppresses the thermal conductivity.[54] The results for the field dependence of the thermal Drude weight K_{th} at low temperatures ($T=0.25J$) are shown in Fig. 8(b). The corrected Drude weight K_{th} [Eq. (10)] decreases as the magnetic field increases, which is the systematic behavior in the whole field-induced phase. Shifting λ toward $\lambda=0$ lowers the overall values while only slightly affecting the field dependence. Figure 9 is a comparison of the three Drude weights associated with thermal transport, D_{th}, D_{22}, and K_{th}, where

$$D_{22} = D_{th} - 2\beta h D_{th,s} + \beta h^2 D_s. \qquad (14)$$

As expected from Eqs. (10) and (14), all three quantities coincide at zero magnetic field. While $D_{22} > D_{th}$ both quantities exhibit a similar field dependence, i.e., it features a maximum in the field-induced gapless phase and a smooth decay to zero as h increases beyond saturation. The magnetothermal correction changes this behavior completely, yielding a monotonous decrease as the field increases.

V. CONCLUSIONS AND SUMMARY

In this work, we studied spin and heat transport in dimerized spin-$\frac{1}{2}$ chains in a magnetic field, in dependence of temperature T, magnetic field h and the strength of dimerization λ. Focusing on the field dependence in the case of $\lambda=0.5$ we found that the transport coefficients at low frequencies for both, spin and heat transport, are strongly enhanced in the field-induced gapless phase. For spin transport at low but finite temperatures, the Drude weight becomes the dominant contribution as the field increases. We stress that this is an observation for finite systems. While one may expect that the Drude weight remains relevant in the field-induced phase in the zero temperature,[71] thermodynamic limit, the theoretically interesting question of a finite Drude weight at low but finite temperatures is beyond the scope of this work.

In the case of heat transport, the emerging picture is more involved. Increasing the magnetic field up to saturation, we find that the regular part of the conductivity is vastly enhanced at all frequencies. Although the thermal Drude

weight has a field dependence similar to its spin counterpart, this leads to a decrease in the relative contribution in the spectral weight at low temperatures. However, the thermal Drude weight remains the dominant contribution on the finite systems studied here. In both transport channels, a temperature larger than the spin gap severely weakens all features related to the magnetic field.

Our main finding is the field-induced increase in both transport coefficients in the low-frequency window, which is robust even on the finite chains accessible to exact diagonalization. While most of our work was concerned with parameters that mimic the energy scales typical for $(C_5H_{12}N)_2CuBr_4$ [Refs. 46–48], we further studied the dependence on the strength of dimerization. There we observe that altering λ changes the overall values while the field dependence remains qualitatively the same. Thus we conclude that our observation of field-enhanced spin and heat transport is valid in dimerized spin chains. We also expect it
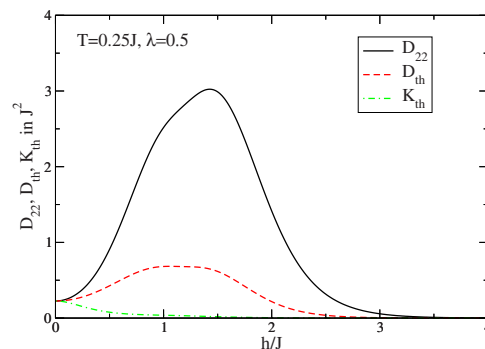

FIG. 9. (Color online) Comparison of the various thermal Drude weights D_{th}, D_{22} [Eq. (7) and [Eq. (14)], K_{th} [Eq. (10)] for thermal transport at $\lambda=0.5$ and $T=0.25J$ for a chain of length $L=16$. While the three curves coincide at $h=0$, the field dependence exhibits huge differences. On the one hand, D_{22} given by Eq. (14) (solid black line) shows a much stronger enhancement than D_{th} (dashed red line). On the other hand, including the magnetothermal correction (dotted-dashed green line) leads to a monotonous decrease in K_{th} as the magnetic field increases.
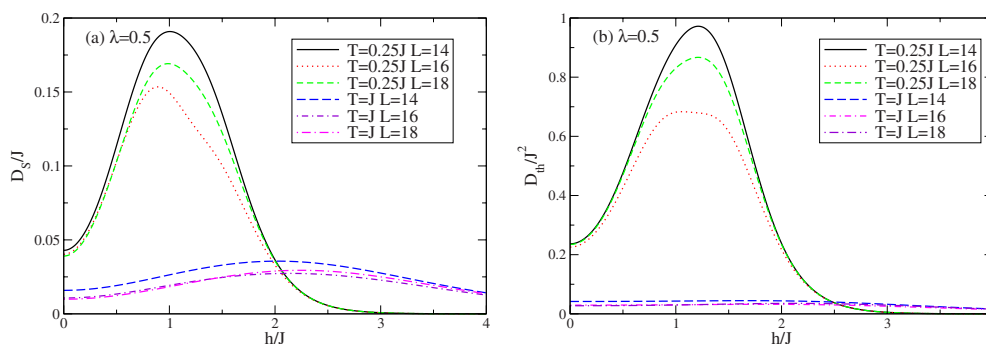
FIG. 10. (Color online) Finite-size effects in the field-dependent spin Drude weight (a) and thermal Drude weight (b) at two different temperatures ($T=0.25J, J$) for the system sizes $L=14, 16, 18$.

to be more generally valid in other dimerized quasi-one-dimensional spin systems, such as two-leg spin ladders.

Finally, the calculation of the magnetothermal coupling at low temperatures unveils a very interesting effect, similar to the *XXZ* chain.[54] The corrected thermal Drude weight shows no increase in the field induced phase, instead, it decreases.

In conclusion, we complemented several experimental and theoretical studies which characterized the field-induced gapless phase,[46–48] by emphasizing here that clear fingerprints of this transition are present in current-current correlation functions and should thus, in principle, manifest themselves in transport measurements. The spin conductivity is inaccessible at the moment but can be extracted from quantities measured in NMR experiments.[76,77]

APPENDIX: FINITE-SIZE SCALING OF THE DRUDE WEIGHTS

The finite-size scaling of the Drude weights in nonintegrable spin chains has been previously studied at zero field and in the limit of infinite temperature[11] without evidence of a finite Drude weight in the thermodynamic limit for nonintegrable systems. Note that the field dependence drops out at $\beta=0$. These studies include the dimerized chain. We present our data for finite magnetic fields in Fig. 10. Due to the interplay between the regular contribution and the Drude weight in the conductivities, the dependence on the system size is nonmonotonic at finite magnetic fields and for the system sizes accessible, especially at low temperatures ($T=0.25J$). Therefore, the accessible system sizes are too small to gain any qualitative insight into $D_{s[th]}$ beyond Ref. 11. The integrated spectral weight (Fig. 4) is a robust quantity in this context.

[1] X. Zotos and P. Prelovšek, *Transport in One Dimensional Quantum Systems* (Kluwer Academic, Doodrecht, 2004).

[2] F. Heidrich-Meisner, A. Honecker, and W. Brenig, Eur. Phys. J. Spec. Top. **151**, 135 (2007).

[3] C. Hess, Eur. Phys. J. Spec. Top. **151**, 73 (2007).

[4] A. V. Sologubenko, T. Lorenz, H. R. Ott, and A. Freimuth, J. Low Temp. Phys. **147**, 387 (2007).

[5] U. Schollwöck, J. Richter, D. Farnell, and R. Bishop, Lect. Notes Phys. **645**, 1 (2004).

[6] H. Evertz, Adv. Phys. **52**, 1 (2003).

[7] U. Schollwöck, Rev. Mod. Phys. **77**, 259 (2005).

[8] X. Zotos, F. Naef, and P. Prelovšek, Phys. Rev. B **55**, 11029 (1997).

[9] A. Klümper and K. Sakai, J. Phys. A **35**, 2173 (2002).

[10] K. Sakai and A. Klümper, J. Phys. A **36**, 11617 (2003).

[11] F. Heidrich-Meisner, A. Honecker, D. C. Cabra, and W. Brenig, Phys. Rev. B **68**, 134436 (2003).

[12] X. Zotos, Phys. Rev. Lett. **82**, 1764 (1999).

[13] J. Benz, T. Fukui, A. Klümper, and C. Scheeren, J. Phys. Soc. Jpn. Suppl. **74**, 181 (2005).

[14] J. Sirker, R. G. Pereira, and I. Affleck, Phys. Rev. Lett. **103**, 216602 (2009).

[15] S. Grossjohann and W. Brenig, Phys. Rev. B **81**, 012404 (2010).

[16] S. Fujimoto and N. Kawakami, Phys. Rev. Lett. **90**, 197202 (2003).

[17] B. N. Narozhny, A. J. Millis, and N. Andrei, Phys. Rev. B **58**, R2921 (1998).

[18] R. Steinigeweg, M. Ogiewa, and J. Gemmer, EPL **87**, 10002 (2009).

[19] M. Michel, O. Hess, H. Wichterich, and J. Gemmer, Phys. Rev. B **77**, 104303 (2008).

[20] G. Benenti, G. Casati, T. Prosen, D. Rossini, and M. Žnidarič, EPL **85**, 37001 (2009).

[21] T. Prosen and M. Znidaric, J. Stat. Mech.: Theory Exp. (2009), P02035.

[22] S. Langer, F. Heidrich-Meisner, J. Gemmer, I. P. McCulloch, and U. Schollwöck, Phys. Rev. B **79**, 214409 (2009).

[23] D. Gobert, C. Kollath, U. Schollwöck, and G. Schütz, Phys. Rev.

E **71**, 036102 (2005).

[24] H. Castella, X. Zotos, and P. Prelovšek, Phys. Rev. Lett. **74**, 972 (1995).

[25] A. Rosch and N. Andrei, Phys. Rev. Lett. **85**, 1092 (2000).

[26] F. Heidrich-Meisner, A. Honecker, D. C. Cabra, and W. Brenig, Phys. Rev. Lett. **92**, 069703 (2004).

[27] X. Zotos, Phys. Rev. Lett. **92**, 067202 (2004).

[28] D. A. Rabson, B. N. Narozhny, and A. J. Millis, Phys. Rev. B **69**, 054403 (2004).

[29] J. V. Alvarez and C. Gros, Phys. Rev. Lett. **88**, 077203 (2002).

[30] D. Heidarian and S. Sorella, Phys. Rev. B **75**, 241104(R) (2007).

[31] P. Jung, R. W. Helmes, and A. Rosch, Phys. Rev. Lett. **96**, 067202 (2006).

[32] P. Jung and A. Rosch, Phys. Rev. B **76**, 245108 (2007).

[33] Sufficiently far away from integrable points, though, exact diagonalization studies (Ref. 11) report a systematic decrease in ballistic contributions to transport.

[34] C. Hess, C. Baumann, U. Ammerahl, B. Büchner, F. Heidrich-Meisner, W. Brenig, and A. Revcolevschi, Phys. Rev. B **64**, 184305 (2001).

[35] C. Hess, H. ElHaes, B. Büchner, U. Ammerahl, M. Hücker, and A. Revcolevschi, Phys. Rev. Lett. **93**, 027005 (2004).

[36] C. Hess, P. Ribeiro, B. Büchner, H. ElHaes, G. Roth, U. Ammerahl, and A. Revcolevschi, Phys. Rev. B **73**, 104407 (2006).

[37] A. V. Sologubenko, K. Gianno, H. R. Ott, U. Ammerahl, and A. Revcolevschi, Phys. Rev. Lett. **84**, 2714 (2000).

[38] A. V. Sologubenko, E. Felder, K. Giannò, H. R. Ott, A. Vietkine, and A. Revcolevschi, Phys. Rev. B **62**, R6108 (2000).

[39] A. V. Sologubenko, K. Giannò, H. R. Ott, A. Vietkine, and A. Revcolevschi, Phys. Rev. B **64**, 054412 (2001).

[40] N. Hlubek, P. Ribeiro, R. Saint-Martin, A. Revcolevschi, G. Roth, G. Behr, B. Büchner, and C. Hess, Phys. Rev. B **81**, 020405 (2010).

[41] C. Hess, H. ElHaes, A. Waske, B. Büchner, C. Sekar, G. Krabbes, F. Heidrich-Meisner, and W. Brenig, Phys. Rev. Lett. **98**, 027201 (2007).

[42] A. V. Sologubenko, K. Berggold, T. Lorenz, A. Rosch, E. Shimshoni, M. D. Phillips, and M. M. Turnbull, Phys. Rev. Lett. **98**, 107201 (2007).

[43] A. V. Sologubenko, T. Lorenz, J. A. Mydosh, A. Rosch, K. C. Shortsleeves, and M. M. Turnbull, Phys. Rev. Lett. **100**, 137202 (2008).

[44] B. R. Patyal, B. L. Scott, and R. D. Willett, Phys. Rev. B **41**, 1657 (1990).

[45] B. C. Watson, V. N. Kotov, M. W. Meisel, D. W. Hall, G. E. Granroth, W. T. Montfrooij, S. E. Nagler, D. A. Jensen, R. Backov, M. A. Petruska, G. E. Fanucci, and D. R. Talham, Phys. Rev. Lett. **86**, 5168 (2001).

[46] B. Thielemann, C. Rüegg, K. Kiefer, H. M. Rønnow, B. Normand, P. Bouillot, C. Kollath, E. Orignac, R. Citro, T. Giamarchi, A. M. Läuchli, D. Biner, K. Krämer, F. Wolff-Fabris, V. Zapf, M. Jaime, J. Stahn, N. B. Christensen, B. Grenier, D. F. McMorrow, and J. Mesot, Phys. Rev. B **79**, 020408(R) (2009).

[47] C. Rüegg, K. Kiefer, B. Thielemann, D. F. McMorrow, V. Zapf,

B. Normand, M. B. Zvonarev, P. Bouillot, C. Kollath, T. Giamarchi, S. Capponi, D. Poilblanc, D. Biner, and K. W. Krämer, Phys. Rev. Lett. **101**, 247202 (2008).

[48] M. Klanjšek, H. Mayaffre, C. Berthier, M. Horvatić, B. Chiari, O. Piovesana, P. Bouillot, C. Kollath, E. Orignac, R. Citro, and T. Giamarchi, Phys. Rev. Lett. **101**, 137207 (2008).

[49] T. Lorenz, O. Heyer, M. Garst, F. Anfuso, A. Rosch, C. Rüegg, and K. Krämer, Phys. Rev. Lett. **100**, 067208 (2008).

[50] F. Anfuso, M. Garst, A. Rosch, O. Heyer, T. Lorenz, C. Rüegg, and K. Krämer, Phys. Rev. B **77**, 235113 (2008).

[51] A. V. Sologubenko, T. Lorenz, J. A. Mydosh, B. Thielemann, H. M. Rønnow, C. Rüegg, and K. W. Krämer, Phys. Rev. B **80**, 220411 (2009).

[52] K. Louis and C. Gros, Phys. Rev. B **67**, 224410 (2003).

[53] K. Sakai and A. Klümper, J. Phys. Soc. Jpn. Suppl. **74**, 196 (2005).

[54] F. Heidrich-Meisner, A. Honecker, and W. Brenig, Phys. Rev. B **71**, 184415 (2005).

[55] G. D. Mahan, *Many Particle Physics* (Plenum Press, New York, London, 1980).

[56] Y. Yan, C.-Q. Wu, and B. Li, Phys. Rev. B **79**, 014207 (2009).

[57] E. Orignac, R. Chitra, and R. Citro, Phys. Rev. B **67**, 134426 (2003).

[58] A. M. Luttinger, Phys. Rev. **135**, A1505 (1964).

[59] A. V. Rozhkov and A. L. Chernyshev, Phys. Rev. Lett. **94**, 087201 (2005).

[60] A. L. Chernyshev and A. V. Rozhkov, Phys. Rev. B **72**, 104423 (2005).

[61] E. Boulat, P. Mehta, N. Andrei, E. Shimshoni, and A. Rosch, Phys. Rev. B **76**, 214411 (2007).

[62] D. C. Cabra and M. D. Grynberg, Phys. Rev. B **59**, 119 (1999).

[63] A. Honecker, Phys. Rev. B **59**, 6790 (1999).

[64] M. C. Cross and D. S. Fisher, Phys. Rev. B **19**, 402 (1979).

[65] G. S. Uhrig, F. Schönfeld, M. Laukamp, and E. Dagotto, Eur. Phys. J. B **7**, 67 (1999).

[66] R. Chitra, S. Pati, H. R. Krishnamurthy, D. Sen, and S. Ramasesha, Phys. Rev. B **52**, 6581 (1995).

[67] W. Yu and S. Haas, Phys. Rev. B **62**, 344 (2000).

[68] R. Chitra and T. Giamarchi, Phys. Rev. B **55**, 5816 (1997).

[69] D. C. Cabra, A. Honecker, and P. Pujol, Phys. Rev. B **58**, 6241 (1998).

[70] A. Klümper, J. R. Martínez, C. Scheeren, and M. Shiroishi, J. Stat. Phys. **102**, 937 (2001).

[71] W. Kohn, Phys. Rev. **133**, A171 (1964).

[72] B. S. Shastry and B. Sutherland, Phys. Rev. Lett. **65**, 243 (1990).

[73] B. S. Shastry, Phys. Rev. B **73**, 085117 (2006).

[74] F. Heidrich-Meisner, A. Honecker, D. C. Cabra, and W. Brenig, Phys. Rev. B **66**, 140406(R) (2002).

[75] K. Totsuka, Phys. Rev. B **57**, 3454 (1998).

[76] M. Takigawa, N. Motoyama, H. Eisaki, and S. Uchida, Phys. Rev. Lett. **76**, 4612 (1996).

[77] K. R. Thurber, A. W. Hunt, T. Imai, and F. C. Chou, Phys. Rev. Lett. **87**, 247202 (2001).

3.5   Experimental observation of anisotropic heat transport in low-dimensional quantum magnets

The theoretical work on the energy dynamics of low-dimensional quantum magnets to be presented in Chap. 3.7 is strongly motivated by the experimental observation of anisotropic heat transport in materials that are known to show strong signatures of low-dimensional quantum magnets. Even though the focus of the theoretical analysis will be on chains, we first discuss the so-called telephone number compounds $(Sr,Ca,La)_{14}Cu_{24}O_{41}$, which are spin ladder materials. They played an important role in realizing that the magnon contribution to thermal transport in magnetic insulators can outweigh the phonon contribution at elevated temperatures (see Ref. [3] for a review). Furthermore, all-optical measurement techniques, that resemble a non-equilibrium setup, have been applied to $Sr_9La_5Cu_{24}O_{41}$ [54, 55]. Second, we discuss recent results for the spin chain material $SrCuO_2$ where an increase in sample purity has led to a drastic increase of the magnetic contribution to the thermal conductivity [154].

The anisotropic heat transport of $Sr_{14}Cu_{24}O_{42}$ has first been reported independently in Refs. [168] and [182], after a thorough investigation of these compounds as part of the search for high-T_C superconductors [183]. In copper based quantum magnets such as $(Sr,Ca,La)_{14}Cu_{24}O_{41}$ the electronic transport properties are dominated by the Cu^{2+} super exchange along the Cu-O-Cu bonds in the CuO layers. In this configuration the Heisenberg type $(\vec{S}\cdot\vec{S})$ superexchange interaction is mediated via hybridization with the intermediate oxygen atoms [18]. Specifically, in $(Sr,Ca,La)_{14}Cu_{24}O_{41}$, every second plane of the crystal lattice consists of Cu_2O_3 ladders. The inter-ladder-coupling is frustrated while the inter-plane coupling is small, effectively isolating the spin ladders [11, 12]. The chains, which constitute the intermediate planes of the crystal lattice, were found to be nearly dispersionless and as such do not contribute to thermal transport [184, 185, 186, 187, 188].

In the following we concentrate on one specific example of the spin ladder compounds, namely $Sr_9La_5Cu_{24}O_{41}$. Replacing Sr with La to a certain degree reduces the intrinsic hole doping of the ladder planes, leading to very clean spin ladders [168]. The left panel of Fig 9 shows the heat conductivity κ of $Sr_9La_5Cu_{24}O_{41}$ as a function of temperature measured along the three different axis of a three dimensional bulk crystal [168]. The two curves with overall smaller values, are obtained from measurements along the a and b axis of the crystal. They can be understood as the standard phonon contribution [168]. However, if the thermal conductivity is measured along the c-axis of
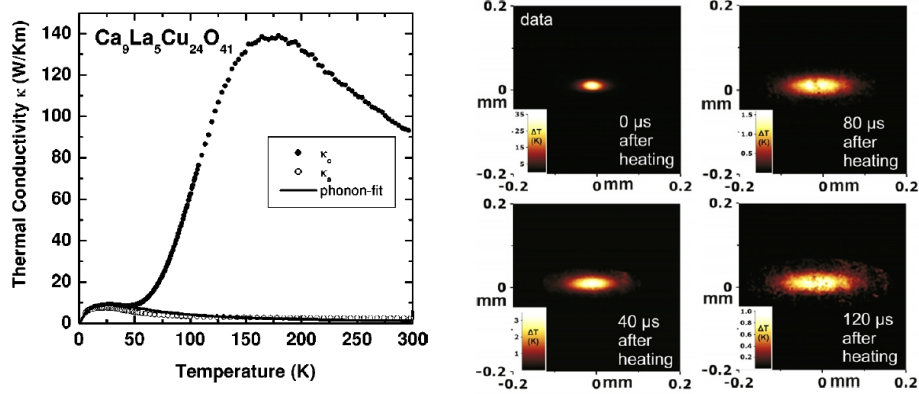
Figure 9: Anisotropic heat conductivity in $Sr_9La_5Cu_{24}O_{41}$. Left: Anisotropic thermal conductivity, taken from Ref. [168] with permission from the author. Right: Snapshots of the time resolved spreading of heat in $Sr_9La_5Cu_{24}O_{41}$ using the microthermal imaging technique [54], taken from [55] with permission from the author.

the crystal the thermal conductivity is broadly peaked around $175K$. The fit based on the phononic conductivity can only describe the behavior at very low temperatures in this case. However, it can be used to isolate the anisotropic contribution by substracting the phononic part and studying $\kappa_{\mathrm{mag}} = \kappa - \kappa_{\mathrm{phonon}}$. The high temperature peak is nowadays understood as the magnon contribution to heat transport [155, 168].

Exhibiting the largest magnetic contribution to the thermal conductivity for a long time, $Sr_9La_5Cu_{24}O_{41}$ was prone to be the best candidate for new experiments. Otter *et al.* used two techniques to measure the time-resolved heat propagation through a bulk sample [54], as opposed to the established steady-state techniques. The so called micro-thermal imaging is especially interesting as far as it motivates the approach to non-equilibrium transport presented in Chap. 3.6 and 3.7. The experimental protocol can be briefly summarized as follows: A bulk sample of $Sr_9La_5Cu_{24}O_{41}$ is coated with a fluorescent substance and subsequently a spot of $40 \mu m^2$ on the sample surface is heated up using an $488nm$ argon laser. While the heat spreads out in the sample, the photoluminescence is collected and imaged by a CCD camera with an integration time of $20 - 30 \mu s$. The right panel of Fig. 9 shows the latest result of this technique [55], the time resolved anisotropic spreading of heat. While these non-equilibrium type-of-experiments are conceptually interesting, it is currently under discussion how to interpret the results to re-
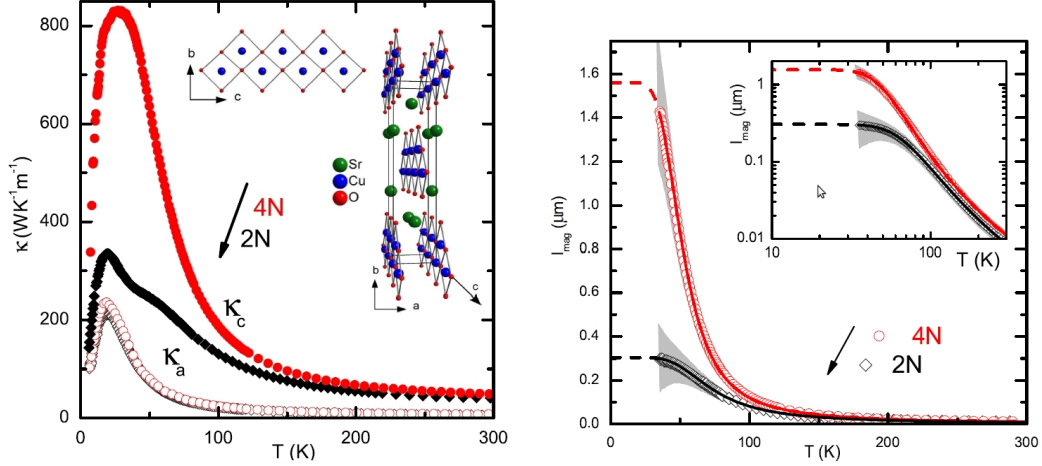
Figure 10: Ballistic heat transport in very pure samples of $SrCuO_2$. Left: Anisotropic heat conductivity along the three axis of the crystal as a function of temperature. Right: Average mean free path of the magnetic excitations as a function of temperature, calculated based on the data for κ using Eq (42). Taken from Ref. [154] with permission from the author

produce the thermal conductivity as known from steady state measurements [189].

Among the spin chain materials, significant progress in has been made for SrCuO$_2$. During the early stages of the field of heat transport in low-dimensional quantum magnets SrCuO$_2$ showed promisingly large magnon contributions to the thermal conductivity but the magnon and phonon contribution are hard to separate [3, 155]. Yet, by preparing samples of previously unachieved purity Hlubek *et al.* recently measured the highest κ_{mag} to that date and a macroscopic mean free path for the magnon $l_{\mathrm{mag}} \gtrsim 1\mu m$ [154]. The left panel of Fig. 10 shows their result for the thermal conductivity measured along the three axis of the crystal and a sketch of the relevant crystal structure. The black dots where reproduced from [155] and illustrate how close the phononic and magnonic contribution are in magnitude in this case, the high-temperature peak being only a shoulder on the low temperature phonon peak (open symbols for a and b axis). For the high purity sample (red dots) the maximal value of the thermal conductivity doubles, and now the phonon fit shows clear magnon contributions, exceeding even those of Sr$_9$La$_5$Cu$_{24}$O$_{41}$. The right panel of Fig. 10 shows the mean free path derived from κ_{mag} within a phenomenological model for the magnon heat

conductivity, introduced in Ref. [190]:

$$l_{\mathrm{mag}} = \frac{3}{\pi N_s k_b^2 T} \kappa_{\mathrm{mag}}, \qquad (42)$$

where N_s is the number of spin chains per unit area. As real bulk samples always have a finite defect density the authors interpret the macroscopical mean free path as an important phenomenological measure of ballistic transport. It is an open question whether or not the data relates to the ballistic heat transport in the Heisenberg chain.

3.6   Non-equilibrium transport and real-time evolution

Our analysis of the spin transport in the XXZ chain and the spin and heat transport in dimerized chains was mainly based on linear response theory. Yet there is a wealth of interesting physics to be found beyond the linear regime, see e.g., Refs. [47, 48, 49, 50, 51, 52]. This chapter presents an approach to study the transport properties of a system at zero temperature, solely based on the analysis of time-dependent density profiles [48]. The motivation to employ such an approach to analyze the spin and heat dynamics in low-dimensional quantum magnets is threefold: First, it is technically simple and provides easy access to initial states far from equilibrium. Hence it complements linear response theory at an important point by treating highly perturbed initial states. Second, in the time-resolved optical measurement of spreading heat in low-dimensional quantum magnets [54] the time dependent temperature distribution can be analyzed in the same fashion [55]. However, in such experiments on bulk materials finite temperature and phonons almost certainly play a role. Here we want to first analyze the fundamental models. A direct comparison with experiments on quantum magnets in bulk materials is thus beyond the scope of this work. The third point is that time-dependent particle density profiles can be experimentally accessed in expansion experiments using ultra-cold atomic gases in optical lattices (see Chap. 4.2). By trying to emulate the fundamental lattice model, those systems realize a setup very similar to the one discussed in the following. Parts of this section have been published in [48] and [191] (see Chap. 3.7).

The general idea is that given a time-dependent density $n(x, t)$ with a well defined second moment, its time dependence contains important information about the nature of the dynamics. As a first example, we consider a normal diffusion equation for a density $n(x, t)$ [48]:

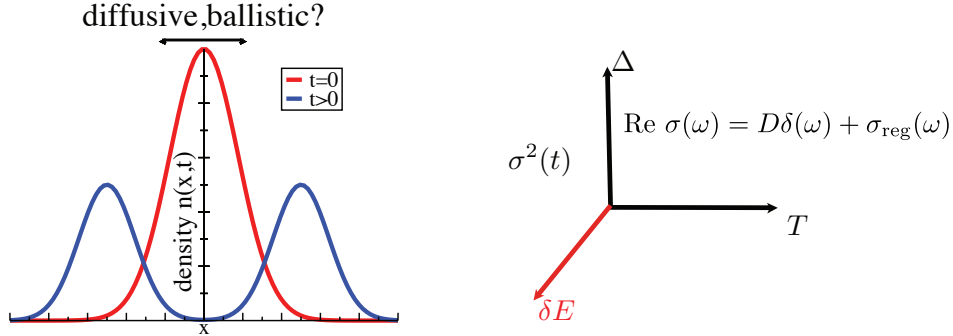$$\partial_t n(x, t) = \nabla \cdot (D \nabla n(x, t)), \qquad (43)$$

Figure 11: Sketch of the approach to non-equilibrium dynamics for spin dynamics pursued in Ref. [48] and applied to energy dynamics in Chap. 3.7.

where D is the diffusion constant. The Green's function for Eq. (43) in γ spatial dimensions is given by

$$G(x, \acute{x}, t) = \frac{1}{(4\pi Dt)^{\gamma/2}} \cdot e^{-\frac{(x-\acute{x})^2}{4Dt}}, \tag{44}$$

which we can use to calculate the expectation values

$$\langle x \rangle = \acute{x} \text{ and } \langle x^2 \rangle = |\acute{x}|^2 + 2\gamma Dt, \tag{45}$$

and obtain for the spatial variance

$$\sigma^2(t) = \langle x^2 \rangle - \langle x \rangle^2 = 2\gamma Dt + \sigma^2(t=0) \tag{46}$$

Therefore, $\sigma^2(t) - \sigma^2(0) \sim t$ is a necessary condition for normal diffusive dynamics. The same result can also be obtained from a classical random walk [192]. On the other hand ballistic dynamics is supposed to resemble the dynamics of free particles. One example would be a Gaussian wave-packet in single particle quantum mechanics[193]. In this case we find for the spatial variance

$$\sigma^2(t) = \sigma^2(0)(1 + \xi^2 t^2). \tag{47}$$

where $\xi^2\sigma^2(0) = 1/(4m^2)$ and m is the mass of the particle described by the wave-packet. We can thus define the average expansion velocity V describing the spreading of the wave-packet via $V^2 = \xi^2\sigma^2(0)$. Qualitatively
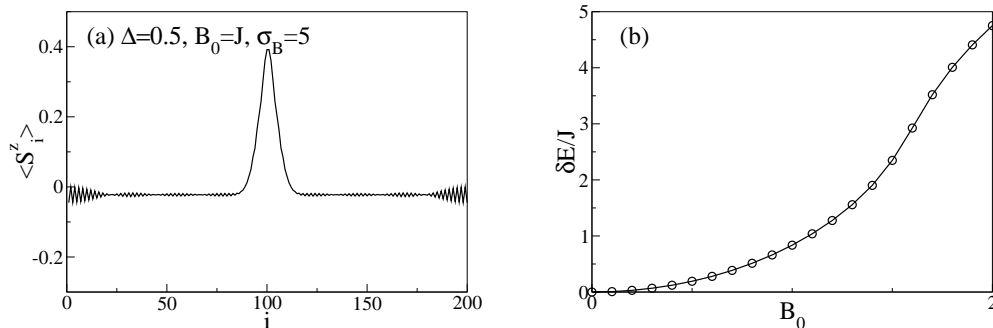
Figure 12: Preparation of initial states far from equilibrium using a gaussian magnetic field. (a) Initial magnetization profile for $\Delta = 0.5$, $B_0 = J$ and $\sigma_B = 5$. (b) Energy difference δE between the initial state and the ground state as a function of B_0 for $\sigma_B = 5$ and $\Delta = 0.5$.

similar behavior is obtained from Luttinger Liquids, free spinless fermions (see Chap. 3.7 for both), so-called quantum random walks [194] or a quantum boltzmann equation in the absence of scattering [195], to name only a few examples. In each case the prefactor V in $\sigma^2(t) - \sigma^2(0) = V^2 t^2$ has dimensions of a velocity. We can therefore use the spatial variance not only as a necessary condition to identify parameter regimes which are candidates for diffusive or ballistic dynamics respectively, but also to define an average expansion velocity in the ballistic regimes.

The paradigm pursued in the following (see Fig. 11 for a sketch) is now to prepare an initial state far from equilibrium, where linear response theory does not apply, calculate the time-dependent spatial variance using adaptive time-dependent DMRG, and determine whether $\sigma^2(t)$ grows linear or quadratic in time. As DMRG is used in the most common formulation for pure states at zero temperature we employ the energy difference δE between the groundstate and the initial state as a tuning parameter. The great advantage is that local densities can be accessed much more efficiently than current-current correlation functions. Yet, as in studies of $C(\beta, t)$ [Eq. (37)], for instance Ref. [58], the time scales have to be sufficiently large to allow for a conclusion [48]. For the open boundary conditions we apply as usual in DMRG, the simulation times are inherently limited by the system size as reflection of the wavepacket at the boundary has drastic influences on the variance. The downside of studying the variance is that we have only a

necessary condition for both respective classes of dynamics.

As an example of state preparation we revisit Ref. [48], where we studied the spin dynamics of the anisotropic Heisenberg chain. The panel (a) of Fig. 12 shows the magnetization profile of the initial state at $\Delta = 0.5$ that is obtained as the groundstate of:

$$H = H_{XXZ} + B_0 e^{\frac{(i-i_0)^2}{2\sigma_B^2}} \, , \tag{48}$$

that is, we have a gaussian magnetic field centered around site $i_0 = 100.5$ with width $\sigma_B = 5$ and amplitude B_0. Panel (b) illustrates how the gaussian magnetization wave-packets generated by this approach explore the regime of non-linear transport. We plot the energy difference δE between the initial state and the true groundstate at $B_0 = 0$.

Our main results for the spin dynamics are that for a single Heisenberg chain we have ballistic transport for $\Delta \leq 1$ as suggested by Eq. (39) while our results for $\Delta > 1$ were consistent with diffusive dynamics, namely $\sigma_S^2(t) \sim t$ for large times. As examples for non-integrable systems we studied the isotropic two-leg spin ladder and a frustrated chain model. For the frustrated chain we found ballistic dynamics in the gapless phase and $\sigma_S^2(t) \sim t$ for large times in the gapped phase. For the isotropic ladder, which also has a gap, we found the clearest notion of diffusive spin dynamics obtained from the spatial variance so far. The real-time dynamics of XXZ spin chains induced by a gaussian magnetic field was also studied in Ref. [49] where they argue that even though $\sigma^2(t) - \sigma^2(0) \propto t^2$, there are still features of ballistic dynamics, namely fast wave fronts. Even though, those do decay on accessible time scales, it cannot be excluded that finite-size effects in the background density play a role in that context. Yet, the advantage of an analysis of the spatial variance is that all excitations are treated on equal footing which makes it a useful approach to identify candidates for systems that can exhibit diffusion.

3.7 Real-time energy dynamics in spin-$1/2$ Heisenberg chains

Here the approach introduced in Chap. 3.6 will be extended to the energy dynamics in the XXZ-chain. To this end we analyze initial states where the dynamics only gives rise to a finite energy current but no spin current and states where the dynamics is driven by a magnetic field. For both scenarios the expansion of a density wave-packet is analyzed in the exactly solvable limit $\Delta = 0$ and using Luttinger liquid theory for $0 \leq \Delta < 1$. We then treat the fully interacting system driven far from equilibrium using adaptive time-dependent DMRG. The main result is that the energy dynamics is ballistic independently of the anisotropy and the distance from equilibrium. Hence, our data suggests the validity of the linear response results for non-equilibrium. We furthermore show that the average expansion velocity, which we defined based on the spatial variance as outlined in Chap. 3.6, can be understood in terms of the momentum distribution of the perturbed initial state. We also study the time-dependent energy current during the expansion and establish a connection between the spatial variance and the time-dependent current. Revisiting the dynamics driven by a gaussian magnetic field we recover the Luttinger liquid result, which is propagation with the sound velocity u in the limit of small perturbations. While, for the field-induced dynamics in the gapless phase, spin and energy density are qualitatively the same, we find a huge qualitative difference in the gapped phase. Namely the energy dynamics stays ballistic while the spin dynamics is consistent with diffusive behavior for large times.

Real-time energy dynamics in spin-$\frac{1}{2}$ Heisenberg chains

Stephan Langer,[1,*] Markus Heyl,[1] Ian P. McCulloch,[2] and Fabian Heidrich-Meisner[1]

[1]*Department of Physics and Arnold Sommerfeld Center for Theoretical Physics, Ludwig-Maximilians-Universität München, DE-80333 München, Germany*

[2]*School of Physical Sciences, The University of Queensland, Brisbane, QLD 4072, Australia*

We study the real-time dynamics of the local energy density in the spin-1/2 XXZ chain starting from initial states with an inhomogeneous profile of bond energies. Numerical simulations of the dynamics of the initial states are carried out using the adaptive time-dependent density matrix renormalization group method. We analyze the time dependence of the spatial variance associated with the local energy density to classify the dynamics as either ballistic or diffusive. Our results are consistent with ballistic behavior both in the massless and the massive phase. We also study the same problem within Luttinger liquid theory and obtain that energy wave packets propagate with the sound velocity. We recover this behavior in our numerical simulations in the limit of very weakly perturbed initial states.

I. INTRODUCTION

The understanding of transport properties of low-dimensional systems with strong correlations still poses viable challenges to theorists. These include, on the one hand, the fundamental problem of calculating transport coefficients for generic models such as the Heisenberg chain,[1,2] and on the other hand, the theoretical modeling of experiments that typically require the treatment of spin or electronic degrees of freedom coupled to phonons, in particular, in the case of the thermal conductivity.[3,4] Most theoretical work is focused on the linear-response regime, in which the properties of current-current autocorrelation functions determine transport properties (see Refs. 1 and 2 for a review).

More recently, the out-of-equilibrium properties of one-dimensional systems have evolved into an active field of research, one reason being recent advances in experiments with ultracold atoms.[5] These have paved the way for studying the dynamics of quantum many-body systems that are driven far away from equilibrium in a controlled manner, with little or no coupling to external degrees of freedom. Much attention has been paid to the question of thermalization, typically studied in so-called quantum quenches (see Ref. 6 and references therein). While global quantum quenches in homogeneous systems usually do not induce any finite net currents (of either spin, energy, or particles), we will be particularly interested in setups that feature finite net currents. Such situations are realized in, for instance, the sudden expansion of particles in optical lattices after the removal of trapping potentials.[7] Further examples are spin and/or particle currents induced by connecting two regions with opposite magnetizations or by letting two particle clouds collide (see, for instance, Refs. 8–11).

Theoretical work in this context ranges from the expansion dynamics of bosons and fermions in optical lattices[12–18] over the dynamics of wave packets in spin chains,[19–28] to the demonstration of signatures of spin-charge separation in such setups.[29,30] In the aforementioned examples, nonequilibrium situations were studied with either finite spin or particle currents. In our work, we address the energy dynamics for a model that is prototypical for systems with strong correlations, namely, the spin-1/2 XXZ chain:

$$
\begin{aligned}
H_{XXZ} &= \sum_{i=1}^{L-1} h_i \\
&:= J \sum_{i=1}^{L-1} \left[\frac{1}{2}(S_i^+ S_{i+1}^- + \text{H.c.}) + \Delta S_i^z S_{i+1}^z \right],
\end{aligned} \quad (1)
$$

where S_i^μ and $\mu = x, y, z$ are the components of a spin-1/2 operator acting on site i and $S_i^\pm$ are the corresponding lowering/raising operators. The global energy scale is set by the exchange coupling J, Δ is the exchange anisotropy in the z direction, and L denotes the number of sites. Equation (1) describes either interacting quantum spins or, via the Jordan-Wigner transformation,[31] spinless fermions.

Specifically, we follow the time evolution of the local energy density $\langle h_i \rangle$ starting from initial states that are far away from the ground state of Eq. (1) and that feature an inhomogeneous profile in the local energy density (see Fig. 1 for a sketch). We emphasize that, in the main part of our work, we choose the initial conditions such that only finite energy currents exist, whereas the spin (particle) density is constant during the time evolution, hence all spin (particle) currents vanish. Obviously, an initial state with an inhomogeneous spin density profile leads to both finite spin and energy currents, and we revisit this case, previously studied in Refs. 20 and 28.

Our work is motivated by and closely related to a specific experiment on a spin-ladder material. Many low-dimensional quantum magnets are known to be very good thermal conductors with heat predominantly carried by magnetic excitations at elevated temperatures.[32,33] Examples for materials that exhibit particularly large thermal conductivities are $(Sr,La,Ca)_{14}Cu_{24}O_{41}$ (Refs. 34 and 35) and $SrCuO_2$ (Ref. 36). While these experiments are carried out under steady-state conditions and in the regime of small external perturbations, more recently, time-resolved measurements have been performed on $La_5Ca_9Cu_{24}O_{41}$ (Ref. 37). For this spin ladder material, two approaches have been implemented:
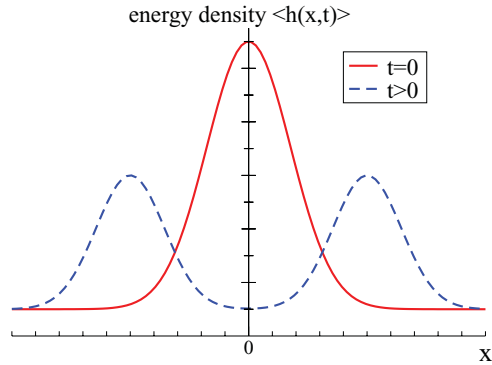
energy density <h(x,t)>

FIG. 1. (Color online) Sketch of our setup: we prepare initial states with an inhomogeneous distribution of local energies and then study the time evolution of the local energy density.

a time-of-flight measurement in which one side of the sample is heated up with a laser pulse and the time-dependent response is recorded on the other side. Second, a nonequilibrium local heat distribution was generated in the surface of the material by shining laser light on it. It is possible to record the heat dynamics via thermal imaging that uses the response of an excited thin fluorescent layer placed on top of the spin ladder material.

It is the latter case that we mimic in our work: the time evolution of local energy densities induced by inhomogeneous initial distributions. We utilize the time-dependent density matrix renormalization group (tDMRG)[38–42] technique. It allows us to simulate the dynamics of pure states whereas in the experiment, temperature likely plays a role. Our work thus addresses qualitative aspects in the first place, while a direct comparison with experimental results is beyond the scope of this study. The goal is to demonstrate that in a spin-1/2 chain described by Eq. (1), the energy dynamics is ballistic, irrespective of how far from equilibrium the system is and also irrespective of the presence or absence of excitation gaps. To this end, we use the same approach as in Ref. 20. We classify the dynamics based on the behavior of the spatial variance $\sigma_E^2(t)$ of the local energy density. The ballistic case is $\sigma_E^2(t) \sim t^2$, whereas diffusion implies $\sigma_E^2 \sim t$. Our main result for the XXZ chain, based on numerical tDMRG simulations, is that energy propagates ballistically at sufficiently long times, independently of model parameters (such as Δ). One can then interpret the prefactor V_E in $\sigma_E^2(t) = V_E^2 t^2$ as a measure of the average velocity of excitations contributing to the expansion. The velocity V_E can be calculated analytically and exactly in noninteracting models, which (in the absence of impurities or disorder) typically have ballistic dynamics, and we consider two examples: (i) the noninteracting limit of the XXZ Hamiltonian ($\Delta = 0$), i.e., spinless fermions and (ii) the Luttinger liquid, which is the universal low-energy theory in the continuum limit of Eq. (1) for $|\Delta| < 1$. We show that our tDMRG results agree with the exactly known expansion velocity V_E in these two examples.

Our main result, namely, the numerical observation of $\sigma_E^2(t) \sim t^2$ independently of initial conditions or model parameters such as the exchange anisotropy Δ, is consistent with

the qualitative picture derived from linear-response theory. Within that theory, transport properties of the XXZ chain have intensely been studied in recent years, both the energy[43–47] and the spin transport.[1,2,47–62] Ballistic dynamics is associated with the existence of nonzero Drude weights. Since the total energy current of the anisotropic spin-1/2 chain is a conserved quantity for all Δ, the thermal conductivity $\kappa(\omega)$ diverges in the zero-frequency limit and is given by $\mathrm{Re}\,\kappa(\omega) = D_E \delta(\omega)$, where D_E is the thermal Drude weight.[43–46] This behavior is different from the spin conductivity $\sigma(\omega)$. This quantity takes the form $\mathrm{Re}\,\sigma(\omega) = D_s \delta(\omega)$ only at the noninteracting point $\Delta = 0$, whereas for $0 < \Delta \leqslant 1$, many numerical studies[1,2,60,61] indicate $D_s(T > 0) > 0$, with a finite weight at finite frequencies, though. Therefore, for $0 < \Delta \leqslant 1$, $\mathrm{Re}\,\sigma(\omega) = D_s \delta(\omega) + \sigma_{\mathrm{reg}}(\omega)$. Recent field-theoretical and numerical work suggests that the regular part $\sigma_{\mathrm{reg}}(\omega)$ of $\sigma(\omega)$ in massless phases is consistent with diffusive behavior.[54,56,62] A finite value of the current-current correlation function in the long time limit is associated with a finite Drude weight. Finite Drude weights can be traced back to the existence of conservation laws,[43,60] and, in consequence, a potential relation between integrability[63] and ballistic behavior—in the sense of nonzero Drude weights—has been intensely discussed (see, e.g., Refs. 1, 2, 47, 60–62 and further references cited therein). Very recently, Prosen has presented results that provide a lower bound to the spin Drude weight that is non zero for $\Delta < 1$.[60] This is in qualitative agreement with earlier exact diagonalization studies.[2,47,48] The particular point $\Delta = 1$ is still discussed controversially;[47,49,52,54,59–61] first, no finite lower bound to the Drude weight is known,[60] and second, the qualitative results of exact diagonalization studies seem to depend on details of the extrapolation of finite-size data to the thermodynamic limit and the statistical ensemble that is considered.[47,48,59]

Our approach that analyzes the time dependence of spatial variances, albeit restricted to the analysis of densities, is numerically easily tractable and is an alternative to the numerically cumbersome evaluation of current correlation functions. tDMRG has, for instance, been applied to evaluate current-current autocorrelation functions in the thermodynamic limit.[54] However, the accessible time scales are quite limited ($t \sim 10/J$), making an unambiguous interpretation of the results difficult and the approach is not applicable to nonequilibrium. Our approach allows us, at least in principle, to study the entire regime of weakly perturbed states to maximally excited ones. An earlier analysis of spin-density wave packets in various spin models has yielded the following picture (all based on the time-dependence of the spatial variance);[20] in massless phases, ballistic dynamics is seen, whereas in massive ones, examples of diffusive dynamics have been identified. It is important to stress that the observation of a variance that increases linear in time is a necessary condition for the validity of the diffusion equation.

Finally, to complete the survey of related literature, recent studies have addressed steady-state spin and energy transport in open systems coupled to baths with no restriction to the linear-response regime.[28,61,64–66] These studies suggest spin transport to be ballistic in the gapless phase of the XXZ spin chain and to be diffusive in the gapped phase with a negative differential conductance at large driving strengths. The heat

current has been addressed in Ref. 64 where Fourier's law has been validated for the Ising model in a tilted field.

A byproduct of any tDMRG simulation is information on the time-evolution of the entanglement entropy. While this is not directly related to this article's chief case, it nevertheless provides valuable information on the numerical costs of tDMRG simulations. Qualitatively, speaking (see the discussion in Ref. 42 and references therein), the faster the entanglement growth is the shorter are the time scales that can be reached with tDMRG. We here show that the quenches studied in this work generate a mild logarithmic increase of entanglement, which is why this problem is very well suited for tDMRG. Such a behavior is typical for so-called local quenches.[67] This result might be useful for tDMRG practitioners.

This paper is organized as follows. First, we introduce the model and the quantities used in our analysis in Sec. II. Section III A reviews the framework of bosonization, which is applied in Sec. III B to give an analytical derivation of ballistic spin and energy dynamics in the low-energy case, valid in the massless phase of Eq. (1). Sections IV and V contain our numerical results. First, we study the energy dynamics in the absence of spin currents in Sec. IV. To this end, we generate an initial state consisting of a variable number of ferromagnetic bonds in the center of an antiferromagnetic chain. We calculate the time evolution of these states under Eq. (1) finding ballistic energy dynamics independent of the phase and the strength of the perturbation. To supplement these findings we derive an observable, which depends on the local currents, and whose expectation value is time-independent whenever $\sigma_E^2(t) \sim t^2$. The numerical calculation of this quantity indicates ballistic dynamics as well. Section V revisits the scenario of Ref. 20 where local spin and energy currents are present during the dynamics as we start from states with an inhomogeneous spin density. In that case, the energy density shows ballistic dynamics in the massless phase with a velocity matching the bosonization result in the limit of small perturbations. In the massive phase, we observe a different behavior of the two transport channels, i.e., ballistic energy dynamics while the spin dynamics looks diffusive.[20] Finally, we summarize our findings in Sec. VI. Additionally, we discuss the entanglement growth induced by coupling two regions with an opposite sign of the exchange coupling in the Appendix.

II. SETUP AND DEFINITIONS

A. Preparation of initial states and definition of spatial variance

In this work, we focus on spin-1/2 XXZ chains of a finite length L given by Eq. (1) where our goal is to study the dynamics of an inhomogeneous distribution of the local energy density originating from a local quench of system parameters. The inhomogeneous distributions are generated by preparing the system in the respective ground states of the following Hamiltonians that are perturbations of H_{XXZ} from Eq. (1). First,

$$H_{\text{init}}^J = \sum_{i=1}^{L-1} \frac{J_i}{J} h_i \,, \tag{2}$$

where h_i is defined in Eq. (1), and second,

$$H_{\text{init}}^B = H_{XXZ} - \sum_i B_i S_i^z \,, \tag{3}$$

where

$$B_i = B_0 \, e^{\frac{-(i-L/2)^2}{2\sigma_0^2}} \,. \tag{4}$$

In the first case, we quench site-dependent exchange couplings. In this scenario, we obtain initial states with large local energy densities. Typical initial states that are ground states of Eq. (2) are shown in Fig. 2. These states have b bonds with ferromagnetic $J_i < 0$ in the center while the rest has antiferromagnetic $J_i > 0$. We refer to this setup as the J_i quench.

In the second case, the dynamics is driven by an inhomogeneous spin density, enforced by an external magnetic field applied in the initial state. This allows us to generate smooth spatial perturbations of $\langle h_i \rangle$ with small differences in energy compared to the ground state of Eq. (1). We refer to this setup as the B_0 quench. A more detailed discussion of the initial states generated by a J_i quench will be given in Sec. IV A. The B_0 quench was introduced in detail in Ref. 20.

The definition of the local energy density from the Hamiltonian Eq. (1) is not unambiguous. For instance, it is always possible to add local terms to the Hamiltonian whose total contribution by summation over all lattice sites vanishes. However, this seeming ambiguity can be resolved up to constants by requiring that any block of adjacent lattice sites $\sum_{i=l}^m h_i$ is Hermitian and yet to have the same structure as the
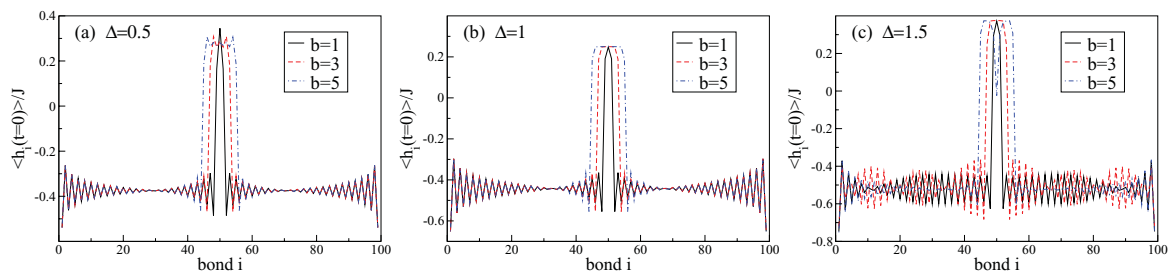

FIG. 2. (Color online) Profile of the local energy density $\langle h_i \rangle$ in the initial states induced by a J_i quench for $b = 1,3,5$ [compare Eq. (30)] for (a) $\Delta = 0.5$, (b) $\Delta = 1$, and (c) $\Delta = 1.5$. In all cases, the system forms a region with ferromagnetic nearest-neighbor spin correlations in the middle of the chain. In the regions with antiferromagnetic $J_i > 0$, the local energy density oscillates, reflecting the antiferromagnetic nearest-neighbor correlations.

total Hamiltonian H. These details seem to be rather specific, yet for the definition of the appropriate local energy density within the Luttinger liquid description, see below, these formal considerations are important. For the XXZ chain the local energy density is therefore determined by the bond energies $\langle h_i \rangle$.

To classify the dynamics of a density e_i we study its spatial variance

$$\sigma_E^2(t) = \sum_{i=1}^{L-1} (i - \mu)^2 e_i(t), \qquad (5)$$

where μ is the first moment of e_i. The e_i are the normalized distribution linked to the energy density via

$$e_i = \delta E^{-1} \langle \tilde{h}_i \rangle \qquad (6)$$

where $\langle \tilde{h}_i \rangle = \langle h_i \rangle - \langle h_i \rangle_0$ denotes the expectation value of h_i in the initial state shifted by the ground state expectation value $\langle h_i \rangle_0 = \langle \psi_0 | h_i | \psi_0 \rangle$.

$$\delta E := E_{\text{init}} - E_0 = \sum_i \langle \tilde{h}_i \rangle \qquad (7)$$

is the energy difference between the initial state $|\psi_{\text{init}}\rangle$ [i.e., the ground state of either H_{init}^J or H_{init}^B] and the ground state $|\psi_0\rangle$ of Eq. (1), both energies measured with respect to the unperturbed Hamiltonian from Eq. (1):

$$E_0 = \langle \psi_0 | H_{XXZ} | \psi_0 \rangle, \quad E_{\text{init}} = \langle \psi_{\text{init}} | H_{XXZ} | \psi_{\text{init}} \rangle. \qquad (8)$$

On physical grounds, the energy density should be normalized by the amount of energy transported by the propagating perturbation. This is well approximated by the energy difference δE between the initial state and the ground state of Eq. (1), as we have verified in many examples. In some cases, though, the propagating energy is, on a quantitative level, better described by estimating the area under the perturbations, as δE may also contain contributions from static deviations from the ground state bond energies in the background. Nevertheless, δE does not depend on the overall zero of energy and is an obvious measure of how far the system is driven away from the ground state. This, all together, justifies our definition of the e_i.

To remove static contributions depending only on the initial distribution $e_i(t=0)$, we subtract $\sigma_E^2(t=0)$ and study $\delta \sigma_E^2(t) := \sigma_E^2(t) - \sigma_E^2(0)$. $\delta \sigma_E^2(t) \sim (V_E t)^2$ is expected to grow quadratically in time in the case of ballistic behavior, where V_E has the dimensions of a velocity. For diffusive behavior, we expect, from the fundamental solution of the diffusion equation,[69] that $\delta \sigma_E^2(t) \sim Dt$ grows linearly in time, where D is the diffusion constant (see, e.g, the discussion in Ref. 20). Within linear response theory the diffusion constant can be related to transport coefficients via Einstein relations, see, e.g., Ref. 70. To be clear, the observation of $\delta \sigma_E^2 \sim t^2$ or $\delta \sigma_E^2 \sim t$ is a necessary condition for the respective type of dynamics and time-dependent crossovers are possible.

B. Spatial variance in the noninteracting case

For pedagogical reasons and to guide the ensuing discussion, we next calculate the spatial variance in the noninteracting limit of Eq. (1), i.e., at $\Delta = 0$. Using the

Jordan-Wigner transformation, we can write the Hamiltonian as

$$H = \frac{J}{2} \sum_i (S_i^+ S_{i+1}^- + \text{H.c.}) = -\frac{J}{2} \sum_i (c_i^\dagger c_{i+1} + \text{H.c.}), \qquad (9)$$

where $c_i^\dagger$ creates a spinless fermion on site i. A subsequent Fourier transformation diagonalizes the Hamiltonian:

$$H = \sum_k \epsilon_k c_k^\dagger c_k. \qquad (10)$$

Since we will compare with numerical results on systems with open boundary conditions, we obtain

$$\epsilon_k = -J \cos(k), \quad k = \frac{\pi n}{L+1}, \quad n = 1, \dots, L. \qquad (11)$$

Next, we compute

$$\delta \sigma_E^2(t) = \sum_i e_i(t)(i - i_0)^2 - \sum_i e_i(t=0)(i - i_0)^2$$

with e_i from Eq. (6) and $h_i = -J(c_i^\dagger c_{i+1} + \text{H.c.})/2$. By expressing $c_i^{(\dagger)}$ through their Fourier transform and by plugging in the time evolution of $c_k^{(\dagger)}$, we finally obtain, after straightforward calculations:

$$\delta \sigma_E^2(t) = V_E^2 t^2, \qquad (12)$$

i.e., ballistic dynamics independently of the initial state. Terms linear in t will be absent if in the initial state, the density is symmetric with respect to its first moment, i.e., $e_{\mu+\delta} = e_{\mu-\delta}$ and if the wave packet has no finite center-of-mass momentum at $t = 0$ already. In the remainder of the paper, we will work under these two additional assumptions that are valid for all initial states considered in our work. The prefactor V_E^2 is given by

$$V_E^2 = \frac{1}{\delta E} \sum_k \epsilon_k v_k^2 \delta n_k, \qquad (13)$$

where $v_k = \partial \epsilon_k / \partial k$ and

$$\delta n_k = n_k^{\text{init}} - n_k$$

is the difference between the momentum distribution function (MDF) in the initial state and the one in the ground state of Eq. (1). Since we use open boundary conditions, we compute n_k from

$$n_k = \langle c_k^\dagger c_k \rangle := \frac{2}{L+1} \sum_{r,r'} \sin(kr) \sin(kr') \langle c_r^\dagger c_{r'} \rangle. \qquad (14)$$

We can also express δE via δn_k:

$$\delta E = \sum_k \epsilon_k \delta n_k.$$

The expression (13) suggests that V_E is the average velocity of excitations contributing to the propagation of the wave packet. Characteristic for ballistic dynamics, V_E^2 is fully determined by the initial conditions through δn_k.

For completeness, we mention that an analogous calculation can be done for the spatial variance σ_S of the spin density. This quantity is defined as

$$\sigma_S^2(t) := \frac{1}{\mathcal{N}} \sum_{i=1}^{L} (i - \mu)^2 \langle S_i^z(t) + 1/2 \rangle. \qquad (15)$$

The normalization constant $\mathcal{N}$ measures the number of propagating particles. The spin density is, in terms of spinless fermions,

$$S_i^z = c_i^\dagger c_i - 1/2 = n_i - 1/2 \,.$$

The result for the spatial variance of the spin density is

$$\delta\sigma_S^2(t) = \sigma_S^2(t) - \sigma_S^2(0) = V_S^2 t^2 \qquad (16)$$

with

$$V_S^2 = \frac{1}{\mathcal{N}} \sum_k v_k^2 \delta n_k \,. \qquad (17)$$

Although we started from the Hamiltonian for $\Delta = 0$, we stress that Eqs. (12), (16), (13), and (17) are valid for any dispersion relation ϵ_k, irrespective of the presence of a gap, provided that k has the meaning of a momentum.

C. Energy current

Another aspect worth noting is that the time-evolving state carries a nonzero energy current, a situation that usually does not appear in the case of a global quench. From the equation of continuity for the energy density, one can derive the well-known expression for the local energy current operator,[43]

$$j_i^E = J^2 \tilde{\vec{S}}_{i-1} \cdot (\vec{S}_i \times \tilde{\vec{S}}_{i+1}), \qquad (18)$$

where $\tilde{\vec{S}} = (S^x, S^y, \Delta S^z)$. With periodic boundary conditions, the total current $J_E = \sum_i j_i^E$ is a conserved quantity, i.e., $[H, J_E] = 0$ (see Ref. 43). On a system with open boundary conditions such as the ones that are well suited for DMRG, this property is lost, yet the dynamical conductivity still has a quasi-Drude peak at very low frequencies, reminiscent of the true Drude peak $\mathrm{Re}\kappa(\omega) = D_E \delta(\omega)$ of a system with periodic boundary conditions.[68] The latter form is recovered on a system with open boundary conditions as $L \to \infty$ (see Ref. 68), showing that ballistic dynamics due to the existence of globally conserved currents can still be probed on systems with open boundary conditions.

To connect the local energy currents to the spatial variance of the time-dependent density one can rewrite the time derivative of $\sigma_E^2(t)$ using the equation of continuity, assuming no current flow to sites at the boundary (this assumption is justified in our examples as long as we restrict ourselves to times before reflections occur at the boundary in our simulations):

$$\partial_t \sigma_E^2(t) \sim \sum_{r=1}^{L} (r - \mu)^2 \partial_t \langle h_r(t) \rangle$$

$$= -\langle j_1^E \rangle + \sum_{r=1}^{L} (2r - 2\mu + 1)\langle j_r^E(t) \rangle. \qquad (19)$$

If $\sigma_E^2(t) = V_E^2 t + b$ and $\mu \neq \mu(t)$, then using $\langle J_E \rangle = 0$ leads to

$$\sum_{r=1}^{L} r \, \partial_t \langle j_r^E(t) \rangle \sim \frac{1}{2} \partial_t^2 \sigma_E^2(t) = V_E^2 = \mathrm{const}\,. \qquad (20)$$

If we interpret this equation as an operator equation, then we see that we can define a quantity J_E^* via

$$J_E^* = \sum_{r=1}^{L} r \, \partial_t j_r^E \,. \qquad (21)$$

If for a given initial state and over a certain time window, $\langle J_E^*(t) \rangle = \mathrm{const}$, then we have identified a regime with ballistic dynamics, $\delta\sigma_E^2(t) \sim t^2$. If $\langle J_E^*(t) \rangle = \mathrm{const}$ holds for all times and initial states, then J_E^* is a conserved quantity, $[H, J_E^*] = 0$. This is the case at $\Delta = 0$, the noninteracting limit of Eq. (1), where $\langle J_E^* \rangle = V_E^2 \delta E$ from Eq. (13).

We emphasize that we have here identified an operator that connects the phenomenological observation of a quadratic increase of $\sigma_E^2(t)$ to the local energy currents. In ballistic regimes, its expectation value becomes stationary.

For completeness, we mention an analogous result in the diffusive regime where $\sigma_E^2 \sim t$. Then, expectation values of the operator

$$J_E^D = \sum_{r=1}^{L} (r - \mu) j_r^E(t) \qquad (22)$$

are time independent. Obviously, similar expressions can be written down for the spatial variance associated with the spin density.

III. PROPAGATING ENERGY AND SPIN WAVE PACKETS IN A LUTTINGER LIQUID

In the gapless phase, i.e., for $|\Delta| < 1$, the low-energy and low-momentum properties of the XXZ chain can be described by an effective Luttinger liquid theory.[71] In the following, we want to analyze the energy density and the spin dynamics of the XXZ chain in this exactly solvable hydrodynamic limit. Specifically, we show that at least asymptotically for large times, the spatial variance always grows quadratically both in the case of spin and energy dynamics. In addition, we work out the precise dependence of the prefactor in front of the t^2 increase of the spatial variance on system parameters. Since our DMRG results to be presented in Secs. IV and V show that $\sigma_E^2(t) \sim t^2$ at any Δ, we did not investigate the influence of marginally relevant perturbations at $\Delta = 1$ on the wave-packet dynamics. In passing, we mention that in the massive phase, where the appropriate low-energy theory is the sine-Gordon model, the expansion velocity could also be derived at the Luther-Emery point (this case was studied in, e.g., Refs. 25 and 26).

A. Bosonization of the anisotropic spin-1/2 chain

The Hamiltonian (1) can be mapped onto a system of interacting spinless fermions via the Jordan-Wigner transformation.[31] Within a hydrodynamic description in terms

of a linearized fermionic dispersion relation, the Hamiltonian can be represented in terms of a Luttinger liquid theory (LL),

$$H_{LL} = \frac{u}{4} \int \frac{dx}{2\pi} \left[K(\rho_L - \rho_R)^2 + \frac{1}{K}(\rho_L + \rho_R)^2 \right], \quad (23)$$

using the notation of Ref. 72. The sum of the two left- and right-moving densities $\rho_L(x) + \rho_R(x)$ of the spinless Jordan-Wigner fermions is proportional to the continuum approximation of the local magnetization S_i^z up to a constant. The sound velocity u can be related to the parameters of the XXZ chain in Eq. (1) via the group velocity[73]

$$u = v_g = J \frac{\pi}{2} \frac{\sin(\nu)}{\nu}, \quad (24)$$

with $\cos \nu = \Delta$. Similarly, the Luttinger parameter K is given by the relation $K = \pi/[2(1 - \nu)]$. In the noninteracting case, $\Delta = 0$, we have $K = 1$ and $u = J$.

B. Ballistic dynamics in the gapless phase

Within the Luttinger liquid description for $\Delta < 1$, an initially inhomogeneous local energy density profile always propagates ballistically independently of the details of the perturbation as can be seen from general arguments. For the effective low-energy Hamiltonian, the probability distribution $e(x,t)$ associated with the local energy density is given by

$$e(x,t) = \mathcal{E}^{-1} \langle \psi_{\text{init}} | \hat{h}(x,t) | \psi_{\text{init}} \rangle, \quad (25)$$

where $|\psi_{\text{init}}\rangle$ is the initial state,

$$\hat{h}(x) = u(K + K^{-1})/(8\pi) \sum_\eta \partial_x \varphi_\eta^\dagger(x) \partial_x \varphi_\eta(x)$$
$$- u(K - K^{-1})/(8\pi)[\partial_x \varphi_L^\dagger(x) \partial_x \varphi_R^\dagger(x)$$
$$+ \partial_x \varphi_R(x) \partial_x \varphi_L(x)] \quad (26)$$

and

$$\mathcal{E} = \int dx \, \langle \psi_{\text{init}} | \hat{h}(x, t = 0) | \psi_{\text{init}} \rangle. \quad (27)$$

For the exact definition of the fields $\varphi_\eta^{(\dagger)}$, see, e.g., Ref. 72. The local energy density operator consists of decoupled left- and right-moving contributions in the basis in which the Hamiltonian for the time evolution is diagonal. This allows for a separation of $e(x,t)$ into left- and right-moving contributions, which both propagate with the sound velocity v_g: $e(x,t) = e_L(x + v_g t, t = 0) + e_R(x - v_g t, t = 0)$.

Assuming an $L \leftrightarrow R$ symmetry in the initial state, i.e., a state with zero total momentum, one obtains for the variance from Eq. (5):

$$\delta \sigma_E^2(t) = \sigma_E^2(t) - \sigma_E^2(t = 0) = (V_E t)^2 \quad (28)$$

for all times t with $V_E = v_g = u$. This result can also be obtained from evaluating Eq. (13) in the continuum limit.

In the case of an initial $L \leftrightarrow R$ asymmetry in the initial state, we get $\delta \sigma_E^2(t) \rightarrow (v_g t)^2$ for $t \rightarrow \infty$, but the short-time behavior may differ. Thus within the validity of a Luttinger liquid description the energy transport is always ballistic for all initial conditions. This is evident from a physical point of view as all excitations propagate with exactly the same velocity v_g, the left movers to the left and the right movers

to the right. Note that the applicability of a Luttinger liquid description is manifestly restricted to cases in which the initial energy density profile is a smooth one in the sense that the associated excitations do not feel the nonlinearity of the fermionic dispersion relation. Thus, the time-evolution starting from initial profiles such as the ones shown in Fig. 2 is beyond the scope of this low-energy theory.

In analogy to the above arguments, the dynamics of spin-density wave packets is also ballistic in the XXZ chain for $\Delta < 1$ in the Luttinger liquid limit. In the bosonic theory, the spin density is proportional to $\rho_L(x) + \rho_R(x)$ up to a constant, see Sec. III A. The associated probability distribution $\rho(x,t) = \mathcal{Q}^{-1} \langle \rho_L + \rho_R \rangle / 2\pi$, with $\mathcal{Q} = \int dx \langle \rho_L + \rho_R \rangle / 2\pi$, can again be separated into a left- and a right-moving contribution, i.e.,

$$\rho(x,t) = \rho_L(x + v_g t, t = 0) + \rho_R(x - v_g t, t = 0). \quad (29)$$

Thus similar to the case of the energy dynamics, one finds ballistic behavior for $|\Delta| < 1$ consistent with the numerical results of Ref. 20.

IV. DMRG RESULTS FOR THE J_i QUENCH

Now we turn to the numerical simulations. Using the adaptive time-dependent DMRG[38–42] method, we can access the real-time dynamics of initial bond-energy distributions. Within this approach, we can probe the microscopic dynamics including the time dependence of bond energies or the entanglement entropy starting from various initial states in an essentially exact manner without limitations in the range of parameters. We discuss the pure energy dynamics in the absence of spin currents induced by the J_i quench in this section. We detail the construction of initial states and their specific features, then move on to the analysis of the time evolution of the bond energies. We calculate the spatial variance and the related quantity J_E^* and discuss the emergent velocities of the energy dynamics. Within the numerical accuracy of our simulations we find a quadratic increase of $\sigma_E^2(t)$ in all cases studied. However, it seems that for a J_i quench a large number of different velocities contribute as opposed to the Luttinger liquid theory result, the latter valid at low energies. Our study of the energy current during the time evolution and the time evolution of the expectation value $\langle J_E^*(t) \rangle$, defined in Eq. (21), gives additional insights into short-time dynamics and further validates the conclusion of ballistic energy dynamics.

A. Initial states

Let us first describe the typical shape of initial states induced by a J_i quench on a few bonds in the middle of the spin chain. To be specific, in the Hamiltonian (2), we set

$$J_i = \begin{cases} J, & i < L/2 - b, \\ -J, & \text{for} \quad L/2 - b \leqslant i \leqslant L/2 + b, \\ J, & i > L/2 + b, \end{cases} \quad (30)$$

which provides us with initial states with an inhomogeneous energy density profile with a width of $2b$ of the ferromagnetic region. Outside this ferromagnetic region, we obtain antiferromagnetic nearest-neighbor correlations.
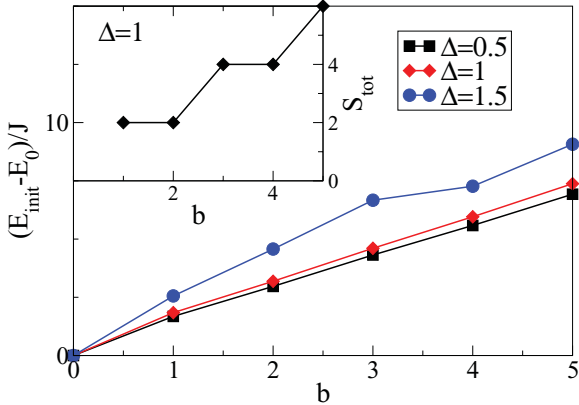
FIG. 3. (Color online) Energy difference δE between the initial state and the ground state for the J_i quench as a function of b for $\Delta = 0.5, 1, 1.5$. The inset shows the hierarchy of states with increasing total spin, which appear as initial states when the total spin is a good quantum number, i.e., at $\Delta = 1$.

Figure 2 shows the profile of the local energy density of XXZ chains with $L = 100$ sites with (a) $\Delta = 0.5$, (b) $\Delta = 1$, and (c) $\Delta = 1.5$, induced by a sign change of J_i on $b = 1, 3, 5$ bonds [compare Eq. (30)], obtained using DMRG with $m = 200$ states exploiting the U(1) symmetry to ensure zero global magnetization $S_{\text{tot}}^z = \sum_i \langle S_i^z \rangle = 0$ and, in consequence, $\langle S_i^z \rangle = 0$. In all cases shown in Fig. 2, the system forms a region with ferromagnetic nearest-neighbor correlations in the middle of the chain. Note that for $\Delta \neq 1$, $\langle h_i \rangle$ is the sum of the nearest-neighbor transverse and longitudinal spin correlations, the latter weighted with Δ. In the regions with antiferromagnetic $J_i > 0$, the local energy density oscillates, reflecting the antiferromagnetic nearest-neighbor correlations. Figure 3 shows the energy difference δE. As a function of b, the energy difference δE increases linearly once the smallest possible ferromagnetic region has been established. The minimum energy difference $\delta E = E_{\text{init}} - E_0$ is of the order of $2J$, i.e., initial states that are only weak perturbations of the respective ground state cannot be generated using a J_i quench.

At the isotropic point $\Delta = 1$, we can explain the dependence of the initial state on the width b in a transparent manner. The ground-state energy per site for the antiferromagnetic ground state is known from the Bethe Ansatz to be $\lim_{L \to \infty} E_0(L)/L = -\ln(2) + 1/4,$[74] while for the ferromagnetic ground state, $E_0/(L-1) = 1/4$, excluding the boundary sites, which gives rise to a very small system-size dependence. By growing the ferromagnetic region symmetrically with respect to the center of the chain and taking $E_0(L)$ from the unperturbed ground state with open boundaries, we obtain states with an energy that increases as

$$\delta E(b) = (2b - 1)[E_0/(L-1) - 0.25] + \delta E^0, \quad (31)$$

for our finite system size (δE^0 is simply an offset). Equation (31) exactly reproduces the data for $\Delta = 1$ shown in Fig. 3.

Furthermore, at $\Delta = 1$, the total spin

$$S_{\text{tot}}^2 = \sum_i \vec{S}_i \cdot \sum_j \vec{S}_j \quad (32)$$

is a conserved quantity. Since the ground-state calculation only respects the conservation of magnetization ($S_{\text{tot}}^z = 0$), we obtain a hierarchy of states with $S > 0$. This can be easily understood by considering the block structure of the initial state. Taking, e.g., a total of $L = 100$ spins and assuming a ferromagnetic region of only two spins (i.e., $b = 1$), the two ferromagnetic spins are fully polarized with a total spin of $S = 1$, while each of the antiferromagnetic blocks has 49 spins and therefore a total spin of $S = 1/2$. Thus the total spin of the whole chain is $S_{\text{tot}} = 2$. Increasing the width of the ferromagnetic region by one, i.e., to $b = 2$, we have $S = 2$ in the middle, and the antiferromagnetic blocks are of even length, both having $S = 0$ in their ground state. This pattern repeats itself upon increasing the length $2b$ of the ferromagnetic region.

B. Time evolution of bond energies after a J_i quench

Now we focus on the time evolution of the local energy density induced by the aforementioned perturbation. At time $t = 0^+$, we set all $J_i = J$ and then evolve under the dynamics of Eq. (1). The DMRG simulations are carried out using a Krylov-space based algorithm[75,76] with a time step of typically $0.25J$ and by enforcing a fixed discarded weight. We restrict the discussion to times smaller than the time needed for the fastest excitation to reach the boundary.

1. J_i quench: qualitative features

Figure 4 shows the time evolution of the bond energies $\langle h_i(t) \rangle$ as a contour plot for $\Delta = 0.5, 1, 1.5$ at $b = 1$. Despite the different ground states for the selected values of anisotropy, all features of the dynamics such as two distinct rays starting at the edges of the block of ferromagnetic correlations, are similar. The solid white lines for $\Delta = 0.5$ and $\Delta = 1$ indicate an excitation spreading out from the center of the ferromagnetic region with the group velocity given by Eq. (24) (these lines are parallel to the outer rays visible in the figure, i.e., the fastest propagating particles). Note that Eq. (24) holds only in the gapless phase ($|\Delta| \leqslant 1$). Besides the outer rays that define a light-cone structure, Fig. 4 unveils the presence of more such rays inside the light cone. Since our particular initial states have a sharp edge in real space, there ought to be many excitations with different momenta k contributing to the expansion.

2. J_i quench: spatial variance

Our main evidence for ballistic dynamics in both phases is based on the analysis of the spatial variance, shown in Fig. 5. Fitting a power law (straight lines) to the data, i.e., $\sigma_E^2(t) - \sigma_E^2(0) = \alpha t^\beta$ yields a quadratic increase with $\beta \approx 2$, classifying the dynamics as ballistic.

In order to estimate uncertainties in the fitting parameter α, we compare this to the results of fitting a pure parabola $\sigma_E^2(t) - \sigma_E^2(0) = V_E^2 t^2$ to the data. Typically, V_E^2 deviates from α by about 10% while the exponent of the power-law fit is
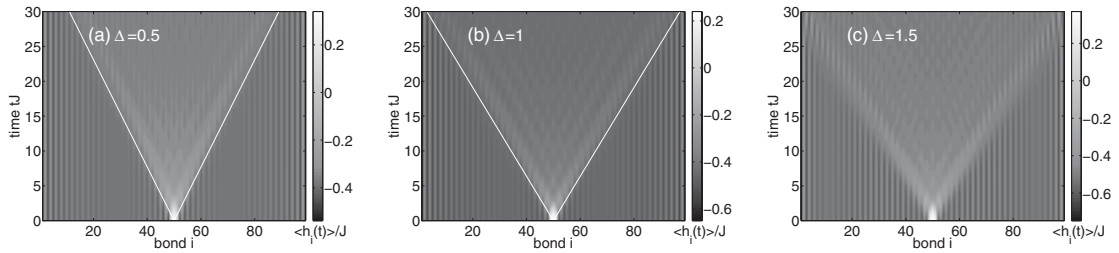
FIG. 4. Time evolution of the bond energy distribution starting from initial states with $b = 1$ from Fig. 2 for (a) $\Delta = 0.5$, (b) $\Delta = 1$, and (c) $\Delta = 1.5$. Despite the different ground-state phases, for the selected values of the exchange anisotropy Δ, main features of the dynamics such as two distinct rays extending from the edges of the perturbation are similar. The solid white lines for $\Delta = 0.5$ and $\Delta = 1$ indicate the propagation of a single excitation starting in the middle of the chain at time $t = 0$ moving with the group velocity v_g from Eq. (24). This is also the velocity in the outer rays.

usually different from 2 by 5%. As an example, for $\Delta = 0.5$ and $b = 1$, we obtain $\beta = 2.03$ and $\alpha = 0.53$ versus $V_E^2 = 0.6J^2$. The main reason for the deviation of β from two is, in fact, that the short-time dynamics is not well described by a power law at all over a b-dependent time window. We shall see later, in Sec. IV C, that the ballistic dynamics sets in

FIG. 5. (Color online) Spatial variance of the evolving energy distribution for (a) $b = 1$, (b) $b = 5$, and $\Delta = 0.5, 1, 1.5$. Fitting a power law (straight lines) to $\sigma_E^2(t) - \sigma_E^2(0) = \alpha t^\beta$ yields a quadratic increase with sufficient accuracy, classifying the dynamics as ballistic. For instance, we find $\alpha = 0.53$, $\beta = 2.03$ for $\Delta = 0.5$ and $b = 1$ [black circles in (a)]. We do not find any qualitative difference between the massless ($|\Delta| \leqslant 1$) and the massive ($\Delta > 1$) phases. The deviations between the fit and the tDMRG data in the $\Delta = 1.5$ curves at the largest times simulated are due to the boundaries.

only after the block of ferromagnetically correlated bonds has fully "melted." Indeed, by excluding several time steps at the beginning of the evolution from the power-law fit, we observe that $\beta \to 2$ and $\alpha \to V_E^2$. Therefore we will present results for V_E^2, obtained by fitting $\sigma_E^2(t) - \sigma_E^2(0) = V_E^2 t^2$ to our tDMRG data.

3. Exploiting SU(2) symmetry at $\Delta = 1$ for the J_i quench

Before proceeding to the discussion of the expansion velocity V_E^2, we wish to discuss the long-time limit, which can be accessed in the case of $\Delta = 1$. Since our perturbation is proportional to the operators for the local energy density, global symmetries of the unperturbed Hamiltonian are respected by the initial states of the type in Eq. (30). Therefore, at $\Delta = 1$, we can exploit the conservation of total spin S, a non-Abelian symmetry. This can be used to push the simulations to much longer times, since we can perform the time evolution in an SU(2) invariant basis.[77] The number of states needed to ensure a given accuracy is reduced substantially compared to a simulation that only respects U(1) symmetry. Therefore we can work with larger system sizes and study the long-time dynamics of the energy density. As we can reach longer times, we can also analyze and discuss finite-size effects for $\Delta = 1$ here. Figure 6 shows our result for the time evolution respecting SU(2) symmetry (blue triangles) for a system of $L = 200$ sites and $\Delta = 1$, $b = 1$ compared to the result from Fig. 5 for $L = 100$ sites (red squares). We still find a quadratic increase of $\sigma_E^2(t)$ and thus ballistic dynamics for times up to $t \sim 60/J$ and in addition, the prefactor does not depend on the system size. Both simulations were carried out keeping the discarded weight below 10^{-4}, which requires at most $m = 900$ states using only U(1) symmetry on $L = 100$ sites versus a maximum of $m = 400$ using SU(2) for $L = 200$ sites.

4. Expansion velocity

The results for V_E^2 are collected in Fig. 7 and plotted as a function of δE for $\Delta = 0, 0.5, 1, 1.5$. In the noninteracting case, $\Delta = 0$, V_E^2 is constant for $b \geqslant 2$, while at $b = 1$ (the smallest possible δE), $V_E^2 = 0.5J^2$. For all $\Delta > 0$, V_E^2 slightly decreases with δE and V_E^2 is much smaller than v_g^2 given by Eq. (24), suggesting that indeed, many velocities contribute during the expansion of the energy wave packet.
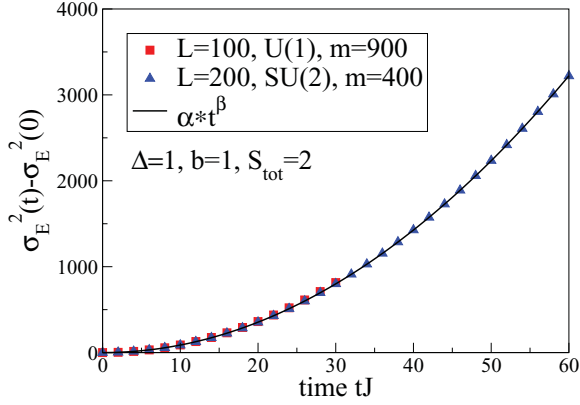
FIG. 6. (Color online) Long-time evolution exploiting the conservation of total spin S_{tot} at $\Delta = 1$ for $L = 200$ sites using an initial state with $b = 1$. For comparison, we plot the result for $L = 100$ sites using only U(1) symmetry. Fixing the discarded weight to 10^{-4}, we need less than half the number of states. Furthermore, we find that the spatial variance is very robust against finite-size effects.

Intuitively, one might associate the decrease of V_E^2, which is a measure of the average velocity of propagating excitations contributing to the expansion, to band curvature: the higher δE, the more excitations with velocities smaller than v_g are expected to factor in.

It is instructive to consider the noninteracting limit first by comparing the numerical results obtained from a time evolution with exact diagonalization to the analytical (and also exact result) from Eq. (13). To that end, we need to compute the MDF [see Eq. (14)] of the initial state. Our results for $\Delta = 0$, which are shown in Fig. 8, unveil a peculiar property: the J_i quench always induces changes at all k, i.e., the system is not just weakly perturbed in the vicinity of k_F. This is not surprising since our initial states have sharp edges in real space (compare Fig. 2). Moreover, the J_i quench changes the MDF in
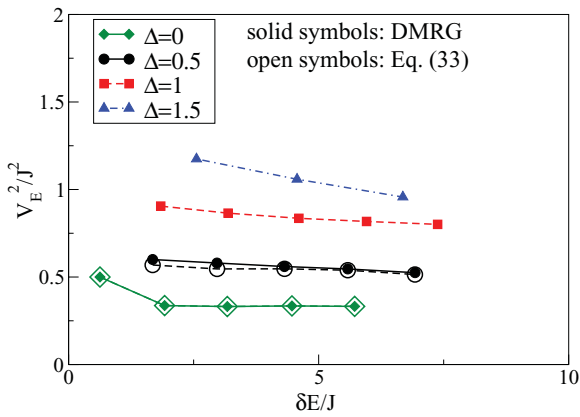
FIG. 7. (Color online) Prefactors V_E^2 of the fits $\sigma_E^2 - \sigma_E^2(0) = V_E^2 t^2$ as functions of δE for $\Delta = 0, 0.5, 1, 1.5$ and J_i quenches with $b = 1, 2, 3, 4, 5$ (for $\Delta = 1.5$, we show $b = 1, 2, 3$ only). For $\Delta > 0$, V_E^2 decreases slightly with b, while $V_E^2 < v_g^2$. At $\Delta = 0$, V_E^2 is roughly constant for $b > 2$.
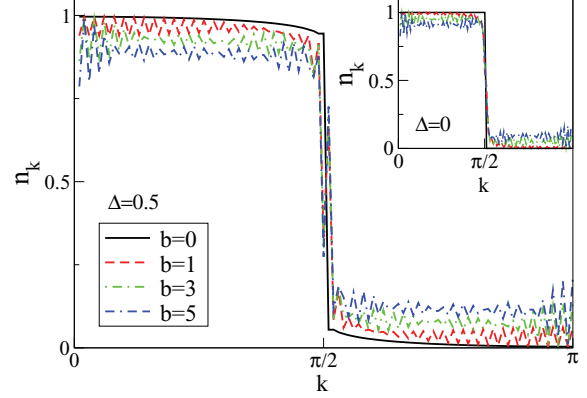
FIG. 8. (Color online) MDF of the initial states generated by a J_i quench at $\Delta = 0.5$ and $\Delta = 0$ (inset) with $b = 1, 3, 5$. For comparison, we include the MDF of the ground state (solid black line).

such a way that $\delta n_k(b) = n_k^{init}(b) - n_k$ is point symmetric with respect to $k_F = \pi/2$, where k_F is the Fermi wave vector. As Fig. 7 shows, V_E^2 as extracted from fits to $\delta\sigma_E^2$ (solid symbols) and V_E^2 from Eq. (13) (open symbols) perfectly agree with each other, as expected.

The MDF of initial states for the interacting systems are also such that $\delta n_k \neq 0$ at all momenta and we may therefore conclude that the observation $V_E < v_g$ is due to the fact that the J_i quench induces many excitations with velocities smaller than v_g (compare the data shown for $\Delta = 0.5$ shown in Fig. 8). Of course, Eq. (13) is not directly applicable to the interacting case since, first, it does not account for the correct eigenstates at $\Delta \neq 0$ and second, in general, $\langle h_i \rangle \neq \langle J(S_i^+ S_{i+1}^- + \text{H.c.})/2\rangle$. Nevertheless, by numerically calculating δn_k for the interacting system and by using the renormalized velocity in Eq. (13) instead of J [i.e., $J \rightarrow v_g(\Delta)$], we obtain an estimate for V_E^2 from

$$V_E^2 \approx \frac{v_g^2}{\delta E} \sum_k \cos(k) \sin^2(k) \delta n_k . \qquad (33)$$

This reproduces the qualitative trend of the tDMRG results for V_E^2 as we exemplify for $\Delta = 0.5$ in Fig. 7.

To summarize, the overall picture for the time evolution of the bond energies after a J_i quench is that energy propagates ballistically with an expansion velocity V_E that is approximately given by Eq. (33). Combined with the observation that on a finite system, a J_i quench induces changes in the MDF at all momenta k, we conclude that many excitations contribute to the wave-packet dynamics, resulting in $V_E < v_g$, both in the noninteracting and in the interacting case.

C. Energy currents

To conclude the discussion of the J_i quenches we present our results for the local energy currents at $\Delta = 1$ in Fig. 9. By comparison with Fig. 4(b), we see that the local current is the strongest in the vicinity of the wave packet. The energy current in each half of the system becomes a constant after a few time steps, i.e., $J_{L/2}^E := \sum_{i=1}^{L/2-1} j_i^E$ reaches a constant value. We
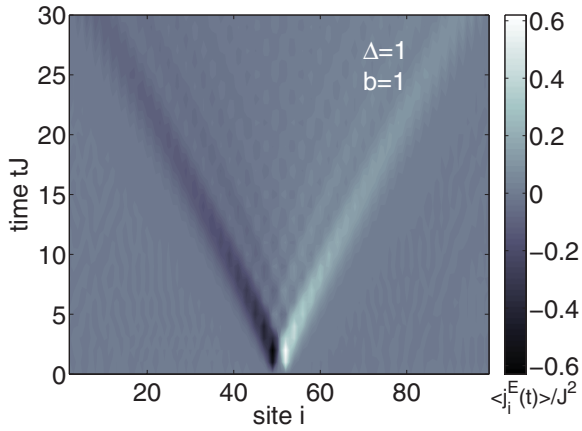
FIG. 9. (Color online) Real-time evolution of the local energy current, Eq. (18), at $\Delta = 1$ for a J_i quench with $b = 1$.

plot the absolute value of $\langle J_{L/2}^E \rangle$ for $\Delta = 0.5, 1, 1.5$ for $b = 1$ in Fig. 10(a). The qualitative behavior is independent of Δ: as soon as the initial perturbation has split up into two wave packets, we have prepared each half of the chain in a state with a constant, global current $\langle J_{L/2}^E \rangle = $ const. For a system with periodic boundary conditions, the total current $J_E = \sum_i j_i^E$ is a conserved quantity.[43] Since the effect of boundaries only factors in once these are reached by the fastest excitations, we directly probe the conservation of a global current with our setup, after some initial transient dynamics. Therefore we can link the phenomenological observation of ballistic wave-packet dynamics to the existence of a conservation law in the system.

While the currents $\langle J_{L/2}^E \rangle$ clearly undergo some transient dynamics [see Fig. 10(a)], we have derived a quantity in Sec. II, called J_E^*, whose expectation value is stationary if $\sigma_E^2 \sim t^2$. We now numerically evaluate $\langle J_E^*(t) \rangle$ from Eq. (21), which provides an independent probe of ballistic dynamics. Figure 10(b) shows our results for $\Delta = 1$ and J_i quenches with $b = 1, 2, 3, 4, 5$. It turns out that $\langle J_E^*(t) \rangle$ is indeed constant at sufficiently large times, consistent with the observation of $\delta\sigma_E^2 \sim t^2$. In Sec. IV B, we have noted that $\delta\sigma_E^2 \nsim t^2$ at short times $t \lesssim b/J$. This renders $\langle J_E^*(t) \rangle$ a time-dependent quantity over the same time window. Clearly, the time window over which $\langle J_E^*(t) \rangle \neq$ const depends on b [see Fig. 10(b)], which suggests that the deviation of ballistic dynamics is associated to the "melting" process of the region with ferromagnetic correlations. We have carefully checked that these observations are robust against errors in the calculation of time derivatives in Eq. (21) induced by the finite time step. Since $\langle J_E^*(t) \rangle$ is time dependent (at least at short times), we conclude that J_E^* is not a conserved quantity in the interacting case. Finally, within our numerical accuracy and as an additional consistency check, we find that $\langle J_E^* \rangle / \delta E = \alpha$ in the stationary state as expected from the discussion in Sec. II C.

To summarize, $\langle J_E^*(t) \rangle = $ const whenever $\delta\sigma_E^2 \sim t^2$ but $\langle J_E^* \rangle$ is very sensitive to the initial transient dynamics in the energy dynamics and becomes constant after a time $\approx bJ$. Furthermore, our setup serves to prepare each half of the system in a state with a finite global energy current $\langle J_{L/2}^E \rangle$
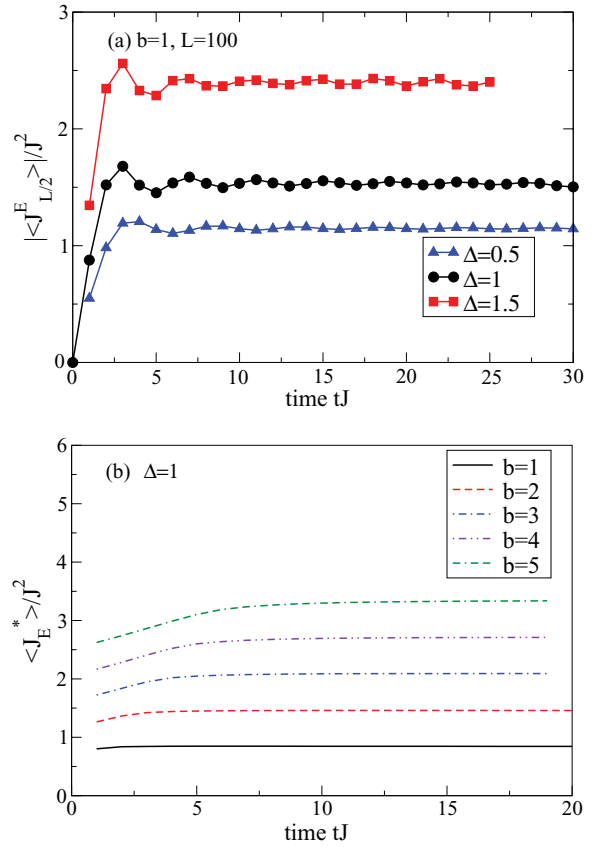

FIG. 10. (Color online) (a) Absolute value of the current in each half of the system. A constant value is reached after $t \approx 5/J$. (b) The quantity $\langle J_E^*(t) \rangle$ from Eq. (21) derived from a pure quadratic increase of the spatial variance for $\Delta = 1$ and $b = 1, 2, 3, 4, 5$. This quantity is constant, as expected from the discussion in Sec. IV C, except for the initial transient dynamics at $t < b/J$.

that, after some transient dynamics, does not decay since the global energy current operator is a conserved quantity.

V. COUPLED SPIN AND ENERGY DYNAMICS

After focusing on the energy dynamics in the absence of spin/particle currents we now revisit the case of spin dynamics starting from states with $\langle S_i^z(t = 0) \rangle \neq 0$. Thus during the time evolution, the local spin and energy currents are both nonzero. In Ref. 20, the dynamics of the magnetization was studied, where the inhomogeneous spin-density profile was induced by a Gaussian magnetic field in the initial state. We take the initial state to be the ground state of Eq. (3) in the sector with zero global magnetization, i.e., $S_{\text{tot}}^z = \sum_i \langle S_i^z \rangle = 0$. Such a perturbation naturally also results in an inhomogeneous energy density in the initial state, which is coupled to the spin dynamics during the time evolution.[28]
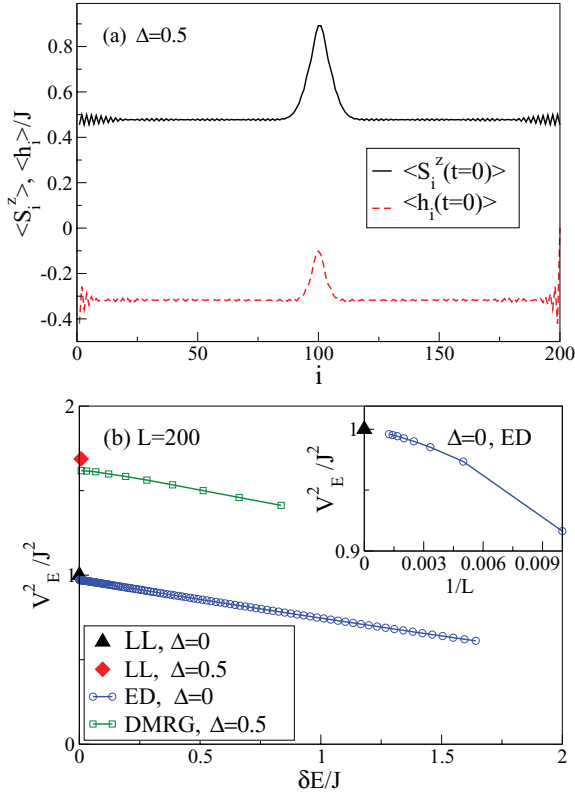
FIG. 11. (Color online) (a) Magnetization (solid black line) and energy density (dashed red line) in the initial state, for a B_0 quench with $B_0 = J$ and $\sigma_0 = 5$ for $\Delta = 0.5$ on a lattice of $L = 200$ sites. (b) Prefactor V_E^2 of $\delta\sigma_E^2(t) = V_E^2 t^2$ for the energy dynamics after a B_0 quench in the massless phase of the XXZ chain, compared to the group velocity [Eq. (24)] for $\Delta = 0, 0.5$ and $L = 200$. On this system size and in the limit of small perturbations, V_E^2 is approximately 5% smaller than the prediction from the Luttinger liquid theory for both Δ. For $\Delta = 0$, finite-size scaling of $V_E^2(\delta E \to 0)$ using $L = 100, 200, \ldots, 800$ yields $V_E^2 \to v_g^2$ as shown in the inset.

A. Massless phase

In Fig. 11(a), we compare the initial magnetization (black solid line) and the local bond energies (dashed red line) induced by a Gaussian magnetic field with $B_0 = J$ and $\sigma_0 = 5$ at $\Delta = 0.5$ finding qualitatively the same pattern; both the spin and the energy density follow the shape of the magnetic field, resulting in a smooth perturbation with small oscillations in the background away from the wave packet.

For the time evolution of the bond energies at $0 < \Delta \leqslant 1$, we perform an analysis of their spatial variance analogous to the discussion of the J_i quench, finding ballistic dynamics in the massless phase. Since with a B_0 quench, initial states with very small δE can be produced, we next connect our numerical results to the predictions of LL theory, valid in the limit $\delta E \ll J$ (compare Sec. III).

Since we enforce zero global magnetization, we draw magnetization from the background into the peak.[14] Therefore one has to carefully estimate the contributions to δE that

do not contribute to the time dependence of bond energies yet change the background density n_{bg}. The latter, in turn, affects the expected group velocity and we thus expect to recover the LL result derived for the half-filled case, i.e., propagation with v_g from Eq. (24), in the limit of large systems where $n_{\text{bg}} \to 1/2$. Furthermore, B_0 quenches induce $2k_F$ oscillations in the spin and energy density.[20] To account for this, we use coarse graining, i.e., averaging the energy density over neighboring sites, and we take the sum only over the area of the peak when estimating δE. We obtain $\delta E^{\text{peak}} := \sum_{L/2-x}^{L/2+x} (\langle h_i \rangle - \langle h_i \rangle_0)$, where $\langle h_i \rangle_0$ denotes the ground-state expectation value. From this quantity we calculate the velocity via $V_E^2 \to V_E^2 \cdot \delta E/\delta E^{\text{peak}}$, which is shown in Fig. 11(b). Note that while δE_{peak} is the correct normalization to obtain the correct velocities, we label our initial states via δE. At $\Delta = 0$ (blue circles), V_E^2 decreases linearly as a function of δE. Next we compare the result from the low-energy theory from Sec. III (solid symbols at $\delta E = 0$) to our tDMRG data. For both $\Delta = 0$ and $\Delta = 0.5$, V_E^2 for $L = 200$ sites is approximately 5% smaller than v_g^2 from Eq. (24), which is mainly due to the deviation of the background density from half filling. While it is hard to get results for larger systems than $L \sim 200$ in the interacting case, we can solve the $\Delta = 0$ case numerically exactly in terms of free spinless fermions, allowing us to go to sufficiently large L to observe $V_E^2(L) \to v_g^2$ as $L \to \infty$. The inset of Fig. 11(b) shows the finite-size scaling of $V_E^2(L)$ for $\Delta = 0$ using $L = 100, 200, \ldots, 800$, which yields $V_E^2 \to v_g^2$ in the limit $L \to \infty$, taking first $\delta E \to 0$ for each system size. We thus, in principle, have numerical access to the dynamics in the low-energy limit well described by Luttinger liquid theory using a B_0 quench.

B. Massive phase

In Ref. 20, examples of a linear increase of the spatial variance of the magnetization $\sigma_S^2(t)$, defined in Eq. (16), were found in the massive phase, which were interpreted as an indication of diffusive dynamics. We now demonstrate that while the spin dynamics may behave diffusively, i.e., $\delta\sigma_S^2 \sim t$ over a certain time window, the energy dynamics in the same quench is still ballistic, i.e., $\delta\sigma_E^2 \sim t^2$.

In Fig. 12, we show the full time evolution of the bond energies for a Gaussian magnetic field with $B_0 = 1.5J$ and $\sigma_0 = 5$ on a chain of $L = 200$ sites at $\Delta = 1.5$. It consists of two rays propagating with opposite velocities. In Fig. 13, we compare the spatial variance of the magnetization $\sigma_S^2(t)$ to the one of the bond energies $\sigma_E^2(t)$ calculated in the same time evolved state. The main panel of Fig. 13 shows $\sigma_E^2(t) - \sigma_E^2(0)$, which is very well described by a power-law fit with an exponent $\beta = 2.03$ on the accessible time scales. The inset of Fig. 13 displays the data for $\delta\sigma_S^2(t) = \sigma_S^2(t) - \sigma_S^2(0)$ taken from Ref. 20. The spatial variance of the energy density is quadratic in time, even at times $t \gtrsim 12/J$ where the spatial variance of the magnetization increases only linearly. This example reflects the qualitative difference between spin and energy transport in the massive phase of the XXZ model at zero global magnetization. The conservation of the global energy current is consistent with the observation of ballistically propagating energy wave packets, while spin clearly does not propagate ballistically. Our result, obtained in the nonequilibrium case with a
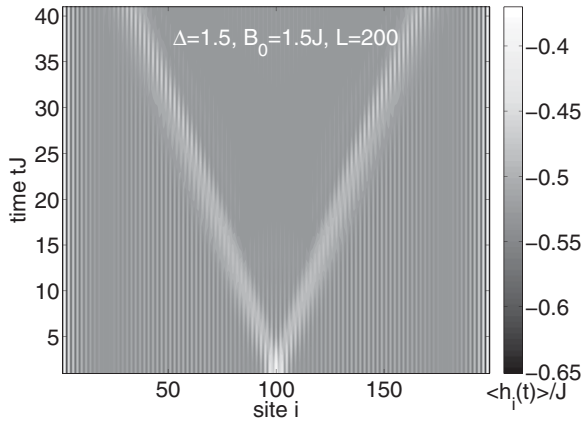
FIG. 12. (Color online) Time-dependent bond energies for the dynamics induced by a B_0 quench with $B_0 = 1.5J$, $\sigma_0 = 5$ on a chain of $L = 200$ sites at $\Delta = 1.5$. In this case, both local spin and local energy densities are perturbed and the corresponding local currents are nonzero.

zero-temperature background density, is consistent with the picture established from both linear-response theory[51,55] and steady-state simulations.[28,61,64]

Very recently, Jesenko and Žnidarič have also studied the time evolution of spin and energy densities induced by a B_0 quench.[28] They concentrate their analysis on the velocity of the fastest wave fronts, contrasting energy against spin dynamics. Based on the presence of these rays of fast propagating particles, they claim that the wave packet dynamics still has ballistic features. However, their analysis neglects the influence of slower excitations that also contribute to the dynamics of the wave packet, which is captured by the variance, and it ignores the decay of the intensity in the outer rays that we typically observe whenever $\delta\sigma_S^2 \sim t$.[20] The latter is, if at all, weak in a ballistic expansion characterized by
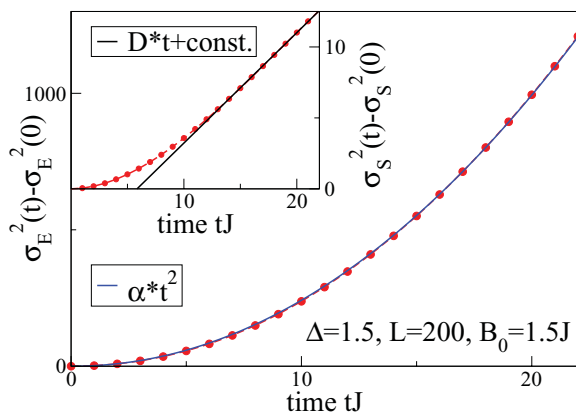
$\delta\sigma_S^2 \sim t^2$. Therefore, while the analysis of Ref. 28 unveils interesting details of the time evolution of densities during a B_0 quench, we maintain that the variance is a useful quantity to identify candidate parameter sets for spin diffusion in, e.g., the nonequilibrium regime. Final proof of diffusive behavior then needs to be established by either demonstrating the validity of the diffusion equation or by computing correlation functions, see, e.g., Refs. 55 and 61. For instance, in Ref. 28, Jesenko and Žnidarič analyze the steady-state currents in the $\Delta > 1$ regime at finite temperature and obtain diffusive behavior.

VI. SUMMARY

We studied the real-time energy dynamics in XXZ spin-1/2 chains at zero temperature in two different scenarios. First, we investigated the energy dynamics in the absence of spin currents induced by a local sign change in the exchange interactions. The spatial variance behaves as $\delta\sigma_E^2(t) \propto t^2$ for all Δ, consistent with ballistic dynamics. In the gapless regime, the velocity of the fastest excitation present in the dynamics is the group velocity v_g of spinons, yet our particular quench also involves excitations with much smaller velocities resulting in expansion velocities $V_E < v_g$. Furthermore, the ballistic dynamics can be related to properties of energy currents. While the total current vanishes in our setup, i.e., $\langle J_E \rangle := \sum_i \langle j_i^E \rangle = 0$, the current in each half of the chain $\langle J_{L/2}^E \rangle > 0$ takes a constant value, after some transient dynamics. Therefore, in each half of the system, we prepared a state with a conserved global current, allowing us to make a direct connection to the predictions of linear-response theory where the existence of ballistic dynamics is directly linked to conservation laws that prohibit currents from decaying.[43] Moreover, we identified an observable J_E^* built from local currents whose expectation value $\langle J_E^*(t) \rangle$ is time independent if $\delta\sigma_E^2 \propto t^2$ and vice versa. This carries over to other types of transport as well and, in fact, the analysis of the time dependence of $\langle J_E^* \rangle$ can be used as an independent means to identify ballistic regimes, or to unveil the absence thereof.
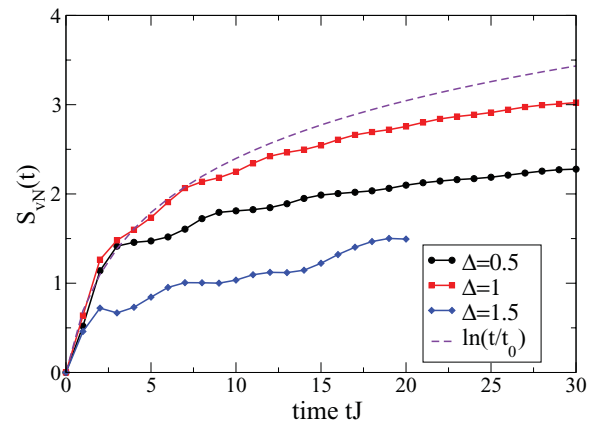

FIG. 13. (Color online) Spatial variance of the energy density (main panel) and the spin density (inset), induced by a B_0 quench with $B_0/J = 1.5$ and $\sigma_0 = 5$ [compare Eq. (3)] at $\Delta = 1.5$. In this case, both local spin and local energy densities are non zero during the time evolution. The inset was reproduced from Ref. 20.

FIG. 14. (Color online) Time dependence of the von Neumann entropy S_{vN} for a bipartition that cuts the system across the central bond during the time evolution starting from a ferromagnetic region coupled to an antiferromagnetic one at $\Delta = 0.5, 1, 1.5$

In the second part, we studied the energy dynamics induced by quenching a Gaussian magnetic field, with two main results. These quenches allow us to access the regime of weakly perturbed initial states and in that limit, we recover the predictions from Luttinger liquid theory for the wave-packet dynamics. Their variance simply grows as $\delta\sigma_E^2 = v_g^2 t^2$. In the massive phase, a very interesting phenomenon occurs, since the energy dynamics is ballistic on time scales over which the spin dynamics behaves diffusively although both are driven by the same perturbation. This resembles the picture established from linear-response theory,[43] there applied to the finite-temperature case, in the nonequilibrium setup studied here. While our numerical results cover spin chains on real-space lattices and initial states far from equilibrium, the extension of our work to a finite temperature of the background will be crucial to tackle the most important open questions.

APPENDIX: ENTANGLEMENT GROWTH

Here, we want to study the growth of entanglement across a junction separating regions in a spin chain with ferromagnetic correlations from ones with antiferromagnetic ones.

To that end, we take initial states inspired by Ref. 19 where one half of the system has a positive and the other one a negative J. We obtain this configuration as a variation of J_i-quench choosing:

$$J_i = \begin{cases} J, & i < L/2, \\ 0, & \text{for} \quad i = L/2, \\ -J, & i > L/2, \end{cases} \tag{A1}$$

in Eq. (2). We then perform the time evolution under the antiferromagnetic Hamiltonian [Eq. (1)]. As a measure of the entanglement we calculate the von Neumann entropy

$$S_{\text{vN}} = -\text{Tr}(\rho_A \ln \rho_A) \tag{A2}$$

of the reduced density matrix $\rho_A = \text{Tr}_B \rho$, where $\rho = |\psi(t)\rangle\langle\psi(t)|$ and $|\psi(t)\rangle$ is the time-evolved wave function, for a bipartition in which we cut the chain into two halves of length $L/2$ across the central link. Our results are plotted in Fig. 14. We observe that the von Neumann entropy grows at most logarithmically (purple dashed line), in agreement with Ref. 21. The overall largest values of $S_{\text{vN}}(t)$ are found at the critical point $\Delta = 1$ (red squares). This behavior is very similar to the observations made in Ref. 19 for spin dynamics starting from a state with all spins pointing up (down) in the left (right) half.

---

*stephan.langer@physik.uni-muenchen.de

[1]X. Zotos and P. Prelovšek, *Strong Interactions in Low Dimensions* (Kluwer, Doodrecht, 2004), Chap. 11.

[2]F. Heidrich-Meisner, A. Honecker, and W. Brenig, Eur. J. Phys. Special Topics **151**, 135 (2007).

[3]A. V. Rozhkov and A. L. Chernyshev, Phys. Rev. Lett. **94**, 087201 (2005).

[4]E. Boulat, P. Mehta, N. Andrei, E. Shimshoni, and A. Rosch, Phys. Rev. B **76**, 214411 (2007).

[5]I. Bloch, J. Dalibard, and W. Zwerger, Rev. Mod. Phys. **80**, 885 (2008).

[6]A. Polkovnikov, K. Sengupta, A. Silva, and M. Vengalattore, Rev. Mod. Phys. **83**, 863 (2011).

[7]U. Schneider, L. Hackermüller, J. P. Ronzheimer, S. Will, S. Braun, T. Best, I. Bloch, E. Demler, S. Mandt, D. Rasch, and A. Rosch, e-print arXiv:1005.3545 (unpublished).

[8]P. Medley, D. M. Weld, H. Miyake, D. E. Pritchard, and W. Ketterle, Phys. Rev. Lett. **106**, 195301 (2011).

[9]A. Sommer, M. Ku, and M. W. Zwierlein, New J. Phys. **13**, 055009 (2011).

[10]A. Sommer, M. Ku, G. Roati, and M. W. Zwierlein, Nature (London) **472**, 201 (2011).

[11]J. Joseph, J. E. Thomas, M. Kulkarni, and A. G. Abanov, J. Stat. Mech.: Theory Exp. (**2011**) P04007.

[12]M. Rigol and A. Muramatsu, Phys. Rev. Lett. **93**, 230404 (2004).

[13]M. Rigol and A. Muramatsu, Phys. Rev. Lett. **94**, 240403 (2005).

[14]C. Kollath, U. Schollwöck, J. von Delft, and W. Zwerger, Phys. Rev. A **71**, 053606 (2005).

[15]F. Heidrich-Meisner, M. Rigol, A. Muramatsu, A. E. Feiguin, and E. Dagotto, Phys. Rev. A **78**, 013620 (2008).

[16]F. Heidrich-Meisner, S. R. Manmana, M. Rigol, A. Muramatsu, A. E. Feiguin, and E. Dagotto, Phys. Rev. A **80**, 041603(R) (2009).

[17]D. Karlsson, M. O. C. Verdozzi, and K. Capelle, Europhys. Lett. **93**, 23003 (2011).

[18]J. Kajala, F. Massel, and P. Törmä, Phys. Rev. Lett. **106**, 206401 (2011)

[19]D. Gobert, C. Kollath, U. Schollwöck, and G. Schütz, Phys. Rev. E **71**, 036102 (2005).

[20]S. Langer, F. Heidrich-Meisner, J. Gemmer, I. P. McCulloch, and U. Schollwöck, Phys. Rev. B **79**, 214409 (2009).

[21]V. Eisler and I. Peschel, J. Stat. Mech.: Theory Exp. (**2009**) P02011.

[22]J. Lancaster and A. Mitra, Phys. Rev. E **81**, 061134 (2010).

[23]J. Lancaster, E. Gull, and A. Mitra, Phys. Rev. B **82**, 235124 (2010).

[24]J. Mossel, G. Palacios, and J.-S. Caux, J. Stat. Mech.: Theory Exp. (**2010**) L09001.

[25]M. S. Foster, E. A. Yuzbashyan, and B. L. Altshuler, Phys. Rev. Lett. **105**, 135701 (2010).

[26]M. S. Foster, T. C. Berkelbach, D. R. Reichman, and E. A. Yuzbashyan, Phys. Rev. B **84**, 085146 (2011).

[27]L. F. Santos and A. Mitra, Phys. Rev. E **84**, 016206 (2011).

[28]S. Jesenko and M. Žnidarič e-print arXiv:1105.6340v1 (unpublished).

[29]C. Kollath, U. Schollwöck, and W. Zwerger, Phys. Rev. Lett. **95**, 176401 (2005).

[30]M. Polini and G. Vignale, Phys. Rev. Lett. **98**, 266403 (2007).

[31]P. Jordan and E. Wigner, Z. Phys. **47**, 631 (1928).

[32]C. Hess, H. ElHaes, A. Waske, B. Büchner, C. Sekar, G. Krabbes, F. Heidrich-Meisner, and W. Brenig, Phys. Rev. Lett. **98**, 027201 (2007).

[33]A. V. Sologubenko, T. Lorenz, H. R. Ott, and A. Freimuth, J. Low Temp. Phys. **147**, 387 (2007).

[34]C. Hess, C. Baumann, U. Ammerahl, B. Büchner, F. Heidrich-Meisner, W. Brenig, and A. Revcolevschi, Phys. Rev. B **64**, 184305 (2001).

[35]A. V. Sologubenko, K. Gianno, H. R. Ott, U. Ammerahl, and A. Revcolevschi, Phys. Rev. Lett. **84**, 2714 (2000).

[36]N. Hlubek, P. Ribeiro, R. Saint-Martin, A. Revcolevschi, G. Roth, G. Behr, B. Büchner, and C. Hess, Phys. Rev. B **81**, 020405 (2010).

[37]M. Otter, V. Krasnikov, D. Fishman, M. Pshenichnikov, R. Saint-Martin, A. Revcolevschi, and P. van Loodsrecht, J. Mag. Mag. Mat. **321**, 796 (2009).

[38]A. Daley, C. Kollath, U. Schollwock, and G. Vidal, J. Stat. Mech.: Theory Exp. (2004) P04005.

[39]S. R. White and A. E. Feiguin, Phys. Rev. Lett. **93**, 076401 (2004).

[40]G. Vidal, Phys. Rev. Lett. **93**, 040502 (2004).

[41]U. Schollwöck, Rev. Mod. Phys. **77**, 259 (2005).

[42]U. Schollwöck, Ann. Phys. (NY) **326**, 96 (2011).

[43]X. Zotos, F. Naef, and P. Prelovšek, Phys. Rev. B **55**, 11029 (1997).

[44]A. Klümper and K. Sakai, J. Phys. A **35**, 2173 (2002).

[45]K. Sakai and A. Klümper, J. Phys. A **36**, 11617 (2003).

[46]F. Heidrich-Meisner, A. Honecker, D. C. Cabra, and W. Brenig, Phys. Rev. B **66**, 140406(R) (2002).

[47]F. Heidrich-Meisner, A. Honecker, D. C. Cabra, and W. Brenig, Phys. Rev. B **68**, 134436 (2003).

[48]B. N. Narozhny, A. J. Millis, and N. Andrei, Phys. Rev. B **58**, R2921 (1998).

[49]X. Zotos, Phys. Rev. Lett. **82**, 1764 (1999).

[50]X. Zotos, Phys. Rev. Lett. **92**, 067202 (2004).

[51]P. Prelovšek, S. El Shawish, X. Zotos, and M. Long, Phys. Rev. B **70**, 205129 (2004).

[52]J. Benz, T. Fukui, A. Klümper, and C. Scheeren, J. Phys. Soc. Jpn. Suppl. **74**, 181 (2005).

[53]P. Jung, R. W. Helmes, and A. Rosch, Phys. Rev. Lett. **96**, 067202 (2006).

[54]J. Sirker, R. G. Pereira, and I. Affleck, Phys. Rev. Lett. **103**, 216602 (2009).

[55]R. Steinigeweg and J. Gemmer, Phys. Rev. B **80**, 184402 (2009)

[56]S. Grossjohann and W. Brenig, Phys. Rev. B **81**, 012404 (2010).

[57]R. Steinigeweg, Phys. Rev. E **84**, 011136 (2011).

[58]R. Steinigeweg and W. Brenig, e-print arXiv.1107.3103 (unpublished).

[59]J. Herbrych, P. Prelovšek, and X. Zotos, Phys. Rev. B **84**, 155125 (2011).

[60]T. Prosen, Phys. Rev. Lett. **106**, 217206 (2011).

[61]M. Žnidarič, Phys. Rev. Lett. **106**, 220601 (2011).

[62]J. Sirker, R. G. Pereira, and I. Affleck, Phys. Rev. B **83**, 035115 (2011).

[63]J.-S. Caux and J. Mossel, J. Stat. Mech. (2011) P02023.

[64]T. Prosen and M. Žnidarič, J. Stat. Mech: Theor. Exp. (2009) P02035.

[65]G. Benenti, G. Casati, T. Prosen, and D. Rossini, Europhys. Lett. **85**, 37001 (2009).

[66]G. Benenti, G. Casati, T. Prosen, D. Rossini, and M. Žnidarič, Phys. Rev. B **80**, 035110 (2009).

[67]P. Calabrese and J. Cardy, J. Stat. Mech.: Theory Exp. (2007) P10004.

[68]M. Rigol and B. S. Shastry, Phys. Rev. B **77**, 161101(R) (2008)

[69]S. Chandrasekhar Rev. Mod. Phys. **15**, 1 (1943).

[70]R. Steinigeweg and R. Schnalle, Phys. Rev. E **82**, 040103(R) (2010).

[71]J. Solyom, Adv. Phys. **28**, 209 (1979).

[72]J. von Delft and H. Schoeller, Ann. Phys. (Leipzig) **7**, 225 (1998).

[73]J. des Cloizeaux and M. Gaudin, J. Math. Phys. **7**, 1384 (1966).

[74]L. Hulthěn, Arkiv. Mat. Astron. Fysik 26A No. 11 (1938).

[75]T. Park and J. Light, J. Chem. Phys. **85**, 5870 (1986).

[76]M. Hochbruck and C. Lubich, SIAM J. Numer. Anal. **34**, 1911 (1997).

[77]I. McCulloch and M. Gulasci, Europhys. Lett. **57**, 852 (2002).

4 Dynamics of ultra-cold atomic gases in one spatial dimension

In the discussion of the results for the low-dimensional quantum magnets, the experimental motivations where based upon real materials. While the question of ballistic versus diffusive dynamics in the models used to describe some features of such materials is a interesting, fundamental question, especially out of equilibrium, the gap to experiments done at room temperature on three-dimensional macroscopic bulk crystals is quite large. Especially phonons are likely to play a role in the whole picture and difficult to incorporate into numerical simulations.

The fairly young field of cold atomic gases can nowadays provide us with well controlled quantum systems, which, to a certain degree, emulate the physics of interesting model Hamiltonians [196]. It originated from the experimental observation of Bose-Einstein condensation [197] in ultra-cold Bose gases [61, 62, 63] and the resulting investigation of macroscopic coherent matter waves (see [198] for a review). Compared to Bosons, cooling fermions to the quantum degenerate regime is technically more demanding but has also been achieved [66, 67, 68].

Beyond cooling bosons and fermions to the quantum regime, the two following developments then forged the bond between ultra-cold gases and strongly correlated lattice models: The first one is the realization of strong periodic potentials, so called optical lattices, by the means of counter-propagating laser beams [64, 65]. The second one is the precise control of the two particle interaction strength via Feshbach resonances [199, 200, 201]. Combining those two techniques allows to study the physics of the Hubbard model with tunable interactions and dimensionality (see, e.g., [7, 69, 70, 95]).

The investigation of non-equilibrium properties of ultra-cold atomic gases is often driven by questions such as thermalization [202], or state engineering [21]. In the discussion of whether or not relaxation dynamics give rise to thermalization [6] finite net currents are usually sought to suppress. Yet, several recent experiments deliberately addressed scenarios with finite particle currents [7, 71, 74, 75, 76, 77].

This chapter presents our results for the real-time dynamics that bosons and fermions undergo upon being released from a confining potential into the empty optical lattice. Our motivation to study such sudden expansions is two-fold: First, we want to extend the discussion of ballistic and diffusive dynamics from perturbations of a homogeneous background density to the case of a cloud of particles expanding into the vacuum. In the sudden

expansion all particles participate in the dynamics and thus the background density itself is time-dependent. Second, the sudden expansion into an empty optical lattice is gaining attention as an experimental technique to study the dynamical properties of the underlying model system using ultra-cold atomic gases [7]. Therefore we want to make to make exact predictions for further experiments and identify possibly interesting systems.

To this end, we use time-dependent DMRG to analyze the sudden expansion in three different setups: (i) A spin-balanced mixture of repulsively interacting fermions starting from the groundstate of the trap, repulsively interacting, (ii) spinless bosons starting from initial states with a fixed particle number per site and a finite defect density and (iii) a spin-imbalanced fermi gas in the presence of attractive interactions, again starting from the groundstate of the trap.

For similar purposes the time-dependent density profiles of two component Fermi gases have recently been simulated [203, 204, 205, 206] and also unveiled effects that are likely to influence further experiments. One example important in the following, is the so-called quantum distillation [204], a very fast process that mediates the spatial separation of pairs and single particles immediately after opening the trap. We will show that this process is also the dominant process behind the drastic changes in the momentum distribution our third setup, which are of high experimental relevance [95]. Another approach is taken for instance in Ref. [206], where the experimental setup of Ref. [7] was directly translated to one spatial dimension. Finally, the long-time limit of the sudden expansion can again be discussed in the context of thermalization, see, e.g., Ref. [205].

In the following we first introduce the physics that allow the trapping of atomic gases and the engineering of lattices and two-body interactions in Chap. 4.1.

In Chap. 4.2 we discuss the experiment performed in Ref. [7] in detail as it covers two aspects important for the following theoretical analysis. First, its experimental protocol realizes the expansion into the empty lattice in the absence of residual potentials, thus the experiment really studies the homogenous Hubbard model. Second, it relates the real-time dynamics of density profiles to the electronic transport properties of the Hubbard model in two and three spatial dimensions.

The possibility to study the expansion into a homogeneous empty lattice [7] and the possibility to study one-dimensional Fermi gases [95, 207, 208] serve as motivation for the following investigation of the sudden expansion of a two-component Fermi gas in Chap. 4.3. There we study the time evolution

of a spin-balanced mixture expanding, in the presence of repulsive interactions, from either a box trap or a harmonic trap. For the box trap, we find that the dynamics is ballistic in nature whenever the density in the initial state is smaller than one. The hallmark of ballistic transport we observe is a linear growth of the cloud's radius $R_n(t)$. We define the cloud radius as second moment of the fermion density which allows us to define the average expansion velocity via $R_n(t) = V_{\text{ex}}t$ in analogy to Chap. 3.6. Studying V_{ex} as a function of density n and on-site interaction U we find that the expansion velocity is determined by only a small subset of the initial conditions, namely density and energy of the initial state, over a wide range of parameters. Furthermore the expansion velocity is completely determined by symmetry in the Mott insulating phase ($n = 1$) and thus independent of U in that case. The qualitative dependence of V_{ex} on n and U is remarkably stable against the presence of a harmonic trap where the initial density is no longer homogeneous but can develop a shell structure depending on U and n [209]. In the presence of a Mott insulating shell in the trap we find the same clear signature in the expansion velocity as for the box trap, namely $V_{\text{ex}} = \sqrt{2}$ in units of hopping, as in the homogenous case. Therefore the expansion velocity could also serve as a probe to determine quantum phase transitions.

In Chap. 4.4 we perform a similar analysis for spinless bosons, but here we focus on the effect of defects in the initial state that could be present in a typical experimental setup. The expansion velocity is studied for initial states which are pure Fock states in real space, i.e., states with a well defined number of particles per site, each one localized on their respective site. We then introduce an admixture of defects, either holes, double occupied sites, or both and study the effect of such configurations on the expansion velocity and the time-dependent momentum distribution functions. For the expansion velocity we find that it could serve as a probe for the density of defects in the initial state. The investigation of time-dependent momentum distribution functions is motivated by the observation of dynamical quasi-condensation in the momentum distribution of bosonic Fock states and Mott insulators at large interactions [78, 79, 203, 80]. Our data suggests that the dynamical quasi-condensation is remarkable stable against the presence of defects.

Chapter 4.5 then revisits the Fermi-Hubbard model, studying the expansion of a spin-imbalanced mixture in the presence of attractive interactions. Attractive spin-imbalanced Fermi gases in one spatial dimension have been shown to exhibit the analogue of the famous Fulde-Ferrel-Larkin-Ochnikov (FFLO) phase [81, 82, 83, 84, 85, 86, 87]. The FFLO phase (see Ref. [88] for a review) has been originally proposed as a model fermionic pairing at

finite polarization [89, 90]. In such a situation, the Fermi surfaces of the two fermionic species mismatch. As a result the fermionic pairs acquire a finite center-of-mass momentum. A partially polarized phase of FFLO-type has been predicted for trapped one-dimensional Fermi gases [91, 92] and numerical data suggests clear signatures of the FFLO state in the momentum distribution functions and the spatial structure of the ground state [82, 87, 93]. Motivated by the recent experimental investigation of spin imbalanced Fermi gases in one spatial dimension [95], we study the time-dependent momentum distribution function of up-spins, down-spins and bound pairs during the the sudden expansion. We find that each momentum distribution function undergoes major changes only over a rather short time interval, until the cloud has expanded roughly by a factor of four. For very large times the momentum distributions become virtually time independent. A possible connection to the asymptotic limit of infinite expansion times and the integrability of the model is discussed based on the Bethe ansatz solution of this model [27].

4.1   Ultra-cold atomic gases in optical lattices

In the following we are going to review the two concepts that allow experimental access to strongly correlated lattice systems, namely optical lattices and Feshbach resonances, following the presentation in [21]. Both, the trapping of atoms and creating a periodic potential originate from the dipole force that the atoms experience in a laser field, which is detuned with respect to a resonance frequency ω_0 of the atom [210]. The dipole potential induced by a gaussian laser beam, propagating in the z-direction can be approximated by [21]:

$$V_{\mathrm{dip}}(r, z) \approx -V_0 \left\{ 1 - \left(2\frac{r}{\omega_0} \right)^2 - \left(\frac{z}{z_R} \right)^2 \right\}, \qquad (49)$$

where z_R is the Rayleigh length of the laser [21] and the trapping strength V_0 is proportional to the laser intensity. The simplest periodic potential can be introduced by overlapping two counter-propagating laser beams, which results in

$$V(r, z) = -V_0 e^{-2r^2/\omega^2(z)} \cdot \sin^2(kz) \qquad (50)$$

on top of the still present trapping potential. As the resulting dipole potential for two or three standing waves is simply the superposition, the resulting lattice can have the dimensionality of choice, allowing one to study either a three-dimensional cubic lattice, or arrays of one-dimensional tubes, in a two
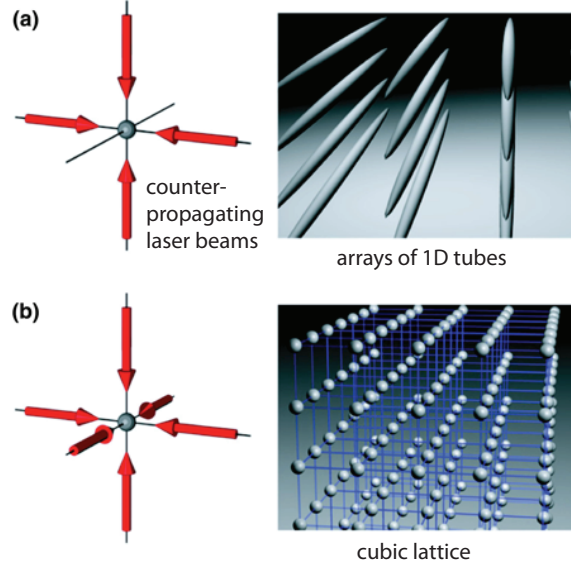
Figure 13: Illlustration of the concept of optical lattices generated by standing waves of laser light. Panel (a) sketches the formation of arrays of one-dimensional tubes using a two dimensional lattice. Panel (b) sketches the emulation of a three dimensional "crystal" of atoms in a three-dimensional optical lattice. Adapted from [21] with permission from the author.

dimensional lattice, as illustrated in Fig. 13. Assuming an infinite homogeneous lattice, the single-particle eigenstates are Bloch waves with quasi-momentum q whose energy in the lowest band and one spatial dimension is given by the dispersion dispersion [211]

$$\epsilon_0(q) = -2J\cos(qa)\,, \tag{51}$$

where a is the lattice constant. J is usually set to unity in theoretical calculations and serves as global energy scale. In optical lattices the energy for many applications scale is set by the recoil energy [21] $E_r = k/(2m)$, where k is the wave-vector of the laser light and m is the mass of the trapped atoms. In the limit of deep lattices $(V_0 >> E_r)$ one can approximate J by

$$J = \frac{4}{\sqrt{\pi}} E_r \left(\frac{V_0}{E_r}\right)^{3/4} e^{-2\left(\frac{V_0}{E_r}\right)^{1/2}}\,. \tag{52}$$

Switching to the Wannier basis, which describes particles localized around particular lattice sites, focussing on only the lowest Bloch band and introduc-

ing creation operators $a_r^\dagger$ which populate exactly the corresponding wannier mode ψ_r, one arrives at a lattice Hamiltonian of the following form [65]:

$$H_0 = \sum_{r,r'} -J_{r,r'}(a_r^\dagger a_{r'} + H.c.) \tag{53}$$

where the $J_{r,r'}$ are the tunneling matrix elements between lattice sites r and r'. Treating the trapping potential on the same footing gives

$$H = H_0 + V \sum_r (r - r_0)^2 a_r^\dagger a_r \tag{54}$$

where r_0 is the center of the trap.

The interactions usually assumed for experiments with ultra-cold atoms in optical lattices are two-body contact interactions [21]. The interaction between two different Wannier functions, which are centered around r and r' respectively, takes the form $U\delta_{r,r'}$, where $U/J = \sim \exp(\sqrt{V_0/E_r})$ [21]. This means that the interactions can be tuned via the lattice depth V_0, which has been used, e.g., to study the superfluid-to-Mott transition of the Bose-Hubbard Hamiltonian [64, 65].

An alternative way to include short ranged interactions is to consider that collisions between bosons or fermions with different spins in the low-energy limit are given by s-wave scattering which corresponds to a point-like potential $V = g\delta(r)$ where g is proportional to the scattering length a. The potential can be either repulsive ($a < 0$) or attractive ($a > 0$). A Feshbach resonance [212] is a divergency of the s-wave scattering length that occurs when the kinetic energy of two colliding atoms is equal to the energy of a bound state of those two atoms. Such a condition can be met in atom-atom scattering due to the different hyperfein states [199]. Phenomenologically, the scattering length around a Feshbach resonance can be parametrized as [21]

$$a(B) = a_0(1 - \frac{\Delta B}{B - B_0}), \tag{55}$$

where a_0 is the bare scattering length far away from the resonance, ΔB is the width of the resonance and B_0 the position of the resonance (see [213, 214, 215] for detailed reviews). Given those parameters, the on-site two-body interactions can be tuned independently of the lattice depth using a magnetic field.

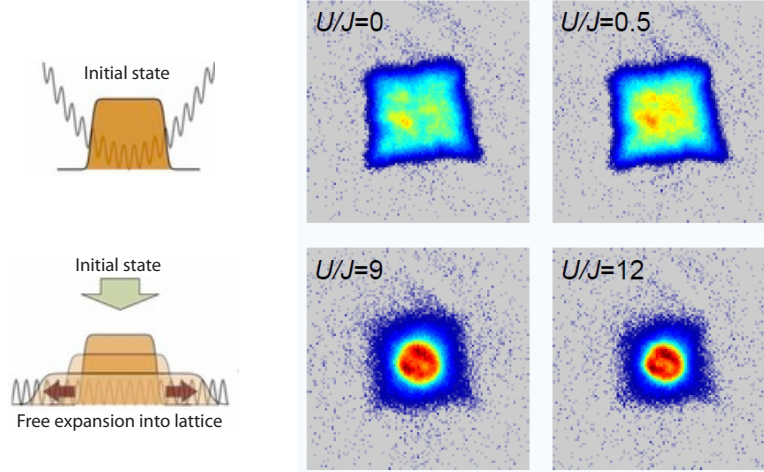Depending on the particles loaded into the lattice and upon including the

Figure 14: Expansion of a fermionic band insulator in two dimensions. Left: Sketches of the initial state (upper panel) and the expanding cloud (lower panel) with the respective shape of the optical lattice. Right: In-situ absorption images of the particle density in the expanding cloud after $25ms$. Adapted from [7] with permission from the author.

two-body term, Eq (53) becomes either the Bose-Hubbard model

$$H_0 = -J \sum_r [(b_r^\dagger b_{r+1} + H.c) + \frac{U}{2} n_r(n_r - 1)] , \qquad (56)$$

where $b_r^\dagger$ creates a boson on site r and $n_r = b_r^\dagger b_r$, or the Fermi Hubbard model

$$H_0 = -J \sum_{r,\sigma} (c_{r,\sigma}^\dagger c_{r+1,\sigma} + H.c) + \sum_r U n_{r,\uparrow} n_{r,\downarrow} , \qquad (57)$$

where $c_{r,\sigma}^\dagger$ creates a fermion with spin $\sigma = \uparrow, \downarrow$ on site r and $n_{r,\sigma} = c_{r,\sigma}^\dagger c_{r,\sigma}$ After detailing how ultra-cold atomic gases can emulate the Hubbard model we will now discuss a particular example of non-equilibrium dynamics relevant for the following numerical simulations.

4.2   Sudden expansion experiments and non-equilibrium transport

In the context of fermionic transport the sudden expansion experiment performed by Schneider *et al.* on two and three-dimensional Fermi gases of ^{40}K

atoms makes two very important points [7]: First, the expansion under the action of a homogeneous Hubbard hamiltonian is studied. This is important because previous experiments with similar setups [69, 70, 216] where carried out in the presence of residual external potentials due to the experimental protocols. Second, the experimental data obtained was discussed in great detail in the context of diffusive versus ballistic dynamics. In the following we are going to briefly summarize the experiment from Ref. [7]. Figure 14 shows sketches of the initial state and the expansion into the empty homogeneous lattice (upper and lower left panel respectively) as well the in-situ absorption images visualizing the local particle density after expanding for $25ms$ for various values of density density interactions (right panel). The experiment was performed with ^{40}K atoms loaded into an optical lattice with a harmonic confining potential in the absence of interactions. The loading sequence is chosen in such a way that the initial state is a band insulator with a thin metallic shell (upper left panel of Fig 14). The density is then frozen by ramping to a very deep lattice before the interactions are turned on using a Feshbach resonance. Finally the lattice lattice and the confining potential are ramped down in such a way that the result is an expansion into a homogenous empty lattice (lower left panel of Fig 14). The main feature is the sudden crossover from the square ballistic halo at $U = 0$ to the presence of a diffusive core at finite U. This feature is very well visible in the particle density imaged after $25ms$ (right panel of Fig 14). Furthermore, they find that already small values of interaction strength drastically reduce the expansion velocity extracted from the density profiles.

In the following we present our results for the sudden expansion in one spatial dimension for three different setups: (i) A spin-balanced two-component Fermi gas, starting from the groundstate of either a box or a harmonic trap, (ii) A bosonic Fock state in real space and (iii) a spin imbalanced Fermi gas, again starting from the ground-state of trapped gas.

4.3   Expansion velocity of a one-dimensional, two-component Fermi gas during the sudden expansion in the ballistic regime

The results of Schneider *et al.* discussed in Chap. 4.2 combined with the possibility of similar expansion experiments for one-dimensional Fermi gases was our motivation to carry over the analysis put forward in Chap. 3.7 to the sudden expansion scenario of Ref. [7]. Here we consider an initially trapped spin-balanced two-component Fermi gas, expanding into an empty lattice. The crucial difference to Chap 3.7 is that the setup changes from a wave-packet expanding on top of a stationary background density to the case where all particles participate in the dynamics, and as such all particles contribute to the average expansion velocity in the ballistic case.

In contrast to Schneider *et al.* we consider one spatial dimension and work with densities $n \leq 1$. We start from the groundstate of either a box or a harmonic trap and study the dynamics at different interaction strengths $U \geq 0$. As a main result we find that the expansion from a box trap is ballistic whenever $n \leq 1$ independently of U. This enables us to study the average expansion velocity as a function of interaction strength and density for the box trap and we find that it can be explained by a non-interacting thermal reference system, based on energy and particle number conservation, over a wide range of parameters. In these cases the expansion is completely characterized by a very small subset of the initial conditions. It follows that the main effect of interactions in the system is to raise the initial energy, and thus to also increase the expansion velocity. At $n = 1$ the groundstate of the box trap is a Mott insulator. In this case we find that the average expansion velocity is completely determined by symmetry and thus $V_{\mathrm{ex}} = \sqrt{2}J$ independently of the interaction strength. Replacing the box trap with a harmonic trap, and thus replacing the homogeneous density by a shell structure of different densities [209], we find that the qualitative dependence on the effective density and the interaction strength is robust against the presence of the harmonic trap. Most importantly the clear signature of the Mott insulator, namely $V_{\mathrm{ex}} = \sqrt{2}J$, is preserved which should be observable in future experiments. Hence, we conclude V_{ex} can also be a tool to detect quantum phase transitions in the initial states.

Expansion velocity of a one-dimensional, two-component Fermi gas during the sudden expansion in the ballistic regime

S. Langer,[1] M. J. A. Schuetz,[1,2] I. P. McCulloch,[3] U. Schollwöck,[1,4] and F. Heidrich-Meisner[1,4]

[1]*Department of Physics and Arnold Sommerfeld Center for Theoretical Physics, Ludwig-Maximilians-Universität München, D-80333 München, Germany*

[2]*Max-Planck-Institut für Quantenoptik, Hans-Kopfermann-Strasse 1, 85748 Garching, Germany*

[3]*Centre for Engineered Quantum Systems, School of Mathematics and Physics, The University of Queensland, St. Lucia, QLD 4072, Australia*

[4]*Kavli Institute for Theoretical Physics, Kohn Hall, University of California, Santa Barbara, California 93106, USA*

We show that in the sudden expansion of a spin-balanced, two-component Fermi gas into an empty optical lattice induced by releasing particles from a trap, over a wide parameter regime, the radius R_n of the particle cloud grows linearly in time. This allow us to define the expansion velocity V_{ex} from $R_n = V_{ex} t$. The goal of this work is to clarify the dependence of the expansion velocity on the initial conditions which we establish from time-dependent density matrix renormalization group simulations, both for a box trap and a harmonic trap. As a prominent result, the presence of a Mott-insulating region leaves clear fingerprints in the expansion velocity. Our predictions can be verified in experiments with ultracold atoms.

I. INTRODUCTION

Research into the nonequilibrium properties of strongly correlated many-body systems has emerged into a dynamic and active field, driven by the possibility to address questions such as thermalization [1,2], the properties of steady states, or state engineering in ultracold atomic gases [3]. While substantial theoretical attention has been devoted to quantum quenches in homogeneous systems [2], more recently, setups that give rise to finite particle or spin currents have been studied as well, both from the theoretical side [4–15] and in experiments (see, e.g., Refs. [16–21]). Using these approaches allows one to investigate transport properties of strongly correlated many-body systems—in and out of equilibrium—in cold atomic gases that are of great interest in condensed matter theory.

Our work is motivated by the experiment by Schneider *et al.* [17] who have studied the expansion of a two-component Fermi gas in an optical lattice in two and three dimensions (described by the Fermi-Hubbard model [22,23]), starting from an almost perfect band insulator. The qualitative interpretation of their results is that, besides a ballistically propagating halo of particles, at finite interaction strengths a core of diffusively expanding particles exists [17]. In the case of one-dimensional (1D) bulk systems relevant for condensed matter problems and on the level of linear response theory, ballistic dynamics of interacting particles can be traced back to the existence of nontrivial conservation laws [24]. For instance, the fact that the energy current is conserved for the 1D Heisenberg model renders its spin transport ballistic away from zero total magnetization [24–26], whereas at zero magnetization there exists a quasilocal quantity [27], which is conserved only for the infinite system, that gives rise to ballistic dynamics. While for the 1D Hubbard model, the understanding of its transport properties is by far less complete than for the Heisenberg chain, one might be tempted to expect similar quantities to play a role for the latter model as well [24].

A qualitative difference between the sudden expansion in an optical lattice compared to steady-state transport measurements in condensed matter systems is that, in the latter case, the background density determines transport coefficients, whereas in the former case, the density itself becomes time dependent [17] and *all* particles participate in the dynamics. As a consequence, in diffusive regimes, the dependence of the diffusion coefficient on density needs to be accounted for. In the ballistic case, as we shall see, the expansion velocity always depends on all momenta that are occupied in the initial state and not on just those close to the Fermi wave vector. Therefore, a parameter regime complementary to condensed matter systems can be accessed with cold atoms.

Theoretical results for the expansion of interacting bosons or fermions in optical lattices are mostly available for the 1D case, for which exact numerical methods give access to at least the short time dynamics via the adaptive time-dependent density matrix renormalization group (tDMRG) method [28–31] or exact diagonalization (ED) [4,5]. The richness of the nonequilibrium physics encountered in the expansion manifests itself in the observation of the dynamical emergence of coherence [4,8,11,32], which, for bosons, leads to the phenomenon of dynamical quasicondensation [4,11,32] and the intriguing phenomenon of the fermionization of the momentum distribution function (MDF) [5,15,33,34]. In the case of a two-component Fermi gas, the short-time dynamics of the MDF and correlation functions [8], the emergence of metastable states [9,10] and the time evolution of density profiles for specific initial conditions have been investigated [8,9,35–37].

In the present work we study the 1D Hubbard model and we concentrate on the sudden expansion starting from initial states that are Mott insulators (MI), that is, that have an integer filling of $n_{init} = 1$, Tomonaga-Luttinger (TL) liquids ($n_{init} < 1$), or systems in a harmonic trap. In the latter case, depending on filling and interaction strength, several phases may coexist in separate shells [38]. We analyze the dependence of the expanding cloud's radius $R_n(t)$ on time t and search for conditions to obtain ballistic dynamics, for which $R_n(t) = V_{ex} t$ is a necessary criterion. In that case, the expansion velocity V_{ex} is a well-defined quantity, and, as a

key result of our work, we clarify its dependence on the initial conditions.

Our main results are: (i) In the regime of low densities, that is, $n_{\text{init}} \leqslant 1$, we observe a linear growth of the cloud's radius with time, allowing us to define V_{ex}. (ii) In general, the expansion speed V_{ex} depends in a nonmonotonic way on the initial density. In the case of the expansion from a MI, $V_{\text{ex}} = \sqrt{2}J$, independently of U. (iii) Our findings are robust against the presence of a harmonic trap in the initial state.

Note that, in a generic system, one expects ballistic dynamics in the *long* time limit, where the gas becomes so dilute that interactions cease to matter. Here we show that ballistic dynamics sets in *immediately* after the gas is released from the trap when the density is actually still comparable to the initial density.

The structure of the paper is the following: In Sec. II we introduce the model and define the radius of the cloud. Section III discusses the expansion from a box trap, that is, starting from a homogeneous density. We first show that the dynamics is ballistic by analyzing the radius and the particle currents and second, we present a detailed analysis of the expansion velocity as a function of density and interaction strength. In Sec. IV we test our findings against the inhomogeneity introduced by a harmonic trap. We summarize our findings in Sec. V. In Appendix A we discuss the diffusion equation in one dimension. Appendix B contains a finite-size analysis of the expansion velocity for various cases.

II. MODEL AND SETUP

Our study is carried out for the 1D Hubbard model:

$$H_0 = -J \sum_{i=1,\sigma=\uparrow\downarrow}^{L-1} (c_{i+1,\sigma}^{\dagger} c_{i,\sigma} + \text{H.c.}) + U \sum_{i=1}^{L} n_{i,\uparrow} n_{i,\downarrow}. \quad (1)$$

$c_{i\sigma}^{\dagger}$ is a fermionic creation operator with spin $\sigma = \uparrow, \downarrow$ acting on site i, $n_{i\sigma} = c_{i\sigma}^{\dagger} c_{i\sigma}$, $n_i = \sum_{\sigma} n_{i\sigma}$, U is the onsite repulsion, and J is the hopping matrix element. Open boundary conditions are imposed, $L \gtrsim 100$ is the number of lattice sites, and N is the number of particles. We set $\hbar$ and the lattice spacing to unity and thus measure time, velocity, and particle current in the appropriate units in terms of the hopping matrix element.

We prepare initial states as the ground state of $H = H_0 + H_{\text{conf}}$ [8]. We consider two cases. First, the expansion from a box trap [i.e., $\langle n_i \rangle \neq 0$ for $i_1 < i \leqslant i_2$; $(i_2 - i_1) = L_{\text{init}}$, $n_{\text{init}} = N/L_{\text{init}}$] enforced by using $H_{\text{conf}} = \sum_i \epsilon_i n_i$ with a large $\epsilon_i \gtrsim U$ for $i \leqslant i_1$; $i_2 < i$ and zero otherwise. The second example is the expansion from a harmonic trap, for which $H_{\text{conf}} = V \sum_i (i - i_0)^2 n_i$. We turn off H_{conf} at $t = 0$. In our tDMRG runs, we use a Krylov-space based method [39,40], with time steps of $\delta t J = 0.25$ and we enforce a discarded weight of 10^{-4} or smaller.

The main quantity of interest is the radius of the particle cloud that we define via

$$R_n = \sqrt{\frac{1}{N} \sum_{i=1}^{L} \langle n_i \rangle (i - i_0)^2 - R_n^2(t=0)}. \quad (2)$$
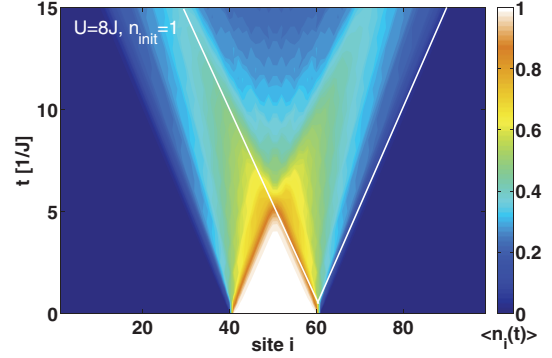
For the expansion from a box, $i_0 = L/2 + 0.5$.

FIG. 1. (Color online) Box trap: Typical contour plot of the density $\langle n_i(t) \rangle$ during the expansion from a MI ($U = 8J$, $n_{\text{init}} = 1$, $L_{\text{init}} = 20$). The slanted lines indicate the speed $2J$ at which the MI melts.

III. EXPANSION FROM A BOX TRAP

We first discuss this idealized case to avoid the complication of dealing with particles originating from different shells, as would be the case with a harmonic trap (note though, that box-like traps can also be generated in experiments [41,42]). A typical example for the time evolution of the density $\langle n_i(t) \rangle$ is shown in Fig. 1 for the expansion from a MI with $U = 8J$. The MI melts on a time scale of $t_{\text{melt}} \lesssim L_{\text{init}}/(2J)$, where $2J$ is the largest possible velocity in the empty lattice since the single-particle dispersion is $\epsilon_k = -2J \cos(k)$ [8]. For $t > t_{\text{melt}}$, two particle clouds form that propagate into opposite directions, visible as two intense jets (compare Refs. [4,5,36,43–45]).

In Fig. 2 we display the radius $R_n(t)$ at $U = 8J$ for various initial densities at $U = 8J$. Clearly, for $n_{\text{init}} \leqslant 1$, $R_n(t) = V_{\text{ex}} t$. We stress that $R_n(t) \sim t$ sets in immediately after the gas is released from the trap. This includes, in particular, the expansion from a MI at any U, while for $n_{\text{init}} > 1$, the radius deviates from $R_n(t) \sim t$ [9]. Based on the observation of $R_n(t) \sim t$ on short and intermediate times, when local densities are still large, together with the fact that *interacting* particles behave similar to noninteracting ones (which, in the absence
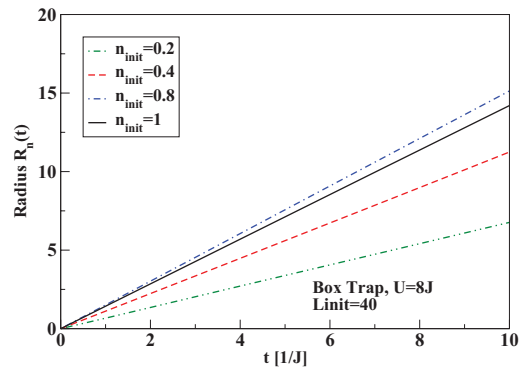

FIG. 2. (Color online) Box trap: Radius $R_n(t)$ for initial densities $n_{\text{init}} = 0.2, 0.4, 0.8, 1$ at $U = 8J$ and $L_{\text{init}} = 40$ (corresponding to $N = 8, 16, 32, 40$).
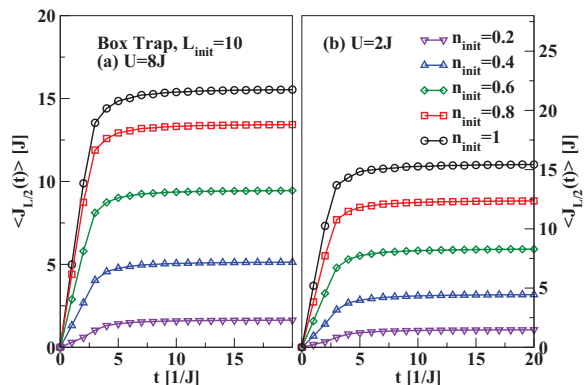
FIG. 3. (Color online) Box trap: Total particle current in each half of the system as a function of time, that is, $J_{L/2}(t) := \sum_{i>L/2} j_i$, for (a) $U = 8J$, (b) $U = 2J$, and $n_{init} = 0.2, 0.4, 0.6, 0.8, 1$. We observe that after some transient dynamics $\langle J_{L/2}(t) \rangle = $ const, supporting the observation of ballistic transport.

of disorder, expand with $R_n \sim t$), we classify the dynamics as ballistic.

In our situation, the notion of ballistic dynamics is strongly corroborated by analyzing the time dependence of the total particle current in each half of the system, $J_{L/2} = \sum_{i>L/2} j_i$ [$j_i = -iJ \sum_\sigma (c_{i+1\sigma}^\dagger c_{i\sigma} - \text{H.c.})$], which is shown for $U/J = 2, 8$ in Fig. 3. After the two jets in Fig. 1 are well separated from each other, $J_{L/2}$ takes a constant value, which we consider a hallmark feature of ballistic dynamics [45].

However, in one dimension, there is a subtlety as certain solutions of the diffusion equation can also give rise to a linear increase of the radius with time (if properly defined). Such a scenario happens in the dilute limit (which we do not study here), yet it results in a strong dependence of the expansion velocity on the total particle, which is clearly different from our case as we shall see below. Further details are given in Appendix A.

The observation of a linear increase of the cloud radius with time implies that V_{ex} should be fully determined by properties of the initial state, such as the MDF, energy per particle, or density. In the noninteracting case, this is obvious since V_{ex} can be calculated from the knowledge of the MDF. To guide the interpretation of the interacting case and to understand the dependence of V_{ex} on U and n_{init}, we next study the two exactly solvable limits $U = 0$ and $U = \infty$.

A. Box trap, V_{ex} at $U = 0$

At $U = 0$, opening the trap simply means that particles will propagate with a velocity $v_k = 2J \sin(k)$ with a probability given by the MDF n_k in the initial state, which is $n_k = (1/N) \sum_{l,m,\sigma} e^{-i(l-m)k} \langle c_{l\sigma}^\dagger c_{m\sigma} \rangle$. The momenta are chosen to match the open boundary conditions in the box, that is, $k = \frac{\pi l}{L_{init}+1}; l = 1, \ldots, L_{init}$. By a straightforward evaluation of $R_n^2(t)$ from Eq. (2) and using the time dependence of creation and annihilation operators, known exactly at $U = 0$, we obtain

V_{ex} as the average velocity of all particles in the initial state:

$$V_{ex}^2 = \frac{1}{N} \sum_k v_k^2 \, n_k \, . \tag{3}$$

In the $U = 0$ case, the initial MDF thus completely determines the expansion velocity. However, this is an over-complete set of constraints: For a very large N, where boundary conditions cease to matter, we can evaluate Eq. (3) analytically:

$$V_{ex}^2 = 2J^2 [k_F - \cos(k_F) \sin(k_F)]/k_F \, , \tag{4}$$

which yields the full dependence on the initial density at $U = 0$ through $k_F \propto n_{init}$ alone. We can interpret Eq. (4) in two ways: If $U = 0, k_F = \pi n_{init}/2$, whereas for $U = \infty, k_F = \pi n_{init}$. Using ED we have verified the validity of Eq. (4) by extracting V_{ex} from the time dependence of $R_n(t)$ for $N \sim 160$ (see Fig. 8 in Appendix B).

B. Box trap, V_{ex} at $U \neq 0$

In the interacting case we extract the expansion velocity V_{ex} from the tDMRG data (i.e., the slope of curves such as the ones shown in Fig. 2). The results for selected values of U are collected in the main panel of Fig. 4 (symbols). We emphasize four main observations: (i) For the expansion from the MI we obtain $V_{ex} = \sqrt{2}J$ at any $U > 0$. (ii) At a fixed density, V_{ex} increases monotonically with U. (iii) For $U > 4J$, the maximum of the expansion velocity is at an incommensurate density $0.5 < n_{init} < 1$. (iv) The expansion velocity is always very different from characteristic velocities of the initial state and much smaller than $2J$, the largest possible velocity. It is also much smaller than the charge velocity [46] at small densities and at $n_{init} = 1$, where the charge velocity drops to zero, V_{ex} remains finite.

At $U = 0$, the first observation is a consequence of particle-hole symmetry, reflected in the MDF: n_k is point symmetric about the point $(k_F = \pi/2, n_{k_F})$. Since $v_{k_F+\delta k_F}^2 = v_{k_F-\delta k_F}^2$, from Eq. (3), we conclude $V_{ex} = \sqrt{2}J$. The MDF at $U > 0$ has the same symmetry property, hence we expect a similar behavior, confirmed by tDMRG. Of course, Eq. (3) does not directly apply to the interacting case. Since the total energy
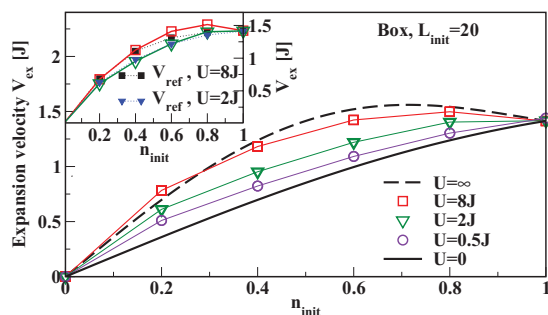

FIG. 4. (Color online) Box trap: Main panel: V_{ex} vs n_{init} at $U/J = 0, 0.5, 2, 8, \infty$ for $L_{init} = 20$ [see the legend, symbols are tDMRG, the solid and the dashed lines are derived from Eq. (4)]. Inset: V_{ex} from tDMRG (open squares: $U = 8J$, open triangles: $U = 2J$) vs V_{ref} (solid symbols) from noninteracting reference systems at a finite temperature (see Sec. III C for details).

$E_U = \langle H_0 \rangle$ is conserved, for $U > 0$, Eq. (3) is incompatible with this initial condition set by $U > 0$ and n_{init}. However, we shall see that the observation of $V_{\text{ex}} = \sqrt{2}J$ for $U > 0$ can also be understood as a consequence of symmetry properties.

We can further use the exact result Eq. (4) to explain the observations (ii)–(iv). The $U = 0$ and $U = \infty$ result are the solid and the dashed lines in the main panel of Fig. 4, respectively, and therefore, increasing U from $U = 0$ to $U = \infty$ at a fixed density simply takes us from the limit of a noninteracting *two-component* Fermi gas to the limit of noninteracting *spinless* fermions. To understand that the maximum of V_{ex} is at an incommensurate n_{init} for $U > 4J$, one needs to take into account that on the one hand, in a 1D cosine band, the maximum velocity is at $k = \pi/2$, but on the other hand, the density of states takes its minimum there. As a consequence of this competition, that is, the decrease of v_k vs the increase of the density of states as one moves away from $\pi/2$, the largest expansion velocity is at $n_{\text{init}} \neq 1$. Finally, property (iv) is a consequence of *all* particles propagating and not just those with momenta close to k_F.

On a technical note, we have checked the dependence of V_{ex} on particle number, keeping $n_{\text{init}} = N/L_{\text{init}}$ fixed. Finite-size effects are the largest at small initial densities, yet for densities $n_{\text{init}} \gtrsim 0.5$, our tDMRG results obtained with $L_{\text{init}} = 40$ show little quantitative differences compared to smaller L_{init} and V_{ex} becomes *independent* of N as shown in Appendix B.

C. Reference systems

It is now a compelling question to ask how many constraints suffice to determine the expansion velocity. From the solution of the noninteracting case, we conclude that density and energy are relevant quantities. To check this conjecture for the interacting case, we construct noninteracting reference systems that are at a *finite* temperature [47]. The temperature is chosen such that the reference system has the same energy as the interacting system and the same particle number, and it lives in the same box potential of length L_{init}.

Hence we solve this set of equations:

$$N = \sum_{k,\sigma} f(\epsilon_k - \mu, T),$$ (5)

$$E_U = \sum_{k,\sigma} \epsilon_k f(\epsilon_k - \mu, T),$$ (6)

$$V_{\text{ref}}^2 = \frac{1}{N} \sum_{k,\sigma} v_k^2 f(\epsilon_k - \mu, T),$$ (7)

where $f(x, T)$ is the Fermi function. We proceed as illustrated in Fig. 5. For a given U and N we compute the total energy E_U in the initial state with DMRG. First, we find the chemical potential $\mu = \mu(T)$ from Eq. (5), which only depends on N. Using this $\mu(T)$ curve, we determine the pair of (μ, T), for which we get the right energy E_U. From these results, Eq. (7) yields the expansion velocity V_{ref} of the reference system. Obviously the maximum velocity that these reference systems, which have the dispersion $\epsilon_k = -2J \cos(k)$ of the empty lattice, can produce is $V_{\text{ref}} = \sqrt{2}J$ at any density $n_{\text{init}} \leqslant 1$ as $T \to \infty$. Within that constraint, the agreement between
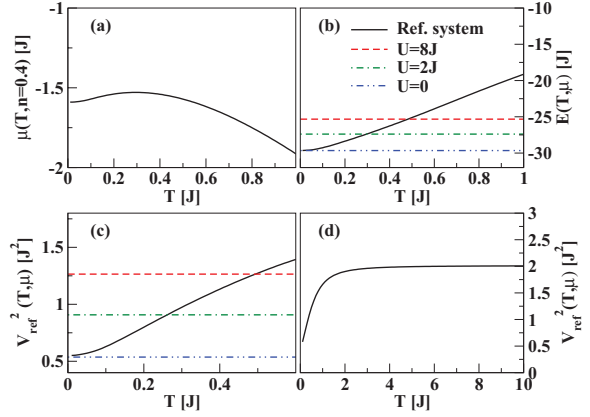

FIG. 5. (Color online) These plots illustrate how the noninteracting reference systems are constructed using Eqs. (5)–(7) for the example of $n_{\text{init}} = 0.4$ for (a)–(c) $L_{\text{init}} = 40$ and (d) $L_{\text{init}} = 160$. (a) Temperature dependence of the chemical potential at fixed $n_{\text{init}} = 0.4$. (b) Total energy from Eq. (6) as a function of temperature. (c) V_{ref}^2 as a function of temperature. The horizontal lines in (b) are DMRG results for E_U for the initial states used in the expansion at zero temperature for $U = 0, 2J, 8J$, while in (c) they mark the resulting $V_{\text{ref}}^2 = V_{\text{ref}}^2(E, n)$. (d) As T increases, $V_{\text{ref}}^2 \to 2J^2$ from below, that is, this is the largest expansion velocity that the reference systems can produce for $n_{\text{init}} \leqslant 1$.

V_{ex} and our reference systems is excellent, as we illustrate for $U/J = 2$ and 8 in the inset of Fig. 4. Apart from those densities for which, at $U = 8J$, $V_{\text{ex}} > \sqrt{2}J$, $V_{\text{ref}} \approx V_{\text{ex}}$ within our numerical accuracy. In the particular case of $n_{\text{init}} = 1$, our reference systems also yield $V_{\text{ref}} = \sqrt{2}J$ independently of E_U, consistent with the tDMRG results of Fig. 4. This is a consequence of the aforementioned symmetry property of the MDF, which also applies to $T > 0$.

IV. EXPANSION FROM A HARMONIC TRAP

Our results so far establish a relation between properties of the initial state and the expansion velocity that could be probed in experiments. We next test the robustness of our predictions for $V_{\text{ex}} = V_{\text{ex}}(U, n_{\text{init}})$ against the inhomogeneity induced by a harmonic potential.

We focus on three types of initial states: (i) Only a TL, that is, $\langle n_i \rangle < 1$ in the entire trap, (ii) a MI shell in the center, surrounded by TL wings, and (iii) a three-shell structure with an incommensurate density in the center $\langle n_i \rangle > 1$, surrounded by first, a MI shell and second, a TL shell with $\langle n_i \rangle < 1$. For a given $U > 0$, these regimes are separated by critical characteristic densities ρ_1 and ρ_2, where $\rho = N\sqrt{V/J}$ is the effective density in a system with a harmonic trap [3,38].

For all three cases, $R_n(t)$ is shown in Fig. 6 for $U/J = 2$ and 8. We observe that, after releasing the particles from the harmonic trap, the cloud still expands with $R_n(t) \sim t$ in cases (i) and (ii), that is, $R_n(t) \sim t$ [see Figs. 6(a) and 6(b)], whereas in case (iii) the increase of the radius is slower than linear in t [see Figs. 6(c) and 6(d)]. In that regime and for $U > 4J$, the
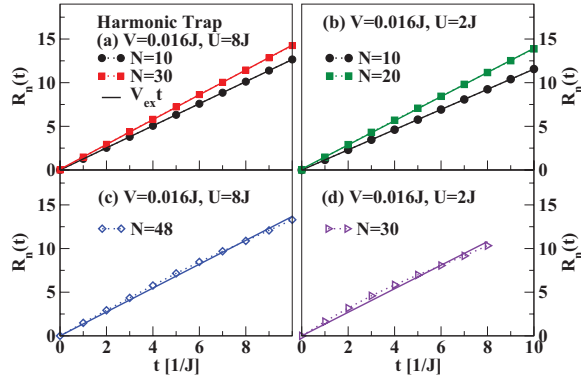
FIG. 6. (Color online) Harmonic trap: Radius of the particle cloud
for the expansion from a harmonic trap for (a) $N = 10, 30$ at $U = 8J$,
(b) $N = 10, 20$ at $U = 2J$, (c) $N = 48$ at $U = 8J$, and (d) $N = 30$
at $U = 2J$. For $U = 8J$, these parameters correspond to the initial
states shown in the insets of Fig. 7. The solid lines are fits to the
data, dotted lines are guides to the eye. We find $R_n(t) \nsim t$ whenever
densities in the center of the trap are larger than one and $R_n(t) \sim t$
otherwise.

system can be viewed as a mixture of single atoms propagating
with velocities $v_k \sim J$ and two fermions repulsively bound
into a doublon, which, due to energy conservation, does not
decay on time scales $\propto 1/J$ and is much slower with typical
velocities $v_k^d \sim J^2/U$ [9,16]. For illustration, the values of ρ_1
and ρ_2 as well as typical density profiles are included in Fig. 7
for $U = 8J$ (vertical lines and lower insets, respectively). As
is evident from Fig. 7, the overall dependence of $V_{ex} = V_{ex}(\rho)$
resembles that of the expansion from a box trap, with a
maximum in V_{ex} emerging as $U \gtrsim 4J$. Most importantly, as
soon as the MI forms in the center of the trap, indicated by the
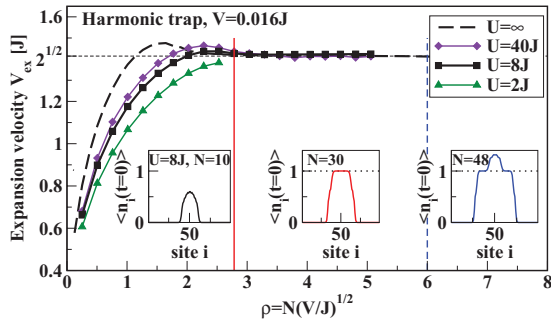vertical solid line at $\rho = \rho_1$, the expansion velocity approaches

a constant value at $V_{ex} \gtrsim \sqrt{2}J$ from above. The contribution
to V_{ex} of low-density shells surrounding the MI is suppressed
by increasing U or ρ since both favor a large relative fraction
of all particles in the MI shell to minimize the contribution
from the interaction energy. In contrast to the expansion from
the box, the limit of $U = \infty$ (dashed line) is approached very
slowly since the shell structure in a trap depends strongly on
U and ρ.

V. SUMMARY

We studied the sudden expansion of a spin-balanced two-
component gas in 1D, released from a trap. Our main results
are twofold: First, the cloud expands ballistically as long as
initial densities are small, including, in particular, the MI
state. Second, the expansion velocity, defined through $R_n(t) = V_{ex}t$
strongly depends on initial density and thus its measurement
can provide information on the initial state. For instance,
deviations from our predictions could indicate the presence
of defects in the initial state preparations. Our quantitative
predictions can be tested in an experiment that realizes the
setup of Ref. [17] in 1D.

Furthermore, it would be interesting to study the radius
of an expanding cloud and the expansion velocity for other
experimentally relevant systems such as the Bose-Hubbard
model or spin imbalanced mixtures. While we have presented
phenomenological evidence for ballistic dynamics, we have
here not touched upon a potential relation with integrability
and nontrivial conservation laws [24], leaving this for future
research. It also remains as an open question to identify
interacting models in one dimension and parameter regimes
in which diffusive dynamics dominates during the sudden
expansion, which might be challenging since even noninte-
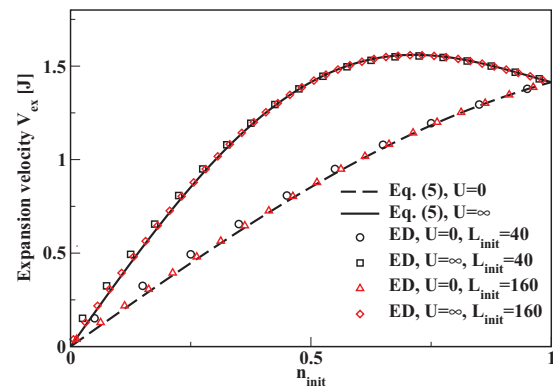grable models may have very large conductivities (see, e.g.,
Ref. [26]).

FIG. 7. (Color online) Harmonic trap: V_{ex} vs ρ ($U/J =
2, 8, 40, \infty$, $V = 0.016J$). The vertical solid line marks the forma-
tion of a MI shell in the trapped system at ρ_1 and the vertical dashed
line the formation of a core with $\langle n_i \rangle > 1$ at ρ_2, both for $U = 8J$.
The horizontal line is $V_{ex} = \sqrt{2}J$. Symbols are tDMRG results, the
dashed line was obtained from ED. We have verified that the results
are remarkably stable against changes in the particle number at fixed
ρ by producing the $V_{ex} = V_{ex}(\rho)$ curve at a different V (see Fig. 10
in Appendix B). Lower insets: typical initial density profiles in the
regimes $\rho < \rho_1$, $\rho_1 < \rho < \rho_2$, and $\rho_2 < \rho$ for $U = 8J$.

FIG. 8. (Color online) Box trap: Comparison between the exact
result for V_{ex} [Eq. (4) of the main text, valid in the limit of large
particle numbers] and exact diagonalization in the limits $U = 0$ and
$U = \infty$. ED data are shown for $L_{init} = 40$ and $L_{init} = 160$. In the
latter case we find very good agreement between the analytical result
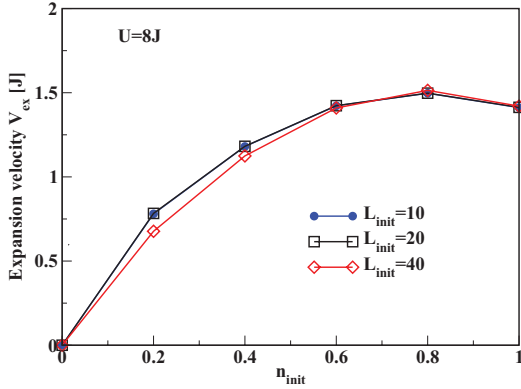(lines) and the ED data (symbols) for all densities.

FIG. 9. (Color online) Box trap: Expansion velocity as a function of initial density for $U = 8J$ and different $L_{init} = 10, 20, 40$. For $n_{init} \gtrsim 0.6$, finite-size effects are remarkably small.
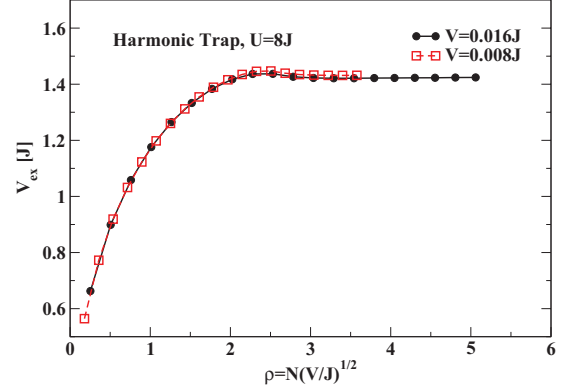

FIG. 10. (Color online) Harmonic trap: Expansion velocity for $V = 0.008J$ and $V = 0.016J$ as a function of effective density $\rho = N \cdot \sqrt{V/J}$ for $U = 8J$. The expansion velocity is remarkably stable against changing the particle number at fixed ρ.

APPENDIX A: LINEAR INCREASE OF THE RADIUS FROM A NONLINEAR DIFFUSION EQUATION

Here we discuss solutions of the diffusion equation in one dimension in the limit of a very dilute gas. Since the sudden expansion scenario considered in this paper involves the propagation of all particles, the dependence of the diffusion constant D on the local density $n(x,t)$ becomes relevant, and as a consequence, the relevant diffusion equation is in general a nonlinear one (see, e.g., [17]). Focusing on the very dilute limit we use $D \sim 1/n(x,t)$ (see the discussion in Refs. [17,48]). The resulting diffusion equation (after rescaling of the time variable)

$$\partial_t n(x,t) = \partial_x \frac{1}{n} \partial_x n \qquad (8)$$

has a self-similar solution with particle number conservation in 1D [49]:

$$n(x,t) = \frac{2t}{x^2 + v^2 t^2} . \qquad (9)$$

First of all, one realizes that our definition of the radius $R_n(t)$ [Eq. (2)] cannot be used here. In the analysis of experimental data, it is common practice to define the radius as the half-width at half-maximum of the expanding cloud [17]. Using this definition, the solution Eq. (9) yields indeed $R_n(t) = vt$, similar to the ballistic dynamics discussed in our work.

We would like to stress, though, that the sudden expansion described in the main text is genuinely different in some important respects. First, Eq. (8) is only valid in the dilute limit while the time-dependent DMRG gives us access to short and intermediate time scales only where the gas is not necessarily a dilute one yet. Second, Eq. (9) is a solution for which the expansion velocity v depends strongly on the particle number via $N = \int_{-\infty}^{\infty} n(x,t)dx = 2\pi/v$, which is not observed in our case (compare Figs. 4 and 9). Based on these differences, we conclude that diffusive dynamics is very unlikely to be realized for the 1D Hubbard model in the sudden expansion.

APPENDIX B: FINITE-SIZE EFFECTS

Here we address the question of how our results for the expansion velocity depend on the overall particle number at a fixed density n_{init}. First, we consider the box trap and we compare our analytical result for large N [Eq. (3)] to exact diagonalization in the noninteracting limits in Fig. 8. For $N = 40$ we find good qualitative agreement with small finite-size effects, which are the most pronounced for $n_{init} < 0.5$. For $N = 160$, the deviations between the analytical expression for $N \to \infty$ and data for a finite N are already barely visible except for very low densities. Second, we study the interacting system expanding from different box traps with $L_{init} = 10, 20, 40$ at a fixed density for $U = 8J$. Figure 9 shows V_{ex} as a function of density. As in the noninteracting case finite-size effects are remarkably small whenever $n_{init} \geq 0.6$ even for the smaller particle numbers.

Finally, we turn to the expansion from a harmonic trap and analyze V_{ex} for two different trapping potentials, $V = 0.008J$ and $V = 0.016J$. Figure 10 shows V_{ex} as a function of effective density $\rho = N\sqrt{V/J}$. We find that the expansion velocity is very robust against changing the particle number at a fixed ρ. Overall, our results for the expansion velocity exhibit only minor finite-size effects in all studied cases.

[1] M. Rigol, V. Dunjko, and M. Olshanii, Nature (London) **452**, 854 (2008).

[2] A. Polkovnikov, K. Sengupta, A. Silva, and M. Vengalattore, Rev. Mod. Phys. **83**, 863 (2011).

[3] I. Bloch, J. Dalibard, and W. Zwerger, Rev. Mod. Phys. **80**, 885 (2008).

[4] M. Rigol and A. Muramatsu, Phys. Rev. Lett. **93**, 230404 (2004).

[5] M. Rigol and A. Muramatsu, Phys. Rev. Lett. **94**, 240403 (2005).

[6] A. Rosch, D. Rasch, B. Binz, and M. Vojta, Phys. Rev. Lett. **101**, 265301 (2008).

[7] S. Mandt, A. Rapp, and A. Rosch, Phys. Rev. Lett. **106**, 250602 (2011).

[8] F. Heidrich-Meisner, M. Rigol, A. Muramatsu, A. E. Feiguin, and E. Dagotto, Phys. Rev. A **78**, 013620 (2008).

[9] F. Heidrich-Meisner, S. R. Manmana, M. Rigol, A. Muramatsu, A. E. Feiguin, and E. Dagotto, Phys. Rev. A **80**, 041603(R) (2009).

[10] For bosons, see: D. Muth, D. Petrosyan, and M. Fleischhauer, Phys. Rev. A **85**, 013615 (2012).

[11] I. Hen and M. Rigol, Phys. Rev. Lett. **105**, 180401 (2010).

[12] M. Jreissaty, J. Carrasquilla, F. A. Wolf, and M. Rigol, Phys. Rev. A **84**, 043610 (2011).

[13] E. Lundh, Phys. Rev. A **84**, 033603 (2011).

[14] A. del Campo and J. G. Muga, Europhys. Lett. **74**, 965 (2006).

[15] A. del Campo, Phys. Rev. A **78**, 045602 (2008).

[16] T. Kinoshita, T. Wenger, and S. D. Weiss, Nature (London) **440**, 900 (2006).

[17] U. Schneider, L. Hackermüller, J. P. Ronzheimer, S. Will, S. Braun, T. Best, I. Bloch, E. Demler, S. Mandt, D. Rasch, and A. Rosch, Nat. Phys. **8**, 213 (2012).

[18] P. Medley, D. M. Weld, H. Miyake, D. E. Pritchard, and W. Ketterle, Phys. Rev. Lett. **106**, 195301 (2011).

[19] J. A. Joseph, J. E. Thomas, M. Kulkarni, and A. G. Abanov, Phys. Rev. Lett. **106**, 150401 (2011).

[20] T. Anker, M. Albiez, R. Gati, S. Hunsmann, B. Eiermann, A. Trombettoni, and M. K. Oberthaler, Phys. Rev. Lett. **94**, 020403 (2005).

[21] A. Sommer, M. Ku, G. Roati, and M. W. Zwierlein, Nature (London) **472**, 102 (2011).

[22] U. Schneider, L. Hackermüller, S. Will, T. Best, I. Bloch, T. A. Costi, R. W. Helmes, D. Rasch, and A. Rosch, Science **322**, 1520 (2008).

[23] R. Jördens, N. Strohmaier, K. Günter, H. Moritz, and T. Esslinger, Nature (London) **455**, 204 (2008).

[24] X. Zotos, F. Naef, and P. Prelovšek, Phys. Rev. B **55**, 11029 (1997).

[25] See, e.g., F. Heidrich-Meisner, A. Honecker, and W. Brenig, Eur. Phys. J Spec. Topics **151**, 135 (2007); C. Karrasch, J. H. Bardarson, and J. E. Moore, e-print arXiv:1111.4508, and further references cited therein.

[26] A. Rosch and N. Andrei, Phys. Rev. Lett. **85**, 1092 (2000).

[27] T. Prosen, Phys. Rev. Lett. **106**, 217206 (2011).

[28] A. Daley, C. Kollath, U. Schollwöck, and G. Vidal, J. Stat. Mech.: Theory Exp. (2004) P04005.

[29] S. R. White and A. E. Feiguin, Phys. Rev. Lett. **93**, 076401 (2004).

[30] U. Schollwöck, Ann. Phys. (NY) **326**, 96 (2011).

[31] U. Schollwöck, Rev. Mod. Phys. **77**, 259 (2005).

[32] K. Rodriguez, S. Manmana, M. Rigol, R. Noack, and A. Muramatsu, New J. Phys. **8**, 169 (2006).

[33] A. Minguzzi and D. M. Gangardt, Phys. Rev. Lett. **94**, 240404 (2005).

[34] V. Gritsev, P. Barmettler, and E. Demler, New J. Phys. **12**, 113005 (2010).

[35] D. Karlsson, C. Verdozzi, M. Odashima, and K. Capelle, Europhys. Lett. **93**, 23003 (2011).

[36] J. Kajala, F. Massel, and P. Törmä, Phys. Rev. Lett. **106**, 206401 (2011).

[37] J. Kajala, F. Massel, and P. Törmä, Phys. Rev. A **84**, 041601(R) (2011).

[38] M. Rigol and A. Muramatsu, Phys. Rev. A **69**, 053612 (2004).

[39] T. Park and J. Light, J. Chem. Phys. **85**, 5870 (1986).

[40] M. Hochbruck and C. Lubich, SIAM J. Numer. Anal. **34**, 1911 (1997).

[41] A. Ashkin, PNAS **17**, 12108 (2004).

[42] T. P. Meyrath, F. Schreck, J. L. Hanssen, C.-S. Chuu, and M. G. Raizen, Phys. Rev. A **71**, 041604(R) (2005).

[43] M. Polini and G. Vignale, Phys. Rev. Lett. **98**, 266403 (2007).

[44] S. Langer, F. Heidrich-Meisner, J. Gemmer, I. P. McCulloch, and U. Schollwöck, Phys. Rev. B **79**, 214409 (2009).

[45] S. Langer, M. Heyl, I. P. McCulloch, and F. Heidrich-Meisner, Phys. Rev. B **84**, 205115 (2011).

[46] T. Giamarchi, *Quantum Physics in One Dimension* (Clarendon, Oxford, 2004).

[47] A. Rosch (private communication).

[48] The one dimensional case is discussed in the e-print version arXiv:1005.3545v1 of Ref. 11.

[49] J. L. Vázquez, *Smoothing and Decay Estimates for Nonlinear Diffusion Equations* (Oxford University Press, Oxford, 2006).

4.4 Sudden expansion of a one-dimensional Bose gas in the presence of defects

After the discussion of the two-component Fermi gas it is an intriguing question what a similar expansion setup would yield for bosonic particles. For the sudden expansion of bosons the dynamical emergence of coherence in the form of a dynamical quasi-condensation at finite momenta has been reported for both, the expansion of hardcore ($U \to \infty$) bosons [78] and the expansion from a bosonic Mott insulators in the presence of strong repulsive interactions [79]. This phenomenon consist of dynamically developing quasi-long range correlations emerging during the sudden expansion of the bosonic gas. As a signature, the time-dependent momentum distribution function of the bose gas develops sharp peaks at two distinct momenta. In the case of hardcore bosons, these momenta are given by $k = \pm\pi/2a$, where a is the lattice spacing [78]. The value can be explained taking into account global energy conservation: Since the initial Fock state of hardcore bosons has a total energy of zero, energy conservation requires that if a quasi-condensate or Bose-Einstein condensate to forms, it should form at points with zero average kinetic energy. Given the dispersion relation of the hardcore bosons

$$\epsilon_k = -2J\cos(k)\,, \tag{58}$$

and setting the lattice spacing to unity, such points are given by $k = \pm\pi/2a$. While a Fock state of hardcore bosons is completely uncorrelated, the Mott insulating state has exponentially decaying correlations. Yet, the qualitative features of the dynamical quasi-condensation are also found in the latter case, studying softcore bosons at large repulsive interactions. The precise position of the peaks in the momentum distribution functions has been shown to have a weak U-dependence by time-dependent DMRG simulations [79].

Here we revisit both, hardcore and repulsively interacting softcore bosons, to study the expansion velocity in the same manner as in Chap. 4.3, namely by calculating the cloud radius via

$$R_n = \sqrt{\frac{1}{N}\sum_{i=1}^{L}\langle n_i\rangle(i-i_0)^2 - R_n^2(t=0)}\,. \tag{59}$$

where i_0 is the center of the trap. Furthermore, we investigate the time-dependent momentum distribution function to determine whether or not it indicates dynamical quasi-condensation:

$$n_k(t) = \frac{1}{L} \sum_{l,m} e^{i(l-m)k} \langle b_l^\dagger(t) b_m(t) \rangle \,. \tag{60}$$

The initial states considered in the following are pure Fock states in real space, i.e., states that are generated by applying a string of creation operators to the vacuum

$$|\psi\rangle = \prod_{\{r_i\}} b_{r_i}^\dagger |0\rangle \,. \tag{61}$$

The motivation to study states given by Eq. (61) comes from two aspects: First, the effect of dynamical quasi-condensation at finite momenta in interacting systems is larger for pure Fock states, as each particle is localized and thus the state is completely uncorrelated and. Furthermore all momentum Eigenstates of the initial trap are equally populated. Hence, the change in both, the structure of correlations and the momentum distributions is more drastic starting from a Fock state. Second, an experimental protocol to observe the dynamical quasi-condensation may be chosen similar to the one described in Chap. 4.2, namely using a ramp of the optical lattice that effectively "freezes" the density distribution [217]. In that case, the initial state will be a Fock state in real-space and, depending on the two-body interactions during the preparation, is prone to have defects in the form of empty or doubly occupied lattice sites. In the following, we first present our results for the exact time evolution of hardcore bosons and then discuss preliminary results for the interacting case, restricted to small systems and a number of bosons per site of three.

4.4.1   Hardcore Bosons

For simplicity we start with hardcore bosons described by

$$H_0 = -J \sum_i (b_{i+1}^\dagger b_i + H.c.) \,, \tag{62}$$

with a hardcore constraint $(b_i^\dagger)^2 = 0$. This Hamiltonian can be exactly mapped to free spinless fermions via the Jordan-Wigner transformation allowing for full diagonalization of very large systems, see, e.g., Ref. [218]. The results for the hardcore bosons are summarized in Fig. 4.3 and 16. The panel (a) of Fig 4.3 shows the initial density profiles. Since in the hardcore limit, there are no double occupancies, we restrict the discussion to a number I of holes in the initial state. Panel (b) of Fig. 4.3 shows an exemplary result
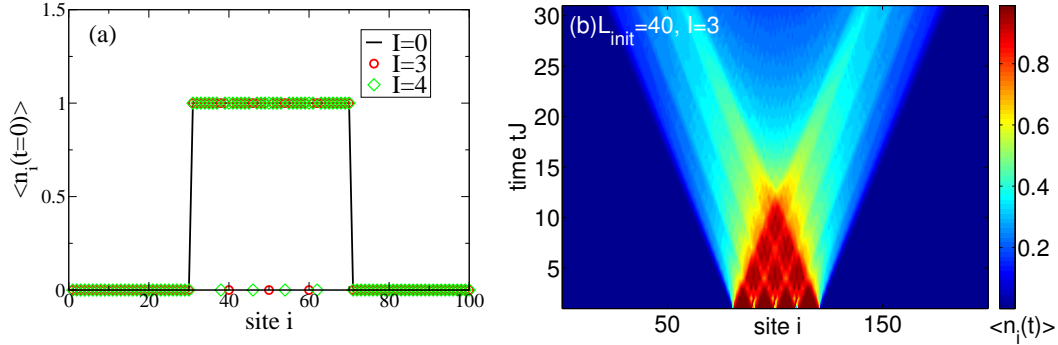
Figure 15: Real-time evolution of hardcore bosons starting from a Fock state with $L_{\mathrm{init}} = 40$, $N = L_{\mathrm{init}} - I$ particles and I defects. (a) Initial particle density at $t = 0$ for $I = 0, 3, 7$. (b) Time-dependent particle density for $I = 3$. The initial state melts at a velocity of $2J$ which defines a "light cone" for the dynamics. The dynamics of the impurities in the center of the trap does not influence V_{ex} (see Fig 16).

of the time evolution, namely for $I = 3$. Since this is a non-interacting system, the dynamics is those of free particles. Mapping Eq. (62) to spinless fermions, one obtains the usual dispersion relation of the tight binding chain, namely Eq. (58). The velocity of a particle with momentum k is given by the derivative of Eq. (58) and thus

$$v_k = 2J\sin(k)\,. \tag{63}$$

This implies that the maximum velocity cannot exceed $2J$ which defines the light cone like structure formed by the boundaries of the cloud in the panel (b) of Fig 4.3. Furthermore, for the non-interacting system, the average velocity has to be fully determined by the momentum distribution in the initial state, namely

$$V_{\mathrm{ex}}^2 = 4J^2 \sum_k \sin^2(k)n_k\,. \tag{64}$$

For a pure Fock state in real space, the initial momentum distribution is flat, therefore $V_{ex} = \sqrt{2}2J$. This is confirmed by calculating the radius $R_n(t)$ for clouds of hardcore bosons with different defect numbers I in panel (a) of Fig 16. The curves coincide perfectly for any I studied. Panel (b) of Fig 16 addresses the dynamical quasi-condensation at finite momenta in
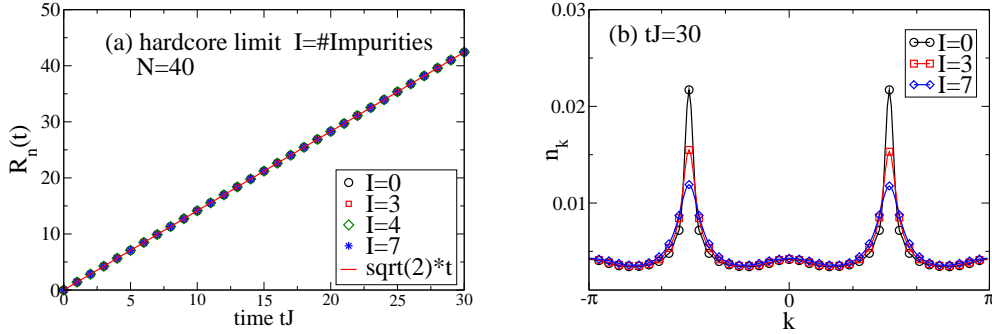
Figure 16: (a) Time-dependent radius of the cloud for different defect concentrations. Independently of the defect concentration the cloud expands with an average expansion velocity of $V_{\mathrm{ex}} = \sqrt{2}J$ as obtained from a linear fit (solid line). (b) Momentum distribution of hardcore bosons at time $tJ = 30$ for $I = 0, 3, 7$. While all defect densities considered still show a clear signature of quasi-condensates at finite momenta, the peaks are less pronounced for larger I.

the presence of defects. We plot the momentum distribution of the hardcore bosons after expanding for $tJ = 30$. Comparing the clean Fock state with $I = 3$ and $I = 7$ we find that only the peak height is affected and scales as $1/\sqrt{N_I}$, where N_I is the number of particles between two defects. Thus, we conclude that the expansion velocity for the sudden expansion from a Fock state and the qualitative notion of dynamical quasi-condensation at finite momenta are not affected by the presence of holes in the case of hardcore bosons.

4.4.2 Expansion velocity for Bosonic Fock states with repulsive interactions

Next we move on to the Bose-Hubbard model with repulsive interactions. To simulate the time-evolution of the interacting system we employ the Krylov subspace approach discussed in Chap. 2.3 with a time step of $\delta t = 0.0625/J$ and keep the discarded weight below 10^{-4}. In addition, the simulation of bosonic dynamics often requires an additional truncation in the local physical dimension. While in principle all bosons can occupy a single lattice site this situation is strongly suppressed by the repulsive interactions. Hence the unfavorable original physical dimension $d = N$, can be replaced by a
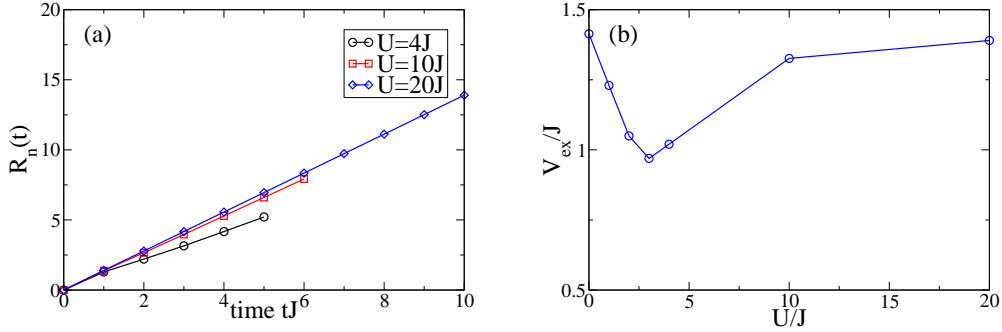
Figure 17: (a) Radius $R_n(t)$ as a function of time for the sudden expansion from a clean $n = 1$ Fock state and different repulsive interactions $U/J = 4, 10, 20$. (b) Preliminary result for the average expansion velocity obtained via a linear fit to $R_n(t)$ for the clean Fock states as a function of interaction U.

more practical number. In line with the previous literature [79], we restrict the number bosons per lattice site to three. It is reasonable that multiply occupied site are more probable in the groundstate than during the dynamics induced by expanding from a Fock state with $\langle n_i \rangle = 1$ for every occupied site. Hence, as a first check, we calculate the ground state of a initial box of $L = 10$ lattice sites at density $n = 1$, which corresponds to the particle number also used to simulate the sudden expansion from the Fock states in the following. For instance, we find $\langle (b_i^\dagger)^4 b_i^4 4 \rangle \leq 10^{-5}$ for $U \geq 10J$. For $U = 4J$, $\langle (b_i^\dagger)^4 b_i^4 \rangle \sim 10^{-3}$, which is still reasonable but indicates that calculations for $U \leq 4J$ have to be repeated with larger d. Also note that all results for the interacting systems are preliminary in the sense that the dependence on the size of the initial box is not discussed. However, if the finite size effects in the expansion velocity are similar to those observed in Chap. 4.3 for Fermions, they will be small at density $n = 1$.

We analyze the dynamics for the sudden expansion in the presence of repulsive interactions starting from pure Fock states in Fig. 17 and 18. Panel (a) of Fig. 17 shows the radius of an expanding cloud with $N = 10$ particles for $U/J = 4, 10, 20$ and a local particle number cutoff $d = 3$, where $R_n(t) \sim t$ within reasonable accuracy. Hence, we can define the expansion velocity V_{ex} as in Chap. 4.3 to obtain a preliminary result for the expansion velocity V_{ex} as a function of U, which is depicted in panel (b) of Fig 17. The data exhibits
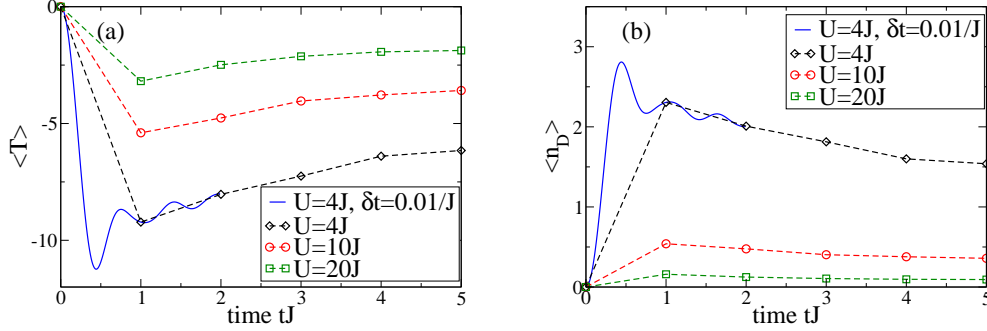
Figure 18: Time dependence of the kinetic energy $\langle T \rangle$ (a) and number of double occupancies $\langle n_D \rangle$ for the sudden expansion from a clean Fock states in the presence of repulsive interactions $U/J = 4, 10, 20$. Dashed lines are guides to the eye. The solid blue line is a short time evolution with high accuracy and smaller time step for $U = 4J$. The Fock state we use as initial state has a higher kinetic energy than the groundstate, except for the hardcore limit. Hence the formation of double occupancies is allowed at finite U and we find that it takes place at very short time scales. The data shown in panel (b) is directly obtained from the one in panel (a) via energy conservation.

a distinct minimum close to the critical $U \approx 3.3J$ for the superfluid-to-Mott-insulator-transition [219, 220, 221] and as stated above $V_{\mathrm{ex}} = \sqrt{2}J$ in both non-interacting limits. Note that this behavior is different from the dynamics expected from the groundstate of the trap. In that case $V_{\mathrm{ex}} \to 0$ as $U \to 0$ and $L_{\mathrm{init}} \to \infty$, since the groundstate is a quasi-condensate at the smallest momentum eigenstate of the trap.

Next, we investigate the dynamical formation of double occupancies and its possible relation to the minimum in our data for $V_{\mathrm{ex}}(U)$. To this end we calculate the time-dependence of the kinetic energy $\langle T \rangle$ and the number of double occupancies

$$\langle n_D \rangle = \sum_{i=1}^{L} \langle (b_i^\dagger)^2 b_i^2 \rangle \,. \tag{65}$$

The results are shown in Fig. 18: While $\langle T \rangle = 0$ and $\langle n_D = 0 \rangle$ in the initial state by construction, there is a tendency to dynamically form double occupancies to lower the kinetic energy. This process is forbidden in the hardcore limit and does not change the kinetic energy for non-interacting
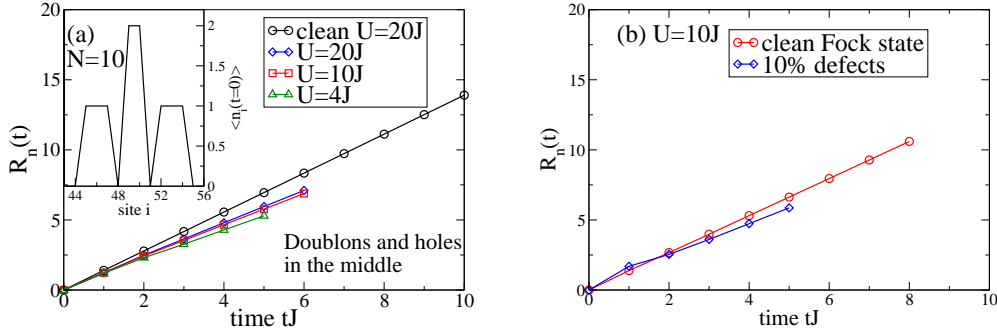
Figure 19: Radius for the sudden expansion starting from bosonic Fock states
with defects. (a) Single simulation of the density profile shown in the inset,
which contains two doublons and two holes for different interaction strengths
$U/J = 4, 10, 20$. The result for a clean Fock state with $U = 20J$ is plotted
for comparison. (b) Result obtained from taking the average over all defect
configurations with ten particles, one hole and one doublon in direct com-
parison with the result for a clean Fock state with the same particle number
at $U = 10J$. In both panels the slope of the radius is qualitatively smaller in
the presence of defects, yet $R_n(t)$ also deviates from an increase linear in t.

bosons. For $U/J = 4, 10, 20$ though, we find that the number of double
occupancies has a maximum after very short times $tJ \leq 1$. This observation
is a possible explanation for the minimum in our data for $V_{\mathrm{ex}}(U)$ around the
critical U where the system seems to be able to decrease its kinetic energy
most.

Finally, we investigate the sudden expansion in the presence of defects.
Figure 19 shows the time-dependent radius $R_n(t)$ for two different setups.
Panel (a) shows simulations of the initial state depicted in the inset at
$U/J = 4, 10, 20$. We place two doublons and two holes in the initial density,
symmetrically distributed around the center of the trap. For comparison
we plot the result for a clean Fock state at $U = 20J$, which is close to the
hardcore limit. Panel (b) shows the radius at $U = 10J$ for a clean Fock state
compared to the result obtained by taking the average over all initial states
that contain one doublon and one hole. In both studied cases the slope of
the radius exhibits an overall slight decrease. Yet, $R_n(t)$ is no longer clearly
linear, hence the average expansion velocity has to be determined by appro-
priate approximations. While fitting only large times would work, one could,
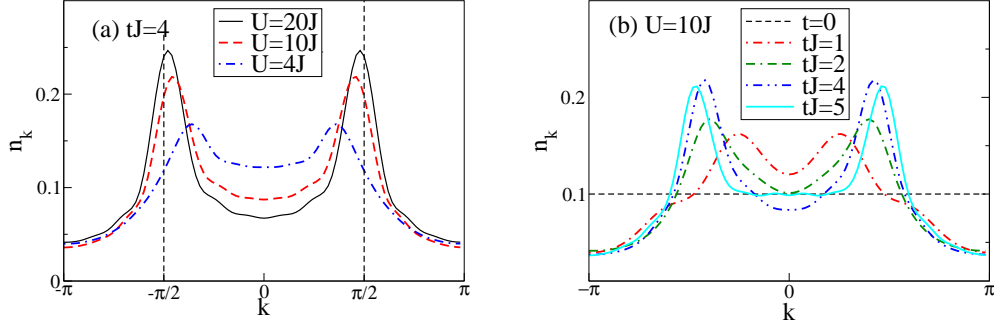
Figure 20: Dynamically emerging peaks in the momentum distribution as indicator of dynamical quasi-condensation during the sudden expansion from Fock states in the presence of repulsive interactions. (a) Momentum distribution at $tJ = 4$ for the sudden expansion from clean Fock states at $U/J = 4, 10, 20$. We find clear peaks close to $\pi/2$ (vertical black dashed lines) for $U \geq 10J$. (b) Snapshots of the momentum distribution function of an interacting bose gas expanding from a clean Fock state with $U = 10J$ at $tJ = 0, 1, 2, 3, 4, 5$. The flat momentum distribution function of the initial state immediately develops two peaks which then move to $\pm\pi/2$.

if the density profile was close enough to a gaussian, study the width of a gaussian fitted to the density as function of time.

4.4.3   Dynamical quasi-condensation during the sudden expansion from bosonic Fock states with repulsive interactions

The last point we address in our study of the dynamics of bosonic Fock states is if there is the possibility of dynamical quasi-condensation at finite momenta in the presence of defects for the fully interacting system. In panel (a) of Fig. 20 we plot the momentum distribution function of a Fock state evolving in the presence of repulsive interaction $U/J = 4, 10, 20$ after a short time $tJ = 4$. The momentum distributions already exhibit a clear notion of a peak at finite momentum. However, the peak position only approaches $\pi/2$ for $U \geq 10J$. While for a Fock state $\langle T(t = 0) \rangle = 0$, Fig 18(a) suggests a finite kinetic energy for long times, possibly explaining the deviation of the peak position from $\pi/2$. Now we want to investigate the observed peak positions in the clean case in more detail. To this end, Fig. 20 (b) compares the momentum distribution function during the sudden expansion from a
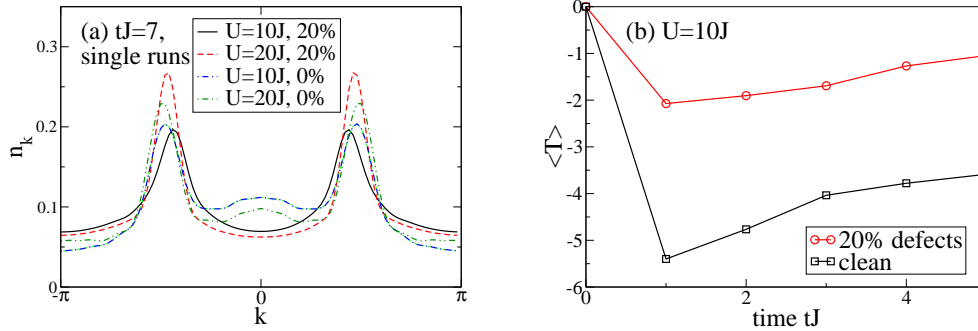
Figure 21: (a) Momentum distribution for the expansion from initial states with 20% defects for $U/J = 10, 20$ at $tJ = 7$ compared to the result from a clean Fock state with the same particle number. The curves qualitatively agree in the sense that momenta close to $\pm\pi/2$ are macroscopically occupied, indicating that this effect is robust against the presence of defects. (b) Time-dependence of the kinetic energy for the sudden expansion starting from the initial state depicted in the inset of Fig. 19, which has a defect concentration of 20%.

clean Fock state at $U = 10J$. We observe how the momentum distribution develops from the flat distribution of the initial state to the one with peaks close to $\pm\pi/2$. A possible explanation for the peak positions could be to relate the average kinetic energy per particle $\langle T \rangle / N$ and the peaks in the momentum distribution function at a given time t via the dispersion relation [Eq. (58)]. Yet, this simple picture cannot explain the actual peak positions. If it would, the momentum distribution function for the expansion from a clean Fock state at $U = 10J$ at $t = 5/J$ would correspond to a kinetic energy per particle of $\langle T \rangle / N = -0.209J$. Based on our data for $\langle T \rangle /$ at $U - 10J$ in Fig 18 (a) this is not the case.

Now we repeat the calculations in the presence of defects, namely doubly occupied and empty lattice sites. To work with a fixed particle number ($N = 10$), we assume that we have exactly one hole per doubly occupied site. Fig. 21 (a) shows the momentum distribution at $tJ = 7$ for $U/J = 10, 20$ for two fixed symmetric configurations with 20% defects, namely two holes and two doublons. The macroscopic occupation of finite momenta is still a visible feature at strong repulsive interactions. However, the peak positions do not agree exactly. To shed more light on this matter Fig. 20(b) presents the time
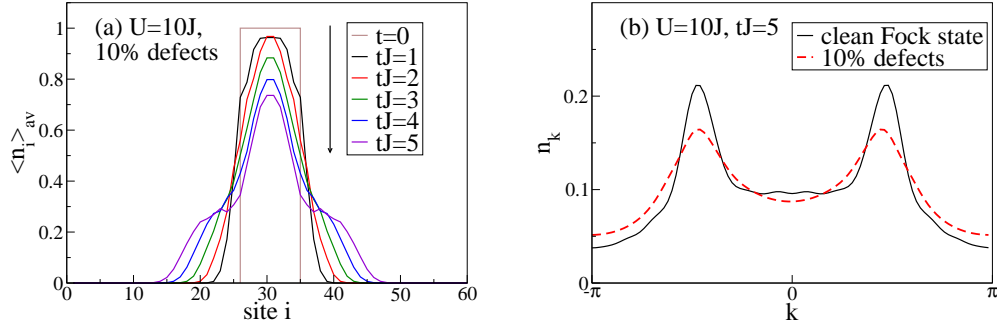
Figure 22: Averaged results for 10% defects. (a) Snapshots of the averaged particle density during the sudden expansion from states with 10% defects. (b) Momentum distribution at $tJ = 5$ averaged over all defect configurations for $N = 10$, compared to the one obtained from a clean Fock state.

dependence of the kinetic energy $\langle T \rangle$ for the sudden expansion starting from a clean Fock state compared to the result obtained for the Fock state with 20% defects. While the qualitative features, namely a minimum at short times and the approach of a stationary value at large times, remain unchanged, the quantitative values depend on the defect concentration much stronger than the position of the peaks in n_k. The reduced dynamical formation of double occupancies is no big surprise since the state with 20% defects has less unpaired particles. Yet, the open question remains what determines the exact position of the peak in n_k.

Finally, to obtain a more quantitative result for the robustness of the dynamical emergence of peaks in the momentum distribution function at finite momentum in the presence of defects, we consider a defect concentration of 10%, but average the expectation values of interest over all possible defect configurations. With a box size of 10, $N = 10$ particles, one hole and one doublon, the number of possible configurations is 90. First we study snapshots of the averaged particle density $\langle n_i \rangle_{\mathrm{av}}$ in Fig 22(a) for times $t \leq 5/J$. The averaging gives rise to smooth density profiles that could for instance be fitted by gaussians, which is not the case for densities like the one shown in the inset of Fig 19(a). In Fig 22(b) we compare the momentum distribution at $tJ = 5$ to the one obtained from the dynamics of a clean Fock state. Besides slightly smaller and broader peaks, this clearly shows our main result, namely that the dynamical quasi-condensation at finite momenta is robust against small

defect concentrations for sufficiently large repulsive interactions.

To summarize our results for the sudden expansion of bosons starting from Fock states we have investigated the phenomenon of dynamical quasi-condensation in the presence of defects. For hardcore bosons, we find that neither the dynamical quasi-condensation nor the expansion velocity are influenced by a finite concentration of holes in the initial state. For the interacting case we present preliminary results using a small box trap of 10 sites and study the sudden expansion for clean Fock states in the presence of double occupancies and holes. For true quasi-condensation a scaling of the peak height with linear the particle number N is required [222]. Yet, we observe a macroscopically occupation of momenta close to $\pi/2$, which is qualitatively robust against the presence of defects. Furthermore we investigate the dynamical formation of double occupancies and the time-dependence of the kinetic energy. While the interacting system indeed balances kinetic energy and interaction energy dynamically, the time-dependence of the kinetic energy alone cannot explain the observed peak positions on the limited timescales studied up to now.
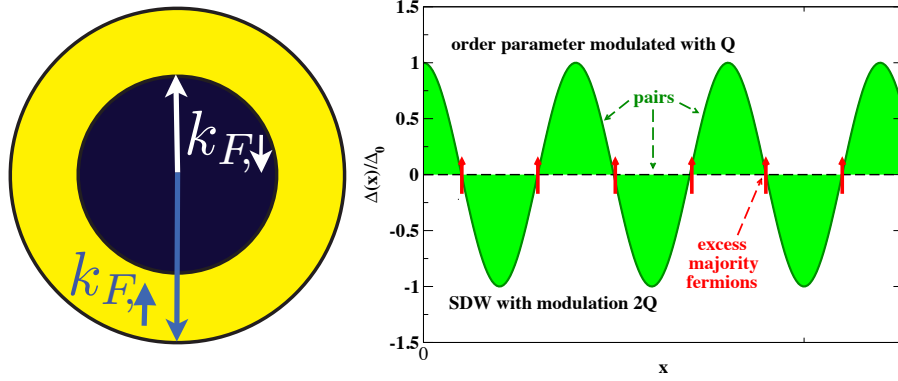
Figure 23: Sketch of the signatures of the FFLO-state. Left: Pairing across the mismatched Fermi surface at finite polarization. The resulting pairs have a finite center of mass momentum $Q = k_{F,\uparrow} - k_{F,\downarrow}$, which is proportional to the polarization. Right: Sketch of the spatial structure of the groundstate spin imbalanced Fermi gas in the partially polarized phase. The superfluid order parameter is modulated with Q, while the excess majority fermions form a spin-density wave with modulation $2Q$. The distribution of single fermions is thus peaked at the nodes of the pair distribution.

4.5   Long-time behavior of the momentum distribution during the sudden expansion of a spin-imbalanced Fermi gas in 1D

In this chapter we study the attractive Hubbard model and analyze the time dependence of the momentum distribution functions (MDF) of spin imbalanced mixtures, during the sudden expansion. In one spatial dimension and in the presence of attractive interactions, a two-component Fermi gas exhibits a partially polarized phase which has been shown to be the analogue of the FFLO phase [81, 82, 83, 84, 85, 86, 87]. The FFLO state (see Ref. [88] for a review) was originally proposed to allow for superfluidity at a finite polarization of the system [89, 90]. The mechanism that allows for fermionic pairing across the mismatched Fermi surfaces is to form pairs with a finite center-of-mass momentum $Q = k_{F,\uparrow} - k_{F,\downarrow}$ which is proportional to the magnetization

(see the left panel of Fig. 23 for a sketch). In that phase the superfluid order parameter, which is proportional to the Schrödinger wave function of the condensate (see Ref. [222] for a review), oscillates with a spatial modulation Q. The right panel of Fig. 23 sketches this characteristic feature of FFLO phase: The pair wavefunction oscillates with $1/Q$ while the excess majority fermions, in this case spin-up, form a spin density waves with modulation $1/(2Q)$. Pictorially speaking, the majority fermions occupy the nodes of the pair condensate. Since true long-range-order in one spatial dimension replaced by a power-law decay of correlations the one-dimensional analogue is usually called "of FFLO-type" in the literature (see Ref. [94] for a recent review).

Motivated by the recent experimental investigation of one-dimensional spin-imbalanced ultra-cold fermions [95], we want to study the fate of FFLO-like correlations. In particlular, Ref. [95] has experimentally accessed the spatial structure of a spin-imbalanced fermi gas in a harmonic confining potential, and reports a partially polarized phase in the center of the trap and fully polarized wings, in agreement with the theoretical predictions [87, 91, 93]. Yet, a strong experimental indication that the initial state in the trap really is of the FFLO-type is missing. Hence, our aim is to investigate whether a sudden expansion setup is suitable to prove that the initial state is of the FFLO-type. Furthermore, we are interested in the long-time limit where the behavior of the then very dilute gas should be fully determined by its initial conditions through its conserved quantities.

We work with the Fermi-Hubbard model [Eq. (57)] but as opposed to Chap. 4.3 now with attractive interactions and a global polarization of $P = (N_\uparrow - N_\downarrow)/N$ where $N_\sigma = \sum \langle n_{i\sigma} \rangle$. To determine the fate of the FFLO state during the sudden expansion, we first simulate the real-time evolution of the three momentum distributions of interest: The one for the minority fermions, the one for the majority fermions and the one of the pairs. Furthermore, we investigate the spatial structure by calculating the lowest natural orbital, i.e., the eigenvector of the pair-pair density matrix corresponding to the largest eigenvalue. In both cases we find that while the initial state clearly is of the FFLO-type, the distinct features, namely the peaks at $\pm Q$ in the momentum distribution of the pairs, and the nodal structure of the lowest natural orbital that accommodates the excess majority spins, are quickly lost during the sudden expansion. We find the dominant mechanism behind their disappearance to be a quantum distillation [204]. This fast process causes a spatial separation of pairs and single majority fermions on very short time scales. Afterwards the expansion of the separated gases is described by almost

time-independent momentum distributions.

In addition to obtaining a fast convergence towards stationary momentum distributions from the DMRG data, we are able to relate their shape to the initial conditions and the conserved quantities of the integrable Fermi-Hubbard model in terms of the corresponding Bethe ansatz solution [27]. The stationary form of the momentum distributions should in principle be observable in the corresponding expansion experiment and could serve as indirect indicator for the FFLO correlations in the initial state.

Long-time behavior of the momentum distribution during the sudden expansion of a spin-imbalanced Fermi gas in one dimension

C. J. Bolech,[1,2] F. Heidrich-Meisner,[2,3] S. Langer,[3] I. P. McCulloch,[4] G. Orso,[5] and M. Rigol[6]

[1]Department of Physics, University of Cincinnati, Cincinnati, OH 45221, USA
[2]Kavli Institute for Theoretical Physics, Kohn Hall, University of California, Santa Barbara, CA 93106, USA
[3]Department of Physics and Arnold Sommerfeld Center for Theoretical Physics,
Ludwig-Maximilians-Universität München, D-80333 München, Germany
[4]Centre for Engineered Quantum Systems, School of Mathematics and Physics,
The University of Queensland, St Lucia, QLD 4072, Australia
[5]Laboratoire Matériaux et Phénomènes Quantiques, Université Paris Diderot-Paris 7 and CNRS, UMR 7162, 75205 Paris Cedex 13, France
[6]Department of Physics, Georgetown University, Washington, DC 20057, USA

We study the sudden expansion of spin-imbalanced ultracold lattice fermions with attractive interactions in one dimension after turning off the longitudinal confining potential. We show that the momentum distribution functions of majority and minority fermions approach stationary values very fast due to a quantum distillation mechanism that results in a spatial separation of pairs and majority fermions. As a consequence, Fulde-Ferrell-Larkin-Ovchinnikov (FFLO) correlations are lost during the expansion. Furthermore, we argue that the shape of the stationary momentum distribution functions can be understood by relating them to the integrals of motion in this integrable quantum system. We discuss our results in the context of proposals to observe FFLO correlations, related to recent experiments by Liao *et al.*, Nature **467**, 567 (2010).

The combination of strong correlations and quantum fluctuations makes one-dimensional (1D) systems the host of exotic phases and physical phenomena [1, 2]. Those phases and phenomena, in many occasions first predicted theoretically, have been observed in condensed matter experiments and have begun to be studied with ultracold atomic gases [2]. A system of particular interest in recent years has been the spin imbalanced 1D Fermi gas. Following theoretical predictions [3–8], its grand canonical phase diagram has recently been investigated experimentally [9]. The major interest in this model comes from the fact that its entire partially polarized phase has been theoretically shown [5, 6, 10–14] (for a review, see [15]) to be the 1D-analogue of the Fulde-Ferrell-Larkin-Ovchinnikov (FFLO) state [16, 17]. The FFLO phase was introduced to describe a possible equilibrium state in which magnetism and superconductivity coexist thanks to the formation of pairs with finite center-of-mass momentum leading to a spatially oscillating order parameter. The existence of such a phase has remained controversial in dimensions higher than one, both in experimental [18, 19] and theoretical studies [20–22].

An important challenge in ultracold fermion experiments, which may have already realized the FFLO state [9], is to confirm the existence of FFLO correlations (for recent proposals see, *e.g.*, [23–26]). A direct measurement of the pair momentum distribution function (MDF) in the partially polarized state [5, 6, 13] has been suggested to provide such an evidence [27]. However, this remains very difficult because after turning off all confining potentials, the transverse expansion (in the directions of very tight confinement) dominates over the longitudinal one [28]. Another interesting possibility is to let the gas expand in the 1D lattice after turning off the longitudinal confining potential, and then measure the density profiles or the MDFs of the independent species and/or pairs

after some expansion time. Crucial aspects of such an experiment have already been successfully carried out, namely the control over the trapping potential and the measurement of the density profiles after the expansion [29–31]. For 1D gases, interactions effects during the expansion cannot in general be neglected, leading to fundamentally different behavior of observables before and after the expansion. For example, the expansion of the Tonks-Girardeau gas in 1D results in a bosonic gas with a fermionic MDF [32–34], and initially incoherent (insulating) states of bosons [35, 36] and fermions [37] can develop quasi-long range correlations during the expansion.

The question we are set to address is the fate of the MDFs of fermions and pairs during an expansion in one dimension, as described by the attractive Hubbard model. We use a combination of numerical simulations, based on the time-dependent renormalization group approach (*t*-DMRG) [38, 39], and analytical (Bethe-Ansatz) results. We first show that the MDFs of majority and minority fermions become stationary after a relatively short expansion time, $t \sim L_0/J$, where L_0 is the initial size of the cloud and J is the hopping amplitude. For strong interactions, we explain this behavior in terms of a quantum distillation process [40], as a consequence of which FFLO correlations get destroyed during the expansion. Finally, we discuss how these stationary MDFs can be theoretically understood within the framework of the Bethe-Ansatz. Our results suggest that the final form of the MDFs of minority and majority fermions are related to the distributions of Bethe-Ansatz rapidities (a full set of conserved quantities) of this integrable lattice system.

The Hubbard model (in standard notation [41]) reads:

$$H_0 = -J \sum_{\ell=1}^{L-1} (c_{\ell+1,\sigma}^\dagger c_{\ell,\sigma} + \text{H.c.}) + U \sum_{\ell=1}^{L} n_{\ell\uparrow} n_{\ell\downarrow}. \quad (1)$$

As the initial state, we always take the ground state of a trapped system. Two different trapping potentials are considered: (i) a box (*i.e.*, particles confined into a region of length L_0 and (ii) a harmonic trap, $H_{\text{trap}} = V_0 \sum_{\ell=1}^{L} n_\ell (\ell - L/2)^2$. We study lattices with L sites, N particles, and a global polarization of $p = (N_\uparrow - N_\downarrow)/N$, where $N_\sigma = \sum_\ell \langle n_{\ell\sigma} \rangle$. All positions are given in units of the lattice spacing and momenta in inverse units of the lattice spacing ($\hbar = 1$).

The expansion is triggered by suddenly turning off the confining potential, thus allowing particles to expand in the lattice. We then follow the time-evolution using the numerically exact *t*-DMRG algorithm [38, 39]. We use a Krylov-space based time-evolution method and enforce discarded weights of 10^{-4} or smaller with a time-step of $\delta t = 0.25/J$. Our main focus is on the time-evolution of the three MDFs: the ones for majority ($\sigma = \uparrow$) and minority fermions ($\sigma = \downarrow$), denoted by $n_{k,\sigma}$ and the pair MDF, $n_{k,\mathrm{p}}$. These functions are computed from the corresponding one-particle density matrices via a Fourier transform

$$n_{k,\lambda} = \frac{1}{L} \sum_{\ell,m} e^{i(\ell-m)k} \langle \psi_{\ell,\lambda}^\dagger \psi_{m,\lambda} \rangle \tag{2}$$

where $\psi_{\ell,\sigma}^\dagger = c_{\ell\sigma}^\dagger$, $\psi_{\ell,p}^\dagger = c_{\ell,\uparrow}^\dagger c_{\ell,\downarrow}^\dagger$ and λ stands for $\uparrow, \downarrow, p$. We normalize the MDFs so that $\sum_k n_{k,\lambda} = N_\lambda$. In particular, $N_p = \sum_\ell \langle n_{\ell\uparrow} n_{\ell\downarrow} \rangle$ is the total double occupancy.

We first discuss the expansion from a box. The initial density is fixed to $n = N/L_0 = 0.8$. In our *t*-DMRG simulations, which were carried out for $N = 8$ and $N = 16$ ($L_0 = 10$ and 20, respectively) and various values of U, we were able to reach times of order $t_{\max} \sim 80/J$ for large U and $t_{\max} \sim 40/J$ for intermediate values of $U \sim 4J$. $t_{\max}$ also depends on p, with small values of p being more demanding.

Typical results for the three MDFs of interest are presented in Fig. 1 for $U = -10J$ and $p = 0.5$ (see the supplementary material for more data [42]). During the time evolution, they are all seen to quickly approach time-independent forms. In Fig. 1(a), it is apparent that the MDF of the majority fermions becomes narrower and develops small oscillations in the vicinity of $k = 0$ as time passes. We find that those oscillations become smaller in amplitude and get restricted to smaller values of k after long expansion times, *i.e.*, they seem to be a transient feature not present in the asymptotic distributions. The momentum distribution of the minority spins [Fig. 1(b)], on the other hand, becomes broader during the time evolution.

The time evolution of the MDF of the pairs, depicted in Fig. 1(c), yields information on the fate of FFLO correlations in the expanding cloud. In the FFLO state, $n_{k,p}$ has maxima at $Q = \pm(k_{F\uparrow} - k_{F\downarrow})$ [5]. These are visible in the $t = 0$ curve (dashed line), where $\pm Q$ are marked by vertical lines. As the comparison of $n_{k,p}(t > 0)$ with the initial $n_{k,p}(t = 0)$ shows, the peaks at $\pm Q$ rapidly disappear, and $n_{k,p}(t)$ becomes narrower. In addition, new and shallower peaks form at $k < Q$. Since we do not find those peaks at the same values of k for other values of N when N/L_0 and P are the same, and we do not find them for all values of U, N/L_0, and P studied,
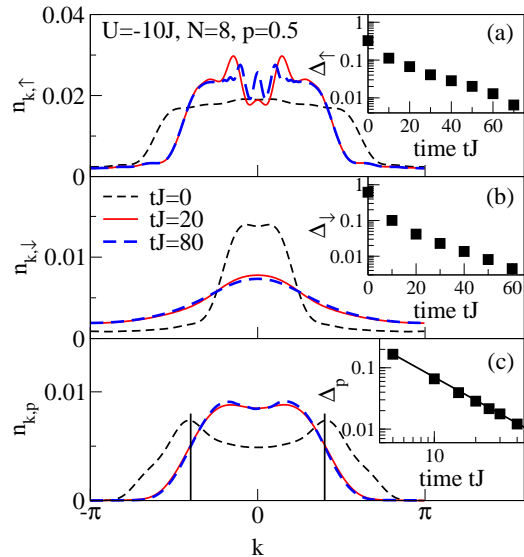

FIG. 1: (Color online) MDF for the expansion from a box trap ($U = -10J$, $N = 8$, $p = 0.5$): (a) $n_{k,\uparrow}$, (b) $n_{k,\downarrow}$, and (c) $n_{k,p}$. The insets show the difference Δ_λ ($\lambda = \uparrow, \downarrow, p$, see text) between the MDF at a time t compared to the one at the largest time reached in the simulation. The vertical lines in the main panel in (c) mark the position of the FFLO wave-vector $Q = \pm \pi n p$.

they appear to be related to finite-size effects. Hence, the double peak structure in $n_{k,p}(t = 0)$, which makes evident the presence of FFLO correlations in the initial state, is found to disappear during the expansion. Even though the FFLO correlations are lost during the expansion, the integral over the pair MDF, which equals the total double occupancy, does not vanish. This implies that not all interaction energy is converted into kinetic energy and that some fraction of the original pairs remains by the time the MDFs have become stationary. While in most experiments the particle clouds can only expand by a factor of $\mathcal{O}(10)$ or less [31], the stationarity of the various MDFs should be observable as well as the fact that the total double occupancy is finite.

In order to quantify how the three MDFs above approach stationary forms, in the insets in Fig. 1, we plot $\Delta_\lambda(t) = \sum_k |n_{k,\lambda}(t) - n_{k,\lambda}(t_{\max})| / \sum_k n_{k,\lambda}(t_{\max})$ vs t. These results make apparent that the approach is close to exponential for $n_{k,\uparrow}$ and $n_{k,\downarrow}$ [insets in Fig. 1(a) and 1(b)], while it is power law for $n_{k,p}$ [inset in Fig. 1(c)] [43]. Remarkably, for the parameters of Fig. 1, already at $tJ \sim 10$, all Δ_λ are $\lesssim 10\%$. This means that the stationary MDFs obtained in this work should be achievable in current optical lattice setups [31]. A comparison between expansions from different box sizes suggests that the emerging time scale in the observables with exponential relaxation is proportional to L_0. The origin of that time scale will be unveiled in the discussion below.

To understand how the FFLO state breaks down as the gas expands, we calculate the eigenvector $\Phi_{0,\ell}$ of the pair-pair density matrix $P(\ell, m) = \langle \psi_{\ell,p}^\dagger \psi_{m,p} \rangle$ that corresponds to the largest eigenvalue. $|\Phi_{0,\ell}|$, shown in Fig. 2(a), unveils the
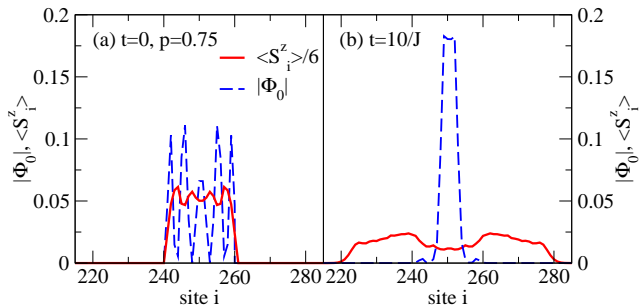
FIG. 2: (Color online) Natural orbital $|\Phi_0|$ corresponding to the largest eigenvalue of the pair-pair correlator $P(\ell, j)$ (dashed lines) and spin density $\langle S_i^z \rangle$ (solid lines, rescaled by a factor of $1/6$). (a) $t = 0$, (b) $tJ = 10$. These results are for $U = -10J$, $p = 0.75$, $L = 500$, and $N = 16$.

FIG. 3: (Color online) MDFs for the expansion from a harmonic trap: (a) $n_{k,\uparrow}$, (b) $n_{k,\downarrow}$ and (c) $n_{k,p}$. These results were obtained for $N = 8$, $U = -10J$, $p = 0.75$, $V = 0.016J$, and at times $tJ = 0, 90, 100$. Inset in (a): initial density $\langle n_i \rangle$ (solid line) and spin-density profile $2\langle S_i^z \rangle$ (dashed line).

spatial structure of the quasi-condensate in the initial state: it has an oscillatory behavior with nodes (see also Ref. [5]). In these nodes, the spin density has its maxima to accommodate the majority fermions [Fig. 2(a)], indicative of the spin-density wave character with a modulation of $(2Q)^{-1}$ in the FFLO state. During the expansion, the nodes in $|\Phi_{0,\ell}|$ disappear while $|\Phi_{0,\ell}|$ develops a maximum at $L/2$, exceeding its initial value [see Fig. 2(b)]. The latter is a consequence of a quantum distillation mechanism, described in Ref. [40] for $U > 0$, which allows the unpaired fermions to move away from the center of the system (*i.e.*, they escape from the nodes of $|\Phi_{0,\ell}(t = 0)|$). Loosely speaking, during first-order processes unpaired fermions exchange their positions with the pairs (a minority fermion hops towards the center of the trap), allowing the former to expand while the pairs move towards the center of the trap. This occurs over a time scale proportional to L_0 and inversely proportional to J, which explains the time scale observed in the exponential approach of the majority and minority fermions to their stationary values. Once the unpaired fermions have spatially separated themselves from the pairs, they form a non-interacting gas whose MDF is stationary. On much longer time scales (assuming $U > 4J$), we expect the pairs to slowly expand as well. This transient dynamics of the pairs may be the reason for the power-law, as opposed to exponential, relaxation observed for $n_{k,p}(t)$ in Fig. 1(c).

In a recent work [44], extrema in the spin-density of the expanding gas were observed in numerical calculations using various approaches. By comparing with the time-dependence of the order parameter within a time-dependent Bogoliubov-deGennes approach, it was argued that they are related to FFLO correlations. Our results show that, in a lattice system, the nodal structure of the FFLO state is ultimately lost as the system expands. Note, however, that in Ref. [44] the main focus was on rather small polarizations p [3, 4, 8] leading to a wide partially polarized core before the expansion. We therefore expect the quantum distillation mechanism to take much longer to depolarize the core than what has so far been reached in numerical simulations [44], leaving this case
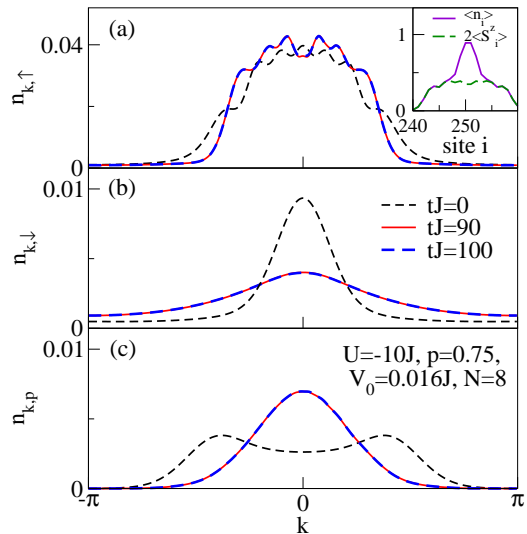
as an open question.

We are now in a position to explain the anticorrelated behavior of $n_{k,\uparrow}$ and $n_{k,\downarrow}$ mentioned in the discussion of Fig. 1. For large values of U, N_p is essentially equal to $N_\downarrow$ and is approximately unchanged during the expansion, rendering the interaction energy almost time independent. This implies that also the kinetic energy $E_{\text{kin}} = -2J\sum_k \cos k(n_{k,\uparrow} + n_{k,\downarrow})$ is approximately conserved, which is only possible if the two MDFs behave in the opposite way during the expansion. The broadening of the minority MDF $n_{k,\downarrow}$ with respect to the initial state is a direct consequence of the spatial separation of excess fermions from the pairs, leaving the latter confined in the center of the cloud. Since in the center the local polarization decreases, the stationary form of $n_{k,\downarrow}$ is well approximated by the equilibrium one for equal populations $N_\uparrow = N_\downarrow$ instead of $N_\uparrow > N_\downarrow$ [42].

In relation with experiments, it is also important to incorporate the harmonic confinement. To that end, we have prepared a spin-imbalanced system with $U = -10J$ in a harmonic trap with $V_0 > 0$ for $t < 0$, and then quenched the trapping potential to $V_0 = 0$ at $t = 0$. For the parameters of Fig. 3, the partially polarized phase that sits in the core is surrounded by fully polarized wings (see the inset in Fig. 3). During the expansion, one can see that the behavior of the MDFs is very similar to the one starting from a box in Fig. 1. All MDFs become stationary shortly after the release from the trap. The stationary $n_{k,\uparrow}$ is narrower while $n_{k,\downarrow}$ is broader than their corresponding initial distributions, and the double peak structure in $n_{k,p}$ disappears.

The fact that the MDFs become stationary after the expansion from a box or a harmonic trap is in itself not surprising, as

in the limit of long expansion times, the cloud becomes very dilute with, for the attractive case, the typical inter-particle distance being much larger than the bound-state size. Hence, one may assume that pairs and unpaired particles are essentially noninteracting. The MDF in such an asymptotic limit should be determined by the initial conditions right after the quench. For instance, for generic models, the total energy (which is conserved during the expansion) plays a fundamental role in determining the expansion dynamics (see Ref. [45] for a related work for $U > 0$). For an integrable model, such as the (attractive) Hubbard model of Eq. (1), all integrals of motion are in principle known from the Bethe Ansatz and are conserved during the expansion [41]. We will argue below how to interpret the shape of certain stationary MDFs in terms of such integrals of motion. This is closely related to the previously studied fermionization of the MDF of an expanding gas of hard-core bosons [32–34].

For the model studied here, we first note that the formation of a distinct minimum in the difference distribution $\delta n_k = n_{k,\uparrow} - n_{k,\downarrow}$ is reminiscent of the corresponding distribution of real-valued charge rapidities (for intermediate U) in the ground state in a box. From the point of view of the rapidity distributions, they need to be determined right after turning off the trap and the subsequent expansion does not play any role; it is the MDFs which will evolve and asymptotically approach the former as the expansion proceeds [46]. We can calculate the pre-quench values of the rapidities by numerically solving the Bethe-Ansatz equations for a system of size L_0 and open boundary conditions [47]. For the ground state of the attractive Hubbard model, we have two types of rapidities present: real- and complex-valued charge rapidities (κ_ν and κ_σ) which correspond to unpaired fermions and pairs, respectively ($\nu = 1, \ldots, N_\uparrow - N_\downarrow$, $\sigma = 1, \ldots, 2N_\downarrow$, with κ_σ and κ_σ^* appearing pairwise.).

To calculate the effect of the quench of the trapping potential exactly is in principle possible but complicated in practice [48], so we will make some simplifying assumptions. To start, we assume that the number of pairs is conserved during the quench, and thus no pure-spin excitations are produced. Further, we use the observation that the overlap between the pre-quench eigenstate and the post-quench state has a maximum amplitude for components of the latter with the same set of rapidities [48]. We then identify, asymptotically, the distribution of real-valued charge rapidities with that of unpaired fermions (δn_k), and of the real part of complex-valued (string) charge rapidities with that of minority fermions ($n_{k,\downarrow}$) – since they remain paired. Finally, we model the quench by convolving the pre-quench distributions $\rho_1 = (1/2) \sum_\nu \delta(k \pm \kappa_\nu)$ and $\rho_2 = (1/2) \sum_\sigma \delta(k \pm \mathrm{Re}\kappa_\sigma)$ with the (periodized) kernels: (i) $L_0 \operatorname{sinc}^2(kL_0/2)$ for the former and (ii) a simple Lorentzian for the latter. The first choice is inspired by the exact result for the release of a single particle from a box, while the second choice is done for simplicity given that the results are relatively featureless in comparison. Illustrative results are shown in Fig. 4 and the agreement is very good, specially away from the Brillouin-zone center. Note that there
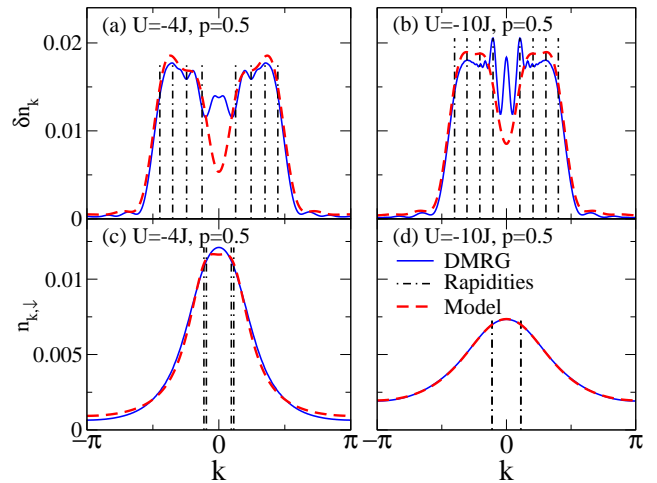

FIG. 4: (Color online) Comparison of the stationary MDFs $\delta n_k = n_{k,\uparrow} - n_{k,\downarrow}$ [(a),(b)] and $n_{k,\downarrow}$ [(c),(d)] for the expansion from a box with $N = 8$, $p = 0.5$ [(a),(c): $U = -4J$, (b),(d): $U = -10J$] to the form expected from the rapidities known from the Bethe-Ansatz: t-DMRG (solid lines), models discussed in the text (dashed lines). The vertical lines mark the positions of the rapidities.

are no fitting parameters in the case of δn_k and a single fitting parameter, the width of the Lorentzian, in the case of $n_{k,\downarrow}$.

In conclusion, we demonstrated that the initial FFLO state is destroyed during the expansion of an attractively interacting partially polarized 1D Fermi gas, and that direct signatures of the FFLO phase in the initial pair MDF are washed out. In addition, the MDFs of majority and minority fermions as well as the one of pairs rapidly take a stationary form, on time scales accessible to experiments. Our analysis further suggests that the shape of the MDFs can be related to the distribution of rapidities, which constitute a full set of integrals of motion for this integrable quantum model. Measuring such asymptotic distributions and comparing them to the ones expected theoretically for an FFLO state can provide an indirect proof of the realization of that putative phase in the experiments such as the one in Ref. [9].

[1] T. Giamarchi, *Quantum Physics in One Dimension* (Oxford University Press, 2004).
[2] M. A. Cazalilla, R. Citro, T. Giamarchi, E. Orignac, and M. Rigol, Rev. Mod. Phys. **83**, 1405 (2011).
[3] G. Orso, Phys. Rev. Lett. **98**, 070402 (2007).
[4] H. Hu, X.-J. Liu, and P. D. Drummond, Phys. Rev. Lett. **98**,

070403 (2007).

[5] A. Feiguin and F. Heidrich-Meisner, Phys. Rev. B **76**, 220508(R) (2007).

[6] M. Casula, D. M. Ceperley, and E. J. Mueller, Phys. Rev. A **78**, 033607 (2008).

[7] P. Kakashvili and C. J. Bolech, Phys. Rev. A **79**, 041603 (2009).

[8] F. Heidrich-Meisner, G. Orso, and A. Feiguin, Phys. Rev. A **81**, 053602 (2010).

[9] Y. A. Liao, A. S. C. Rittner, T. Paprotta, W. Li, G. B. Partridge, R. G. Hulet, S. K. Baur, and E. J. Mueller, Nature **467**, 567 (2010).

[10] K. Yang, Phys. Rev. B **63**, 140511 (2001).

[11] M. Tezuka and M. Ueda, Phys. Rev. Lett. **100**, 110403 (2008).

[12] G. G. Batrouni, M. H. Huntley, V. G. Rousseau, and R. T. Scalettar, Phys. Rev. Lett. **100**, 116405 (2008).

[13] M. Rizzi, M. Polini, M. Cazalilla, M. Bakhtiari, M. Tosi, and R. Fazio, Phys. Rev. B **77**, 245105 (2008).

[14] A. Lüscher, R. M. Noack, and A. Läuchli, Phys. Rev. A **78**, 013637 (2008).

[15] A. Feiguin, F. Heidrich-Meisner, G. Orso, and W. Zwerger, Lect. Not. Phys. **836**, 503 (2011).

[16] P. Fulde and R. A. Ferrell, Phys. Rev. **135**, A550 (1964).

[17] A. I. Larkin and Y. N. Ovchinnikov, Sov. Phys. JETP **20**, 762 (1965).

[18] G. B. Partridge, W. Li, R. I. Kamar, Y.-A. Liao, and R. G. Hulet, Science **311**, 503 (2006).

[19] M. W. Zwierlein, A. Schirotzek, C. H. Schunck, and W. Ketterle, Science **311**, 492 (2006).

[20] R. Casalbuoni and G. Nardulli, Rev. Mod. Phys. **76**, 263 (2004).

[21] L. Radzihovsky and D. Sheehy, Rep. Prog. Phys **73**, 076501 (2010).

[22] F. Chevy and C. Mora, Rep. Prog. Phys. **73**, 112401 (2010).

[23] J. M. Edge and N. R. Cooper, Phys. Rev. Lett. **103**, 065301 (2009).

[24] T. Roscilde, M. Rodriguez, K. Eckert, O. Romero-Isart, M. Lewenstein, E. Polzik, and A. Sanpera, New. J. Phys. **11**, 055041 (2009).

[25] R. M. Lutchyn, M. Dzero, and V. M. Yakovenko, Phys. Rev. A **84**, 033609 (2011).

[26] J. Kajala, F. Massel, and P. Törmä, Phys. Rev. A **84**, 041601(R) (2011).

[27] K. Yang, Phys. Rev. Lett. **95**, 218903 (2005).

[28] This can be understood in terms of Heisenberg uncertainty: a tighter confinement implies a larger population of higher canonically–conjugate momentum modes, which in turn contribute to a faster expansion rate.

[29] T. Kinoshita, T. Wenger, and D. S. Weiss, Science **305**, 1125 (2004).

[30] T. Kinoshita, T. Wenger, and D. S. Weiss, Nature **440**, 900 (2006).

[31] U. Schneider, L. Hackermüller, J. P. Ronzheimer, S. Will, S. Braun, T. Best, I. Bloch, E. Demler, S. Mandt, D. Rasch, et al., Nature Phys. **8**, 213 (2012).

[32] M. Rigol and A. Muramatsu, Phys. Rev. Lett. **94**, 240403 (2005).

[33] A. Minguzzi and D. M. Gangardt, Phys. Rev. Lett. **94**, 240404 (2005).

[34] M. Rigol and A. Muramatsu, Mod. Phys. Lett. **19**, 861 (2005).

[35] M. Rigol and A. Muramatsu, Phys. Rev. Lett. **93**, 230404 (2004).

[36] K. Rodriguez, S. R. Manmana, M. Rigol, R. M. Noack, and A. Muramatsu, New J. Phys. **8**, 169 (2006).

[37] F. Heidrich-Meisner, M. Rigol, A. Muramatsu, A. E. Feiguin, and E. Dagotto, Phys. Rev. A **78**, 013620 (2008).

[38] A. Daley, C. Kollath, U. Schollwöck, and G. Vidal, J. Stat. Mech.: Theory Exp. P04005 (2004).

[39] S. R. White and A. E. Feiguin, Phys. Rev. Lett. **93**, 076401 (2004).

[40] F. Heidrich-Meisner, S. R. Manmana, M. Rigol, A. Muramatsu, A. E. Feiguin, and E. Dagotto, Phys. Rev. A **80**, 041603 (2009).

[41] F. H. L. Essler, H. Frahm, F. Göhmann, A. Klümper, and V. E. Korepin, *The One-Dimensional Hubbard Model* (Cambridge University Press, 2004).

[42] See the supplementary material.

[43] For the exponent of the power–law decay of $\Delta_p \propto (tJ)^{-\alpha}$, we find $\alpha \approx 1.25$.

[44] H. Lu, L. O. Baksmaty, C. J. Bolech, and H. Pu, Phys. Rev. Lett. **108**, 225302 (2012).

[45] S. Langer, M. Schuetz, I. McCulloch, U. Schollwöck, and F. Heidrich-Meisner, Phys. Rev. A **85**, 043618 (2012).

[46] B. Sutherland, Phys. Rev. Lett. **80**, 3678 (1998).

[47] E. K. Sklyanin, J. Phys. A **21**, 2375 (1988).

[48] J. Mossel, G. Palacios, and J.-S. Caux, J. Stat. Mech.: Theory Exp. L09001 (2010).

Supplementary material

Additional results for the MDFs of a spin-imbalanced Fermi gas with attractive interactions

We here provide additional t-DMRG results for the MDFs $n_{k,\lambda}$ of a spin-imbalance Fermi gas with attractive interactions, expanding from a box trap. Figure 5 contains data for $N = 16$ (with $U = -10J$, $p = 0.75$, $L_0 = 20$). In this case we were able to reach maximum times of $t_{\max} \sim 30/J$. Nevertheless, a fast approach towards a stationary form is obvious from this figure, corroborating the conclusions of the main text (see the discussion of Fig. 1 of the main text). The same applies to the qualitative trends: $n_{k,\uparrow}$ shrinks while $n_{k,\downarrow}$ broadens.

In Fig. 6, we display results for $U = -4J$ and $N = 8$ with a polarization of $p = 0.5$. In this case, the convergence to a stationary form is evident in all three MDFs. Note that, in contrast to the case of $U = -10J$ discussed in the main text, $n_{k,\uparrow}$ does not exhibit any transient fluctuations at small k.
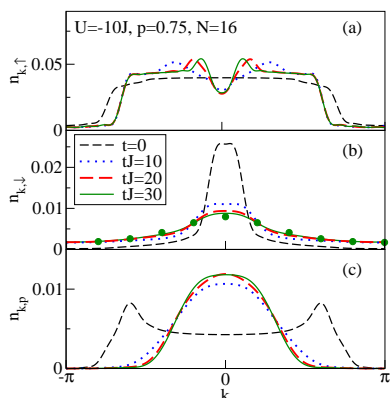

FIG. 5: MDFs for (a) spin up, (b) spin down, and (c) pairs for the expansion from a box trap with $U = -10J$, $N = 16$, $p = 0.75$, $L_0 = 20$, plotted at times $tJ = 0, 10, 20, 30$. The circles in the central panel represent the MDF of an unpolarized gas with $N_\uparrow = N_\downarrow = 1$.

Discussion of the qualitative behavior of the MDFs of the spin-imbalanced Fermi gas with attractive interactions

Comparing Figs. 1(a)-(b) of the main text, as well as Fig. 6(a) and (b) shown here in the supplementary material, we see that the momentum distribution $n_{k,\uparrow}$ of the majority component shrinks during the expansion, whereas the distribution $n_{k,\downarrow}$ of the minority component broadens significantly. This is the result of collisions between up and down fermions which take place in the inner part of the system, where both spin components are present, and transfer momenta between them. In the long time limit and for $|U| > J$, the pairs phase separate from unbound fermions, such that the cloud develops

a two-shell structure with a fully paired core and fully polarized wings containing the excess $N_\uparrow - N_\downarrow$ fermions. This suggests that the asymptotic momentum distribution of the minority component should be approximated by its ground state value before the expansion calculated *in the absence* of excess fermions, that is for $N_\uparrow = N_\downarrow$. The results for the MDF $n_{k,\downarrow}$ that we obtain using this assumption are plotted in Figs. 5 and 6 with circles. Indeed, we see a rather good agreement with the stationary form of the MDF $n_{k,\downarrow}$, where the latter was calculated with t-DMRG. In particular, in the limit of large initial polarization $p \to 1$, the number of pairs is very small. In this low density (or equivalently, strong-coupling) regime the ground state momentum distribution becomes equal to the square of the Fourier transform of the molecular wave-function for the relative motion:

$$n_{k\downarrow} = n_\downarrow \frac{|U|^3}{\sqrt{U^2 + 16J^2}} \frac{1}{(-4J\cos k + \sqrt{U^2 + 16J^2})^2}. \quad (3)$$

The corresponding shrinking of the majority momentum distribution during the expansion can then be understood from conservation of total energy. Indeed, for $|U| \gg J$ the number of double occupancies remains close to $N_p = N_\downarrow$ during the expansion, implying that the interaction energy in the Hubbard model is essentially time independent. As a consequence, the kinetic energy $E_{\mathrm{kin}} = -2J \sum_k \cos k(n_{k,\uparrow} + n_{k,\downarrow})$ is also conserved, implying that the distribution $n_{k,\uparrow}$ must shrink to compensate the broadening of $n_{k,\downarrow}$.

Time-evolution of the MDFs of a two-component Fermi gas with repulsive interactions

We have also studied the time-evolution of other 1D models during the expansion, including most notably the repulsive Hubbard model with $p = 0$ (compare [1]).

The $U > 0$ case turns out to be a numerically much harder problem for t-DMRG, as entanglement grows much faster
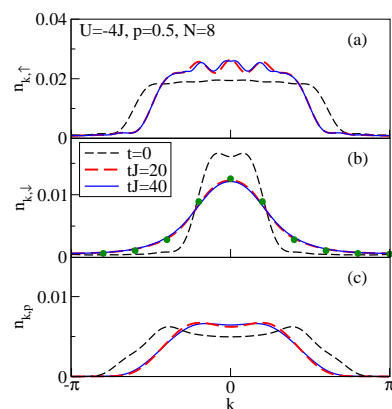

FIG. 6: MDFs for (a) spin up, (b) spin down, and (c) pairs for the expansion from a box trap with $U = -4J$, $N = 8$, $p = 0.5$, $L_0 = 10$, plotted at times $tJ = 0, 20, 40$. The circles in the central panel represent the MDF of an unpolarized gas with $N_\uparrow = N_\downarrow = 2$.
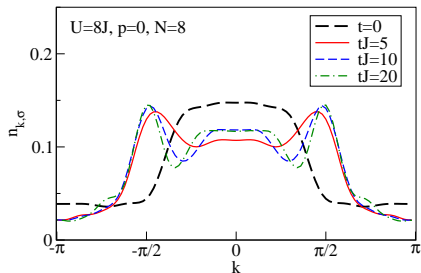
FIG. 7: MDF $n_{k,\sigma} = n_{k,\uparrow} = n_{k,\downarrow}$ for the expansion from a box trap with $U = 8J$, $N = 8$, $p = 0$, plotted at times $tJ = 0, 5, 10, 20$. We observe that in the case of repulsive interactions, much shorter times can be reached than for $U < 0$. On the accessible time scales, the MDF still changes, yet at its edge, the curves for $tJ = 10$ and $tJ = 20$ lie on top of each other.

(see the review [2] for how entanglement growth limits t-DMRG). Therefore, we resorted to exploiting non-Abelian symmetries as well, restricting the analysis to $p = 0$, allowing us to reach $t \sim 25/J$ for $U = 8J$ (see Fig. 7). In the case of $U = 8J$, there are no pairs, and hence over the full extent of the expanding cloud, majority and minority fermions can still interact, whereas in the case of $U < 0$ and $p > 0$, fast majority fermions escape [3] and the pairs and majority fermions mostly decouple due to the quantum distillation mechanism that is described in the main text. This is likely the reason why in the repulsive gas with $U > 0$ and $p = 0$, there is a stronger entanglement during the expansion. On the accessible time scales, the MDF $n_{k,\sigma}$ of the repulsive gas still undergoes changes, yet in the edge of the MDF, the curves at the longest times coincide (see also [1]). The case of $U > 0$ thus sets an example where the quantum simulation with ultracold atomic gases could help us to go to longer times than what is currently possible with numerical methods to clarify the asymptotic behavior of the MDF (compare the relaxation dynamics problem studied in Ref. [4]). Note that for the expansion of a repulsive gas with initial densities $\langle n_i \rangle \leq 1$, the double-occupancy *decreases* [1], in contrast to the attractive case, discussed in the main text. In the attractive case, the survival of a certain fraction of the initial double occupancy is expected due to the presence of pairs.

[1] F. Heidrich-Meisner, M. Rigol, A. Muramatsu, A. E. Feiguin, and E. Dagotto, Phys. Rev. A **78**, 013620 (2008).
[2] U. Schollwöck, Ann. Phys. (NY) **326**, 96 (2011).
[3] J. Kajala, F. Massel, and P. Törmä, Phys. Rev. A **84**, 041601(R) (2011).
[4] S. Trotzky, Y.-A. Chen, A. Flesch, I. P. McCulloch, U. Schollwöck, J. Eisert, and I. Bloch, Nature Phys. **8**, 325 (2012).

5   Summary and Outlook

In this work we studied transport properties and real-time dynamics of low-dimensional quantum magnets and ultra-cold atomic gases in optical lattices. The main results, as well as a recurrent theme, were the identification of ballistic regimes based on the analysis of the real-time evolution of density profiles and the theoretical explanation and interpretation of the expansion velocities.

For instance, the dynamics of energy wave-packets in the anisotropic Heisenberg chain was first analyzed in the exactly solvable XY-limit by diagonalizing the lattice Hamiltonian and in the low energy limit using Luttinger liquid theory. We then proceeded by analyzing the wave-packet dynamics far from equilibrium for the fully interacting lattice model using adaptive time-dependent DMRG. The expansion velocities far from equilibrium could then be explained in terms of the differences between the momentum distribution function of the initial state and those of the ground state, combined with the sound velocity from Luttinger liquid theory.

In the case of cold atomic gases we focussed on the case of the sudden expansion of an initially trapped cloud of particles. One reason for this approach is that sudden expansion experiments recently gained interest in the field of cold atomic gases as a technique to probe the non-equilibrium dynamics of the underlying lattice Hamiltonian [7]. Here we investigated the sudden expansion for three installations of the Hubbard model, namely a spin-balanced Fermi gas with repulsive interactions, a bosonic gas with repulsive interactions and spin-imbalanced Fermi gases with attractive interactions. In each of the three cases we investigated a different aspect of the non-equilibrium dynamics.

First, we considered a spin-balanced fermionic gas with repulsive interactions and analyzed the radius of the expanding cloud. We found purely ballistic dynamics whenever the initial density is smaller or equal to one, independently of the strength of the repulsive interaction. We showed that the average expansion velocity, which we define as slope of the cloud's radius, is determined by the initial conditions over a large parameter range. This allows to use the expansion velocity as a probe of the initial momentum distribution, for instance in the search for quantum phase transitions. To give an example, we showed that the expansion velocity for the expansion from the Mott insulating phase is completely determined by symmetry with $V_{\mathrm{ex}} = \sqrt{2}J$ independently of the strength of interactions as a signature.

The expansion of hardcore bosons exhibits intriguing physical features

such as the dynamical emergence of coherence [78, 79, 80] or the fermion-ization of the momentum distribution [223, 224]. We studied the sudden expansion of both hardcore and softcore bosons, which where initially pre-pared in a Fock state, over a wide range of repulsive interaction strengths. We investigated the dynamical emergence of a quasi-condensate at finite momenta and the expansion velocity in the presence of defects likely to be present in a typical experiment. We find that the phenomenon of dynamical quasi-condensation is very robust for small systems at large interactions. Fur-thermore we show that an admixture of defects influences the time-dependent radius of the cloud, which can serve as an indicator of the doublon density in the initial state.

The third type of sudden expansions studied is that of spin imbalanced fermions in the presence of attractive interactions. This was motivated by the ongoing search for the FFLO state [94]. The FFLO phase [89, 90], origi-nally proposed to allow for pair condensation at a finite polarization has not yet been detected experimentally in one-dimensional Fermi gases [95], even though the whole partially polarized phase had been shown theoretically to be of FFLO-type [94]. Here we investigated the time-dependent momentum distribution functions and the spatial structure of the wave function to see whether a sudden expansion experiment can unveil a "smoking gun signa-ture". While features of the FFLO phase, such as the finite center-of-mass momentum of the pairs, and the modulated spin texture, are quickly lost in the expansion, we find that all relevant momentum distribution functions quickly converge to stationary forms. The stationary form is then suggested to exhibit signatures of conserved the quantities from the Bethe ansatz so-lution [27]. Its distinct features and the fast convergence should make the stationary momentum distribution observable and it may even serve as an indirect indicator of presence of FFLO-correlations in the initial state.

Yet, all real-time dynamics presented in this thesis take place at zero tem-perature. For the studies of low-dimensional quantum magnets we employed linear response theory to discuss the transport properties at finite tempera-tures. We revisited the long standing question of the temperature dependent spin Drude weight D_s in the anisotropic spin-1/2 Heisenberg chain and ob-tained reasonable agreement with recent numerical [58] and analytical results [59]. Especially for the controversially discussed point of isotropic exchange interactions our data suggests a finite Drude weight at large and interme-diate temperatures, in agreement with the DMRG data from Ref. [58]. We also showed how problematic the finite size extrapolation at this isotropic point becomes when using a canonical ensemble [60]. This open question

necessitates a conclusive theory for $D_s = D_s(1/L)$.

We then moved on to study transverse components of the current-current correlation functions. These are usually neglected as one considers only a Zeeman field B^z in the theory. Including a transverse field B^x gives rise to a qualitatively different behavior of the different spatial components of the current-current correlation function. Here, we could show that the previously unexplored transverse current-current correlation function oscillates with a non-trivial frequency in the presence of a transverse magnetic field. These oscillations become coherent at low-temperatures and for large B^z. We also showed they could also be observed in simulations of the time-dependent current density's transverse component at zero temperature using time-dependent DMRG.

Finally we calculated the response functions for spin and heat transport in dimerized spin chains which feature a field-induced gapless phase. This work was motivated by recent experimental evidence for a similar phase diagram in organic superconductors. We find that the spin and heat conductivity are both greatly enhanced throughout the field-induced gapless phase due to clear signatures of the phase transition in the current-current correlation functions. While the study of spin and heat conductivity in the field-induced gapless phase of dimerized spin chains, and the analysis of the transverse current-current correlation functions yielded interesting results, we had to resort to the exact diagonalization of small systems in both cases.

While there are still interesting problems at zero temperature like the dynamics of energy wave-packets in spin ladders, spin chains with impurities or the sudden expansion of bosons starting from their groundstate, the road to improved predictions for experiments and probably additional fundamental insights is clearly to include finite temperatures in the real-time simulations. For the quantum magnets, we have the copper-based materials in mind most of the time [3]. Due to exchange couplings of the order of a thousand Kelvin, experiments at room temperature are performed at a very small temperature for this specific material. Ultra-cold atomic gases [21] are cooled to the coldest temperatures technology allows. Still, both types of systems have small thermal fluctuations, which might or might not change the physics compared to the results we obtained here. For instance, the dynamics of spin wave-packets in the Heisenberg chain suggests ballistic dynamics in the whole gapless phase [48], but there is also evidence for a large diffusive contribution to spin transport at low but finite temperatures [163, 164]. If such a diffusive contribution is an inherent feature of the Heisenberg chain, it should be observable simulating the wave-packet dynamics at finite temperature.

One extension of time-dependent DMRG to describe states at finite temperature is the so-called purification method [225, 165]. It is based on the mathematical fact that any mixed state can be rewritten as a pure state on a larger Hilbert space. For practical purposes one uses an exact copy of the system to serve as auxiliary space, then writes down a state where the reduced density matrix of the system $\rho_{\mathrm{sys}} = Tr_{aux}\rho$ is proportional to unity. Since for a thermal ensemble, $\rho = e^{-\beta H}$, this is a state at infinite temperature. Now, evolving the state in imaginary time down to a smaller β can be seen as cooling. For instance, this approach has been applied to calculate the specific heat of a Heisenberg chain [165] and time-dependent correlation functions at finite temperature [226]. However, cooling down to the desired temperature first and then performing the time evolution may generate significantly more entanglement than a time evolution at zero temperature [226]. One way to circumvent the increased entanglement growth has been discovered by realizing that arbitrary unitary transformation acting on the auxiliary system do not change the state of the system. Such transformations have been used in Ref. [58] to calculate the spin Drude weight by reaching the long time limit of the current-current correlation function. While a complete understanding of the entanglement growth of purified mixed states is highly desirable, simply finding the right unitary for the system of interest might allow one to simulate the setups of the chapters 3.8, 4.2, 4.3 and 4.4 at a small but finite temperature.

A conceptually different approach are so called minimally entangled typical thermal states (METTS). Within this approach the full ensemble is approximated by a set of the least entangled states much smaller than the full Hilbert space. The algorithm is formulated in Ref. [227] along with a proof of the ergodicity of this method. Details about the implementation and the convergence with respect to the size of the ensemble can be found in Ref. [228]. The outline of the algorithm is the following: One starts from a classical state with no entanglement and calculates the imaginary time evolution until up to the final temperature. Then the next classical state is obtained by consecutive local projective measurements on every lattice site. While METTS have been used to calculate the specific heat of spin chains at lower temperatures [227] than previously achieved by purification [165], the applicability beyond spin chains has to be investigated. Yet, time-evolution of a METTS-ensemble might be a serious competitor to the purification approach outlined above.

References

[1] X. Zotos and P. Prelovsek, *in: Transport in one dimensional quantum systems*, Chapter 11, Kluwer, Doodrecht, 2003.

[2] F. Heidrich-Meisner, A. Honecker, and W. Brenig, The European Physical Journal - Special Topics **151**, 135 [2007].

[3] C. Hess, The European Physical Journal - Special Topics **151**, 73 [2007].

[4] S. Andergassen, V. Meden, H. Schoeller, J. Splettstoesser, and M. R. Wegewijs, Nanotechnology **21**, 272001 [2010].

[5] Y. V. Nazarov and Y. M. Blanter, *Quantum Transport: Introduction to Nanoscience*, Cambridge University Press, 2009.

[6] A. Polkovnikov, K. Sengupta, A. Silva, and M. Vengalattore, Reviews of Modern Physics **83**, 863 [2011].

[7] U. Schneider, L. Hackermüller, J. P. Ronzheimer, S. Will, S. Braun, T. Best, I. Bloch, E. Demler, S. Mandt, D. Rasch, and A. Rosch, Nature Physics **8**, 213 [2012].

[8] T. Giamarchi, *Quantum Physics in One Dimension*, Oxford University Press, 1st edition, 2004.

[9] S. Tomonaga, Progress of Theoretical Physics **5**, 544 [1951].

[10] J. M. Luttinger, Journal of Mathematical Physics **4**, 1154 [1963].

[11] E. Dagotto and T. M. Rice, Science **271**, 618 [1996].

[12] E. Dagotto, Reports on Progress in Physics **62**, 1525 [1999].

[13] H. F. Fong, P. Bourges, Y. Sidis, L. P. Regnault, A. Ivanov, G. D. Gu, N. Koshizuka, and B. Keimer, Nature **398**, 588 [1999].

[14] H. F. Fong, P. Bourges, Y. Sidis, L. P. Regnault, J. Bossy, A. Ivanov, D. L. Milius, I. A. Aksay, and B. Keimer, Physical Review B **61**, 14773 [2000].

[15] P. Bourges, Y. Sidis, H. F. Fong, L. P. Regnault, J. Bossy, A. Ivanov, and B. Keimer, Science **288**, 1234 [2000].

[16] U. Schollwöck, J. Richter, D. J. J. Farnell, and R. F. Bishop, editors, *Quantum Magnetism*, LNP 645, Springer, 1st edition, 2004.

[17] M. Matsuda, K. Katsumata, R. S. Eccleston, S. Brehmer, and H. Mikeska, Physical Review B **62**, 8903 [2000].

[18] K. R. Thurber, A. W. Hunt, T. Imai, and F. C. Chou, Physical Review Letters **87**, 247202 [2001].

[19] H. O. H. Churchill, F. Kuemmeth, J. W. Harlow, A. J. Bestwick, E. I. Rashba, K. Flensberg, C. H. Stwertka, T. Taychatanapat, S. K. Watson, and C. M. Marcus, Phys. Rev. Lett. **102**, 166802 [2009].

[20] P. Gambardella, Nature Materials **5**, 431 [2006].

[21] I. Bloch, J. Dalibard, and W. Zwerger, Reviews of Modern Physics **80**, 885 [2008].

[22] P. W. Anderson, Physical Review **115**, 2 [1959].

[23] H. Mikeska and A. Kolezhuk, in *Quantum Magnetism*, edited by U. Schollwöck, J. Richter, D. Farnell, and R. Bishop, Springer, 2004, LNP 645.

[24] S. Trotzky, P. Cheinet, S. Fölling, M. Feld, U. Schnorrberger, A. M. Rey, A. Polkovnikov, E. A. Demler, M. D. Lukin, and I. Bloch, Science **319**, 295 [2008].

[25] T. Stapelfeldt, R. Wieser, E. Y. Vedmedenko, and R. Wiesendanger, Physical Review Letters **107**, 027203 [2011].

[26] J. Hubbard, Proceedings of the Royal Society A: Mathematical, Physical and Engineering Sciences **276**, 238 [1963].

[27] F. H. L. Essler, H. Frahm, F. Göhmann, A. Klümper, and V. E. Korepin, *The One-Dimensional Hubbard Model*, Cambridge University Press, 2005.

[28] H. Bethe, Zeitschrift f?r Physik **71**, 205 [1931].

[29] A. W. Sandvik, AIP Conference Proceedings **1297**, 135 [2010].

[30] S. R. White, Physical Review Letters **69**, 2863 [1992].

[31] G. D. Mahan, *Many-Particle Physics*, Springer, 2000.

[32] W. Kohn, Physical Review **133**, A171 [1964].

[33] K. Fabricius and B. M. McCoy, Physical Review B **57**, 8340 [1998].

[34] S. R. White and A. E. Feiguin, Physical Review Letters **93**, 076401 [2004].

[35] A. J. Daley, C. Kollath, U. Schollwöck, and G. Vidal, Journal of Statistical Mechanics: Theory and Experiment **2004**, P04005.

[36] X. Zotos, F. Naef, and P. Prelovsek, Physical Review B **55**, 11029 [1997].

[37] A. Klümper and K. Sakai, Journal of Physics A: Mathematical and General **35**, 2173 [2002].

[38] F. Heidrich-Meisner, A. Honecker, D. C. Cabra, and W. Brenig, Physical Review B **66**, 140406 [2002].

[39] K. Sakai and A. Klümper, Journal of Physics A: Mathematical and General **36**, 11617 [2003].

[40] B. N. Narozhny, A. J. Millis, and N. Andrei, Physical Review B **58**, R2921 [1998].

[41] X. Zotos, Physical Review Letters **82**, 1764 [1999].

[42] J. V. Alvarez and C. Gros, Physical Review Letters **88**, 077203 [2002].

[43] F. Heidrich-Meisner, A. Honecker, D. C. Cabra, and W. Brenig, Physical Review B **68**, 134436 [2003].

[44] D. A. Rabson, B. N. Narozhny, and A. J. Millis, Physical Review B **69**, 054403 [2004].

[45] J. Benz, T. Fukui, A. Klümper, and C. Scheeren, J. Phys. Soc. Jpn. Suppl. **74**, 181 [2005].

[46] D. Heidarian and S. Sorella, Physical Review B **75**, 241104 [2007].

[47] D. Gobert, C. Kollath, U. Schollwöck, and G. Schütz, Physical Review E **71**, 036102 [2005].

[48] S. Langer, F. Heidrich-Meisner, J. Gemmer, I. P. McCulloch, and U. Schollwöck, Physical Review B **79**, 214409 [2009].

[49] S. Jesenko and M. Žnidarič, Physical Review B **84**, 174438 [2011].

[50] G. Benenti, G. Casati, T. Prosen, and D. Rossini, EPL (Europhysics Letters) **85**, 37001 [2009].

[51] T. Prosen and M. Žnidarič, Journal of Statistical Mechanics: Theory and Experiment **2009**, P02035 [2009].

[52] T. Prosen, Physical Review Letters **107**, 137201 [2011].

[53] A. Sologubenko, T. Lorenz, H. Ott, and A. Freimuth, Journal of Low Temperature Physics **147**, 387 [2007].

[54] M. Otter, V. Krasnikov, D. Fishman, M. Pshenichnikov, R. Saint-Martin, A. Revcolevschi, and P. van Loosdrecht, Journal of Magnetism and Magnetic Materials **321**, 796 [2009].

[55] M. Otter, G. Athanasopoulos, N. Hlubek, M. Montagnese, M. Labois, D. Fishman, F. de Haan, S. Singh, D. Lakehal, J. Giapintzakis, C. Hess, A. Revcolevschi, and P. van Loosdrecht, International Journal of Heat and Mass Transfer **55**, 2531 [2012].

[56] M. Klanjšek, H. Mayaffre, C. Berthier, M. Horvatić, B. Chiari, O. Piovesana, P. Bouillot, C. Kollath, E. Orignac, R. Citro, and T. Giamarchi, Physical Review Letters **101**, 137207 [2008].

[57] C. Rüegg, K. Kiefer, B. Thielemann, D. F. McMorrow, V. Zapf, B. Normand, M. B. Zvonarev, P. Bouillot, C. Kollath, T. Giamarchi, S. Capponi, D. Poilblanc, D. Biner, and K. W. Krämer, Physical Review Letters **101**, 247202 [2008].

[58] C. Karrasch, J. H. Bardarson, and J. E. Moore, Physical Review Letters **108**, 227206 [2012].

[59] T. Prosen, Physical Review Letters **106**, 217206 [2011].

[60] J. Herbrych, P. Prelovšek, and X. Zotos, Physical Review B **84**, 155125 [2011].

[61] K. B. Davis, M. O. Mewes, M. R. Andrews, N. J. van Druten, D. S. Durfee, D. M. Kurn, and W. Ketterle, Physical Review Letters **75**, 3969 [1995].

[62] M. H. Anderson, J. R. Ensher, M. R. Matthews, C. E. Wieman, and E. A. Cornell, Science **269**, 198 [1995].

[63] C. C. Bradley, C. A. Sackett, J. J. Tollett, and R. G. Hulet, Physical Review Letters **75**, 1687 [1995].

[64] M. Greiner, O. Mandel, T. Esslinger, T. W. Hänsch, and I. Bloch, Nature **415**, 39 [2002].

[65] D. Jaksch, C. Bruder, J. I. Cirac, C. W. Gardiner, and P. Zoller, Physical Review Letters **81**, 3108 [1998].

[66] B. DeMarco and D. S. Jin, Science **285**, 1703 [1999].

[67] A. G. Truscott, K. E. Strecker, W. I. McAlexander, G. B. Partridge, and R. G. Hulet, Science **291**, 2570 [2001].

[68] D. C. McKay and B. DeMarco, Reports on Progress in Physics **74**, 054401 [2011].

[69] R. Jördens, N. Strohmaier, K. Günter, H. Moritz, and T. Esslinger, Nature **455**, 204 [2008].

[70] U. Schneider, L. Hackermüller, S. Will, T. Best, I. Bloch, T. A. Costi, R. W. Helmes, D. Rasch, and A. Rosch, Science **322**, 1520 [2008].

[71] A. Sommer, M. Ku, G. Roati, and M. W. Zwierlein, Nature **472**, 201 [2011].

[72] M. Greiner, O. Mandel, T. W. Hänsch, and I. Bloch, Nature **419**, 51 [2002].

[73] S. Trotzky, Y. Chen, A. Flesch, I. P. McCulloch, U. Schollwöck, J. Eisert, and I. Bloch, Nature Physics [2012].

[74] T. Kinoshita, T. Wenger, and D. S. Weiss, Nature **440**, 900 [2006].

[75] P. Medley, D. M. Weld, H. Miyake, D. E. Pritchard, and W. Ketterle, Physical Review Letters **106**, 195301 [2011].

[76] J. A. Joseph, J. E. Thomas, M. Kulkarni, and A. G. Abanov, Physical Review Letters **106**, 150401 [2011].

[77] T. Anker, M. Albiez, R. Gati, S. Hunsmann, B. Eiermann, A. Trombettoni, and M. K. Oberthaler, Physical Review Letters **94**, 020403 [2005].

[78] M. Rigol and A. Muramatsu, Physical Review Letters **93**, 230404 [2004].

[79] K. Rodriguez, S. R. Manmana, M. Rigol, R. M. Noack, and A. Muramatsu, New Journal of Physics **8**, 169 [2006].

[80] I. Hen and M. Rigol, Physical Review Letters **105**, 180401 [2010].

[81] K. Yang, Physical Review B **63**, 140511 [2001].

[82] A. E. Feiguin and F. Heidrich-Meisner, Physical Review B **76**, 220508 [2007].

[83] M. Tezuka and M. Ueda, Physical Review Letters **100**, 110403 [2008].

[84] G. G. Batrouni, M. H. Huntley, V. G. Rousseau, and R. T. Scalettar, Physical Review Letters **100**, 116405 [2008].

[85] M. Rizzi, M. Polini, M. A. Cazalilla, M. R. Bakhtiari, M. P. Tosi, and R. Fazio, Physical Review B **77**, 245105 [2008].

[86] A. Lüscher, R. M. Noack, and A. M. Läuchli, Physical Review A **78**, 013637 [2008].

[87] M. Casula, D. M. Ceperley, and E. J. Mueller, Physical Review A **78**, 033607 [2008].

[88] D. E. Sheehy and L. Radzihovsky, Annals of physics **322**, 1790 [2007].

[89] P. Fulde and R. A. Ferrell, Physical Review **135**, A550 [1964].

[90] A. I. Larkin and Y. N. Ovchinnikov, Zh. Eksp. Teor. Fiz. **47**, 1136 [1964].

[91] G. Orso, Physical Review Letters **98**, 070402 [2007].

[92] H. Hu, L. X.-J., and P. Drummond, Physical Review Letters **98**, 070403 [2007].

[93] F. Heidrich-Meisner, G. Orso, and A. E. Feiguin, Physical Review A **81**, 053602 [2010].

[94] A. E. Feiguin, F. Heidrich-Meisner, G. Orso, and W. Zwerger, in *The BCS-BEC Crossover and the Unitary Fermi Gas*, edited by W. Zwerger, Springer, Berlin, Heidelberg, 2012, LNP 836.

[95] Y.-a. Liao, A. S. C. Rittner, T. Paprotta, W. Li, G. B. Partridge, R. G. Hulet, S. K. Baur, and E. J. Mueller, Nature **467**, 567 [2010].

[96] U. Schollwöck, Annals of Physics **326**, 96 [2011].

[97] I. P. McCulloch and M. Gulácsi, Europhysics Letters (EPL) **57**, 852 [2002].

[98] D. C. Cabra, A. Honecker, and P. Pujol, Physical Review B **58**, 6241 [1998].

[99] A. Honecker, Physical Review B **59**, 6790 [1999].

[100] J. Richter, J. Schulenburg, A. Honecker, and D. Schmalfuß, Physical Review B **70**, 174454 [2004].

[101] M. Troyer and U. Wiese, Physical Review Letters **94**, 170201 [2005].

[102] U. Schollwöck, Reviews of Modern Physics **77**, 259 [2005].

[103] I. Peschel, X. Wang, M. Kaulke, and K. Hallberg, *Density-matrix renormalization: a new numerical method in physics*, LNP 528, Springer, 1999.

[104] G. Vidal, Physical Review Letters **93**, 040502 [2004].

[105] C. Kollath, U. Schollwöck, and W. Zwerger, Physical Review Letters **95**, 176401 [2005].

[106] C. Kollath and U. Schollwöck, New Journal of Physics **8**, 220 [2006].

[107] A. Kleine, C. Kollath, I. P. McCulloch, T. Giamarchi, and U. Schollwöck, Physical Review A **77**, 013607 [2008].

[108] A. Flesch, M. Cramer, I. P. McCulloch, U. Schollwöck, and J. Eisert, Physical Review A **78**, 033608 [2008].

[109] M. Cramer, A. Flesch, I. P. McCulloch, U. Schollwöck, and J. Eisert, Physical Review Letters **101**, 063001 [2008].

[110] E. Boulat, H. Saleur, and P. Schmitteckert, Physical Review Letters **101**, 140601 [2008].

[111] F. Heidrich-Meisner, A. E. Feiguin, and E. Dagotto, Physical Review B **79**, 235336 [2009].

[112] S. R. White, Physical Review B **72**, 180403 [2005].

[113] S. R. White, Physics Reports **301**, 187 [1998].

[114] J. D. Bekenstein, Physical Review D **7**, 2333 [1973].

[115] M. Srednicki, Physical Review Letters **71**, 666 [1993].

[116] M. B. Plenio, J. Eisert, J. Dreißig, and M. Cramer, Physical Review Letters **94**, 060503 [2005].

[117] T. Barthel, M. Chung, and U. Schollwöck, Physical Review A **74**, 022329 [2006].

[118] P. Calabrese and J. Cardy, Journal of Statistical Mechanics: Theory and Experiment **2004**, P06002.

[119] J. Eisert, M. Cramer, and M. B. Plenio, Reviews of Modern Physics **82**, 277 [2010].

[120] N. Schuch, M. M. Wolf, F. Verstraete, and J. I. Cirac, Physical Review Letters **100**, 030504 [2008].

[121] F. Verstraete and J. I. Cirac, Physical Review B **73**, 094423 [2006].

[122] I. Affleck, T. Kennedy, E. H. Lieb, and H. Tasaki, Physical Review Letters **59**, 799 [1987].

[123] M. Fannes, B. Nachtergaele, and R. Werner, Communications in Mathematical Physics **144**, 443 [1992].

[124] S. Östlund and S. Rommer, Physical Review Letters **75**, 3537 [1995].

[125] J. Dukelsky, M. A. Martín-Delgado, T. Nishino, and G. Sierra, Europhysics Letters (EPL) **43**, 457 [1998].

[126] M. Suzuki, Progress of Theoretical Physics **56**, 1454 [1976].

[127] M. Suzuki, Journal of Mathematical Physics **32**, 400 [1991].

[128] M. Hochbruck and C. Lubich, SIAM Journal on Numerical Analysis **34**, 1911 [1997].

[129] T. J. Park and J. C. Light, The Journal of Chemical Physics **85**, 5870 [1986].

[130] Y. Saad, *Numerical Methods for Large Eigenvalue Problems, Revised Edition*, SIAM - Society for Industrial & Applied Mathematics, revised edition edition, 2011.

[131] I. P. McCulloch, http://physics.uq.edu.au/people/ianmcc/mptoolkit/ .

[132] G. Vidal, Physical Review Letters **91**, 147902 [2003].

[133] M. C. Bañuls, M. B. Hastings, F. Verstraete, and J. I. Cirac, Physical Review Letters **102**, 240603 [2009].

[134] M. J. Hartmann, J. Prior, S. R. Clark, and M. B. Plenio, Physical Review Letters **102**, 057202 [2009].

[135] P. Calabrese and J. Cardy, Journal of Statistical Mechanics: Theory and Experiment **2005**, P04010.

[136] J. Eisert and T. J. Osborne, Physical Review Letters **97**, 150404 [2006].

[137] G. D. Chiara, S. Montangero, P. Calabrese, and R. Fazio, Journal of Statistical Mechanics: Theory and Experiment **2006**, P03001.

[138] I. Peschel and V. Eisler, Journal of Physics A: Mathematical and Theoretical **45**, 155301 [2012].

[139] P. Calabrese and J. Cardy, Journal of Statistical Mechanics: Theory and Experiment **2007**, P10004.

[140] A. Alex, M. Kalus, A. Huckleberry, and J. von Delft, Journal of Mathematical Physics **52**, 023507 [2011].

[141] I. P. Mcculloch and M. Gulácsi, Philosophical Magazine Letters **81**, 447 [2001].

[142] J. Serre, *Linear Representations of Finite Groups (Graduate Texts in Mathematics)*, Springer, 1977.

[143] E. P. Wigner, *Group Theory and Its Application to the Quantum Mechanics of Atomic Spectra*, Academic Press, 1959.

[144] J. F. Cornwell, *Group Theory in Physics: An Introduction*, Academic Press, 1997.

[145] J. J. Sakurai, *Modern Quantum Mechanics*, Prentice Hall, revised edition, 1993.

[146] A. Weichselbaum, arXiv:1202.5664 [2012].

[147] I. U. Heilmann, G. Shirane, Y. Endoh, R. J. Birgeneau, and S. L. Holt, Physical Review B **18**, 3530 [1978].

[148] D. A. Tennant, R. A. Cowley, S. E. Nagler, and A. M. Tsvelik, Physical Review B **52**, 13368 [1995].

[149] H. Kühne, A. A. Zvyagin, M. Günther, A. P. Reyes, P. L. Kuhns, M. M. Turnbull, C. P. Landee, and H. Klauss, Physical Review B **83**, 100407 [2011].

[150] H. J. Schulz, Physical Review B **34**, 6372 [1986].

[151] A. M. Tsvelik, *Quantum Field Theory in Condensed Matter Physics*, Cambridge University Press, 2nd edition, 2006.

[152] S. Grossjohann and W. Brenig, Physical Review B **79**, 094409 [2009].

[153] D. C. Johnston, R. K. Kremer, M. Troyer, X. Wang, A. Klümper, S. L. Bud'ko, A. F. Panchula, and P. C. Canfield, Physical Review B **61**, 9558 [2000].

[154] N. Hlubek, P. Ribeiro, R. Saint-Martin, A. Revcolevschi, G. Roth, G. Behr, B. Büchner, and C. Hess, Physical Review B **81**, 020405 [2010].

[155] A. V. Sologubenko, E. Felder, K. Giannò, H. R. Ott, A. Vietkine, and A. Revcolevschi, Physical Review B **62**, R6108 [2000].

[156] N. Hlubek, X. Zotos, S. Singh, R. Saint-Martin, A. Revcolevschi, B. Büchner, and C. Hess, Journal of Statistical Mechanics: Theory and Experiment **2012**, P03006.

[157] M. Steiner, J. Villain, and C. Windsor, Advances in Physics **25**, 87 [1976].

[158] H. Mikeska and M. Steiner, Advances in Physics **40**, 191 [1991].

[159] G. Jo, Y. Lee, J. Choi, C. A. Christensen, T. H. Kim, J. H. Thywissen, D. E. Pritchard, and W. Ketterle, Science **325**, 1521 [2009].

[160] K. Kim, M. Chang, S. Korenblit, R. Islam, E. E. Edwards, J. K. Freericks, G. Lin, L. Duan, and C. Monroe, Nature **465**, 590 [2010].

[161] J. Simon, W. S. Bakr, R. Ma, M. E. Tai, P. M. Preiss, and M. Greiner, Nature **472**, 307 [2011].

[162] S. Mukerjee and B. S. Shastry, Physical Review B **77**, 245131 [2007].

[163] J. Sirker, R. G. Pereira, and I. Affleck, Physical Review Letters **103**, 216602 [2009].

[164] S. Grossjohann and W. Brenig, Physical Review B **81**, 012404 [2010].

[165] A. E. Feiguin and S. R. White, Physical Review B **72**, 220401 [2005].

[166] R. Steinigeweg, S. Langer, F. Heidrich-Meisner, I. P. McCulloch, and W. Brenig, Physical Review Letters **106**, 160602 [2011].

[167] F. Heidrich-Meisner, A. Honecker, and W. Brenig, Physical Review B **71**, 184415 [2005].

[168] C. Hess, C. Baumann, U. Ammerahl, B. Büchner, F. Heidrich-Meisner, W. Brenig, and A. Revcolevschi, Physical Review B **64**, 184305 [2001].

[169] H. Bruus and K. Flensberg, *Many-body Quantum Theory In Condensed Matter Physics: An Introduction*, Oxford University Press, 2004.

[170] J. M. Luttinger, Physical Review **135**, A1505 [1964].

[171] P. Mazur, Physica **43**, 533 [1969].

[172] M. Suzuki, Physica **51**, 277 [1971].

[173] D. Forster, *Hydrodynamic Fluctuations, Broken Symmetry, and Correlation Functions*, Westview Press, new ed edition, 1995.

[174] M. Grabowski and P. Mathieu, Annals of Physics **243**, 299 [1995].

[175] B. S. Shastry and B. Sutherland, Physical Review Letters **65**, 243 [1990].

[176] D. J. Scalapino, S. R. White, and S. Zhang, Physical Review B **47**, 7995 [1993].

[177] S. Fujimoto and N. Kawakami, Journal of Physics A: Mathematical and General **31**, 465 [1998].

[178] B. Thielemann, C. Rüegg, K. Kiefer, H. M. Rønnow, B. Normand, P. Bouillot, C. Kollath, E. Orignac, R. Citro, T. Giamarchi, A. M. Läuchli, D. Biner, K. W. Krämer, F. Wolff-Fabris, V. S. Zapf, M. Jaime, J. Stahn, N. B. Christensen, B. Grenier, D. F. McMorrow, and J. Mesot, Physical Review B **79**, 020408 [2009].

[179] T. Lorenz, O. Heyer, M. Garst, F. Anfuso, A. Rosch, C. Rüegg, and K. Krämer, Physical Review Letters **100**, 067208 [2008].

[180] F. Anfuso, M. Garst, A. Rosch, O. Heyer, T. Lorenz, C. Rüegg, and K. Krämer, Physical Review B **77**, 235113 [2008].

[181] A. V. Sologubenko, T. Lorenz, J. A. Mydosh, B. Thielemann, H. M. Rønnow, C. Rüegg, and K. W. Krämer, Physical Review B **80**, 220411 [2009].

[182] A. V. Sologubenko, K. Giannó, H. R. Ott, U. Ammerahl, and A. Revcolevschi, Physical Review Letters **84**, 2714 [2000].

[183] J. G. Bednorz and K. A. Müller, Zeitschrift fur Physik B Condensed Matter **64**, 189 [1986].

[184] T. Osafune, N. Motoyama, H. Eisaki, and S. Uchida, Physical Review Letters **78**, 1980 [1997].

[185] N. Nücker, M. Merz, C. A. Kuntscher, S. Gerhold, S. Schuppler, R. Neudert, M. S. Golden, J. Fink, D. Schild, S. Stadler, V. Chakarian, J. Freeland, Y. U. Idzerda, K. Conder, M. Uehara, T. Nagata, J. Goto, J. Akimitsu, N. Motoyama, H. Eisaki, S. Uchida, U. Ammerahl, and A. Revcolevschi, Physical Review B **62**, 14384 [2000].

[186] L. P. Regnault, J. P. Boucher, H. Moudden, J. E. Lorenzo, A. Hiess, U. Ammerahl, G. Dhalenne, and A. Revcolevschi, Physical Review B **59**, 1055 [1999].

[187] M. Matsuda, T. Yosihama, K. Kakurai, and G. Shirane, Physical Review B **59**, 1060 [1999].

[188] U. Ammerahl, B. Büchner, L. Colonescu, R. Gross, and A. Revcolevschi, Physical Review B **62**, 8630 [2000].

[189] C. Hess, private communication .

[190] C. Hess, H. ElHaes, A. Waske, B. Büchner, C. Sekar, G. Krabbes, F. Heidrich-Meisner, and W. Brenig, Physical Review Letters **98**, 027201 [2007].

[191] S. Langer, M. Heyl, I. P. McCulloch, and F. Heidrich-Meisner, Physical Review B **84**, 205115 [2011].

[192] W. Feller, *Introduction to Probability Theory and Its Applications: 1*, John Wiley & Sons, 3rd edition, 1968.

[193] F. Schwabl, *Quantum Mechanics*, Springer Berlin Heidelberg, 4th edition, 2007.

[194] J. Kempe, Contemporary Physics **44**, 307 [2003].

[195] J. J. Duderstadt and W. R. Martin, *Transport Theory*, John Wiley & Sons Inc, 1979.

[196] I. Bloch, J. Dalibard, and S. Nascimbène, Nature Physics **8**, 267 [2012].

[197] Einstein, Sitzungsber Preuss Akad Wiss **Bericht 3**, 18 [1925].

[198] F. Dalfovo, S. Giorgini, L. P. Pitaevskii, and S. Stringari, Reviews of Modern Physics **71**, 463 [1999].

[199] H. T. C. Stoof, M. Houbiers, C. A. Sackett, and R. G. Hulet, Physical Review Letters **76**, 10 [1996].

[200] P. Courteille, R. S. Freeland, D. J. Heinzen, F. A. van Abeelen, and B. J. Verhaar, Physical Review Letters **81**, 69 [1998].

[201] S. Inouye, M. R. Andrews, J. Stenger, H. Miesner, D. M. Stamper-Kurn, and W. Ketterle, Nature **392**, 151 [1998].

[202] M. Rigol, V. Dunjko, and M. Olshanii, Nature **452**, 854 [2008].

[203] F. Heidrich-Meisner, M. Rigol, A. Muramatsu, A. E. Feiguin, and E. Dagotto, Physical Review A **78**, 013620 [2008].

[204] F. Heidrich-Meisner, S. R. Manmana, M. Rigol, A. Muramatsu, A. E. Feiguin, and E. Dagotto, Physical Review A **80**, 041603 [2009].

[205] D. Karlsson, C. Verdozzi, M. M. Odashima, and K. Capelle, EPL (Europhysics Letters) **93**, 23003 [2011].

[206] J. Kajala, F. Massel, and P. Törmä, Physical Review Letters **106**, 206401 [2011].

[207] L. Pezzè, L. Pitaevskii, A. Smerzi, S. Stringari, G. Modugno, E. de Mirandes, F. Ferlaino, H. Ott, G. Roati, and M. Inguscio, Physical Review Letters **93**, 120401 [2004].

[208] H. Ott, E. de Mirandes, F. Ferlaino, G. Roati, G. Modugno, and M. Inguscio, Physical Review Letters **92**, 160601 [2004].

[209] M. Rigol and A. Muramatsu, Physical Review A **69**, 053612 [2004].

[210] R. Grimm, M. Weidemüller, and Y. B. Ovchinnikov, Advances in Atomic, Molecular and Optical Physics **42**, 95 [2000].

[211] N. W. Ashcroft and N. D. Mermin, *Solid State Physics*, Cengage Learning Emea, 1976.

[212] H. Feshbach, Annals of Physics **5**, 357 [1958].

[213] E. Timmermans, K. Furuya, P. W. Milonni, and A. K. Kerman, Physics Letters A **285**, 228 [2001].

[214] R. Duine and H. Stoof, Physics Reports **396**, 115 [2004].

[215] T. Köhler, K. Góral, and P. S. Julienne, Reviews of Modern Physics **78**, 1311 [2006].

[216] M. Köhl, H. Moritz, T. Stöferle, K. Günter, and T. Esslinger, Physical Review Letters **94**, 080403 [2005].

[217] U. Schneider, private communication .

[218] M. Rigol, Physical Review A **72**, 063607 [2005].

[219] M. P. A. Fisher, P. B. Weichman, G. Grinstein, and D. S. Fisher, Physical Review B **40**, 546 [1989].

[220] T. D. Kühner and H. Monien, Physical Review B **58**, R14741 [1998].

[221] T. D. Kühner, S. R. White, and H. Monien, Physical Review B **61**, 12474 [2000].

[222] A. J. Leggett, Reviews of Modern Physics **73**, 307 [2001].

[223] M. Rigol and A. Muramatsu, Physical Review Letters **94**, 240403 [2005].

[224] A. Minguzzi and D. M. Gangardt, Physical Review Letters **94**, 240404 [2005].

[225] F. Verstraete, J. J. García-Ripoll, and J. I. Cirac, Phys. Rev. Lett. **93**, 207204 [2004].

[226] T. Barthel, U. Schollwöck, and S. R. White, Physical Review B **79**, 245101 [2009].

[227] S. R. White, Physical Review Letters **102**, 190601 [2009].

[228] E. M. Stoudenmire and S. R. White, New Journal of Physics **12**, 055026 [2010].

Acknowledgements

Many people contributed to this thesis, scientifically as well as by ensuring I never moved too far from sanity. Special thanks go to:

- Jens, for the munich-metal-november, the annual trip to switzerland and being so easy to localize on concerts.

- Stefi, Stefan, Aki, and many others who made learning japanese at LMU a fun experience.

- Stefan, Dagmar and Thomas for all those nice cooking and board game evenings.

- Stefan, Caro, Lukas, Peter and Marin for being great office-mates.

- To any person who is able to tell all the $\text{Ste}\{ph, f\}\text{ans}$ apart.

- Last but not least of course, thanks to whole my family for their love and their support, even though they do not understand the least of what I do.

Selbstständigkeitserklärung

Hiermit versichere ich, dass ich die vorliegende Arbeit selbstständig und ohne Benutzung anderer als der angegebenen Quellen und Hilfsmittel verfasst habe. Sämtliche Zitate habe ich als solche kenntlich gemacht.

München im Mai 2012

Stephan Langer